Relevance of Alfvénic turbulence for Jupiter's auroral emissions

INAUGURAL-DISSERTATION

ZUR

ERLANGUNG DES DOKTORGRADES

(Dr. rer. nat.)

DER MATHEMATISCHEN-NATURWISSENSCHAFTLICHEN FAKULTÄT

DER UNIVERSITÄT ZU KÖLN

VORGELEGT VON

SASCHA JANSER

AUS SOLINGEN

Köln, 2022

Erstgutachter Prof. Dr. Joachim Saur
Zweitgutachter Prof. Dr. Bülent Tezkan

Tag der mündlichen Prüfung: 03. März 2022

Abstract

In this thesis, we investigate the relevance of Alfvénic turbulence and related wave-particle interaction processes for Jupiter's auroral emissions. Low-altitude Juno spacecraft observations above Jupiter provide strong hints on a dominating role of Alfvén waves in related particle energization processes. Besides bi-directional electron pitch-angle distributions, data prominently reveal broadband energy distributions for auroral electrons connected to the Io flux tube and the main emissions. Furthermore, low-frequency power spectra of magnetic field fluctuations exhibit a power law-like behavior, which is indicative for turbulence. Using these and further system-related information, we characterize turbulence in these regions and examined the spectral dispersion and dissipation properties of associated kinetic Alfvén waves.

Turbulence in the Io flux tube is established by the complex interaction of Io and the streaming torus plasma. Alfvénic perturbations are generated, which propagate along the magnetic field lines. Based on wave reflections at the Jovian ionosphere and at the Io torus boundary, an energy cascade process is established. By the related non-linear wave-wave interactions, wave energy is transported towards smaller spatial and temporal scales. The generated waves turn into kinetic Alfvén waves during their propagation in the inhomogeneous plasma environment. On kinetic scales of the plasma, the waves develop dispersive and dissipative properties and generate parallel electric fields, which allow for intense Landau damping. In the high-latitude region of Jupiter, we assume the kinetic Alfvén waves to significantly heat particles responsible for the Io footprint emissions. For the middle magnetosphere, i.e., radial distances of 20 - 30 Jupiter radii, flux tube interchange motions are thought to be the generator of the observed Alfvénic turbulence in the plasma sheet. By similar reflection processes, we hypothesize kinetic Alfvén waves to efficiently generate auroral particle precipitation.

To study turbulence in both regions, we start with a basic characterization of the large-scale wave fields to constrain models for Alfvénic turbulence at generator locations inside and outside the plasma sheet. We demonstrate that these wave fluctuations would be observed by Juno at high latitudes as spatially convected wave fields, structured perpendicular to the background magnetic field. Consequently, we reinterpret the spectral indices from observations by *Sulaiman et al.* (2020) and *Gershman et al.* (2019). We suggest the related lower-frequency power spectra to be the result of weak-MHD inside the plasma sheet or subion scale kinetic Alfvén wave turbulence outside the plasma sheet. Calculated turbulence heating rates are consistent with observed energy fluxes in the Io flux tube and the middle magnetosphere and represent efficient drivers for particle acceleration.

Based on this characterization of turbulence, we examine the dispersive and dissipative properties of monochromatic kinetic Alfvén waves along auroral magnetic field lines, connected to the Io footprint and the main emissions. We use a local description for the wave properties based on the hot plasma dispersion relation and also a simplified model from *Lysak* (2008). We show that for a wide range of parameters both models give coinciding results. In this context, we demonstrate that electron Landau damping plays a major role for dissipation of wave energy. We analytically show that its onset is related to the ion acoustic length ρ_s and the electron inertial length scale λ_e in the warm and cold Alfvén regime, respectively. Ion Landau damping only contributes to heating at smallest wave scales considered.

To quantify wave damping, we develop a model for the residual wave energy density along the magnetic field lines based on the electromagnetic Poynting theorem. We include dissipation processes from resonant and non-resonant wave-particle interaction in the model description. With this model, we are able to evaluate implemented expressions for the spectral perpendicular and parallel wave electric field components and corresponding particle responses. We calculated a peak electric field strength of $10^{-4}\,\mathrm{Vm}^{-1}$, which corresponds to a characteristic electron heating of 6.5 keV. Based on a different approach over heating rates, we estimated a heating of 26 keV. These values are in a range required to drive UV auroral emissions.

Furthermore, we find that the dissipated power density at high latitudes due to kinetic Alfvén waves is determined by a trade-off between available small-scale wave energy and the damping strength of the waves. Consequently, there is a wavenumber band in the dissipation spectra for which auroral heating maximizes. Furthermore, we identify that the density profile above the Jovian ionosphere is a major driver to control the amount of transferred energy. Small ionospheric scale heights are associated with a shift in the location of maximum auroral heating due to smaller wave scales and associated stronger background magnetic field. From parameter studies considering thermal and hot particle species, we conclude that the latter ones are heated more efficiently by kinetic Alfvén waves. By integrating over the dissipation volume and the spectral range of maximized dissipation, we determine maximum input powers of $8.4 \cdot 10^{13}\,\mathrm{W}$ and $13 \cdot 10^{13}\,\mathrm{W}$ in the main auroral acceleration region due to weak and KAW turbulence, respectively. These values coincide with observations in this region and suggest Alfvénic turbulence as potential driver for the main emissions.

In a similar analysis for the Io flux tube, we detemined a maximum input power of $7 \cdot 10^{10}\,\mathrm{W}$ for the electrons. Our calculations stress the importance of the presence of an auroral density cavity at high latitudes to generate sufficient strong wave-particle interactions.

Finally, we investigate perpendicular ion heating in the Io flux tube motivated by JADE and JEDI observations of heated proton populations from *Szalay et al.* (2020a) and *Clark et al.* (2020), respectively. We consider the non-resonant heating mechanism according to *Lu and Li* (2007). Our study reveals that only initially hot protons at high latitudes can be sufficiently heated in the presence of the density cavity to explain observed energies.

Zusammenfassung

In dieser Arbeit untersuchen wir die Relevanz von Alfvénischer Turbulenz, sowie die damit zusammenhängenden Welle-Teilchen Wechselwirkungsprozesse für das Entstehen von Jupiters Aurora-Emissionen. Beobachtungen der Juno Raumsonde in geringer Höhe über Jupiter legen nahe, dass die Alfvénwellen eine wichtige Rolle im Zusammenhang mit den Teilchen-Beschleunigungsprozessen einnehmen. Neben bidirektionalen Pitchwinkel-Verteilungen zeigen die Daten breitbandige Energieverteilungen der Aurora-Elektronen, welche mit der Io Flussröhre und den Hauptemissionen zusammenhängen. Des Weiteren zeigen niederfrequente Leistungsspektren von Magnetfeldfluktuationen ein Potenzgesetz auf, welches charakteristisch für Turbulenz ist. Unter Verwendung von systembezogenen Größen, charakterisieren wir die Art der Turbulenz in diesen Regionen. Ferner untersuchen wir dort das spektrale Dispersions- und Dissipationsverhalten der dazugehörigen kinetischen Alfvénwellen.

Die Turbulenz innerhalb der Io Flussröhre entsteht durch die komplexe Interaktion von Io und dem zuströmenden Torusplasma. Durch diesen Prozess werden Alfvénischen Störungen erzeugt, welche sich entlang der Magnetfeldlinien ausbreiten. Basierend auf den Wellenreflexionen an der Jupiter Ionosphäre und am Io Torusrand, wird ein Energie Kaskadierungsprozess angeregt. Dies ist bedingt durch die nicht-linearen Welle-Welle Interaktionen bei denen die Wellenenergie zu kleineren räumlichen und zeitlichen Skalen transportiert wird. Die generierten Wellen transformieren sich während ihrer Ausbreitung in der inhomogenen Plasmaumgebung zu kinetischen Alfvénwellen. Die Wellen entwickeln dispersive und dissipative Eigenschaften auf kinetischen Skalen des Plasmas und erzeugen parallele elektrische Felder, welche eine intensive Landau Dämpfung ermöglichen. Es wird angenommen, dass in Jupiters hohen Breiten kinetische Alfvénwellen die Teilchen signifikant beschleunigen. Diese sind für die Io-Fußpunktemission verantwortlich. Für die mittlere Magnetosphäre, also in einem Bereich von 20-30 Jupiter-Radien, vermutet man, dass Flussröhren Austauschbewegungen ursächlich für die Alfvénischen Turbulenz in der Plasmaschicht sind. Wir nehmen an, dass durch ähnliche Reflexionsprozesse wie in der Io Flussröhre kinetische Alfvénwellen verantwortlich für die Hauptaurora Emissionen sind.

Um die Turbulenz in beiden Regionen zu untersuchen, starten wir zunächst mit einer grundlegenden Charakterisierung der großen Skalen des Wellenfeldes, um Modelle für die Alfvénische Turbulenz innerhalb und außerhalb der Plasmaschicht festzulegen. Wir zeigen, dass solche Wellenfluktuation in den hohen Breiten von Juno als räumlich transportiertes Wellenfeld beobachtet werden würde. Daraus folgend reinterpretieren wir die spektralen Indizes von *Sulaiman et al.* (2020) und *Gershman et al.* (2019). Wir schlagen vor, dass das zugehörige niederfrequente Leistungsspektrum das Resultat von schwacher MHD Turbulenz innerhalb der Plasmaschicht oder kinetischer Alfvénwellenturbulenz außerhalb der Plasmaschicht ist. Abschätzungen des Turbulenzheizpotenzials sind konsistent mit beobachteten Energieflüssen in der Io Flussröhre und der mittleren Magnetosphäre. Daher repräsentieren diese Turbulenzgeneratoren effiziente Mechanismen für Teilchenbeschleunigung.

Basierend auf der Charakterisierung der Turbulenzmodelle untersuchen wir die dispersiven und dissipativen Eigenschaften von monochromatischen kinetischen Alfvénwellen entlang von Magnetfeldlinien, die mit dem Io-Fußpunkt und den Hauptemissionen zusammenhängen. Wir nutzen lokale Beschreibungen für die Welleneigenschaften basierend auf der heißen Plasmadispersionsrelation, sowie ein vereinfachtes Modell von *Lysak* (2008). Wir zeigen, dass beide Modelle für ein großes Spektrum an Parametern übereinstimmende Ergebnisse liefern. In diesem Kontext zeigen wir, dass die Elektronen Landau Dämpfung eine dominante Rolle bei der Dissipation von Wellenenergie spielt. Wir stellen analytisch dar, dass ihr Einsetzen direkt mit der Ionen-akustischen Radius ρ_s und der Elektronenträgheitslänge λ_e in dem jeweiligen warmen und kalten Alfvénischen Bereichen zusammenhängt. Die Ionen Landau Dämpfung hat hingegen meist nur Beiträge auf den kleinsten angenommenen Wellenskalen.

Um die Wellendämpfung zu quantifizieren, entwickeln wir ein Modell für die Wellenenergiedichte entlang der Magnetfeldlinien, basierend auf dem Poynting Theorem. Wir beziehen die Dissipationsprozesse von resonanter und nicht-resonanter Welle-Teilchen Wechselwirkung in die Beschreibung des Modells ein. Mit diesem Modell können wir implementierten Ausdrücke für das parallele und elektrische Feld der kinetischen Alfvénwellen und dazugehörige Teilchenbewegungen bestimmen. Wir berechnen ein Peak der elektrischen Feldstärke von bis zu $10^{-4}\,\mathrm{V/m}$, welcher einer charakteristischen Elektronenheizung von 6.5 keV entspricht. Basierend auf einem alternativen Ansatz schätzen wir eine Elektronenheizung von 26 keV. Diese Werte liegen innerhalb des Bereichs, welcher notwendig ist, um UV Aurora-Emissionen anzuregen.

Des Weiteren finden wir heraus, dass die dissipative Energiedichte aufgrund von Alfvénwellen in den hohen Breiten durch den Kompromiss von verfügbarer Energie auf kleinen Wellenskalen und der Dämpfungsstärke der Welle bestimmt wird. Somit existiert ein begrenztes Wellenzahlband in der Spektralen Dissipationsverteilung, für das die Aurora am stärksten angeregt wird. Weiterhin identifizieren wir das Dichteprofil oberhalb von Jupiters Ionosphäre als ausschlaggebenden Faktor für die Kontrolle der übertragenen Energie. Kleinere Ionosphärische Skalenhöhen sind mit einer Verschiebung der Lokation der stärksten Heizung verbunden, als Resultat von kleineren Wellenskalen, sowie einem stärkeren Magnetfeld. Auf Grundlage von Parameterstudien mit thermischen und heißen Teilchenspezies schließen wir, dass wärmere Teilchenspezies effizienter von den kinetischen Alfvénwellen geheizt werden können. Durch die Integration über das Dissipationsvolumen und des Wellenzahlbereichs, für den die Dissipation maximal ist, haben wir auf der Grundlage von schwacher und KAW Turbulenz die Inputenergie in der Beschleunigungsregion für die Hauptemission abgeschätzt. Die maximalen Inputenergien von $8.4 \cdot 10^{13}\,\mathrm{W}$ und $13 \cdot 10^{13}\,\mathrm{W}$ sind im Einklang mit Beobachtungen und legen daher Alfvénische Turbulenz als Ursachen für die Hauptemissionen nahe.

In einer ähnlichen Analyse für die Io Flussröhre bestimmen wir für die Elektronen eine maximale Inputenergie von $7 \cdot 10^{10}\,\mathrm{W}$. Unsere Berechnungen unterstreichen die Wichtigkeit eines Dichtehohlraums oberhalb der Ionosphäre, um ausreichend starke Welle-Teilchen Wechselwirkung zu generieren.

Abschließend untersuchen wir das senkrechte Heizen von Ionen in der Io Flussröhre, basierend auf Juno/JADE und JEDI Beobachtungen von geheizten Protonenspezies durch *Szalay et al.* (2020a) und *Clark et al.* (2020). Wir beziehen dafür den nicht-resonanten Heizmechanismus nach *Lu and Li* (2007) ein. Unsere Studie zeigt, dass nur ursprünglich heiße Protonen in einer dichtearmen Region oberhalb der Ionosphäre erhitzt werden können, um die beobachteten Energien erklären zu können.

Contents

CHAPTER 1

Introduction

Terrestrial aurorae have fascinated humankind for thousands of years and shaped mythological beliefs and legends. However, aurorae are not unique to the planet Earth, but also other celestial bodies are known to exhibit such emissions as well. These are namely the planets Jupiter, Saturn, Uranus, Neptune, and the Galilean satellite Ganymede. Recently, *Hallinan et al.* (2015) and *Kao et al.* (2016) found hints for aurora on brown dwarfs for the first time. However, observational studies from *Saur et al.* (2018a) and *Saur et al.* (2021) could not confirm these. The general occurrence, morphology, and characteristics of auroral emissions heavily depend on the object's atmospheric composition, its magnetic field, the surrounding particle reservoir and especially the detailed physical plasma interaction and acceleration of involved particles (*Chakrabarti and Galand*, 2010). Thus, a commonly used definition considering the wide range of aurorae refers to light emissions excited by the precipitation of external energetic particles onto a celestial body's atmosphere (*Clarke et al.*, 2004). The unique characteristics of Jupiter, but also of the Jovian system in general, make it outstanding in the solar system for several reasons. Especially the system of the Galilean moons and their electromagnetic interaction with Jupiter serve as a role model for exoplanetary research. Thus, a deeper understanding of the Jovian aurora will give valuable insight into Jupiter's system itself but also into exoplanets.

Today's research on the Jovian system was initiated by the discovery of the Galilean moons (initially called the 'Medician Stars' (*Van Helden* (1989)) by Galileo Galilei (1564-1642) in 1610, who significantly improved the recently invented telescope at that time and thus enabled his observations. The moons' discovery can be considered as an early proof against the widely accepted Geocentric world model back then. However, it took another four centuries until technical progress in both, spacecraft and telescope research, enabled the detection of Jupiter's vast magnetosphere and also the magnificent auroral lights. Since then, Jupiter and its moons have been fascinating objects of high scientific interest expressed by several telescope observations and spacecraft missions. Telescope surveys from IUE (1976-1996), Hubble (since 1990) and earth-based radio observations have significantly contributed to the current understanding of the magnetospheric dynamics and electromagnetic interactions. The first observations of the Jupiter system date back to 1955, when *Burke and Franklin* (1955) detected radio emissions at decametric wavelengths. Together with decimectric radio data, Jupiter's strong magnetic field was confirmed later on (*Bagenal et al.* (2017)). *Bigg* (1964) showed that Jupiter and Io form an electromagnetic connection.

The kind of their proposed interaction was fundamentally changed by the detection of the dense Io plasma torus by *Brown* (1976). Spacecraft research started with the Pioneer 10 and 11 flyby missions in 1973 and 1974, which amongst others detected the ionosphere of Jupiter and explored the expanse of the magnetosphere (*Bagenal et al.* (2017)). Data collected during the subsequent Voyager missions broadly extended the understanding of the magnetosphere and also allowed *Broadfoot et al.* (1979) to first detect Jupiter's ultraviolet (UV) aurora. Most outstanding were the observation of volcanic activity, which has been proven on the moon Io. Ulysses (1992), Cassini (2000) and the New Horizons (2007) flyby missions provided further insight into the magnetosphere of Jupiter. From 1995 to 2003, the Galileo spacecraft was the first orbiting mission with a major focus on the multiple flybys of the Galilean moons exploring them in more detail than ever before.

Since July 2016, the Juno spacecraft is in a highly inclined orbit around Jupiter in order to explore the high latitude region of Jupiter at low altitude in unprecedented detail for the first time. One of the highlighted scientific objectives of the mission is to "*characterize and explore the three-dimensional structure of Jupiter's polar magnetosphere and auroras*" (*NASA*, 2021). First publications on early Juno measurements of auroral particles in regions of expected acceleration indicated a paradigm change of established models for the acceleration mechanism of energetic particles. The observations revealed a bi-directionality in pitch-angle distributions and additionally broadband energy distributions as well. This is in contrast to the traditional mono-energetic energization approach known from Earth. Based on these findings, an acceleration mechanism of stochastic nature seems to be more appropriate to describe the generation process of auroral particles. Together with the commonly observed Alfvén mode in the Jovian magnetosphere, wave-particle interaction seem to take a more prominent role in the mediation of magnetospheric stresses at Jupiter than expected prior to the Juno mission. Furthermore, low-frequency turbulence is observed in the plasma sheet but also recently by Juno in the high latitudes, which suggests a connection between the wave fields in both in regions.

The kinetic Alfvén wave (KAW) is a promising mode to meet the observational constraints in the middle magnetosphere. *Saur et al.* (2018b) suggested it to be an essential driver for particle acceleration accounting for the auroral power input. This mode is a kinetic extension of the MHD Alfvén mode and develops dispersive and dissipative characteristics on small perpendicular wave scales. Thus, the KAW can undergo efficient wave-particle interaction via parallel electric fields. In the magnetospheric environment, there are several conceivable processes to generate such waves. One of these generation processes concerns phase mixing of neighboring Alfvénic wave packages due to perpendicular density gradients with respect to the ambient magnetic field as proposed by *Hasegawa and Chen* (1974). This mechanism is generally evoked in non-local field line resonance models such as applied by e.g., *Lysak and Song* (2020) or in the Ionospheric resonator model by e.g., *Lysak and Song* (2008). A second possible process in an inhomogeneous plasma is resonant mode conversion by which propagating Alfvén waves evolve into a KAW (e.g., *Hasegawa and Chen* (1976)). Besides this incomplete list of mechanisms, MHD turbulence is suggested to be an important generator of small-scale Alfvén waves (e.g., *Saur et al.* (2002), *Saur et al.* (2018b)), already well-known from solar wind turbulence studies (e.g. *Howes et al.* (2006); *Schreiner and Saur* (2017)), but in a different parameter regime than in the Jovian magnetosphere. Due to non-linear interactions of counter-propagating Alfvén waves, available input energy on large-scales is transported anisotropically towards smaller temporal and spatial scales. This filamentation process establishes a turbulent cascade and thus highly structured wave fields (*Saur et al.*, 2003). In the present work, we will investigate Alfvénic turbulence as driver for the generation of auroral particles connected to Jupiter's main emissions and Io's footprint emissions on the basis of new results from the Juno mission.

To quantify the dissipation associated with kinetic Alfvén waves, we proceed as follows: In Chapter 2, we give an introduction to the Jupiter system and into the current state of research regarding auroral emissions and established models for generation. We also shortly present observations from the Juno spacecraft, which contradicts the conventional particle energization process associated with the auroral power input. In Section 3, we present the theoretical framework to describe linear wave modes in a hot plasma. In particular, we focus on the dispersive and dissipative properties of the Alfvén mode and its small-wavelength limit. In this context, we present expressions to quantify wave electric fields and particle responses in terms of current densities. These quantities will be used in the thesis to assess the properties of the kinetic Alfvén wave. Chapter 4 includes the field line models of the plasma parameters used for the modeling studies. We additionally develop a model for the residual Alfvén wave fluctuation amplitude undergoing changes in the inhomogeneous medium in the presence of dissipation. In Chapters 5 and 6, we analyze the implications for occurring turbulence from recent Juno observations in the Io flux tube tail and the main emissions from *Sulaiman et al.* (2020) and *Gershman et al.* (2019). These studies lay the foundation for the turbulence models studied in the subsequent chapters. With these information, we go on to analyze the spectral behavior of the kinetic Alfvén wave for different turbulence models and related generator regions in Chapter 7. Thereby we distinguish the contributions from different resonant damping processes. With these prestudies, we discuss the dissipation characteristics of monochromatic turbulent KAWs along main auroral field lines, described in Chapter 8. We assess the wave scales which are relevant to damping and analyze the influence of parameters affecting the dissipated power. We complete our discussion with estimates of the total power transferred to the particles by Alfvénic turbulence for a generator location inside and outside the plasma sheet. We do an equivalent analysis for the Io flux tube in Chapter 9. Furthermore, we examine non-resonant ion heating in this region and compare our modeling results with Juno observations of heated proton populations. In the final Chapter 10, we summarize our results and elaborate on future aspects of research.

CHAPTER 2

Jupiter's aurora, the current state of research

In this chapter, we give an overview of the current state of auroral research regarding its historical development. For this, we start with an introduction into the basic peculiarities of the Jupiter system in order to understand the associated auroral physics. Afterwards, we present observations related to the main auroral emissions and the Io footprint tail by the current Juno mission. The implications from these observations will be the foundation for the analysis carried out in this thesis. Finally, we discuss the established model for aurora emissions in general and review the approaches to acceleration processes in the literature.

2.1. Jupiter's Magnetosphere and Satellites

The gas giant Jupiter is outstanding in our solar system in several aspects. Not only is it the most massive and largest planet, but is also the fastest rotator equipped with a strong dynamo magnetic field. The corresponding values to these quantities are summarized in Table 2.1. The intrinsic magnetic field, with a tilted dipole moment of about 9.9° with respect to the rotation axis, creates a huge and dynamic magnetosphere with a dayside extension of 63 - 92 R_J (*Bagenal et al.*, 2017). The four Galilean satellites orbit Jupiter at close-in distances and serve as sources of plasma material to their surroundings (see Table 2.2). The strongest contribution comes from the innermost satellite Io, which provides about one ton of material per second to the Io plasma torus, which formed around Io's orbit (*Kivelson et al.*, 2004). By the rotation of Jupiter's tilted magnetic field, the Io torus co-rotates with it and thereby undergoes a wobbling up and down motion. Due to the centrifugal force and plasma pressure gradient force, the plasma diffuses radially outward in an equatorial sheet, which makes up the so-called plasma sheet. It is mainly constituted of sulfur and oxygen ions (*Dougherty et al.*, 2017). In the equatorial region, the plasma density is largest, but rapidly falls off above and below the sheet. In radial direction, it is observed to decrease (*Bagenal and Delamere*, 2011). Close to Jupiter, the magnetospheric density is lowest and the plasma is mainly made up of hydrogen ions originating from Jupiter. This aspect will be important later in discussing properties of Alfvén waves, which propagate in these regions. Within the plasmasheet, the density is observed to radially decrease, but plasma temperature increases (see e.g., *Saur* (2004)). Parameter models used in the context of this thesis are presented in Section 4.

	Jupiter
Rotation period [h]	9.9
Equatorial radius R_J [km]	71492
Mass [kg]	$1.9{\cdot}10^{27}$
Equatorial magnetic field [nT]	$4.3 \cdot 10^5$
Dipole field inclination [°]	9.9

Table 2.1.: *Physical properties of Jupiter, taken from Bagenal et al. (2017).*

	Io	Europa	Ganymede	Callisto
Distance to Jupiter [R_J]	5.9	9.4	15.0	26.3
Orbital period [days]	1.77	3.55	7.16	16.69
Radius [km]	1821	1561	2631	2410
Mass [kg]	$8.9{\cdot}10^{22}$	$4.8{\cdot}10^{22}$	$1.5{\cdot}10^{23}$	$1.1{\cdot}10^{23}$
Mass loss rate [ions/s]	$\sim 10^{28}$	$<6 \cdot 10^{26}$	$<6 \cdot 10^{26}$	$<5{\cdot}10^{25}$
Rel. plasma flow [km/s]	57	76	139	192

Table 2.2.: *Physical properties of the Galilean moons. Mass loss rates were taken from Kivelson et al. (2004), all other quantities from Weiss (2004).*

The dynamics of the inner and middle magnetosphere is, unlike Earths', not controlled by the interaction with the impinging solar wind but instead is fully dominated by the strong and rotating magnetic field in combination with the radially diffusing plasma. The associated physics is discussed in Section 2.3.1. In this context, extraction of Jupiter's rotational energy is thought to be a major driver for the auroral processes. The available total energy goes partly into the enforcing of the co-rotation of the plasma sheet. An open question is the amount of remaining energy that goes into the generation of meridional current systems, i.e. the auroral current systems, or Alfvénic turbulence. Plasma turbulence is commonly observed in the equatorial plasma sheet as shown by *Saur et al.* (2002) and *Tao et al.* (2015), who analyzed highly resolved magnetic field data collected over several years during the Galileo mission. Associated magnetic field fluctuation amplitudes were found to be small compared the Jovian background field. The corresponding power spectra established the idea of an anisotropic energy cascading process in the middle magnetosphere perpendicular to the background magnetic field with a spectral index of $\alpha = -2$. That was interpreted by *Saur et al.* (2002) as weak Alfvénic MHD turbulence. In a later study based on a combination of Galileo data, with high and low time resolution, *Tao et al.* (2015) came up with spectral indices in a range of -0.6 and -1.9 for frequencies smaller than ion scales. For sub-ion scales, the observed turbulent structures showed a steeping towards a range of -1.7 and -2.5 in spectral index. *Saur* (2004) proposed the available turbulent energy as a potential source for the observed radially increased heating of plasma. Alternatively, *Saur et al.* (2002) suggested that the turbulence is linked to particle energization associated with the main auroral emissions. Recent observations in the context of the Juno mission, from *Gershman et al.* (2019) regarding the main emissions and *Sulaiman et al.* (2020) in a region connected to the Io flux tube, revealed highly structured magnetic field fluctuations for low frequencies. The authors interpreted these observations as a result of Alfvénic turbulence, which is a key argument for the interconnection of magnetospheric processes in the plasma sheet and at high latitudes. In case of the Io flux tube, filamented wave spectra are reminiscent of turbulence. Turbulent power spectra are also present in the vicinity of Io as investigated by *Chust et al.* (2005). These observations hint that Alfvénic turbulence plays a role in or even drives the energetics of Io's Alfvén wings.

2.2. Jupiter's auroral emissions

Jupiter hosts the brightest aurora compared to other planets in our solar system. With a total emitted power on the order of $10^{13}\,W$, the emissions are a hundred times stronger than these of the Earth (*Clarke et al.*, 2004). Dominant contributions originate from thermal emissions in the infrared (IR) wavelengths (*Satoh et al.*, 1996) mainly by currents heating the auroral atmosphere and ionosphere, and emissions in the ultraviolet (UV) wavelengths (*Prangé et al.*, 1998) from direct energetic particle precipitation. Emissions in the visible (*Vasavada et al.*, 1999) and radio range contribute to a lesser extent, with powers up to 100 GW (*Bhardwaj and Gladstone*, 2000). Broad and more detailed reviews are provided by the works of *Bhardwaj and Gladstone* (2000) and *Clarke et al.* (2004).

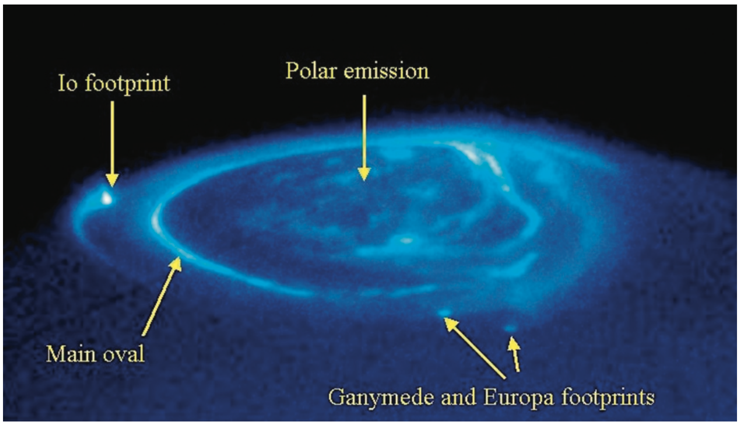

Figure 2.1.: *Image of Jupiters northern UV aurorae taken with the Hubble Space Telescope Spectrograph (STIS) in November 1998. Figure is taken from Clarke (2012), originally published in Clarke et al. (2004). Courtesy of this figure belongs to NASA and John Clarke (University of Michigan).*

Also the auroral morphology is manifold as one can be seen in Figure 2.1, which is a Hubble-STIS ultraviolet image of the northern hemisphere taken in 1998. The most prominent feature and subject of current research is the oval-shaped and stable band of emissions rotating with Jupiter at a co-latitude of ∼15° around the magnetic pole. On the southern hemisphere, there are similar emissions as well. These are called the "main emissions" or earlier "main (auroral) ovals" and map along the magnetic field towards equatorial distances of 20 - 30 Jupiter radii in the equatorial magnetosphere (*Gérard et al.*, 1994; *Prangé et al.*, 1998; *Bagenal et al.*, 2017). They are currently thought to be driven by field-aligned currents and are therefore categorized as discrete aurora. The latitudinal thickness of the "oval" ranges between 100 - 1000 km (e.g.,*Cowley and Bunce* (2003); *Clarke et al.* (2004)). The temporally variable and more diffuse "polar emissions" inside the main aurora subdivide into three regions, called the active, swirl, and dark polar region. Although their detailed origins are not fully understood, it is thought that magnetopause interactions with the solar wind (and related solar activity) and associated dawn storm events cause and shape these emissions (*Gérard et al.*, 2019). Wave-particle interactions of electrons with the high-frequency Whistler mode is evoked to be relevant for the diffuse aurora (*Elliott et al.*, 2018a,b, 2020; *Li et al.*, 2021). The localized footprint emissions stem from the electromagnetic interaction of the Galilean moons with the overtaking corotating plasma (see Table 2.2), which induce perturbations in the local magnetic field environments. The total emitted power associated with this interaction in case of the Io footprint is on the

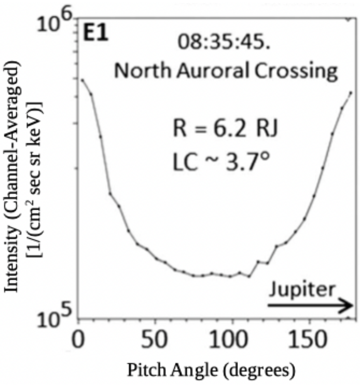

Figure 2.2: *Sample pitch angle distribution for electrons measured by the JEDI instrument during the northern main emissions crossing of the first Perijove (PJ1). Figure is taken from Mauk et al. (2017b), reproduced with permission of AGU.*

order of 10^9 - 10^{11} W, mainly from UV and IR contributions and with a order of magnitude smaller contribution from the radio frequency range (*Bhardwaj and Gladstone*, 2000; *Saur et al.*, 2004, 2013). These footprints have substructures, which we discuss in Section 2.5 at the example of Io.

2.2.1. Recent Juno observations

The Juno mission was designed by NASA to enhance the current understanding of Jupiter's aurora and related polar magnetospheric physics besides gaining further insight into atmospheric processes and Jupiter's interior structure. For this purpose, Juno is equipped with several scientific instruments (*Bagenal et al.*, 2017). In the context of auroral acceleration processes, relevant results come from the particle detectors JADE and JEDI and from the MAG and Waves instruments for the detection of plasma waves, especially Alfvén waves. JADE focuses on lower energetic particles, in particular for electrons in an energy range between 100 eV - 100 keV and for ions between 5 eV - 50 keV. The JEDI instrument probes the energy distribution and pitch angles of high energetic particle populations. For electrons, energies range between 25 keV - 1 MeV, whereas ions can be detected in a range of 10 keV - 2 MeV (*Mauk et al.*, 2017a). The MAG instrument consists of Fluxgate magnetometers and samples magnetic fields with a rate of 64 vector samples per second (*Connerney et al.*, 2017). The plasma waves instrument Waves comprises a search coil and an electric field antenna, which detect high-frequency magnetic and electric field signals in a frequency range of 50 Hz - 20 kHz (*Kurth et al.*, 2017).

Since Juno's arrival in 2016, it has completed 38 low-altitude polar Perijoves (PJ) until 29th of November 2021. Two of the unexpected findings regarding auroral processes concern the particle motion with respect to the ambient magnetic field and the energy distribution of the energetic particles. Early publications from *Mauk et al.* (2017b,c) and *Clark et al.* (2018) focusing on JEDI measurements over Jupiter's poles revealed strong bi-directional flow characteristics of energetic electrons above the main emissions. This is exemplarily shown in Figure 2.2. Furthermore, energy distributions only rarely showed hints for mono-energetic peaks as expected for quasi-static potential-driven acceleration processes known from Earth. Instead the distributions were broadband in nature as exemplarily depicted in Figure 2.3c for the first southern main emission crossing. During further Perijoves, *Mauk et al.* (2017c, 2018) and *Clark et al.* (2018) identified such peaked distributions (see Figure 2.3f) known for quasi-static field-aligned electric fields (here up to 400 kV observed). However, these events happen rarely in comparison to broadband distributions, but also seem to exist simultaneously (*Mauk et al.*, 2018). Additionally, electron fluxes associated with broadband distributions (typically 10 - 100 mW/m^2, up to

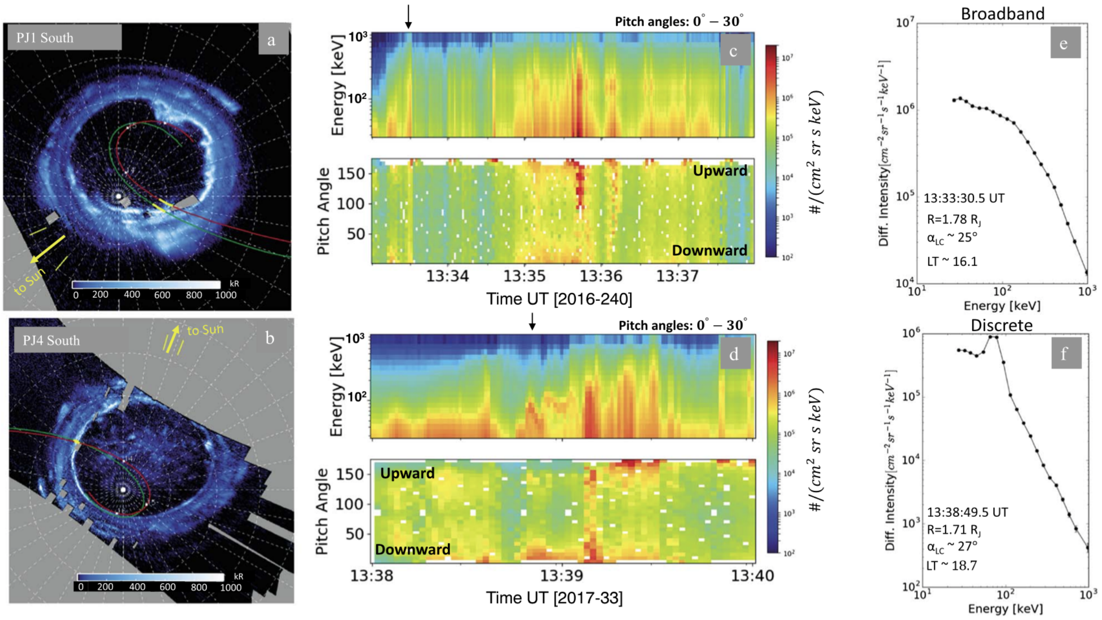

Figure 2.3.: *Broadband and mono-energetic characteristics of different main emission crossings. The top panel (subfigures a,c,e) refers to the southern main emissions crossing of PJ1. It shows the UV emissions during the crossing (subfigure a), the JEDI energy and pitch angle distributions versus time measurements for >30 keV electrons (subfigure c) for the time interval marked by yellow bars in the UV plot and energy spectra (subfigure e) for a time marked in c by the black arrow. The bottom panel (subfigures b,d,f) show the same quantities but for the southern main crossing of PJ4. Figure is taken from Clark et al. (2018), reproduced with permission of AGU.*

3 W/m^2) are significantly stronger than for peak-like events. For the former ones, contributions from electrons even in the MeV range has been observed. In contrast, proton distributions more often show mono-directional characteristics (*Mauk et al.*, 2018). The energetic electron observations were suggested to originate from a stochastic acceleration process. A promising approach to explain these observations is provided by *Saur et al.* (2002), who proposed wave turbulence to be related to the energetics of the main emissions and associated particle acceleration. This hypothesis is supported by observations of *Gershman et al.* (2019) who presented Juno-MAG measurements of low-frequency Alfvénic turbulence above the main emissions. Additionally, kinetic simulations of Alfvén waves in the magnetospheric context by *Damiano et al.* (2019) encourages the prominence of Alfvén waves in the involved heating processes of electrons.

2.3. Three-component model for aurora

The simplest model for the description of aurora consists of three components, namely a generator region, an acceleration region and a screen (*Mauk et al.*, 2002; *Mauk and Bagenal*, 2012). Closely related to the different components are the basic requirements for the existence of aurora, i.e., sources of material and energy, an atmosphere and an intrinsic magnetic field. In the solar system, several generator mechanisms are known to generate field-aligned electric currents. These include magnetopause interactions with the solar wind (*Delamere and Bagenal*, 2010; *Vogt et al.*, 2019); orbiting moons as mechanical obstacles to the ambient plasma flow, which generate stresses in the magnetic field (*Neubauer*, 1980); and the enforcement of corotation of magnetospheric plasma via meridional current systems (*Hill*, 1979). Although all of these generator mechanisms act in the Jovian magnetosphere, it is thought that the rotational mechanism provides the major contribution to Jupiter's energy budget for the main emissions (*Hill*, 1979, 2001; *Cowley and Bunce*, 2001). In the following subsections, we focus on the established processes related to the rotational aurora generator (MI-coupling current system) and moon-magnetosphere interactions. In this context, we discuss theories for auroral particle acceleration proposed in the literature. The screen region represents the final piece of the auroral system with charged particles precipitating onto the upper atmosphere. Collisions between energetic charges and neutral particles cause an excitation of the neutral particles. During the de-excitation process, the neutral particles emit radiation of a certain wavelength depending on their excitation state. In the case of Jupiter, UV emissions are the most prominent contribution to the aurora, but emissions at radio and infrared and visible wavelengths are present as well (*Bhardwaj and Gladstone*, 2000). These planetary emissions are considered to be a "window" to the physical processes acting in the distant magnetosphere, and hence, can be used as a diagnosing tool.

2.3.1. Aspects of the MI-coupling current system

A first model of the magnetosphere-ionosphere (MI)-coupling has been proposed by *Hill* (1979). It subsequently developed into a standard model of MI-coupling, where new data and better understanding of Jupiter's magnetosphere lead to improvements in the model (*Pontius and Hill*, 1982; *Hill*, 2001; *Cowley and Bunce*, 2001; *Cowley et al.*, 2003; *Nichols and Cowley*, 2004; *Ray et al.*, 2010). The idea behind this coupling is the extraction of rotational energy from Jupiter via its strong magnetic field. In general, the magnetic field couples to the magnetospheric plasma due to the frozen-in theorem in the infinitely conducting plasma. As a result, both the plasma and magnetic field corotates with each other. However, iogenic plasma additionally diffuses radially outwards in the equatorial region, as a consequence of centrifugally driven flux tube interchange motions (*Vasyliunas*, 1983; *Kivelson et al.*, 1997). In the torque-free case, this plasma would become subsequently sub-corotational with an azimuthal velocity drop of $v_\varphi \sim r^{-1}$ with distance r by the principle of angular momentum conservation. Likewise, the related magnetic field lines are associated with a stressed bend-back configuration state. The azimuthally deformed magnetic field lines generate a Lorentz force in the direction of the corotation and exert a torque on the sub-corotational plasma. This process causes an acceleration of the lagging plasma towards corotation by which the magnetic field lines relax again. The required torque is extracted from Jupiter's atmosphere through elastic collisions between atmospheric neutral particles and ionospheric ions due to differential velocities. In contrast to the magnetosphere, the torque extraction is associated with a Lorentz force in opposite direction in the ionosphere. The corresponding Pedersen currents flow in merdional direction and connect the radial corotation enforcement currents in the plasma sheet over magnetic field-aligned Birkeland currents. The speed-up mechanism of the magnetospheric plasma and related transport of angular momentum works most efficient up distances of $15\,R_J$ (*Chané et al.*, 2013). However, towards larger distances in the plasma sheet, the communication between both regions becomes less efficient and a so-called breakdown in corotation occurs. This region is thought to be located between $20\text{-}30\,R_J$ and is associated with the strongest field-aligned current flow, which maps towards the main emissions. The resulting meridional MI-coupling current system (shown in Figure 2.4) is generated from the described interplay of the different magnetospheric and ionospheric processes and eventually extracts rotational energy from Jupiter. The breakdown location is controlled by the ionospheric conductivity, the radial mass flux and the magnetic field strength. Observational evidence

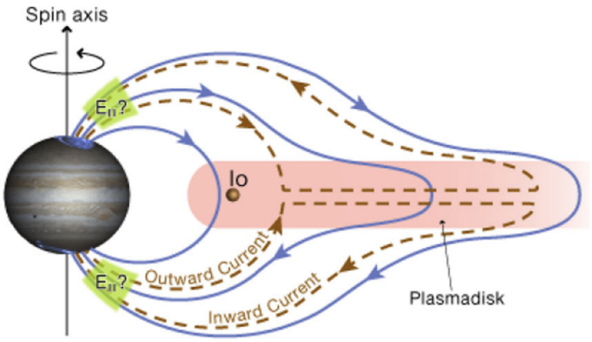

Figure 2.4.: *MI-coupling current system. Magnetic field lines are shown as blue solid lines and the current system is shown as a green dashed line. The physical description is given in the text. Figure is taken from Bagenal et al. (2017), reproduced with permission of Springer Nature.*

---

for the MI-coupling in terms of the corotation lag and also the existence of radial currents is provided and discussed by *McNutt et al.* (1981); *Kane et al.* (1995); *Krupp et al.* (2001) and *Khurana et al.* (2004).

The current density $\vec{j}$ can be written as

$$\vec{j} = ne(\vec{v}_i - \vec{v}_e) \tag{2.1}$$

with the particle density n, the elementary charge e and the velocities of ions $\vec{v}_i$ and electrons $\vec{v}_e$. In the meridional current system one can assume current continuity ($\nabla \cdot \vec{j} = 0$). For the plasma sheet equation (2.1) and current continuity imply that the dense plasma population provides a sufficient abundance of particles to maintain the occurring current. In the sparsely populated high-latitude regions and with the converging magnetic field lines, the current has to be maintained by high energetic particles, i.e., by large particle velocities. Thus, at high latitudes the particles have to be accelerated, which happens in the acceleration region.

2.4. Acceleration mechanisms in Jupiter's environment: State of Research

There is a wide variety of acceleration and heating mechanisms of charged particles acting in the Jupiter system. These play an important role in the plasma dynamics and transport processes in the different magnetospheric regions. In particular, these mechanisms are relevant for the auroral lights (main emissions, diffuse aurora, footprint and tail emissions), radiation belts, and also for the plasma sheet. One can classify the different acceleration mechanisms by their ability to heat different particle species either parallel or perpendicular to the magnetic field. The occurrence and efficiency of these processes are controlled by the detailed plasma properties and also by the time available for heating. In the following, we introduce some important classes for acceleration associated with the Jovian system. Then, we deal with a historical review of mechanisms proposed for the main auroral emissions.

Adiabatic and non-adiabatic transport processes, such as Betatron and Fermi acceleration in converging magnetic field geometries, rely on particle motions violating adiabatic invariants. Regarding the radiation belts, *Brice and Mcdonough* (1973) studied inward diffusion and associated adiabatic compression of solar wind originating electrons towards the inner magnetosphere. *Nishida* (1976) developed a cyclic global-scale mechanism as combination of inward and outward diffusive transport of electrons. They included pitch-angle scattering by whistler wave-interaction close to Jupiter to finally generate a net heating of electrons by the cyclic interplay of these (non-)adiabatic transport processes. More recently, *Kollmann et al.* (2018) concluded that adiabatic heating of radiation belt MeV electrons via radial diffusion is more efficient in the outer magnetosphere ($20 < L < 100$) than wave-particle interaction via whistler waves, which gets important for distances $L < 20$.

Particles can be also accelerated in (quasi-)static electric potentials formed by shock-like structures (e.g., *Erkaev et al.* (2001, 2002) in the Io flux tube), double layers (*Goertz and Ip*, 1982) or due to pitch-angle anisotropies in magnetic mirror geometries (*Mauk et al.*, 2002). Static field-aligned electric fields are commonly considered in the context of Earth as a primary acceleration mechanism of particles (*Knight*, 1973). *Knight* (1973) derived a current-voltage relationship for Earth's auroral emissions. It based on kinetic theory for Maxwellian distributed electrons following adiabatic motions along the field lines, which eventually gets lost to the atmosphere. This approach is considered as mono-energetic because all particles gain the same amount of energy. Thus, related energy spectra in these regions are characterized by mono-energetic peaks in energy distributions.

A very elementary class for acceleration is the interaction of plasma constituents with various kinds of waves, called wave-particle interaction. These are especially important in the nearly collisionless magnetospheric plasma because collisions occur too rarely to significantly modify the momentum of particles via Joule heating. Resonant and non-resonant wave-particle interaction by Ion-cyclotron waves, high-frequency Whistler waves (*Sulaiman et al.* (2020)) and low-frequency Alfvén waves (e.g., *Saur et al.* (2003); *Saur* (2004); *Saur et al.* (2018b)) are invoked. The involved processes such as Landau damping, harmonic cyclotron damping, and transit-time magnetic damping depend on plasma scales, population characteristics and on wave properties in general. For Jupiter's diffuse polar emissions, pitch-angle diffusion is regularly studied by interaction with Whistler mode waves by ,e.g., *Elliott et al.* (2018a,b, 2020)). MHD and kinetic wave turbulence as generator of small-scale waves for heating of ions and electrons is often considered in this context (*Barbosa* (1981); *Barbosa et al.* (1984); *Glassmeier* (1995)). The general occurrence of turbulence in the Jovian system has been reviewed by *Saur* (2021) with a focus on the Alfvén mode as it is expected to take an fundamental role in energy transport and communication of magnetic stresses. Acceleration and plasma heating in combination with kinetic Alfvén waves in the Jupiter system with special attention to the Io plasma torus and the Io flux tube was studied by *Das and Ip* (1992, 2000); *Crary* (1997); *Chust et al.* (2005); *Jones and Su* (2008) and *Hess et al.* (2010).

Acceleration regarding the main emissions

Hill (2001) and *Cowley and Bunce* (2001) summarized early approaches to main auroral particle acceleration at Jupiter in their papers. We adapt their logical structure in the following two paragraphs. Subsequently, we complement the review with approaches and progresses published afterwards.

Early ideas for the acceleration of the jovian auroral particles from *Thorne* (1983) focused on pitch-angle diffusion of magnetospheric plasma related to wave activity. However, the related energy fluxes were 2-3 orders of magnitude too low. A later study from *Tsurutani et al.* (1997) analyzed magnetometer and plasma wave data from a Ulysses flyby of Jupiter and also investigated pitch-angle diffusion with whistler waves. They concluded that such interactions at the magnetopause boundary generate insufficient energy fluxes in order to account for the main emissions.

Basic approaches for discrete auroral acceleration are closely related to the question of field line mapping of the main emissions and hence the physical connection towards different regions in magnetosphere. First ideas considered the main emissions to be connected to the Io plasma torus at $\sim 6\,R_J$ based on Voyager 1 and 2 spacecraft data from *Sandel et al.* (1979) and *Broadfoot et al.* (1979) and reported Earth-orbit based IUE telescope UV observations from *Clarke et al.* (1980). Contained sulfur and oxygen ions were thought to precipitate onto the Jovian atmosphere and generate the emissions (*Mauk et al.*, 2002). In the other extreme, the emissions and related parallel currents were suggested by *Isbell et al.* (1984) to be linked to the magnetopause region and associated solar wind interaction. A mapping towards the middle magnetosphere was eventually proposed by *Dougherty et al.* (1993) by the analysis of field-aligned current signatures in Ulysses spacecraft data. This was validated by HST observations from *Gérard et al.* (1994). In particular, *Connerney et al.* (1993) showed that the Io footprint emissions lie at lower latitudes than the main auroral oval. Thus, the main emissions are linked to the equatorial magnetosphere beyond the Io orbit. Later on, *Clarke et al.* (1998) found that the emissions even map to field lines beyond the Ganymede orbit of $15\,R_J$. *Hill* (2001) and *Cowley and Bunce* (2001) used the concept of MI-coupling (see Section 2.3.1) to relate the maximum field-aligned Birkeland currents in the middle magnetosphere to the main emissions. In this context, *Cowley and Bunce* (2001) applied the theory of *Knight* (1973) to determine a required quasi-static field-aligned potential drop of 100 kV to generate the emissions.

In a further step, the idea of MI-coupling was extended by *Mauk and Saur* (2007) who consider regions of intermixed currents in downward and upward direction, to consistently explain Galileo spacecraft observations of structured currents in the equatorial region. Such currents and related bi-directionality of electron populations were hypothesized by *Mauk and Saur* (2007) to be related to weak equatorial MHD wave turbulence based on former studies by *Saur et al.* (2002, 2003) and *Saur* (2004). On the basis of global energy estimates, *Saur et al.* (2003) suggested that the middle magnetospheric turbulent fluctuations can provide sufficient power for the main aurora. The associated Alfvén waves are thought to originate from non-continuous interchange of flux tubes (*Kivelson et al.*, 1997), which locally leads to an imbalance of the involved stresses. An alternative generator for turbulence was proposed by *Glassmeier* (1995). They suggested that the tilted rotational motion of the jovian magnetic field is associated with large-amplitude variations, which decay non-linearly to drive a turbulent cascade. The turbulent nature and hence structuring of the Alfvénic wave field is suggested by *Saur et al.* (2003) and *Saur et al.* (2018b) to be established by non-linear interactions of counter-propagating waves, which get partially reflected at strong density gradients. An illustration of the situation is presented in Figure 2.5. *Saur et al.* (2002) and *Saur et al.* (2003) brought up the idea that (kinetic) Alfvén waves propagate towards high latitudes in order to drive the MI-coupling towards stress balance. *Saur et al.* (2018b) investigated basic temporal and spatial plasma scales in the equatorial region and in the high latitudes for the potential of kinetic Alfvén waves to undergo wave-particle interaction in these regions. This promising approach is built on the idea that turbulently cascading waves reach kinetic scales, dissipate, and allow for a net energy transfer of the wave field towards the precipitating particles required for the auroral emissions. This acceleration mechanism is of stochastic nature, as the detailed wave-particle interactions depend on the particle distribution within the wave field. In the case of Landau damping, particles are accelerated by the waves in both directions along the background magnetic field depending on the wave phase. The corresponding particle energy distributions are characterized as broadband.

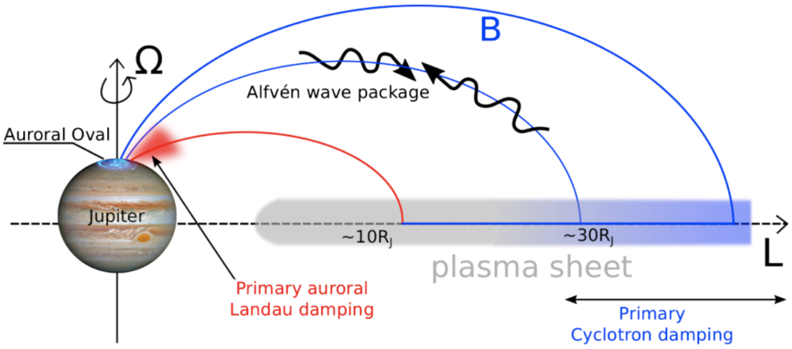

Figure 2.5.: *Overview of Alfvénic wave-particle interaction regions due to counter-propagating waves along magnetic field lines in the Jovian Magnetosphere. Further physical details are discussed in the text. Figure is taken from Saur et al. (2018b), reproduced in accordance with the AGU permission policy for authors.*

2.5. The Io footprint and its tail

The following section on the Io flux tube and its tail is submitted as paper to JGR (*Janser et al.*, 2022, submitted).

Besides the bright main auroral emissions and polar emissions, emissions related to the orbital motion of the Galilean satellites currently attract significant attention. In particular, Io's interaction with Jupiter is a topic of high interest since its discovery by *Bigg* (1964) via measurements of decametric radio emissions. In-situ measurements from Voyager 1 and 2 Jupiter flybys in 1979 revealed flow (*Belcher et al.*, 1981) and magnetic field (*Acuna et al.*, 1981) fluctuations at Io, which are consistent with Alfvénic disturbances resulting from magnetospheric plasma streaming past Io. The unipolar inductor model (*Piddington and Drake* (1968); *Goldreich and Lynden-Bell* (1969)) was the first theoretical model to describe the electromagnetic interaction and related power transmission in the Io flux tube (IFT). With the discovery of the dense Io plasma torus *Broadfoot et al.* (1979), the Alfvén wing model (*Neubauer*, 1980) was established which highlighted the importance of the MHD Alfvén mode. This mode forms stationary Alfvén wings in the rest frame of Io and electromagnetically connects the satellite with Jupiter. Subsequent Galileo flybys of Io since 1995 and also remote sensing of IR (*Connerney et al.*, 1993) and UV emissions (*Clarke et al.*, 1996; *Prangé et al.*, 1996) revealed more aspects of the complex local interaction and gave further observational evidence of the Io footprint emissions.

The morphology of Io's auroral emissions comprises several features. The main Alfvén wing (MAW) spot (*Bonfond et al.*, 2008) is a result of Io's immediate plasma interaction by which the generated power is propagated via Alfvén waves to Jupiter. The understanding of the processes which lead to accelerated electrons and ions was only poorly constrained before the footprint and tail crossing of Juno. Pre-Juno theories for particle acceleration cover electric fields of inertial Alfvén waves at high-latitudes (*Jones and Su*, 2008; *Hess et al.*, 2010), Alfvénic interaction in the torus region (*Crary*, 1997; *Das and Ip*, 1992), quasi-static field-aligned potential drops (*Su et al.*, 2003) and also production of electron beams in the torus by repeated Fermi acceleration with Alfvénic electric fields. Moreover, there are emissions from trans-hemispheric electron beams, originating from the MAW of the other hemisphere (*Bonfond et al.*, 2008). Further emissions are thought to come from Alfvén wave reflections inside the Io torus, considered as reflected Alfvén wing (RAW) spots (*Connerney and Satoh*, 2000; *Jacobsen et al.*, 2007). The Io footprint tail (IFPT) completes the set of observed auroral emissions connected to Io and is related to field lines downstream of Io. The IFPT was proposed to be driven by quasi-static potentials accelerating electrons (*Hill and Vasyliūnas*, 2002; *Delamere et al.*, 2003; *Su et al.*, 2003). Alfvénic mechanisms were suggested alternatively (*Crary and Bagenal* (1997); *Bonfond et al.* (2017)).

Juno measurements shed new light on the high-latitude region associated with the IFPT. Infrared measurements from *Mura et al.* (2018) revealed a highly structured and partially bifurcated morphology of the IFPT, but the corresponding physics remains an open question. Based on observations of broadband electron energy distributions with power-law like behavior and possible bi-directional characteristics in pitch-angle distributions (*Szalay et al.*, 2018, 2020b), current attention is now focused on an Alfvénic cause of the IFPT. This could be the same mechanism as for the MAW, potentially driven by reflections of Alfvén waves between the Io torus and Jupiter's ionosphere (*Hess et al.*, 2010; *Jones and Su*, 2008). Also kinetic simulations from *Damiano et al.* (2019) encourage a dominating role of Alfvén waves to explain electron acceleration. Surprisingly, accelerated upward proton populations were also detected by the JADE and the JEDI instrument (*Clark et al.*, 2020; *Szalay et al.*, 2020a). These charged particle detectors are sensitive to energy ranges of 50 eV to 100 keV for JADE (*McComas et al.*, 2017)) and above up to MeV energies for the JEDI instrument (*Mauk et al.*, 2017a), respectively. The data provide evidence of perpendicular ion heating in regions of expected electron acceleration above Jupiter, but also near the torus boundary, and is discussed in the realm of wave-particle interaction such as ion cyclotron resonance (*Clark et al.*, 2020; *Szalay et al.*, 2020a; *Sulaiman et al.*, 2020). The importance of wave-particle interaction for the Io-Jupiter system and the IFPT was recently further highlighted by *Sulaiman et al.* (2020), who analyzed highly resolved magnetic field (MAG instrument, see *Connerney et al.* (2017)) and electric field (Waves instrument, see *Kurth et al.* (2017)) data of the PJ12 flyby. This flyby was identified as a potential MAW-crossing by *Szalay et al.* (2020b) based on observed intense electron energy fluxes of 580 $\mathrm{mW/m^2}$. In this thesis, we will call this region Io flux tube tail and is associated with field lines connected to the IFPT. *Sulaiman et al.* (2020) reported on electric and magnetic field perturbations in the frequency ranges of 0.2 - 3 Hz and $50 - 2 \cdot 10^4$ Hz from the MAG and Waves instrument, respectively. In particular the frequency range up to 800 Hz shows no dispersion in the frequency-time spectrograms and also nearly transverse electric and magnetic field fluctuations with respect to the background magnetic field as expected for Alfvén and ion cyclotron waves *Sulaiman et al.* (2020). The corresponding power spectrum of the magnetic fluctuations revealed a power law of spectral index -2.35 ± 0.07 up to 800 Hz. The observed fluctuations were interpreted as variations due to the parallel wavenumber with respect to the background magnetic field. *Gershman et al.* (2019) also derived a parallel spectral index of -2.29 ± 0.09 for MAG measurements (0.2 - 5 Hz) connected to the main emissions, which the authors attributed to strong turbulence.

2.6. Guiding research questions

In the framework of this thesis, we will focus on the quantitative aspects of Alfvénic acceleration mechanisms connected to the main emissions and also to the Io footprint (tail) motivated by the ubiquitousness of the Alfvén mode revealed during the Juno era. The corresponding particle characteristics show broadband energy distributions and bi-directional flows. These observations are not consistent with a formerly assumed acceleration mechanism based on quasi-static potentials. Based on the recent observations in the respective high latitude regions of our concern we particularly consider Alfvénic turbulence as potential driver for efficient particle acceleration. For this, we will introduce the theoretical concept to describe properties of monochromatic kinetic Alfvén waves based on a general description in a hot plasma. We also present a simplified model from *Lysak and Lotko* (1996) and *Lysak* (2008) and discuss their differences to the general description. Building on this theoretical foundation, we address the relevance of Alfvénic turbulence for Jupiter's auroral emissions by performing parameter studies. In this context, we formulate the following guiding questions for this thesis:

1. What kind of Alfvénic turbulence and related generator locations explain the recent Juno observations connected to the Io flux tube tail and the main emissions best?
    - Do observed frequencies belong to the spatial or the temporal structure of Alfvénic wave field? What are the implications for the interpretation of the observed power spectra?
2. What are the dispersive and dissipative properties of monochromatic turbulent kinetic Alfvén waves along auroral field lines?
    - Is a description based on the *Lysak* (2008) dispersion relation appropriate for the parameter range encountered in the Io flux tube and along main auroral field lines?
    - What are the differences to a description based on the hot plasma dispersion relation?
    - What wave scales are involved in the damping process?
    - What species is preferentially heated by KAWs? Is proton Landau damping relevant in the considered regions?
3. Can resonant wave-particle interaction with KAWs drive significant particle acceleration to power the auroral emissions?
    - Where is the dissipation of wave energy most strongest along field lines? What is the extent of the acceleration region?
    - Is Alfvénic turbulence a relevant contributor to auroral emissions? Is a dense cold bulk or a dilute superthermal electron species responsible for the auroral power input?
    - Which parameters have significant influence on the auroral input power?
4. Can non-resonant cross-magnetic field ion heating explain observations of observed proton species in the Io flux tube tail?

CHAPTER 3

Theoretical foundations of Kinetic Alfvén Waves

The research field of plasma physics deals with phenomena associated with the interaction and dynamics of charged particles and related electromagnetic fields. Geophysical plasmas, e.g. the solar wind and planetary magnetospheres, are considered quasi-neutral ensembles of charged particles with underlying collective behavior. The basic character of quasi-neutrality ($n_e = n_i$ in case of singly charged ions) is facilitated by the richness of particles which can screen the Coulomb potential of single charges over time scales larger than the inverse of the plasma frequency

$$\omega_{p,s} = \sqrt{\frac{n_s q_s^2}{\varepsilon_0 m_s}}\,, \tag{3.1}$$

and on spatial scales much larger than the Debye length

$$\lambda_D = \left(\sum_s \frac{n_s q_s^2}{\varepsilon_0 k_B T_s} \right)^{-1/2} . \tag{3.2}$$

Here, n_s, m_s and T_s are the number density, atomic mass and temperature of species $s = (e, i)$. In this thesis, we assume the species to be singly charged so that the charge q_s is equal to the elementary charge e. The basic physical quantities such as the elementary charge e, the Boltzmann constant k_B and the dielectric constant ε_0 are defined in Appendix A. The frequency ω_{pe} is the characteristic oscillation frequency of electrons collectively reacting to disturbances in a plasma. The resultant collective plasma behavior is based on the many-particle character of the plasma and the related long-range Coulomb forces associated with the single particles. To describe the macroscopic plasma motion as superposition of the microscopic interactions between particles and fields, there are different approaches available. The choice of the appropriate model description depends on the relevant plasma scales of consideration. In case of a magnetized plasma, the helical single particle motion introduces two further basic scales. These are the cyclotron motion of a charge around the ambient magnetic field lines induced by the Lorentz force with the rotation frequency of

$$\Omega_s = \frac{q_s B_0}{m_s} \tag{3.3}$$

and the associated gyroradius

$$\rho_s = \frac{v_{th,s}}{\Omega_s}. \tag{3.4}$$

The gyroradius characterizes the perpendicular distance of the charge from the guiding center of the cyclotron motion and is determined by the characteristic thermal velocity $v_{th,s} = \sqrt{\frac{2k_B T_s}{m_s}}$ of Maxwellian distributed particle species s. The ambient magnetic field strength is denoted by B_0. Using the ion and electron plasma frequency, the inertial length scales can be defined as

$$\lambda_s = \frac{c}{\omega_{ps}}. \tag{3.5}$$

On spatial scales smaller than the ion inertial length λ_i, the ions decouple from the electron dynamics. The electron inertial length λ_e is the scale at which electron mass becomes important and equals to the skin depth in a cold plasma.

The plasma-β is an important quantity to assess the plasma dynamics, and is defined as the ratio of thermal to magnetic pressure

$$\beta = \frac{nk_B T}{\frac{B^2}{2\mu_0}}. \tag{3.6}$$

Due to the strong background magnetic field of Jupiter, the plasma in the inner and middle jovian magnetosphere possesses a small β. Hence, the magnetic field dominates the dynamics of the plasma constituents.

3.1. Approaches to plasma physical modeling

In a general approach, modeling the dynamics of a plasma system can be realized by simultaneously solving the coupled and self-consistent set of microscopic equations of motion and Maxwell's equations considering all the correlations between fields and particles. Such a modeling approach is not suitable to study global plasma dynamics in case of large scale magnetospheric systems because of the large computational load. In contrast, magnetohydrodynamics (MHD) is a macroscopic theory that considers the plasma as an electromagnetically conducting single or multi-component fluid and fully neglects single particle effects as result of the average process. Adequate MHD simulations are useful for characteristic length scales $L \gg \rho_i$ and times scales $t \gg \frac{2\pi}{\Omega_i}$. However for our means, i.e., modeling the energy exchange processes in a collisionless plasma in the context of wave turbulence, we need to employ a statistical ansatz for the particle distributions using kinetic theory. In this approach, the Vlasov equation

$$\frac{\partial f_s}{\partial t} + \vec{v} \cdot \nabla f_s + \frac{q_s}{m_s}(\vec{E} + \vec{v} \times \vec{B}) \cdot \nabla_v f_s = 0 \tag{3.7}$$

plays a fundamental role in tracking the evolution of the particle distribution functions $f_s(\vec{r}, \vec{v}, t)$ (for each species s separately) in six-dimensional phase space and thus especially in retaining velocity information in a statistical sense. ∇_v is the gradient operator in velocity space and $\vec{v}$ is the velocity of a phase space volume element. The electric and magnetic fields are denoted by $\vec{E}$ and $\vec{B}$ and fulfill the set of Maxwell's equations (3.9)-(3.12), which are introduced in the next section. These equations form, together with the

Vlasov equation and additional constitutive relations for the charge and current density, a non-linear set of coupled equations, the so-called Maxwell-Vlasov system. Maintaining the effects from velocity phase space, which are not captured in the framework of MHD, introduces an important area of momentum and energy exchange processes in a plasma. In particular, plasma waves take the principal role of transporting energy towards distant regions, but also exchanging energy with the plasma via wave-particle interactions. Thus, the study of waves and related kinetic processes is an essential subject in order to understand the plasma dynamical interaction processes such as turbulence and related physical consequences for the system under study. According to *Klein et al.* (2020), wave-particle interaction mechanisms can be classified into resonant interactions such as Landau damping, cyclotron damping and transit-time magnetic pumping (*Landau* (1946); *Barnes* (1966); *Kennel and Engelmann* (1966)), and non-resonant interactions via e.g. stochastic heating by Alfvén waves (*Wang et al.* (2006); *Lu and Li* (2007)). We will explicitly investigate the energization potential of these processes due to dissipation of kinetic Alfvén wave energy in relation to Jupiter's auroral emissions. In the approach followed in this thesis we do not track the evolution of the distribution functions themselves as done with particle-in cell codes (e.g., *Su et al.* (2003, 2006)). Instead, we calculate the linear macroscopic response of the plasma and Alfvén wave characteristics for various spatial scales due to a small perturbation of the distribution function. We assume the species to obey a Maxwell-Boltzmann distribution as it maximizes the entropy of the system and hence considers the plasma to be locally in thermodynamic equilibrium.

The purpose of the following is to present the theoretical description of linear wave modes in a homogeneous, infinite and magnetized plasma considering scale dependent contributions to wave dispersion and dissipation properties and the related plasma response. Building on that we will discuss the physics of the Alfvén wave and its kinetic extension as we expect this mode to be a major driver of energy cascading processes in the realm of turbulence. The equations and variables used in this chapter are presented in SI units.

3.2. Wave equation - General dispersion relation

We seek to describe the kinetic Alfvén mode as a plane wave in the form

$$\delta\vec{E} = \mathrm{Re}\left\{\delta\vec{E}_0(\vec{k},\omega)e^{i(\vec{k}\cdot\vec{r}-\omega(\vec{k})t)}\right\}. \tag{3.8}$$

The corresponding wave properties such as polarization, propagation direction and energy transport are determined by the complex valued Fourier amplitude $\delta\vec{E}_0$, the wave vector $\vec{k}$ and the wave frequency $\omega(\vec{k})$, where the latter is described by a dispersion relation in presence of the plasma. To keep the problem manageable, we employ the fundamental assumptions to deal with small amplitude waves in a magnetized, homogeneous, and infinitely extended plasma in local thermodynamic equilibrium. We consider no background electric field in the plasma frame, i.e., $\vec{E}_0 = \vec{0}$, but only small wave electric field fluctuations $\delta\vec{E}$. The small amplitude assumption, i.e., the smallness of the wave magnetic fluctuation $\delta\vec{B}$ compared to the static background magnetic field $\vec{B}_0 = const.$, allows us to linearize the model equations in which only first order quantities are retained. These are described in the plane wave fashion introduced in equation (3.8).

Our starting point is the linear set of the Maxwell equations

$$\nabla\times\delta\vec{E} = -\frac{\partial\delta\vec{B}}{\partial t} \tag{3.9}$$

$$\nabla\times\delta\vec{B} = \mu_0\delta\vec{j} + \mu_0\varepsilon_0\frac{\partial\delta\vec{E}}{\partial t} \tag{3.10}$$

$$\nabla\cdot\delta\vec{D} = \delta\varrho \tag{3.11}$$

$$\nabla\cdot\delta\vec{B} = 0\,, \tag{3.12}$$

which relate the temporally and spatially variable fluctuations in electric field, $\delta\vec{E}$, electric displacement, $\delta\vec{D}$, and in the magnetic field, $\delta\vec{B}$, to the charged particles they are interacting with via the perturbed current density $\delta\vec{j}$ and perturbed free charge density $\delta\varrho$. In this context, equations (3.9) and (3.10) are generally referred to as *Faraday's law* and *Ampere's law*. The coupling of these equations is further complicated by the circumstance that the current density itself can depend non-linearly on the electric field. Under spatially homogeneous and time stationary equilibrium plasma conditions with weak perturbations, the perturbed current density $\delta\vec{j}(\vec{r},t)$ can be expressed in a linear fashion as convolution integral

$$\delta\vec{j}(\vec{r},t) = \int_{-\infty}^{t} dt' \int_{-\infty}^{\infty} d\vec{r}'\underline{\underline{\sigma}}(\vec{r}-\vec{r}', t-t')\cdot\delta\vec{E}(\vec{r}',t')\,, \tag{3.13}$$

where $\underline{\underline{\sigma}}$ is the conductivity tensor which includes all the particle responses due to the wave perturbation. Calculating the Fourier-Laplace transformation into the wavenumber-frequency domain or equivalently applying the plane-wave approach, $\delta\vec{j}(\vec{r},t)$ transforms into the local amplitude relation

$$\delta\vec{j}(\vec{k},\omega) = \underline{\underline{\sigma}}(\vec{k},\omega)\cdot\delta\vec{E}_0(\vec{k},\omega). \tag{3.14}$$

Dealing with a plasma consisting only of free charges gives us the freedom to formally express the right hand side of Ampere's law in equation (3.10) in the $(\vec{k},\omega)$-domain as a displacement current

$$\mu_0\delta\vec{j}(\vec{k},\omega) + \mu_0\varepsilon_0(-i\omega)\delta\vec{E}_0(\vec{k},\omega) \equiv -i\omega\mu_0\varepsilon_0\underline{\underline{\varepsilon}}(\vec{k},\omega)\delta\vec{E}_0(\vec{k},\omega). \tag{3.15}$$

In essence, the plasma can be likewise regarded as a dielectric or as a conducting medium because current contributions due to polarization or conduction processes of particles cannot be distinguished anymore (*Piel*, 2010). Thus, from relations (3.15) and (3.14) we can define an effective dielectric tensor as

$$\underline{\underline{\varepsilon}}(\vec{k},\omega) = \underline{\underline{1}} + \frac{i}{\varepsilon_0\omega}\underline{\underline{\sigma}}(\vec{k},\omega). \tag{3.16}$$

This tensor includes the vacuum displacement current contribution denoted by the identity matrix $\underline{\underline{1}}$ and the conduction currents carried by the plasma constituents as superimposed total response. Although expression (3.16) resembles the conventional definition of the electric susceptibility, we refer to it in the following as dielectric tensor even though excluding the vacuum permittivity factor ε_0. The tensorial character is especially introduced by the presence of a background magnetic field $\vec{B}_0$ as the particle responses parallel to $\vec{B}_0$ differ from those perpendicular to the field and thus establish anisotropy in the plasma. Further properties and the derivation of the tensor will be discussed in Section 3.4.

From Maxwell equations (3.9) and (3.10), we can easily deduce the wave equation for the electric field fluctuation

$$\nabla \times \nabla \times \delta \vec{E} + \frac{1}{c^2}\frac{\partial^2 \delta \vec{E}}{\partial t^2} = -\mu_0 \frac{\partial \delta \vec{j}}{\partial t}, \tag{3.17}$$

where the term on the right hand side represents the coupling of the plasma to the wave as described by equation (3.13). Inserting the plane wave approach from the beginning of this section, we can express the wave equation in terms of the dielectric tensor as a matrix system

$$\left[\vec{k} \otimes \vec{k} - k^2 \underline{\underline{1}} + \frac{\omega^2}{c^2}\underline{\underline{\varepsilon}}\right] \cdot \delta \vec{E}_0 = \vec{0}. \tag{3.18}$$

The operator ⊗ denotes the dyadic product. In the following, we aim to find mode solutions to this system.

3.3. Hot plasma Dispersion relation

In order to have non-trivial solutions to this system, the matrix must not have an inverse or equivalently, its determinant needs to be zero. Thus, the general dispersion relation for waves in a hot plasma reads

$$\det\left[\vec{k} \otimes \vec{k} - k^2 \underline{\underline{1}} + \frac{\omega^2}{c^2}\underline{\underline{\varepsilon}}\right] = 0. \tag{3.19}$$

Its solutions $\omega(\vec{k}) \in \mathbb{C}$ describe the propagation properties of linear wave modes. Having these, waves can be further characterized in terms of their phase velocity

$$\vec{v}_{ph} = \frac{\omega}{k^2}\vec{k}, \tag{3.20}$$

which describes the propagation direction of constant phases $\Phi = \vec{k} \cdot \vec{r} - \omega t$, and also in terms of their group velocity

$$\vec{v}_{gr} = \nabla_k \, \omega(\vec{k}), \tag{3.21}$$

which expresses the transport of energy by a packet of waves. Here, ∇_k denotes the gradient operator in k-space.

In this thesis, we will use a coordinate system in which the ambient magnetic field is aligned with the z-axis (referred to as the parallel direction), and the perpendicular directions are along the x- and y-axis. Without restriction of generality, we can assume that the wave vector lies in the x-z plane, i.e., $\vec{k} = k_x \vec{e}_x + k_z \vec{e}_z$, where the perpendicular Alfvénic electric field is directed towards the x-axis and the magnetic field fluctuation amplitude along the y-axis. Using this representation, we can express the final determinant as

$$\det \begin{pmatrix} \varepsilon_{xx} - n_z^2 & \varepsilon_{xy} & \varepsilon_{xz} + n_z n_x \\ -\varepsilon_{xy} & \varepsilon_{yy} - n^2 & \varepsilon_{yz} \\ \varepsilon_{xz} + n_z n_x & -\varepsilon_{yz} & \varepsilon_{zz} - n_x^2 \end{pmatrix} = 0 \ , \tag{3.22}$$

where the wavenumber is expressed as the total index of refraction $n = \frac{c}{v_{ph}} = \frac{kc}{\omega}$ with its parallel and perpendicular components, $n_z = \frac{k_z c}{\omega}$ and $n_x = \frac{k_x c}{\omega}$, respectively.

The solutions to this dispersion relation describe the properties of linear waves in terms of the complex wave frequency $\omega = \omega_r + i\gamma$, where the dispersion properties are described by ω_r and γ accounts for the damping. These characteristics depend on the wave scale and related ambient plasma conditions. In its generality, the hot plasma dispersion relation encodes the branches implicitly and thus require numerical root search techniques in order to find and track them. Only under strong simplifying assumptions, such as in the framework of MHD, explicit formulations for $\omega(\vec{k})$ exist.

3.4. General hot dielectric tensor

Obtaining the dispersive and dissipative properties of linear waves propagating in a hot magnetized plasma from the dispersion relation requires to find an expression for the dielectric tensor. In the most general framework it can be derived from kinetic theory. The tensor explicitly includes statistical velocity properties of the plasma species in terms of distribution functions and account for associated kinetic effects. Based on the extensive derivation, we will reduce its presentation to the most important foundations and assumptions used. We refer to the books of *Stix* (1992) and *Brambilla* (1998) for a more complete overview.

The basic idea is to calculate the macroscopic particle response $\delta\vec{j}$ associated with a small perturbation δf_s as a consequence of the presence of the wave by building the first integral velocity moment

$$\delta\vec{j} = \sum_s q_s \int d\vec{v}\,\vec{v}_s \delta f_s \tag{3.23}$$

and relate it to the expression (3.15) based on Ampere's law

$$\delta\vec{j} = \underline{\underline{\sigma}}\delta\vec{E}_0 = -i\varepsilon_0\omega\left(\sum_s \underline{\underline{\varepsilon}}^s\right)\delta\vec{E}_0 = \sum_s \delta\vec{j}^s. \tag{3.24}$$

From comparison, we can then find the final tensor expression due to the different particle species to be shown below.

The equilibrium distribution function $f_{0s}(\vec{r},\vec{v})$ for the particle species s is assumed to be Maxwellian in an homogeneous and stationary plasma with an ambient magnetic field $\vec{B}_0$ but no background electric field. Consequently, the particles perform simple gyrations along the magnetic field lines and lead to isotropy and time independence of f_{0s}. However, this background state is disturbed by the presence of the wave fluctuation and hence perturb the distribution function by a finite $\delta f_s(\vec{r},\vec{v},t)$, which is considered to have an oscillating nature like the wave. By linearizing the Vlasov equation (3.7), we can relate the unknown perturbation δf_s to the equilibrium distribution function via

$$\begin{aligned} 0 = \frac{df_s}{dt} &\approx \frac{d(f_{0s}+\delta f_s)}{dt} \\ &= \underbrace{\frac{\partial f_{0s}}{\partial t} + \vec{v}\cdot\nabla_v f_{0s} + \frac{q_s}{m_s}\left(\vec{v}\times\vec{B}_0\right)\cdot\nabla_v f_{0s}}_{=\left(\frac{df_{0s}}{dt}\right)_0=0} + \underbrace{\frac{\partial\delta f_s}{\partial t} + \vec{v}\cdot\nabla\delta f_s + \frac{q_s}{m_s}\left(\vec{v}\times\vec{B}_0\right)\cdot\nabla_v\delta f_s}_{=\left(\frac{d\delta f_s}{dt}\right)_0} \\ &+ \frac{q_s}{m_s}\left(\delta\vec{E}+\vec{v}\times\delta\vec{B}\right)\cdot\nabla_v f_{0s} + \underbrace{\frac{q_s}{m_s}\left(\delta\vec{E}+\vec{v}\times\delta\vec{B}\right)\cdot\nabla_v\delta f_s}_{\approx 0,\text{ neglect non-linear terms}}. \end{aligned} \tag{3.25}$$

Here, we consider that the equilibrium distribution function $f_{s0} = f_{s0}(v_\perp, v_\parallel)$ is a solution of the Vlasov equation along the unperturbed gyration trajectories (subscript 0) of the particles, i.e., $\left(\frac{df_{0s}}{dt}\right)_0 = 0$. The associated particles obey the non-relativistic equations of motion in the Lagrangian frame

$$\frac{d\vec{r}}{dt} = \vec{v} \tag{3.26}$$

and

$$\frac{d\vec{v}}{dt} = \frac{q_s}{m_s}\vec{v} \times \vec{B}_0 \tag{3.27}$$

in the absence of the wave. This enables us to express the perturbed distribution function due to the wave in terms of the known equilibrium distribution by the remaining linearized terms in equation (3.25) as

$$\delta f_s(\vec{r}, \vec{v}, t) = \int_{-\infty}^{t} \left(\frac{d\delta f_s}{dt}\right)_0 dt' = -\frac{q_s}{m_s}\int_{-\infty}^{t} dt' \left(\delta\vec{E}(\vec{r}', t') + \vec{v}' \times \delta\vec{B}(\vec{r}', t')\right) \cdot \frac{\partial f_{0s}(\vec{v}')}{\partial \vec{v}'} . \tag{3.28}$$

We track the evolution of the perturbation along the characteristics of the unperturbed distribution function, which are described by equations (3.26) and (3.27). In the linear framework, we consider the perturbations on the particle orbits due to the action of the wave small. Thus, tracking these particles along the unperturbed phase space trajectory is a reasonable assumption (*Baumjohann and Treumann*, 2012). Performing the integration over the velocity phase space as required from (3.23) gives after some algebra the macroscopic response from which we can deduce the elements of the dielectric tensor. For a Maxwellian distributed and non-relativistic hot plasma with singly charged constituents, the tensor elements read (*Stix* (1992),*Brambilla* (1998),*Baumjohann and Treumann* (2012))

$$\begin{aligned}
\varepsilon_{xx} =& 1 + \sum_s \frac{\omega_{ps}^2}{\omega^2}\xi_{0s} \sum_{n=-\infty}^{\infty} n^2 \frac{\Gamma_n(\mu_s)}{\mu_s} Z(\xi_{ns}) && (3.29)\\
\varepsilon_{yy} =& 1 + \sum_s \frac{\omega_{ps}^2}{\omega^2}\xi_{0s} \sum_{n=-\infty}^{\infty} \left(n^2 \frac{\Gamma_n(\mu_s)}{\mu_s} - 2\mu_s\Gamma_n'(\mu_s)\right) Z(\xi_{ns}) && (3.30)\\
\varepsilon_{zz} =& 1 - \sum_s \frac{\omega_{ps}^2}{\omega^2}\xi_{0s} \sum_{n=-\infty}^{\infty} \xi_{ns}\Gamma_n(\mu_s) Z'(\xi_{ns}) && (3.31)\\
\varepsilon_{xy} =& -\varepsilon_{yx} = i\sum_s \frac{\omega_{ps}^2}{\omega^2}\xi_{0s} \sum_{n=-\infty}^{\infty} n\Gamma_n'(\mu_s) Z(\xi_{ns}) && (3.32)\\
\varepsilon_{xz} =& \quad \varepsilon_{zx} = -\sum_s \operatorname{sgn}(q_s)\frac{\omega_{ps}^2}{\omega^2}\xi_{0s} \sum_{n=-\infty}^{\infty} n\frac{\Gamma_n(\mu_s)}{\sqrt{2\mu_s}} Z'(\xi_{ns}) && (3.33)\\
\varepsilon_{yz} =& -\varepsilon_{zy} = i\sum_s \operatorname{sgn}(q_s)\frac{\omega_{ps}^2}{\omega^2}\xi_{0s} \sum_{n=-\infty}^{\infty} \sqrt{\frac{\mu_s}{2}}\Gamma_n'(\mu_s) Z'(\xi_{ns}) \ . && (3.34)
\end{aligned}$$

The elements contain the basic plasma scales for all plasma species s as introduced in the beginning of Chapter 3, which we repeat here as follows: $\omega_{ps} = \left(\frac{n_s q_s^2}{\varepsilon_0 m_s}\right)^{1/2}$ and $\Omega_s =$

$\frac{q_s B}{m_s}$ are the plasma frequency and gyrofrequency, respectively; the gyroradius $\rho_s = \frac{v_{th,s}}{\Omega_s}$ enters the tensor over the variable $\mu_s = \frac{1}{2}k_\perp^2\rho_s^2$ as a measure for the finite gyroradius effects, which is embedded in the function $\Gamma_n(\mu_s) = e^{-\mu_s}I_n(\mu_s)$ and its derivative $\Gamma_n'(\mu_s) = \left(I_n'(\mu_s) - I_n(\mu_s)\right)e^{-\mu_s}$. They contain the modified Bessel function $I_n \in \mathbb{R}$ of the first kind and order $n \in \mathbb{Z}$, which enters the expression due to the perpendicular isotropy of the system. The plasma dispersion function $Z(\xi) = i\sqrt{\pi}e^{-\xi^2}\mathrm{erfc}(-i\xi) \in \mathbb{C}$ and its derivative $Z'(\xi) = -2 - 2\xi Z(\xi)$ (*Fried and Conte*, 1961) explicitly introduce damping to the wave over their imaginary part. The wave-particle interaction mechanisms at work are of resonant nature and their efficiency is controlled over the input argument $\xi_{ns} = \frac{\omega - n\Omega_s}{k_\parallel v_{th,s}}$. Most prominent damping processes considered here are Landau and harmonic cyclotron damping for species s, which fulfill the resonance condition

$$\omega - k_\parallel v_\parallel \simeq n\Omega_s\,. \tag{3.35}$$

For the harmonic number $n = 0$, resonant particles, i.e., particles with a parallel speed $v_\parallel$ matching the parallel phase velocity of the wave, $v_{ph} = \frac{\omega}{k_\parallel}$, contribute to so-called Landau damping. These particles can intensively interact with a parallel electric field of the wave mode under consideration and lead to energy exchange (anti-)parallel to the ambient magnetic field. However, there is no necessity for the existence of a background magnetic field for the occurrence of Landau damping. When the resonance condition is satisfied for harmonic numbers $n \neq 0$, gyrating particles see a Doppler-shifted perpendicular wave electric field and thus allow for significant energy transfer. These collisionless damping mechanisms are reversible in nature, meaning that energy exchange can generally occur from the wave towards particles but also in the reverse direction. The important aspect for determining wave damping in this system is given by the Maxwellian distributed particles, which ensure an imbalance with more particles being slightly slower than faster the resonance speed (*Baumjohann and Treumann*, 2012).

Solving dispersion relation (3.22) with the tensor elements for a hot plasma gives rise to various wave modes. The most simple one is the pure electromagnetic branch, $\omega = kc$, for which the tensor takes the shape of the identity matrix and thus decouples the wave properties from the medium, i.e., in the absence of plasma. Neglecting thermal effects from the plasma, i.e., $T \to 0$, and thus removing spatial dispersion, the tensor describes waves in a cold plasma. Considering additionally wave frequencies $\omega \ll \Omega_i$ and large wavelengths compared to plasma length scales, the dispersion relation for the three conventional MHD modes (Alfvén, slow, fast) is recovered. Whereas no damping is included in the simple cold plasma model, adding kinetic effects to the cold plasma wave branches introduces wave-particle interaction as resonant particles are now available. In terms of mathematical properties, the complex valued dielectric tensor can be decomposed into a hermetian and in an anti-hermetian part (*Stix*, 1992; *Brambilla*, 1998)

$$\underline{\underline{\varepsilon}} = \underline{\underline{\varepsilon}}^H + i\underline{\underline{\varepsilon}}^A, \tag{3.36}$$

with the elements $\varepsilon_{ij}^H = \frac{1}{2}\left(\varepsilon_{ij} + \varepsilon_{ji}^*\right)$ and $\varepsilon_{ij}^A = \frac{1}{2i}\left(\varepsilon_{ij} - \varepsilon_{ji}^*\right)$. The anti-hermetian part can be shown to be related to wave damping as the hermetian part is only associated with real-valued eigenvalues. This enables us to assess the different damping mechanisms for a certain mode, which in the context of this thesis is the kinetic Alfvén wave. A further advantage of the dielectric tensor concept is its additive nature for the different plasma species under consideration as can be seen directly from the summation over s. Hence, we additionally can relate damping mechanisms to a certain population.

3.5. The Alfvén wave and its kinetic extension

In this section, we discuss the properties of the Alfvén mode such as dispersion and polarization. We start with the conventional MHD approximation and continue to include kinetic effects from small scales as covered by the general description of a hot plasma introduced in preceding Sections 3.3 and 3.4.

3.5.1. The ideal MHD Alfvén wave

The shear Alfvén mode is a solution to the linearized set of ideal MHD equations. However, as can be shown, the Alfvén wave is also a solution to the fully non-linear ideal MHD equations. As a result, large amplitude magnetic field perturbations, as encountered e.g. in the vicinity of Io, reveal the same wave characteristics as for small perturbations ($\delta B \ll B_0$). The basic characteristics of this mode are expressed by the linear dispersion relation

$$\omega = \vec{k} \cdot \vec{v}_A = \pm\, k_\parallel v_A, \tag{3.37}$$

where the Alfvén velocity is defined by $\vec{v}_A = \frac{\vec{B}_0}{\sqrt{\mu_0 \rho}}$ and $k_\parallel$ is the parallel wavenumber with respect to the background magnetic field $\vec{B}_0$. The mass density is denoted by ρ. Due to the linear dependence of the dispersion relation on the parallel wavenumber, both the parallel phase and the group velocity from equations (3.20) and (3.21) are identical, i.e., $\vec{v}_{gr}^{\parallel} = \vec{v}_{ph}^{\parallel} = \pm\, \vec{v}_A$. In consequence, this mode is dispersionless and strictly transports electromagnetic energy (anti-)parallel to the magnetic field lines. In the case of the dilute and strongly magnetized high-latitude region of Jupiter's magnetosphere and associated fast wave dynamics, a correction due to the displacement current needs to be incorporated. This modification limits the propagation velocity towards the speed of light by replacing the Alfvén speed v_A in equation (3.37) by the semi-relativistic Alfvén speed $v_A^{rel} = \frac{v_A}{\sqrt{1+(v_A/c)^2}}$ (*Lysak and Song*, 2000).

In the magnetohydrodynamic limit, i.e., for slow temporal variations ($\omega \ll \{\Omega_{i,e}, \omega_{i,e}\}$) and large spatial scales ($k_\perp, k_\parallel \ll \{\rho_{i,e}, \lambda_{i,e}\}$) in the plasma, the velocity perturbation δu_y and the magnetic field perturbation δB_y associated with the Alfvén wave are related by

$$\frac{\delta B_y}{B_0} = \mp\, \frac{\delta u_y}{v_A}, \tag{3.38}$$

which illustrates the transversal nature of this mode together with the perpendicular wave electric field $\delta E_x = \pm\, v_A \delta B_y$ as $\delta\vec{u} \perp \vec{k}$. Additionally, the ideal MHD Alfvén wave has no parallel electric field, i.e., $\delta E_\parallel = 0$, and is also considered to be magnetically incompressible in a low-β plasma, i.e., $\delta B_\parallel = 0$ (*Hasegawa*, 1976). Thus, we do not expect the Alfvén wave to be damped on large scales due to wave-particle interaction (see Section 3.4). In contrast to the other two MHD modes (slow and fast mode), the shear MHD Alfvén wave is not accompanied by pressure and density fluctuations as the velocity and magnetic perturbations do not act to compress the plasma, i.e., $\nabla \cdot \delta\vec{u} = 0$ (*Hasegawa and Uberoi*, 1982).

Now, we give a brief insight into the physical processes related to the Alfvén wave. When the plasma flow is perturbed, a perpendicular magnetic perturbation is induced on the background magnetic field as a consequence of the frozen-in theorem, which states that magnetic field and the plasma dynamics are intimately coupled to each other in an infinitely conducting plasma. The related curvature or shear of the magnetic field lines generates a tension (Lorentz) force, $\delta\vec{j} \times \vec{B}_0 \propto \frac{1}{\mu_0}\left(\vec{B}_0 \cdot \nabla\right)\delta\vec{B}$, which acts on the plasma in order to restore the equilibrium state of the perturbed system. However, the plasma inertial response overshoots this relaxed state and sets in an oscillatory exchange of mechanical energy and electromagnetic field energy. The heavy ions, as we will discuss below, are able to respond to perturbations on relevant time scales because the Alfvén mode is restricted to frequencies below the ion cyclotron frequency, i.e., $\omega < \Omega_i$ (*Gary and Borovsky*, 2004). The magnetic tension and related vibrations are carried along the field lines and are associated with an electromagnetic Poynting flux, which communicates the magnetic field stresses. Thus, physical processes related to planets, moons and their magnetospheric environments, in our case the Jupiter system, are interconnected and govern their local plasma dynamics via the magnetic field even though regions are located very distant from each other (*Stasiewicz et al.*, 2000).

For low frequencies, guiding-center theory of the single particles serves as a good approximation to understand the plasma dynamics and generated current densities related to the Alfvénic wave field (*Wu and Fang*, 1999; *Stasiewicz et al.*, 2000). In the presence of the oscillating perpendicular electric field fluctuation δE_x, ions and electrons together perform a drift motion, $\delta\vec{v}_y^{i,e} = \frac{1}{B_0^2}\delta\vec{E}_x \times \vec{B}_0$, alternating in positive and negative y-direction, which is not associated with a current density at least for slow temporal variation of the wave, i.e., $\omega \ll \Omega_i$. For wave frequencies reaching the ion cyclotron frequency Ω_i, Hall currents are induced by the increasingly decoupled ion and electron motion, but this dispersive effect is only present on wave kinetic scales (*Cramer*, 2001; *Lysak*, 2008). On MHD scales, a perpendicular current density $\delta j_x \simeq \frac{1}{\mu_0 v_A^2}\frac{d\delta E_x}{dt}$ is generated in response to the Alfvén wave and is carried by the polarization drift of the ions in the temporally variable wave electric field δE_x. The electron contribution to the polarization current is negligible compared to the ion one due to the linear mass dependency of this drift motion (*Hasegawa and Uberoi*, 1982). Expressing $\frac{d\delta E_x}{dt} = -i\omega\delta E_x$ for a monochromatic plane wave, we can see that the current and wave electric field are out of phase. Thus, there is no net power transfer between the plasma and the MHD Alfvén wave. In the context of the Jovian auroral flux tubes, we expect the perpendicular response to be strongest in the mass-rich and weak background magnetic field in the equatorial plasma sheet environment due to the low Alfvén speed v_A. The polarization current due to the ions gives rise to the Lorentz force $\delta\vec{j}_x \times \vec{B}_0$ in y-direction, which acts to restore the equilibrium state in analogue to the MHD fluid description discussed above.

3.5.2. Inclusion of kinetic effects to the Alfvén wave

Now, we allow the perpendicular wave scale $\lambda_\perp = \frac{2\pi}{k_\perp}$ to be finite compared to the parallel scale, $k_\perp \gg k_\parallel$, on the order of kinetic scales of the plasma, such as ρ_i and λ_e (see introduction to Section 3 for definitions). The shear Alfvén wave couples to the longitudinal ion acoustic mode in the low-β_i regime and develops a dispersive and dissipative character (*Hasegawa and Uberoi*, 1982; *Lysak and Lotko*, 1996; *Hollweg*, 1999) as a consequence of deviating responses of ions and electrons on these scales. These effects and related wave dispersion characteristics are discussed in the following.

A simple physical model for the scale dependent modification of the dispersion relation from equation (3.37) is presented in the literature in terms of two-fluid theory (e.g., *Streltsov et al.* (1998); *Paschmann et al.* (2003)) as the single fluid MHD approximation gets an inaccurate description of the wave dynamics. Within this model, ions and electrons are considered as separate fluids and effects from ion gyroradius, electron pressure and inertia are included in the generalized Ohm's law. According to *Lysak* (2008) and *Paschmann et al.* (2003), its parallel component with respect to the background magnetic field reads

$$\delta E_{\|} = \frac{m_e}{ne^2}\frac{\partial \delta j_{\|}}{\partial t} - \frac{1}{ne}\frac{\partial \delta p_e}{\partial z}. \tag{3.39}$$

From current continuity, $\nabla \cdot \delta \vec{j} = 0$, the divergence-afflicted perpendicular polarization current for finite $k_\perp$ and related charge separation gives rise to the parallel response $\delta j_{\|}$, which together need to form a closed current system (*Glassmeier and Scholer*, 1991; *Borovsky*, 1993). It is assumed that the parallel response $\delta j_{\|}$ is mainly carried by the electrons due to their low mass (see Section 3.5.6), which are considered to be isothermal (T_e=const) so that their pressure perturbation can be expressed as $\delta p_e = k_B T_e \delta n_e$. We can see that the parallel wave electric field $\delta E_{\|}$ from equation (3.39), is driven by the electron inertial response from the first term on the right hand side as $\frac{m_e}{ne^2} = \mu_0 \lambda_e^2$ or by electron pressure effects from the second term. *Lysak* (2008) showed that this latter term can be expressed in terms of the squared ion-acoustic radius $\rho_s^2 = \frac{T_e}{T_i}\rho_i^2$ by using the continuity equation for the perturbed electron density δn_e. However, not only electrons are relevant to the wave dynamics, but also the ion responses participate in the interaction. On perpendicular wave scales on the order of $k_\perp \rho_i \sim 1$, the ions sense the temporal variations of the wave electric field on their gyro trajectory. In essence, *Stéfant* (1970) showed that they feel a reduced effective electric field which leads to a modification of the particle motion, called 'finite Larmor radius effects', and charge separation occurs. Consequently, the dispersion characteristics of the Alfvén wave are controlled by these plasma kinetic scales. The associated relevant quantity is (e.g., *Su* (2009))

$$(\beta_e + \beta_i)\frac{m_i}{m_e} = \frac{\rho_s^2 + \rho_i^2}{\lambda_e^2} \approx \beta_e \frac{m_i}{m_e} = \frac{\rho_s^2}{\lambda_e^2} = \frac{v_{th,e}^2}{v_A^2}, \tag{3.40}$$

where $\beta_{e,i}$ is the electron/ion plasma beta and $m_{e,i}$ is the electron/ion mass. There are two parameter regimes to be distinguished for the wave properties, which are discussed in the following.

The kinetic/warm electron regime is characterized by $\beta_e \frac{m_i}{m_e} > 1$, which is equivalent to saying that the electron thermal speed $v_{th,e}$ exceeds the Alfvén propagation speed v_A. As can be seen from equation (3.40), the ion acoustic radius ρ_s is then larger than the electron inertial scale λ_e and correspondingly, thermal/pressure effects from the electrons favor the emergence of a parallel electric field. This regime is considered as the *kinetic Alfvén limit*. The corresponding normalized dispersion relation for this kinetic wave branch, first derived by *Hasegawa* (1976) with an ion kinetic treatment, is

$$\frac{\omega_r^2}{k_{\|}^2 v_A^2} = 1 + k_\perp^2 \left(\frac{3}{4}\rho_i^2 + \rho_s^2\right). \tag{3.41}$$

Here, ω_r is the real part of the wave frequency which together with the parallel wavenumber $k_{\|}$ defines the parallel phase velocity. As can be seen, finite ion gyroradius and electron pressure effects enter this expression over the ion gyroradius and ion-acoustic radius. Larger plasma length scales or equivalently smaller perpendicular wave scales, lead to an increase of the phase and group velocity compared to the dispersionless MHD Alfvén wave, termed as positive dispersion. Some authors, e.g., *Streltsov et al.* (1998); *Jones and Su* (2008), neglect the factor 3/4 (set to 1), which is simply a result from a different treatment of a term involving the modified Bessel function of first kind, i.e., dealing with it in terms of a Taylor series expansion or use a more global Padé approximation. Due to the $k_\perp$-dependence, this branch also develops a perpendicular group velocity component, which leads to energy transport in perpendicular direction. However, this spreading is of minor importance as is scales with $k_\parallel/k_\perp$, which is assumed to be much smaller than one.

Gekelman et al. (1997) published a generalized version of (3.41) considering finite frequency effects which reads

$$\frac{\omega_r^2}{k_\parallel^2 v_A^2} = \frac{1 + k_\perp^2\left(\rho_i^2 + \rho_s^2\right)}{1 + \frac{k_\parallel^2 v_A^2\left(1 + k_\perp^2 \rho_i^2\right)}{\Omega_i^2}}. \tag{3.42}$$

For frequencies reaching the ion cyclotron frequency Ω_i, the correction term counteracts the increase in phase velocity. These effects were also discussed by *Lysak* (2008).

For the opposite case of $\beta_e \frac{m_i}{m_e} < 1$, thermal effects do not play a major role, i.e., the electrons are considered 'cold'. Solely electron inertia dominates the interaction with the wave, and hence, this case is named the *inertial Alfvén limit*. Here, *Goertz and Boswell* (1979) derived the dispersion relation

$$\frac{\omega_r^2}{k_\parallel^2 v_A^2} = \frac{1}{1 + k_\perp^2 \lambda_e^2} \tag{3.43}$$

for the *inertial Alfvén wave*. Considering the displacement currents requires to replace v_A by the semi-relativistic Alfvén speed $v_{A,rel}$ (*Streltsov et al.* (1998); *Jones and Su* (2008)). Efficient wave-particle interaction can occur as a result of negative dispersion, i.e., electron inertia leads to a reduction of the wave propagation velocity. In this case, we can also observe a slight deviation from parallel wave energy transport. As for the kinetic case, in the large perpendicular scale limit, this dispersion branch converges towards the classic MHD limit from equation (3.37). In this thesis, we use the terminology kinetic Alfvén wave (KAW) equivalently to other publications, e.g., *Lysak and Lotko* (1996); *Saur et al.* (2018b), to indicate small-scale Alfvén waves in both, the kinetic and inertial Alfvén limit.

Using two-fluid theory as discussed earlier, a dispersion relation resembling the dispersive limits from equations (3.41) and (3.43) can be derived as

$$\frac{\omega_r^2}{k_\parallel^2 v_{A,rel}^2} = \frac{1 + k_\perp^2 \rho^2}{1 + k_\perp^2 \lambda_e^2}, \tag{3.44}$$

where $\rho^2 = (3/4)\rho_i^2 + \rho_s^2$ (*Lysak and Lotko* (1996); *Streltsov et al.* (1998)). In the intermediate regime, $\beta \frac{m_i}{m_e} \sim 1$, the positive and negative dispersive effects on the wave propagation are expected to balance each other. This is demonstrated in the context of the modeling studies along Jovian magnetic field lines in Chapter 7.

Regardless of the kinetic or inertial limit, the ions are generally considered cold, i.e., their thermal velocity $v_{th,i}$ is slower than the parallel wave dynamics. This manifests in the assumption $\beta_i = \frac{v_{th,i}^2}{v_A^2} \ll 1$, which was used in expression (3.40). As a result, *Hasegawa and Chen* (1976) showed that for the small-β_i limit in the kinetic regime, ion Landau damping is expected to be much weaker than electron Landau damping, as there are only a few particles which can be in resonance with the wave parallel electric field. In technical terms, the Alfvén phase velocity lies on the tail of the ion distribution function. As the ion plasma beta approaches unity, $\beta_i \sim 1$, which are plasma conditions prevailing in the solar wind

(*Sahraoui et al.*, 2012), ion Landau damping due to kinetic Alfvén waves becomes equally important as electron Landau damping. However, the dispersion relations presented in the context of this thesis lose validity as the KAW then additionally couples to the fast mode, which is associated with an arising parallel magnetic field fluctuation $\delta B_\parallel$, and hence, allow for transit-time damping due to interaction of the particles in form of a diamagnetic drift motion (*Hollweg*, 1999; *Leamon et al.*, 1999).

3.5.3. Dispersion relation for the Kinetic Alfvén Wave

Up to now, we did not include dissipative effects into the dispersion relations, which are absent in the fluid approach. But these are important for us in order to quantify particle energization in association with the auroral emissions. A model for the dispersion relation for the kinetic Alfvén wave considering full kinetic effects in both regimes and the applicability in the transition region was published by *Lysak and Lotko* (1996) and slightly generalized by *Lysak* (2008). Its derivation is based on the general dispersion relation for a hot plasma using the dielectric tensor concept as presented in Section 3.4. *Lysak and Lotko* (1996) applied the various assumptions for the kinetic Alfvén wave introduced in the previous Section 3.5.2. In condensed form, these assumptions are

$$1)\,\omega < \Omega_i \qquad 2)\,\beta_i \ll 1 \qquad 3)\,k_\parallel/k_\perp \ll 1$$
$$4)\,k_\parallel v_{th,i/e} \ll n\Omega_{i/e} \qquad 5)\,k_\parallel^2\lambda_{De}^2 \ll 1 \qquad 6)\,c^2/v_A^2 \gg 1.$$

Conditions 1, 2 and 3 are important for the solely coupling of the Alfvén branch to the ion acoustic wave and therefore the exclusion of the fast mode, where the latter is associated with frequencies above the ion cyclotron frequency Ω_i in this parameter space. The KAW instead goes into resonance reaching frequencies $\omega \sim \Omega_i$, which allow for intense cyclotron wave-particle interaction. Condition 4 is only considered for harmonic numbers $n > 0$ during derivation and allows for the expansion of the plasma dispersion function in the large argument/cold limit, $Z(\xi_{ns} \gg 1)$. However, this is not a strong condition especially for large harmonic numbers compared to condition 1 in the case of the Alfvén wave. Only for frequencies $\omega \sim \Omega_i$, we neglect the contribution to resonant cyclotron interaction ($n = 1$). Plasma dispersion function terms from the zeroth order harmonic, i.e., $Z(\xi_{0s})$, are fully maintained to not exclude the essential effects from the warm and cold electron regime on Landau damping. Conditions 5 and 6 refer to the negligibility of displacement currents in the dispersion relation of *Lysak and Lotko* (1996), which refer to the unity elements of the diagonal tensor elements. Both conditions are relaxed in *Lysak* (2008) and their updated dispersion relation considers semi-relativistic effects on the KAW. Nevertheless, condition 5 still applies in the context of our modelings.

Applying these conditions to the general tensor elements from equations (3.29) - (3.34) in Section 3.4, *Lysak and Lotko* (1996) and *Lysak* (2008) derived the only remaining elements as

$$\varepsilon_{xx}^{L08} = \varepsilon_\perp^{L08} = 1 + \tilde{\varepsilon}_{xx}^{i,L08} = 1 + \frac{c^2}{v_A^2}\frac{1-\Gamma_0(\mu_i)}{\mu_i} \tag{3.45}$$

$$\varepsilon_{zz}^{L08} = \varepsilon_\parallel^{L08} = 1 + \tilde{\varepsilon}_{zz}^{e,L08} = 1 + \frac{\Gamma_0(\mu_e)}{k_\parallel^2\lambda_{De}^2}\left(1 + \xi_{0e}Z(\xi_{0e})\right). \tag{3.46}$$

As can been seen, the ions primarily respond in the perpendicular direction over the term $\mu_i = k_\perp^2\rho_i^2/2$, whereas the major contribution of electrons enters the parallel response (*Lysak and Lotko*, 1996). Due to the very small electron gyroradii in our modelling context, the modified Bessel function involving term can safely be set to unity, thus $\Gamma_0(\mu_e \ll 1) \approx 1$. Taking the ratio of both elements in the MHD limit, we can show that $\frac{\varepsilon_{zz}}{\varepsilon_{xx}} \sim \frac{v_A^2}{k_\parallel^2 \lambda_{De}^2 c^2} \gg \frac{1}{\beta_e} \gg 1$ in our magnetospheric context. This relation illustrates that the parallel conductivity in the MHD limit is much larger than in the perpendicular direction. Thus, particles can move freely along the field lines but not across them as a consequence of the frozen-in theorem. A further important observation is that only the parallel tensor element has an imaginary contribution. The imaginary part enters the expression over the complex valued plasma dispersion function $Z(\xi_{0e})$ or more specific over its derivative $Z'(\xi_{0e}) = -2(1 + \xi_{0e} Z(\xi_{0e}))$. From complex analysis, it can be shown that the imaginary part depends on the derivative of the Maxwellian distribution at the resonance speed (*Baumjohann and Treumann*, 2012). This has the important consequence, that the *Lysak* (2008) model only includes electron Landau damping and neglects all other damping mechanisms such as ion Landau and cyclotron damping. In the course of the thesis, we show that electron Landau damping indeed dominates the wave damping characterstics in the context of auroral heating.

The resulting system for the KAW reduces to

$$\begin{pmatrix} \varepsilon_{xx} - n_\parallel^2 & n_\parallel n_\perp \\ n_\parallel n_\perp & \varepsilon_{zz} - n_\perp^2 \end{pmatrix} \begin{pmatrix} \delta E_x \\ \delta E_z \end{pmatrix} = \vec{0} \tag{3.47}$$

and highlights the coupling of the Alfvén mode to the ion acoustic mode. Here, $n_\parallel = \frac{k_\parallel c}{\omega}$ and $n_\perp = \frac{k_\perp c}{\omega}$ refer to the parallel and perpendicular component of the index of refraction. Rearranging the corresponding determinant gives the governing dispersion relation from *Lysak* (2008)

$$\frac{\omega^2}{k_\parallel^2 v_A^2} = \frac{1}{(v_A/c)^2 + \frac{1-\Gamma_0(\mu_i)}{\mu_i}} + \frac{k_\perp^2 \rho_s^2}{\Gamma_0(\mu_e)\left[1 + \xi_{oe} Z(\xi_{oe})\right] + k_\parallel^2 \lambda_{De}^2}, \tag{3.48}$$

which is an implicit equation for the desired complex valued wave frequency $\omega = \omega_r + i\gamma$. In the large scale limit ($k_\perp \to 0$) and hence also for small ion gyroradii ($\mu_i \to 0$), we can easily recover the dispersion relation for the MHD Alfvén wave from equation (3.37). *Lysak and Lotko* (1996) also showed, that the dispersion relations (3.41) and (3.43) are recovered from equation (3.48) in the cold and the warm electron limit, respectively.

Although not applied in the context of this thesis, future consideration of dispersive and dissipative properties of KAWs in the presence of a multi-species plasma is desirable. Based on the derivation of *Lysak and Lotko* (1996), we can generalize the formulation of the dispersion relation from equation (3.48) to

$$\frac{\omega^2}{k_\parallel^2 \bar{v}_A^2} = \frac{1}{(\bar{v}_A/c)^2 + (\bar{v}_A)^2 \sum_i \frac{1}{v_{A,i}^2} \frac{1-\Gamma_0(\mu_i)}{\mu_i}} + \frac{k_\perp^2 \rho_{s,eff}^2}{k_\parallel^2 \lambda_D^2 + \lambda_D^2 \sum_e \frac{\Gamma_0(\mu_e)}{\lambda_{De}^2}\left[1 + \xi_{oe} Z(\xi_{oe})\right]}. \tag{3.49}$$

Here, $\bar{v}_A = \left(\sum_i \frac{1}{v_{A,i}^2}\right)^{-1/2}$ denotes the multi-fluid Alfvén speed with the species related Alfvén speeds of $v_{A,i}$. $\lambda_D = \left(\sum_e \frac{1}{\lambda_{De}^2}\right)^{-1/2}$ is the effective Debye length according to equation (3.2) and we introduce $\rho_{s,eff} = \frac{c}{\bar{v}_A} \lambda_D$ as effective acoustic length scale.

3.5.4. Analytic damping rates in the kinetic and inertial regime

In the warm and the cold electron limit, we are now able to derive analytic expressions for the Landau damping rate due to the kinetic Alfvén wave based on the dispersion relation (3.48). The damping rate γ, i.e., the imaginary part of the wave frequency, can be estimated from Taylor expansion of the determinant of the complex valued system matrix from equation (3.47), i.e., $D(\vec{k}, \omega_r, \gamma) = 0$, around the real frequency ω_r as

$$\gamma(\vec{k}, \omega) = - \left. \frac{Im(D(\vec{k}, \omega_r))}{\frac{\partial Re(D(\vec{k}, \omega))}{\partial \omega_r}} \right|_{\gamma=0} . \tag{3.50}$$

This expression is well known in literature (e.g., *Glassmeier and Scholer* (1991); *Treumann and Baumjohann* (1997)) and is only valid for weakly damped waves, i.e., $\gamma \ll \omega_r$. The real part of the dispersion relation simultaneously needs to fulfill the dispersion relation so that $\mathrm{Re}(\mathrm{D}(\vec{k}, \omega_r, 0)) = 0$, which justifies the general approach to neglect damping during derivation of dispersion relations and still get meaningful results in terms of a two-fluid theory.

Expanding ε_{zz} from equation (3.46) in the hot electron limit and retaining the imaginary contribution, we can derive the normalized damping rate due to the electrons as

$$\left. \frac{\gamma}{\omega_r} \right|^{hot} = -\frac{\sqrt{\pi}}{2} \left(\frac{k_\perp^2 \rho_s^2}{\sqrt{1 + k_\perp^2 \rho_s^2}} \right) \sqrt{\frac{1}{\beta_e} \frac{m_e}{m_i}} \exp\left(-\frac{1}{\beta_e} \frac{m_e}{m_i} (1 + k_\perp^2 \rho_s^2) \right) \tag{3.51}$$

$$= -\frac{\sqrt{\pi}}{2} \left(\frac{k_\perp^2 \rho_s^2}{1 + k_\perp^2 \rho_s^2} \right) \frac{v_{ph,\|}}{v_{th,e}} \exp\left(-\left(\frac{v_{ph,\|}}{v_{th,e}} \right)^2 \right) . \tag{3.52}$$

Considering larger scales, the normalized damping rate grows quadratic in $k_\perp \rho_s$ and vanishes in the large scale limit as expected. In terms of $\xi_{0e} = \frac{v_{ph,\|}}{v_{th,e}} = \sqrt{\frac{1}{\beta_e} \frac{m_e}{m_i}} \sqrt{1 + k_\perp^2 \rho_s^2}$, the damping maximizes for $v_{ph,\|} = v_A \sqrt{1 + k_\perp^2 \rho_s^2} \sim \frac{v_{th,e}}{\sqrt{2}}$. This is consistent with the idea of intense wave-particle interaction with the resonance located at the most probable particle speed of the distribution function (*Lysak and Lotko*, 1996).

With the same procedure, we can also derive the normalized electron Landau damping rate in the inertial Alfvén regime to

$$\left. \frac{\gamma}{\omega_r} \right|^{cold} = -2\sqrt{\pi} \frac{k_\perp^2 \lambda_e^2}{(1 + k_\perp^2 \lambda_e^2)^{5/2}} \frac{(\frac{1}{\beta_e} \frac{m_e}{m_i})^{3/2}}{(1 + \frac{v_A^2}{c^2})^{3/2}} \exp\left(-\frac{1}{\beta_e} \frac{m_e}{m_i} \frac{(1 + \frac{v_A^2}{c^2})^{-1}}{1 + k_\perp^2 \lambda_e^2} \right) \tag{3.53}$$

$$= -2\sqrt{\pi} \frac{k_\perp^2 \lambda_e^2}{1 + k_\perp^2 \lambda_e^2} \left(\frac{v_{ph,\|}}{v_{th,e}} \right)^3 \exp\left(-\left(\frac{v_{ph,\|}}{v_{th,e}} \right)^2 \right) , \tag{3.54}$$

where the $(1 + v_A^2/c^2)$ terms stem from the semi-relativistic correction to the Alfvén velocity. In this regime, the damping maximizes for $v_{ph,\|} = \frac{v_{A,rel}}{\sqrt{1 + k_\perp^2 \lambda_e^2}} \sim \sqrt{\frac{3}{2}} v_{th,e}$. Similar to the hot electron regime, we observe in the inertial regime a quadratic dependency of the damping rate from the respective electron inertial length scale. For scales $k_\perp \lambda_e > 1$, the damping rate simultaneously experiences a less steep increase. The respective latter damping expressions (3.52) and (3.54) can be potentially used as good proxy for electron Landau damping in cases where the evaluation of the damping rate fails due to the $v_{ph,\|}$ dependence. When the wave frequency, and consequently the parallel phase velocity, can still be successfully retrieved from the numerical dispersion relations, these can be used as input for the analytic damping expressions. We expect that they provide a more realistic estimate of the electron Landau damping rate over a broader parameter range than assumed for the derived expressions (as $T_e \gg T_i$). In the given analytic approximations, dispersive effects from ions have been neglected and thus would underestimate the phase velocity of the kinetic Alfvén wave in the warm regime. Similarly, we did not include thermal effects in the inertial regime.

A further interesting result from both normalized damping rates is that these do not depend on the parallel wavenumber. This behavior of the damping rate was also observed in numerical modeling studies by *Schreiner and Saur* (2017) in the $\beta_i \sim 1$-regime. *Schreiner and Saur* (2017) discuss this in the context of spectral energy flux in turbulence theory, which we forgo for our considerations. We expect a weak non-linear dependency on parallel wavenumber only close to the ion cyclotron frequency such as in the generalized warm analytic wave frequency expression (3.42).

In this thesis, the dispersion relation (3.48) is used to model the dispersive and dissipative properties of the KAW. For comparison, we also use the full hot plasma dispersion relation using the general tensor elements from Section 3.4. The numerical routine involving a two-dimensional Newton root search algorithm to solve these implicit equations has been developed and applied by *Schreiner and Saur* (2017) in the context of solar wind turbulence. We adapted the code for our needs and implemented expressions for the polarization relations and particle responses, which are presented in the subsequent sections.

3.5.5. Implemented polarization relations

With the dispersive properties of the KAW, we now introduce expressions for the wave electric field amplitude of equation (3.8). The perpendicular and parallel electric field components are important indicators for the ability of intense wave-particle interaction. Landau damping is favored by the presence of an electric field parallel to the ambient magnetic field lines, which is absent in the MHD limit. Cyclotron damping instead requires a perpendicular electric field component in-phase with the particle motion. In case of the low-frequency nature of the KAW, ions are favored for this kind of interaction as the electron gyrofrequency scales with $\Omega_e = \frac{m_i}{m_e}\Omega_i \gg \omega$.

From Faraday's law, we gain a general relationship between the parallel and perpendicular KAW electric field component, δE_x and δE_z, as

$$\frac{\delta E_z}{\delta B_y} = \frac{k_z}{k_x}\frac{\delta E_x}{\delta B_y} - \frac{\omega}{k_x} \tag{3.55}$$

with δB_y the magnetic wave fluctuation perpendicular to δE_x and the background magnetic field. Using the convention $\omega = k_z v_A^{rel}\bar{\omega}$, where $\bar{\omega}$ reflects the dispersive character of the wave frequency, we can easily identify that the parallel field component scales with $\frac{k_z}{k_x} \ll 1$ with respect to the perpendicular component. Thus, δE_z can be considered small compared to δE_x in case of the KAW.

Using Ampere's law, we obtain specific expressions for the decoupled electric field components in dependence of the tensor elements as

$$\frac{\delta E_x}{\delta B_y} = \frac{c^2}{\omega}\frac{k_z\varepsilon_{zz} + k_x\varepsilon_{xz}}{\varepsilon_{xx}\varepsilon_{zz} - \varepsilon_{xz}^2} \simeq +\frac{c^2 k_z}{\omega\varepsilon_{xx}} \tag{3.56}$$

$$\frac{\delta E_z}{\delta B_y} = \frac{c^2}{\omega}\frac{k_z\varepsilon_{xz} + k_x\varepsilon_{xx}}{\varepsilon_{xz}^2 - \varepsilon_{xx}\varepsilon_{zz}} \simeq -\frac{c^2 k_x}{\omega\varepsilon_{zz}} \tag{3.57}$$

where the dielectric tensor elements contain the plasma response to the wave electric field. Terms involving ε_{xz} can be neglected as shown by *Lysak and Lotko* (1996).

Using eq (3.55), we can alternatively express the polarization relations from (3.56) and (3.57) as

$$\frac{\delta E_x}{\delta B_y} \simeq \frac{k_x}{k_z}\left(-\frac{c^2 k_x}{\omega \varepsilon_{zz}}\right) + \frac{\omega}{k_z} \tag{3.58}$$

$$\frac{\delta E_z}{\delta B_y} \simeq \left(\frac{c^2 k_z^2}{k_x \omega \varepsilon_{xx}}\right) - \frac{\omega}{k_x} = \frac{k_z}{k_x} v_A \left(\frac{c^2}{v_A^2}\frac{1}{\bar{\omega}\varepsilon_{xx}} - \bar{\omega}\right) \tag{3.59}$$

We found that expressions involving ε_{xx} are numerically more stable than those with ε_{zz} as the latter involve the plasma dispersion function $Z(\xi)$. Thus, we implemented equations (3.56) and (3.59) for the hot and *Lysak* (2008) based case, which corresponds to the expressions stated by *Saur et al.* (2018b). To test the implementations, we use analytic limits for the electric field expressions. These are taken from literature and will be presented in the following.

Analytic limits

Using $\varepsilon_{zz} \sim \frac{1}{k_z^2 \lambda_{De}^2}$ in the hot limit ($\xi_{0e} < 1$) with $k_z^2 \lambda_{De}^2 \ll 1$ together with the dispersion relation (3.41), we can analytically express the real part of the parallel electric field (3.57) as

$$\left.\frac{\delta E_z}{\delta B_y}\right|^{hot} = -\frac{k_z}{k_x} v_A \frac{k_x^2 \rho_s^2}{\sqrt{1 + k_x^2 \rho^2}}, \tag{3.60}$$

which is the expression given by *Lysak and Song* (2003). In line with their interpretation, δE_z is driven by electron pressure effects over the ion acoustic radius whereas on scales $k_\perp \rho \sim 1$ the finite ion gyroradius starts to counteract such an increase. The corresponding perpendicular component δE_x can be retrieved from equations (3.55) and (3.60) and reads in accordance with *Lysak and Song* (2003)

$$\left.\frac{\delta E_x}{\delta B_y}\right|^{hot} = v_A \frac{1 + 0.75 k_x^2 \rho_i^2}{\sqrt{1 + k_x^2 \rho^2}}. \tag{3.61}$$

Here, thermal ions act to increase the perpendicular field and electrons tend to reduce it. The ratio of the given electric field components is given by

$$\left.\frac{\delta E_z}{\delta E_x}\right|^{hot} = -\frac{k_z}{k_x} \frac{k_x^2 \rho_s^2}{1 + 0.75 k_x^2 \rho_i^2}. \tag{3.62}$$

In the opposite cold electron limit ($\xi_{0e} \gg 1$), hence $\varepsilon_{zz} \sim -\frac{\omega_{pe}^2}{\omega^2}$, using equation (3.58) and the two-fluid dispersion relation (3.44), the perpendicular electric field reads

$$\left.\frac{\delta E_x}{\delta B_y}\right|^{cold} = v_A^{rel} \sqrt{(1 + k_x^2 \rho^2)(1 + k_x^2 \lambda_e^2)} \approx v_A^{rel} \sqrt{1 + k_x^2 \lambda_e^2}. \tag{3.63}$$

The latter expression is the pure inertial result neglecting thermal effects. In this regime, electron inertia helps to increase the perpendicular field. It is meaningful to only retain ion gyroradius effects in the two-fluid dispersion relation used for the middle expression in equation (3.63). We formally considered electrons to be cold so that their thermal effects are negligible and this has the consequence that $\rho^2 \approx \rho_i^2$, which then corresponds to the expressions from *Lysak and Song* (2003). The inertial parallel field component can be derived in an equivalent manner as for the components before and is given by

$$\left.\frac{\delta E_z}{\delta B_y}\right|^{cold} = \frac{k_z}{k_x} v_A^{rel} \frac{k_x^2(\lambda_e^2 - \rho^2)}{\sqrt{(1+k_x^2\rho^2)(1+k_x^2\lambda_e^2)}}. \tag{3.64}$$

As for δE_x, also δE_z increases in dependence of the electron inertia. However, for this component finite Larmor radius effects counteract this increase. The field ratio is

$$\left.\frac{\delta E_z}{\delta E_x}\right|^{cold} = \frac{k_z}{k_x}\frac{k_x^2(\lambda_e^2 - \rho^2)}{(1+k_x^2\rho^2)(1+k_x^2\lambda_e^2)} \approx \frac{k_z}{k_x}\frac{k_x^2\lambda_e^2}{1+k_x^2\lambda_e^2}. \tag{3.65}$$

Considering small perpendicular scales, this equation transforms into $k_x\delta E_z - k_z\delta E_x = 0$, which resembles Faraday's law for vanishing $i\omega\delta B_y$. Consequently, in the inertial limit the KAW gets a quasi-electrostatic nature for sufficient small wave scales (*Stasiewicz et al.*, 2000).

Comparing the parallel fields in both regimes we can identify a sign reversal, which expresses that electron pressure and electron inertia counteract in the respective regimes. This can also be seen in inertial expression (3.64) in which ion gyroradius effects are included. *Paschmann et al.* (2003) concluded that in the inertial regime, electrons are accelerated to carry the corresponding current density. In the other regime, the electrons are slowed down by the parallel electric field. In the intermediate regime, $\beta\frac{m_i}{m_e} \sim 1$, the kinetic effects balance each other and the real part of parallel field vanishes.

Considering large scales in both the inertial and the kinetic regime, we recover the conventional MHD characteristics $\delta E_x/\delta B_y = v_A$ and $\delta E_z = 0$ for the Alfvén wave.

3.5.6. Current density

From Ampere's law, one can express the total plasma response due to the KAW in terms of a current density as

$$\delta\vec{j} = -i\varepsilon_0\omega\left(\underline{\underline{\varepsilon}} - \underline{\underline{1}}\right)\delta\vec{E}_0 = -i\varepsilon_0\omega\left(\sum_s \underline{\underline{\varepsilon}}^s\right)\delta\vec{E}_0 = \sum_s \delta\vec{j}^s, \tag{3.66}$$

where we can formally interpret the factor $-i\varepsilon_0\omega\left(\underline{\underline{\varepsilon}} - \mathbf{1}\right)$ as the conductivity kernel $\underline{\underline{\sigma}}$ of the system. Hence, this formulation resembles Ohm's law. Here the superscript $s = (i, e)$ refers to the different ion (i) and electron (e) populations of the plasma which contribute to the total response via the susceptibilities $\underline{\underline{\varepsilon}}^s$. From the additive property of the dielectric tensor (see equation (3.34)), we can easily separate the contributions from ion and electron species in equation (3.66). According to *Stix* (1992), the single contributions $\delta\vec{j}^s$ can be evaluated as

$$\delta\vec{j}^s(\vec{k},\omega) = -i\varepsilon_0\omega\underline{\underline{\varepsilon}}^s\delta\vec{E}_0. \tag{3.67}$$

In the following, we give expressions for current responses for species s in the framework of the hot plasma dispersion relation and these related to the reduced KAW model according to *Lysak* (2008).

Due to the smallness of ε_{xz}^s, we can neglect contributions from δE_z to the hot perpendicular currents for species s, which yields

$$\begin{aligned} \delta j_x^{s,hot} &= -i\varepsilon_0\omega\left(\varepsilon_{xx}^s\delta E_x^{hot} + \varepsilon_{xz}^s\delta E_z^{hot}\right) \\ &\simeq -i\varepsilon_0\omega\varepsilon_{xx}^s\left(\frac{c^2}{\omega}\frac{k_z}{\varepsilon_{xx}}\delta B_y\right) = -i\frac{k_z}{\mu_0}\frac{\varepsilon_{xx}^s}{\varepsilon_{xx}}\delta B_y. \end{aligned} \tag{3.68}$$

Equivalently, for the parallel currents of both species we can formulate

$$\begin{aligned}\delta j_z^{s,hot} &= -i\varepsilon_0\omega\left(\varepsilon_{xz}^s\delta E_x^{hot} + \varepsilon_{zz}^s\delta E_z^{hot}\right)\\ &\simeq -i\varepsilon_0\omega\varepsilon_{zz}^s\left(-\frac{c^2}{\omega}\frac{k_x}{\varepsilon_{zz}}\delta B_y\right) = i\frac{k_x}{\mu_0}\frac{\varepsilon_{zz}^s}{\varepsilon_{zz}}\delta B_y. \end{aligned} \tag{3.69}$$

Responses in y-direction originate from the $\delta\vec{E}_x \times \vec{B}_0$-drift motions due to the KAW and read

$$\begin{aligned}\delta j_y^{s,hot} &= -i\varepsilon_0\omega\left(-\varepsilon_{xy}^s\delta E_x^{hot} + \varepsilon_{yz}^s\delta E_z^{hot}\right)\\ &= -i\varepsilon_0\delta B_y\left[\frac{k_z c^2}{\varepsilon_{xx}}\left(-\varepsilon_{xy}^s + \frac{k_z}{k_x}\varepsilon_{yz}^s\right) - \frac{\omega}{k_x}\varepsilon_{yz}^s\right]. \end{aligned} \tag{3.70}$$

We have to consider that generally only the sum of the current contributions generates a physical current as, e.g., the $\vec{E} \times \vec{B}$ response is not associated with a net current density. However, for this equation these contributions are numerically unstable and hence these results are considered as unreliable.

In the model of *Lysak* (2008), only the tensor elements $\varepsilon_{xx}^{L08} = 1+\varepsilon_{xx}^{i,L08}$ and $\varepsilon_{zz}^{L08} = 1+\varepsilon_{zz}^{e,L08}$ contribute to the current densities:

$$\begin{aligned}\delta j_x^{i,L08} &= -i\varepsilon_0\omega\varepsilon_{xx}^{i,L08}\delta E_x^{L08}\\ &= -i\varepsilon_0\omega\varepsilon_{xx}^{i,L08}\left(\frac{c^2}{\omega}\frac{k_z}{\varepsilon_{xx}^{L08}}\delta B_y\right) = -i\frac{k_z}{\mu_0}\frac{\varepsilon_{xx}^{i,L08}}{1+\varepsilon_{xx}^{i,L08}}\delta B_y \end{aligned} \tag{3.71}$$

$$\begin{aligned}\delta j_z^{e,L08} &= -i\varepsilon_0\omega\varepsilon_{zz}^{e,L08}\delta E_z^{L08} = -i\varepsilon_0\omega\varepsilon_{zz}^{e,L08}\left(-\frac{c^2 k_x}{\omega\varepsilon_{zz}^{L08}}\delta B_y\right)\\ &= i\frac{k_x}{\mu_0}\frac{\varepsilon_{zz}^{e,L08}}{1+\varepsilon_{zz}^{e,L08}}\delta B_y. \end{aligned} \tag{3.72}$$

Consequently, $\delta j_x^{e,L08} = \delta j_z^{i,L08} = \delta j_y^{i/e,L08} = 0$. For reason of numerical stability, we implemented expressions (3.71) and (3.72) for the current responses instead of expressions involving only ε_{xx}^{L08}.

Including electron contributions to the perpendicular tensor element (3.45) in the Lysak model (*Lysak*, 2008), i.e., adding

$$\varepsilon_{xx}^e = \frac{\omega_{pe}^2}{\Omega_e^2}\frac{1-\Gamma_0(\mu_e)}{\mu_e} \simeq \frac{m_e}{m_i}\frac{c^2}{v_A^2} \simeq \frac{m_e}{m_i}\varepsilon_{xx}^i, \tag{3.73}$$

we can see that the perpendicular electron response scales with $\delta j_x^e \simeq \frac{m_e}{m_i}\delta j_x^i$ in case of small electron gyroradii. This meets our expectation that perpendicular currents are mainly carried by ions as the polarization drift is weighted by the mass.

If we incorporate ion contributions to the parallel tensor element (3.46) as $\varepsilon_{zz}^i = -\frac{\omega_{pi}^2}{\omega^2}\Gamma_0(\mu_i)$, we can show that the corresponding current scales with $\delta j_z^i \simeq \frac{m_e}{m_i}\delta j_z^e|^{cold}$ and $\delta j_z^i \simeq \beta_e\delta j_z^e|^{warm}$ in the cold and warm electron regime, respectively. This was also shown by *Lysak and Lotko* (1996) for tensor elements itself. Thus, the parallel response is mainly driven by electrons.

3.5.7. Power dissipation

Now we lay the foundations to quantitatively evaluate energy dissipation due to wave-particle interaction in the presence of Alfvén waves. To generally describe the evolution of the Alfvénic wave energy density, we make use of the Poynting's theorem

$$\frac{\partial u}{\partial t} + \nabla\cdot\vec{S} = -\delta\vec{j}\cdot\delta\vec{E}. \tag{3.74}$$

Here, u describes the electromagnetic energy density of the Alfvén waves in units of J/m^3 and $\vec{S} = \frac{1}{\mu_0}\delta\vec{E}\times\delta\vec{B}$ is the related Poynting flux in units of W/m^2. The term on the right hand side represents the energy added to or extracted from the Alfvén wave per time in a unit volume element (W/m^3). In this description, $\delta\vec{j}\cdot\delta\vec{E} > 0$ indicates a sink of electromagnetic energy, i.e. the energy density which is extracted from the wave per time. Due to the wave nature of the involved quantities, energy sloshes back and forth between the wave and the plasma. However, we are not interested in the instantaneous and reversible energy transfer rate, but instead in the irreversible net energy transfer rate as a result of wave-particle interaction. Consequently, we average equation (3.74) or particularly the dissipation term over a wave period indicated by the brackets:

$$\langle p_{abs}\rangle = \left\langle \mathrm{Re}(\delta\vec{j})\cdot\mathrm{Re}(\delta\vec{E})\right\rangle = \frac{1}{2}\mathrm{Re}(\delta\vec{E}_0\cdot\delta\vec{j}_0^{\,*}) \tag{3.75}$$

$$= \frac{1}{2}\omega_r\varepsilon_0\delta\vec{E}_0^{\,*}\cdot\underline{\underline{\varepsilon}}^A\cdot\delta\vec{E}_0\,. \tag{3.76}$$

In the first line we explicitly applied the notation from equation (3.8) to clearly separate the plane wave factor and the related Fourier amplitude. The real part denotes the physical quantity, which is observable. By using the general equation for the current density (3.66), the expression can finally be related to the anti-hermetian part of the dielectric tensor (see equation (3.36)), which corresponds to the equation given by *Stix* (1992) in cgs-units. This result highlights the importance to include thermal effects in a plasma wave description to allow for damping or instabilities. In a cold plasma framework, this term would vanish. Furthermore, expression (3.76) is useful to distinguish and quantify contributions to heating of single populations in a plasma based on the additive nature of the dielectric tensor. In the description of the kinetic Alfvén wave according to *Lysak and Lotko* (1996) and *Lysak* (2008), there is no anti-hermetian contribution to the dielectric tensor in perpendicular direction, i.e., $(\varepsilon_{xx}^{L08})^A = Im(\varepsilon_{xx}^{L08,i}) = 0$. Hence, there is no ion cyclotron damping included in their model. Additionally, as there is no parallel ion contribution, we can conclude that there is also no ion Landau damping as well and only electron Landau damping is considered via $(\varepsilon_{zz}^{L08})^A = Im(\varepsilon_{zz}^{L08,e})$.

The responses in terms of current density given in the previous section describe the instantaneous and reactive responses due to the kinetic Alfvén wave. We label the instantaneous response as total response for the rest of the thesis. To get the responses solely due to the different damping mechanisms, it is indicative to compare the general expression for power absorption, i.e., $\delta\vec{j}\cdot\delta\vec{E}$, with equation (3.76). From this, we can extract a 'dissipative' current density as

$$\left\langle \delta\vec{j}_s^{\,diss}\right\rangle = \frac{1}{\sqrt{2}}\varepsilon_0\omega_r\underline{\underline{\varepsilon}}_s^A\cdot\delta\vec{E}_0. \tag{3.77}$$

These dissipative currents are in-phase with the respective electric field components and thus allow for intense energy exchange. Consequently, we expect stronger dissipative responses for species at scales which are involved in Landau and cyclotron damping in the related directions. We will investigate this in Chapter 8.1.5.

A second possibility to assess damping mechanisms at work is provided by *Quataert* (1998) and *Stix* (1992). According to them, the normalized damping rate for species s of a multi-component plasma reads

$$\frac{\gamma_s}{\omega_r} = \frac{\delta\vec{E}_0^* \cdot \varepsilon_0(\underline{\underline{\varepsilon}}^s)^A \cdot \delta\vec{E}_0}{4u}. \tag{3.78}$$

With the help of the implemented electric field components from Section 3.5.5, we will make use of this expression in Chapter 7.3 in order to separate contributions to wave damping from the different wave-particle interaction mechanisms with ions and electrons. Furthermore, we now can relate the total power density absorbed by the plasma to the damping rate $\gamma = \sum_s \gamma_s$ via

$$\langle p_{abs} \rangle = 2u(k_\perp)\gamma(k_\perp), \tag{3.79}$$

in accordance with *Howes et al.* (2008), where $u(k_\perp)$ is the wave spectral power density. This expression will be helpful in developing a wave energy model as presented in Chapter 4.

3.6. Non-resonant ion heating according to *Lu and Li* (2007)

In the previous sections, we presented the theoretical foundations of resonant wave-particle interactions with kinetic Alfvén waves based on the dielectric tensor concept. In this approach, the perturbation of the equilibrium distribution function and resulting particle responses were calculated by integrating the linearized Vlasov equation over unperturbed particle trajectories (see equations (3.26) and (3.27)). However, the presence of a wave also alters the particle orbits and correspondingly the equation of motion. For a low-frequency and left-handed circularly polarized MHD Alfvén wave in a low-β_i plasma, *Lu and Li* (2007) formulated a heating process that favors stochastic ion heating. They started with a modified equation of motion

$$\frac{d\vec{v}}{dt} = \frac{e}{m_i}\left(\delta\vec{E}_\perp + \vec{v} \times (\vec{B}_0 + \delta\vec{B}_\perp)\right) \tag{3.80}$$

$$\frac{dz}{dt} = v_\parallel \tag{3.81}$$

for single ions in the presence of the Alfvén wave. The related fluctuations $\delta\vec{E}_\perp$ and $\delta\vec{B}_\perp$ are perpendicular to the background magnetic field $\vec{B}_0$. The simplified solution to this set of equations reads

$$v_\perp(t) = v_\perp(0)e^{-i\Omega_i t} - \delta v_\perp e^{-ik_\parallel(v_A t - z)} + \delta v_\perp e^{ik_\parallel z(0)} e^{-i\Omega_i t} \tag{3.82}$$

$$v_\parallel(t) = v_\parallel(0) + \frac{\delta v_\perp^2}{v_A}\left(1 - \cos(\Omega_i t - k_\parallel v_A t - k_\parallel v_\parallel(0)t)\right). \tag{3.83}$$

The initial conditions for velocity and position are denoted by $v_\perp(0), v_\parallel(0)$ and $z(0)$. The latter two are approximately related by $z = z(0) + v_\parallel(0)t$ with the position z of the ion at time t. The first two terms of the perpendicular component (3.82) describe the simple gyromotion of the ion with gyrofrequency Ω_i and the drift motion $\delta v_\perp = v_A \frac{\delta B_\perp}{B_0} = \frac{\delta E_\perp}{B_0}$ in the wave electric field. The last term is interpreted as the perturbation of the gyro orbit due to the presence of the wave. It is this term which is relevant for the development of phase differences between thermal ions with initially Maxwellian distributed velocities in the wave electric field. Particles will have different velocities after time t at position z depending on their initial velocity. This velocity dispersion results in heating of the population. *Lu and Li* (2007) determines the heating by building the scalar second order velocity moment based on the above solution and corresponding average value. They came up with a perpendicular and parallel proton heating of

$$\Delta T_{\perp}\,[eV] = \frac{\delta B_{\perp}^2}{2e\mu_0 n}\left(1 - e^{-\frac{\pi^2}{2}(\frac{t}{\tau})^2}\right) \tag{3.84}$$

$$\Delta T_{\parallel}\,[eV] = \frac{\delta B_{\perp}^2}{B_0^2}\Delta T_{\perp}\left(1 - \cos(2\Omega_0 t - 2k_{\parallel} v_A t)e^{-\frac{\pi^2}{2}(\frac{t}{\tau})^2}\right), \tag{3.85}$$

which we formulated in units of eV with the help of the elementary charge e. The population density is denoted by n. The time the ions spend in the Alfvén wave is given by t. From the exponential term we can identify a saturation time τ, when the heating or randomization process of the ions in the wave field saturates. In other words, ions are settled at different phases within the Alfvénic electric field. When the average phase reaches π, there is a balance between acceleration and deceleration of the ions with no net further heating. *Lu and Li* (2007) identifies this time as $\tau = \frac{\pi}{k_{\parallel} v_{th,i}}$, where $v_{th,i} = \sqrt{\frac{2k_B T_i}{m_i}}$ is the initial thermal velocity of the ions. From the above representation of the heating, we can clearly see, that parallel heating is much less efficient than perpendicular heating as $\delta B_{\perp}^2 \ll B_0^2$. We will apply this heating mechanism to the Io flux tube in Chapter 9.2 to investigate perpendicular proton heating as observed by *Clark et al.* (2020) and *Szalay et al.* (2020a).

CHAPTER 4

Model parameters along auroral field lines at Io and in the middle magnetosphere

In this chapter, we present models for the basic plasma parameters along field lines connected to the middle magnetosphere and to the Io flux tube. These parameters define the relevant plasma scales introduced in Chapter 3. We discuss our expectations on Alfvén wave dynamics based on the knowledge developed in Section 3.5. Finally, we derive a one-dimensional model for the evolution of the residual Alfvén wave energy along field lines in the presence of dissipative processes.

4.1. Field lines models

For our modeling context, we construct an ion density model in the form

$$n(z, L) = n_{ps}(L)e^{-(z/H_{ps}(L))^2} + n_{floor} + n_{iono}e^{-\frac{r-1.02}{H_{iono}}}, \tag{4.1}$$

similar to the model used by *Lysak and Song* (2020). The first term describes the density distribution within the plasma sheet outside the Io torus and is based on fitted Galileo data by *Bagenal and Delamere* (2011) as

$$n_{ps}(L \geq 6) = 1987(L/6)^{-8.2} + 14(L/6)^{-3.2} + 0.05(L/6)^{-0.65} \tag{4.2}$$

in units of cm^{-3}, where $L = \rho/R_J$ describes the L-shell parameter as measure for the equatorial distance ρ from the Jupiter center. Together with the height z above the equatorial plane, the radial distance r measured from Jupiter in expression 4.1 is given by $r = \sqrt{L^2 + z^2}$. Above the plasma sheet center ($z = 0$), the density rapidly decreases according to the exponential factor (*Hill and Michel*, 1976) in the first term of equation (4.1) with the scale height H_{ps} parameterized by *Bagenal and Delamere* (2011) as

$$H_{ps}(L) = 10^{-0.116+2.14x-2.05x^2+0.491x^3+0.126x^4} \tag{4.3}$$

in units of R_J with $x = \log_{10}(L/6)$.

Whereas heavy ion species are confined to regions close to the equatorial plane and built up the plasma sheet as a result of the increased centrifugal force, protons are able to

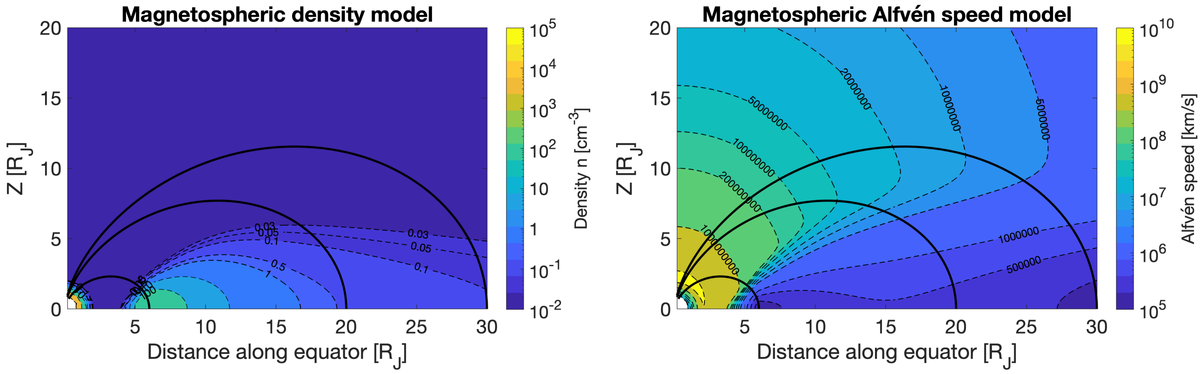

Figure 4.1.: *Magnetospheric density (left) and Alfvén speed (right) model. Solid black lines indicate dipolar magnetic field lines for L=6, 20 and 30.*

---

populate the field line at high latitudes. Therefore, the dilute region between the ionosphere and the plasma sheet is characterized in the model by a background proton density of $n_{floor} = 10^{-2}\,\mathrm{cm}^{-3}$ similar to the studies of *Cowley and Bunce* (2001) and *Saur et al.* (2018b). Towards the Jovian ionosphere, i.e., a large field line distance from the equator, *Su et al.* (2006) consider the density to behave according to a scale height law as described by the third term in equation (4.1). In their study, they take scale heights of $H_{iono} = [800\,\text{-}\,4200]$ km into account. A recent study from *Kotsiaros et al.* (2020) even takes a reduced scale height of 200 km. As we discuss in Chapter 8.1.7, the scale height plays a major role in the dissipation process of Alfvén waves. We take the largest scale height as reference for our modeling studies, such as *Lysak and Song* (2020). But still, we will particularly examine the effect of reduced scale heights. The proton density of the ionosphere is assumed to be $n_{iono} = 2 \cdot 10^5\,\mathrm{cm}^{-3}$, as in *Su et al.* (2006) and *Ray et al.* (2009). It rapidly converges towards the introduced floor value for the protons in the magnetosphere according to the scale height law.

Based on the introduced density models, we construct a 'virtual' ion mass model along the field lines as

$$\bar{m} = \frac{20 n_{ps}(L) e^{-(z/H_{ps}(L))^2} + 1 n_{H+}}{n(z,L)} \tag{4.4}$$

using an average mass of $m_{eq} = 20$ amu for the heavy ion species in the plasma sheet similar to works of *Su et al.* (2006); *Tao et al.* (2015) and *Lysak and Song* (2020). In the equatorial plane, the average mass nearly matches the heavy ion mass m_{eq} as a consequence of vanishing influence of the low proton density. Combining this model with a dipolar magnetic field, as used by *Su et al.* (2006), we can finally obtain the corresponding Alfvén speed $v_A = \frac{B}{\sqrt{\mu_0 n \bar{m}}}$. The models for the Alfvén speed and the density are provided in Figure 4.1. For the presentation of the magnetospheric density and Alfvén speed contour plot, we adapt the fall-off density model from *Lysak and Song* (2020) in the region between Jupiter and Io:

$$n_{ps}(L < 6) = n_{ps}(L = 6) e^{-\left(\frac{L/6-1}{0.1}\right)^2}. \tag{4.5}$$

The value $n_{ps}(L = 6) = 2001.05\,\mathrm{cm}^{-3}$ can be evaluated using equation (4.2) at the position of Io to ensure a continuous transition of the density model. In contrast to *Lysak and Song*

(2020) and *Bagenal et al.* (2017), we decide to display the conventional Alfvén speed v_A instead of the semi-relativistic Alfvén speed v_A^{rel}, as it facilitates to extract information on the used parameters. Especially in the low-density region above Jupiter, where $v_A > c$, used parameters cannot be extracted properly otherwise. Furthermore, as we have already indicated in the theoretical discussion of Alfvén properties, the strongest parallel inertial electric fields above Jupiter are found where the Alfvén speed v_A peaks.

We assign the electron density to be the same as for the ions in order to ensure quasi-neutrality. Although multiple charged states of oxygen and sulfur are also present within the magnetosphere (e.g., see *Dougherty et al.* (2017) and *Mauk et al.* (2004)), we consider only singly-charged ions within our prescription as the evaluation of the dispersion relationship introduced in Chapter 3.4 is restricted to such kind of populations. Anyway, outside the plasma sheet and the Io torus region, the field lines are predominantly populated by singly charged protons.

The equatorial characteristic ion temperature is taken from *Bagenal and Delamere* (2011) as

$$T_i(L) = 20 \cdot \left(\frac{H_{ps}(L)}{0.64}\right)^2, \tag{4.6}$$

using the same empirical scale height law from equation (4.3). It is derived from several Voyager and Galileo plasma sheet crossing data. According to the model, the temperature rises from several tens of eV close to Io's orbit (L=6) up to several hundreds of eV in the middle magnetosphere. For the electrons, we interpolate temperature data for the middle magnetosphere provided by *Scudder et al.* (1981), which are built from the second order scalar velocity moment of the observed distribution functions. They are colder (but still on the same order of magnitude) than the corresponding ions at the same locations. However, the data also shows that populations with different temperatures are available in the magnetosphere. Especially superthermal populations with temperatures up to several keV (e.g. *Mauk et al.* (2004); *Tao et al.* (2015) for the plasma sheet) or even MeV, as Juno data reveal at high latitudes (e.g., *Mauk et al.* (2017b)), might be interesting to investigate in the context of wave-particle interaction. Thus, we not only study thermal particles, but also investigate superthermal populations, as for example *Saur et al.* (2018b) did with parameters of $T_e = T_i = 2.5\,\text{keV}$ based on *Cowley and Bunce* (2001).

For our modelings along the Io flux tube (L=6), we do not consider the density model presented here as reference model. Instead, we take a sophisticated model from *Su et al.* (2006) based on *Su et al.* (2003) and *Ergun et al.* (2000), initially applied for Earth conditions. They used a steady-state, kinetic Vlasov approach and solved a Poisson equation for the Io flux tube considering gravitational, centrifugal, and electric potentials, but also the magnetic mirror force. Whereas the centrifugal and magnetic mirror force dominate the particle density in the plasma sheet, gravitation becomes relevant only close to the Jovian ionosphere. An analytic one-dimensional density model has been developed by *Dougherty et al.* (2017), in which they consider the tilt of the magnetic field with respect to Jupiter's spin axis. They illustrated that most of the plasma is confined to a region between the rotation equator and the magnetic equator, called the 'centrifugal equator'.

As for the middle magnetosphere, also in the Io flux tube temperatures differ between thermal and hot species (e.g., see *Su et al.* (2003), *Frank and Paterson* (1999)), which we will consider in our subsequent modeling studies. For simplicity, we keep the temperatures fixed along the field lines, as also assumed by *Dougherty et al.* (2017) and *Su et al.* (2006)

in the magnetosphere. Especially for the electrons this is a good approximation in a collisionless plasma, owing to their high heat conductivity along the field lines and so their ability to rapidly balance temperature gradients (*Saur et al.* (2004)).

4.2. Expectations for Alfvén wave dynamics along field lines

With the introduced models, we now can perform an initial study for the expected Alfvén wave characteristics along chosen magnetic field lines. These will be along the Io flux tube, i.e., L=6, and also L=20, 25 and 30 in the middle magnetosphere connected to the main emissions. To formulate expectations for the properties of the Alfvén wave, we consider the ion plasma-β_i and additionally $\beta_e \frac{m_i}{m_e}$ as basic parameters.

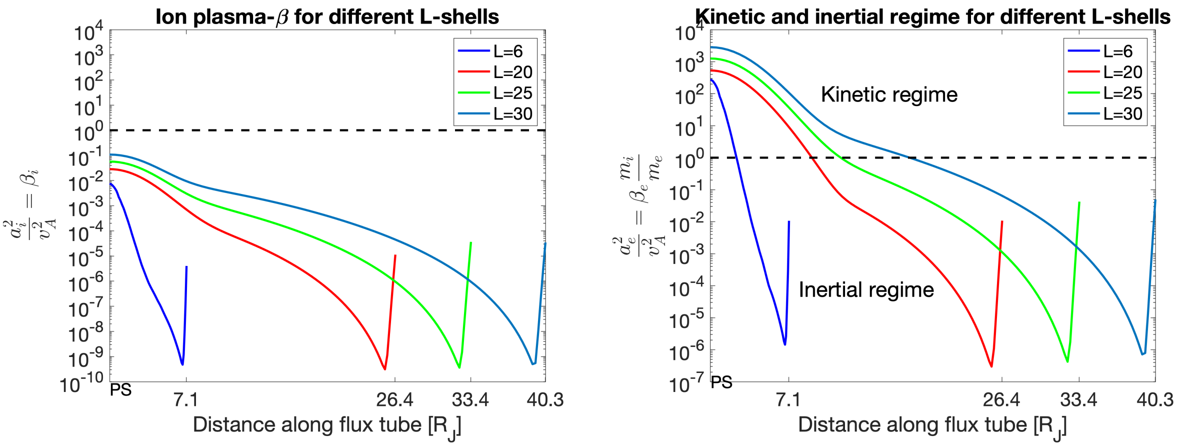

Figure 4.2.: Left) Ion plasma beta. The x-axis labels denote the end of the respective field lines in the Jovian ionosphere and thus their total lengths. Right) Kinetic and inertial regimes of Alfvén waves characterized by the ratio of electron thermal to Alfvén speed for different L-shells. The black dotted line delineates the transition from the kinetic to the inertial regime.

The parameter $\beta_i = \frac{v_{th,i}^2}{v_A^2}$ gives a hint whether ion Landau damping is effective or not. For values much smaller than one, the ion thermal speed is much lower than the Alfvén speed. Consequently, there are only few ions in resonance with the kinetic Alfvén waves compared to the lighter electrons. In the studied cases in Figure 4.2, we can identify that $\beta_i \ll 1$ for all investigated field lines. Thus, we do not expect significant ion Landau damping, as supposed by the model of *Lysak and Lotko* (1996) and *Lysak* (2008). We can observe that the magnetic field loses its dominance for larger L-shells in the middle magnetospheric plasma sheet. Hence, for a warmer ion species, $\beta_i \sim 1$ and ion Landau damping might get efficient in this region.

Equivalently, we can investigate $\beta_e \frac{m_i}{m_e} = \frac{v_{th,e}^2}{v_A^2}$ from the right panel in the same Figure. Here, we can see that all field lines cover both limiting kinetic cases for the Alfvén wave propagation. This highlights the necessity to study the Alfvén wave dynamics along auroral field lines using a generalized dispersion relation, such as the *Lysak* (2008) model. The peaks at the end of the field line are due to the sharp rise in density towards the ionosphere and correspondingly in Alfvén speed. The transition regions are located closer to the equatorial region. As a consequence, the inertial regime is more extended than the warm kinetic

Alfvén regime. This might influence the extend of regions of significant electron Landau damping. From the given representation, we can already conclude that dispersive effects on the phase velocity are important in order to allow for resonant particles in the high latitude region. However, we need to take into account that the parameter $\beta_e \frac{m_i}{m_e}$ does not include corrections from displacement currents, which additionally facilitates the occurrence of electron Landau damping. An equivalent conclusions holds for the ion plasma-β in the dilute region. A detailed analysis for the dispersive and dissipative properties of Alfvén waves in the Io flux tube and along main auroral field lines is performed in Chapters 7 - 9.

4.3. Model for the magnetic field fluctuations along field lines

In this Section, we develop a model for the energy density carried by the Alfvén wave, which gets transported from the equatorial region towards the high latitudes along the field lines and thereby loses energy due to wave-particle interactions. This is important to quantify the wave electric fields and currents we use for our studies in the following chapters.

The rate of change in electromagnetic energy density u [J/m^3] of Alfvén waves is described by the Poynting theorem

$$\frac{\partial u}{\partial t} + \nabla \cdot \vec{S} = p \,, \tag{4.7}$$

where $\vec{S} = \frac{\delta B^2}{\mu_0} \vec{v}_A^{rel} = 2u\vec{v}_A^{rel}$ [W/m^2] is the Alfvénic Poynting flux, i.e., the energy flow carried along the magnetic flux tube. The term $p = \delta\vec{j} \cdot \delta\vec{E} < 0$ denotes the energy density per time lost by the wave and transferred towards the particles and thus used for net heating and particle acceleration in units of W/m^3. Neglecting the energy dissipation term p, the Poynting theorem describes the conservation of electromagnetic energy density. For our needs, we are not interested in the spontaneous energy transfer between the wave and the particles but in the net exchange under stationary conditions for which the time dependence is neglected. In the framework of this thesis, we consider two different kinds of energy dissipation processes, namely resonant damping processes (see Chapter 3.3) and non-resonant perpendicular ion heating (see Chapter 3.6).

The basic idea for a semi-analytic one dimensional model description is to express the dissipative term p in terms of the work done on the particles during a characteristic time as

$$p(s) = \left.\frac{du}{dt}\right|_{\substack{non-res \\ damping}} + \left.\frac{du}{dt}\right|_{\substack{res \\ damping}} \tag{4.8}$$

$$= -\frac{u}{\tau} + 2\gamma u \,. \tag{4.9}$$

The characteristic time in case of the non-resonant mechanism reads $\tau = \frac{\pi}{k_{\parallel} v_{th,i}}$, where the parallel wavenumber is denoted by $k_{\parallel}$ and $v_{th,i}$ is the ion thermal speed. The characteristic resonant damping time is proportional to be the inverse of the damping rate $\gamma < 0$. We include the factor 2 in the expression to account for the effective power loss given by equation 3.79 in Section 3.5.7. The resonant damping contributions from different wave-particle interaction processes can be split up using $\gamma = \sum_s \gamma_s$. The parallel non-resonant ion heating term, would need to be dealt separately, compared to its perpendicular counterpart, as it enters the above energy budget with a quadratic dependency in u. However, parallel heating is much less efficient due to $\Delta T_{\parallel} \sim (\delta B/B_0)^2 \Delta T_{\perp} \ll \Delta T_{\perp}$. Thus, we neglect it in our derivation.

Integrating over a flux tube volume V from the equator to a position s along the field line bundle, we can express the Poynting theorem as

$$-v_{A,rel}^{eq} \int 2u \, dA_{eq} + v_{A,rel}(s) \int 2u \, dA(s) = - \int \frac{u}{\tau} \, dV + \int 2\gamma u \, dV \, . \tag{4.10}$$

We used Gauss's theorem of integration and dropped lateral surface terms, whose surface normal is perpendicular to the field-aligned Poynting vector. This is a good approximation as the Poynting vector, or in particular the Alfvén group velocity, only develops a negligible perpendicular component in the kinetic regime. Considering for simplicity the energy density to be distributed evenly over the cross section allows us to express the cross section integrated energy density as $\int u(x, y, s) \, dA(s) = \bar{u}(s) A(s)$. Here, $\bar{u}(s)$ represents the average wave energy density over the cross section $A(s)$ of the flux tube at field line position s. To obtain a differential equation for the desired $\bar{u}(s)$, we apply the derivative $\frac{\partial}{\partial s}$ to expression 4.10, to obtain

$$\frac{\partial}{\partial s} \Big(v_{A,rel}(s) \bar{u}(s) A(s) \Big) = - \frac{\bar{u}(s)}{2\tau(s)} + \gamma(s) \bar{u}(s) A(s) \tag{4.11}$$

From separation of variables and integrating along the flux tube from the equator to a variable field line position s, we get

$$\int_{s=eq}^{s} \frac{\frac{\partial}{\partial \tilde{s}} \bar{u}(\tilde{s})}{\bar{u}(\tilde{s})} \, d\tilde{s} = - \int_{s=eq}^{s} \frac{\frac{\partial}{\partial \tilde{s}} \left(v_{A,rel}(\tilde{s}) A(\tilde{s}) \right)}{v_{A,rel}(\tilde{s}) A(\tilde{s})} \, d\tilde{s} - \int_{s=eq}^{s} \frac{d\tilde{s}}{2\tau(\tilde{s}) v_{A,rel}(\tilde{s})} + \int_{s=eq}^{s} \frac{\gamma(\tilde{s})}{v_{A,rel}(\tilde{s})} \, d\tilde{s}. \tag{4.12}$$

Carrying out the integration and making further use of $\int \vec{B} \cdot d\vec{A} = 0 \Leftrightarrow B(s)A(s) = B_{eq} A_{eq}$, we get the final expression for the evolution of the wave energy density along the field line

$$\bar{u}(s) = \bar{u}_{eq} \left(\frac{B(s) v_{A,rel}^{eq}}{B_{eq} v_{A,rel}(s)} \right) \cdot e^{- \int_{s=eq}^{s} \frac{d\tilde{s}}{2\tau(\tilde{s}) v_{A,rel}(\tilde{s})}} \cdot e^{+ \int_{s=eq}^{s} \frac{\gamma(s)}{v_{A,rel}(s)} d\tilde{s}} \, . \tag{4.13}$$

The term $\bar{u}_{eq} = \frac{\delta B_{eq}^2}{2\mu_0}$ defines the initial energy density of the Alfvénic wave field in the plasma sheet prior to plasma interaction. The modulation in wave energy density along the field line comprises a geometrical depending term due to the increase in magnetic field strength over the semi-relativistic correction term in $v_A^{rel}(s)$ as well as the decrease in plasma density along the flux tube. Moreover, there is a dissipative contribution, which describes the exponential energy loss based on plasma heating due to wave-particle interaction. In the absence of dissipation, i.e., $\tau \to \infty$ and $\gamma \to 0$ (which both happens for small $k_{\parallel}$), only the modulating term inside the braces survives and illustrates the conservation of power inside the flux tube, prescribed by $\int \vec{S} \cdot d\vec{A} = 0$.

Expression (4.13) equivalently relates the equatorial fluctuation amplitude $\delta B_{eq} = \sqrt{2\mu_0 \bar{u}_{eq}}$ to the propagated fluctuation at field line position s. At the position of Io within the flux tube, observed values for the large-scale fluctuation amplitude δB_{eq} range between 100 - 400 nT according to *Chust et al.* (2005) and *Kivelson et al.* (1996). In the middle magnetosphere, i.e., L-shells of 20 - 30, we use values of 3 - 5 nT based on turbulence studies of *Tao et al.* (2015); *Saur et al.* (2002) and *Saur et al.* (2018b). In order to study the evolution of turbulent monochromatic Alfvén waves, we use our derived model from equation (4.13) combined with equation (B.4) from Appendix B.

CHAPTER 5

Properties of turbulent Alfvénic fluctuations associated with Io's fluxtube tail

In this chapter, we lay the foundation for the analysis of Alfvénic turbulence in the Io flux tube and also for magnetic field lines in the middle magnetosphere connected to the main auroral emissions. The basic assumptions and results for the latter region are concisely presented in the subsequent Chapter 6.

Recent Juno observations of power-law like power spectra published by *Gershman et al.* (2019) and *Sulaiman et al.* (2020) indicate a turbulent nature of the observed magnetic field fluctuations (see Chapter 2.5). Understanding the nature of these fluctuations is important as they can cause wave-particle interactions responsible for the accelerated electrons and ions to account for the footprint emissions. These acceleration processes highly depend on the temporal and spatial characteristics of the turbulent wave field. With the help of the Juno measurements, we constrain the parameter spaces relevant for modeling of wave-particle interaction processes (presented in Chapters 7 - 9). Therefore, we estimate and compare basic spatial and temporal scales associated with the Perijove 12 flyby. We motivate Alfvénic turbulence in the Io flux tube based on the measurements and discuss different source locations of turbulence. Based on the findings, we construct wavenumber spectra to characterize the wavevector structure of the Alfvénic fluctuations in the IFPT. We go on and provide evidence for the importance of Doppler shifting in Alfvénic turbulence. Subsequently, we discuss implications of different turbulence models on the resulting observable frequency ranges in comparison to the observations of *Sulaiman et al.* (2020). We complete the discussion with a comparison of the associated theoretical power spectral indices and related Alfvénic power fluxes with the observations. This chapter is submitted as paper to JGR and is considered as *Janser et al.* (2022, submitted).

5.1. General setup and basic temporal and spacial scales

Our study of turbulence in the Io flux tube tail is motivated by the observation of a power-law like behavior of the magnetic power spectral density (*Sulaiman et al.*, 2020) and the similarities with the main aurora (*Gershman et al.*, 2019). Moreover, turbulence is also observed in the vicinity of Io and also in the middle magnetosphere based on Galileo data (*Chust et al.*, 2005; *Saur et al.*, 2002; *Tao et al.*, 2015). From a theoretical perspective, we expect turbulence in the Io flux tube due to wave reflections at strong gradients in Alfvén velocity, i.e., at the Jovian ionosphere and possibly at the torus boundary (*Hess et al.*, 2010). Counter propagating Alfvén waves generated by Io's interaction with the torus plasma interact via wave-wave interactions and establish a turbulence cascade. In the remainder of this chapter we investigate the implications for the current Juno observations from turbulence generator regions inside and outside the Io torus and various turbulence models.

In order to assess turbulence in the Io flux tube, we start with a basic characterization of relevant time and length scales of the Alfvénic wave field in this section. These scales help to analyze temporal and spatial Alfvén wave patterns contained in the IFPT observations of *Sulaiman et al.* (2020).

5.1.1. General setup

An overview of the general setup used in this work is presented in Figure 5.1. Io acts as an obstacle to the overtaking torus plasma (with $v_0 = 57\,\mathrm{km/s}$) and provides the energy for the generation of Alfvén waves and eventually for turbulence. This interaction significantly alters the plasma flow around Io and causes velocity disturbances at various scales. These disturbances in turn cause magnetic field perturbations, which both propagate as Alfvén waves along the background magnetic field lines towards the high latitudes. As a result of the inhomogeneity of the background plasma parameters along the flux tube, they transform into kinetic/inertial Alfvén waves. The primary waves generated at Io are referred to as main Alfvén wings (MAW) and propagate in both hemispheres. On large scales they are standing waves in the rest frame of Io.

Juno crossed the IFPT in the high latitudes at a speed of 51 km/s during PJ12 (*Sulaiman et al.*, 2020). The corresponding width of this structure is connected to the equatorial region via Jupiters' background magnetic field lines. Its equatorial extent is an indicator for the size of Io's interaction region at least for a direct MAW crossing and will be discussed in the next paragraph. The equatorial size of the mapped structure is larger than in the high latitudes as a consequence of the magnetic field topology, which we assume for simplicity to be dipolar in our analysis. The converging character of the flux tube towards the location of the Juno measurements is indicated in Figure 5.1.

5.1.2. Temporal and spatial scales in the observed IFPT from PJ12

From the electric and magnetic field spectrograms from *Sulaiman et al.* (2020), we can conclude that Juno spent $T_{Juno} = 19 \pm 1\,\mathrm{s}$ in the IFPT structure. This corresponds to a minimal detectable frequency in the spacecraft frame of $f_0^{sc} = \frac{1}{T_{Juno}} = 0.05\,\mathrm{Hz}$, which is within a factor of two in accordance with the processed magnetic power spectrum from *Sulaiman et al.* (2020). An estimation based on the set in of significant particle flux densities from the JADE instrument gives a reduced duration of $T_{Juno} = 17 \pm 1\,\mathrm{s}$ (*Szalay et al.*, 2020b). The crossing trajectory of the structure can be estimated to $D_{Juno} = 969\,\mathrm{km}$ based on the spacecraft speed of $v_{sc} = 51\,\mathrm{km/s}$. Considering the tilt of the crossing according to Figure 1 in *Sulaiman et al.* (2020), we estimate the width of the IFPT to $D_{\perp}^{Juno} = 668\,\mathrm{km}$ assuming an infinitely extended plate representing the flux tube tail. The

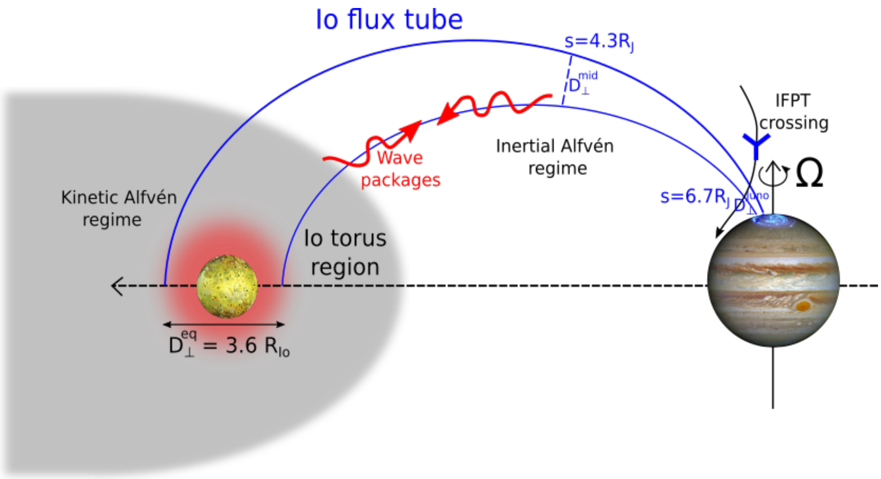

Figure 5.1.: *Overview of the Io-Jupiter system (not to scale). The Io flux tube connected to Jupiter transports energy to the high-latitude region via Alfvén waves. We consider two locations of Alfvénic turbulence activity, which are indicated with superscripts eq (equatorial, within the Io torus) and mid (mid latitude, outside the Io torus). The distance along the flux tube is denoted by variable s (counted from equator in units of the Jupiter radius R_J). These locations distinguish each other regarding the plasma parameters, the width of the flux tube $D_\perp$, and thus also in Alfvénic dispersion characteristics (kinetic vs. inertial limit). The equatorial extent of the Io's interaction region is estimated to $D_\perp^{eq} = 3.6\,R_{Io}$ based on Saur et al. (2013). The resulting wave field at the location of the IFPT measurements in the high latitudes has a width $D_\perp^{Juno}$.*

corresponding equatorial cross section has an extent of $D_\perp^{eq} = 4.7\,R_{Io}$ ($R_{Io} = 1822\,\text{km}$), calculated by employing conservation of magnetic flux in a dipolar magnetic flux tube. Measuring the width of the tail in the infrared observations of *Mura et al.* (2018) and mapping it to the equator, we find a maximal equatorial scale of $D_\perp^{eq} = 5.3\,R_{Io}$. These results are similar to the estimates of *Szalay et al.* (2020b), who found variations of the equatorial width from IFPT crossings depending on Alfvén wave travel times and related longitudinal separations from the MAW.

5.1.3. Theoretical temporal and spacial scales in the Io flux tube

Now we estimate the IFPT width based on expectations of the size of Io's interaction region. We start from the physical notion that Io's interaction with the streaming co-rotational torus plasma defines the largest perpendicular scale at which energy is injected to the system and thus shapes the generated Alfvén wave field. Based on *Saur et al.* (2013), we consider an equatorial interaction scale of $3.6\,R_{Io}$ due to Io's ionospheric extent and the extended region of increased Poynting flux at the flanks of the Alfvén wing. Exploiting conservation of magnetic flux within a flux tube, we estimate the IFPT width to $D_\perp^{Juno} = 513\,\text{km}$ at the location of measurement. The tilted Juno trajectory can be calculated to $D_{Juno} = 749\,\text{km}$.

The corresponding Juno flight time through this structure is

$$T_{Juno} = \frac{D_{Juno}}{v_{sc}} \approx 15\,s. \tag{5.1}$$

The deviation between the theoretically estimated flux tube cross section and the observed width of the IFPT indicates that further effects widen the structure. In the context of turbulence and associated small-scale Alfvén waves within the Alfvén wing, dispersion might be a conceivable explanation for the deviations as well. From calculations shown in Section 5.3.2, we estimate the potential effect of dispersion on swept perpendicular distances of the waves up to several hundred kilometers in the high latitudes on ion gyroradius scales.

Now we turn to the question of physical time scales associated with the Io interaction. The convection time, i.e., the time it takes the co-rotating torus plasma to pass Io, is given by

$$T_{conv} = \frac{3.6 R_{Io}}{v_0(1-\bar{\alpha})}, \tag{5.2}$$

where $\bar{\alpha}$ describes the interaction strength at Io, i.e., how strongly the unperturbed plasma flow ($v_0 = 57$ km/s) is slowed (cf. e.g. *Saur et al.* (2013)). The induced velocity perturbations propagate as Alfvén waves with an associated magnetic field amplitude δB along the field lines. As a result of the increasing Alfvén velocity towards Jupiter, their spatial wavelengths grow in parallel direction. Even if this wave field propagates nearly at the speed of light in the high-latitudes, the slowest temporal variability in a frame moving with the plasma is still linked to the convection time T_{conv}.

As the plasma velocity at the flanks and the center of the Alfvén wings are different, we represent the associated convection time by values for $\bar{\alpha}$ =[0, 0.9] to cover both regions. We choose the strong interaction strength $\bar{\alpha} = 0.9$ according to *Saur et al.* (2013) and *Blöcker et al.* (2018), whereas the limit $\bar{\alpha} = 0$ constitutes the case of the unperturbed plasma flowing at speed v_0 past Io. We obtain values for T_{conv} ranging between 115 s and 1150 s. Comparing these values to the crossing time from equation (5.1), we can conclude that the observed low frequency fluctuations correspond to the time scales of the IFPT crossing and not to the temporal variability caused by Io. Thus, we infer that Juno flew through a quasi-static wave field structure concerning the largest scales, i.e., the instruments cannot sense large scale temporal variability of the wave field in the spacecraft frame during a crossing of 19 s. Only temporal variations in plasma frame on period scales smaller than T_{Juno} can be detected by the MAG and Waves instrument on-board of Juno. This gives us an upper frequency limit $f_0^{sc} = \frac{1}{T_{Juno}} = 0.05\,\mathrm{Hz}$ to interpret the data as being dominated by spatial patterns. This does not mean, that for higher frequencies automatically temporal variations dominate the observable signal as will be shown in the next sections. In summary, we conclude that for the largest wave scales within the flux tube Taylor's frozen-in-field hypothesis holds in the high latitude region. Taylor's hypothesis says that observed temporal variations are caused by advected spatial structure if the advection velocity is sufficiently large (e.g., *Frisch* (1995)). This applies generally for many spacecraft measurements such as in the solar wind (e.g., *Howes et al.* (2014)), Jupiter's equatorial magnetosphere (*Saur et al.* (2002)) or Saturn's equatorial magnetosphere (*von Papen et al.* (2014)).

Finally, we characterize the structure of the wave field parallel to the background magnetic field in the equatorial region. The dispersion relationship for the MHD Alfvén wave provides a link between the maximum parallel wavelength generated at Io and the convection time scale via $\lambda_{\parallel}^{max} = T_{conv} \cdot v_A^{Io}$. This relation allows us to estimate the largest possible parallel wavelength to $\lambda_{\parallel}^{max} = [0.3 - 3.3] \cdot R_J$ near Io for both convection time scales using an Alfvén speed of $v_A^{Io} = 200\,\mathrm{km/s}$ (*Kivelson et al.*, 2004) and the equatorial Jupiter radius $R_J = 71492\,\mathrm{km}$. Thus, the wave field is elongated in the parallel direction, which is important for the existence of kinetic Alfvén waves.

5.2. Alfvénic turbulence in the Io flux tube tail

In this section we motivate the turbulent Alfvénic nature of the observed fluctuations in the IFPT and characterize the turbulence at different source locations in- and outside the torus region.

5.2.1. Alfvénic nature of the observed fluctuations

We focus on the observed (non- and weakly dispersive) lower-frequency regime from the MAG and Waves data presented in *Sulaiman et al.* (2020), i.e., in the spacecraft frequency range of $f^{sc} = \frac{\omega^{sc}}{2\pi}$=[0.2 - 800] Hz. We assume the associated fluctuations to be at least partially Alfvénic based on the established nature of the Io flux tube in the literature close to Io (*Acuna et al.*, 1981; *Neubauer*, 1980). This is also supported by the mainly perpendicular fluctuations in electric and magnetic field components as observed by *Sulaiman et al.* (2020). *Sulaiman et al.* (2020) suggested that the investigated frequency range of the magnetic power spectral data might be connected over a single power law. The authors found a spectral index of α = -2.35 ± 0.07, which they interpret in association to the findings of *Gershman et al.* (2019) for the main auroral emissions as partially developed critically balanced strong MHD turbulence. In this case, the power spectral density exhibits a $P_\perp \sim k_\parallel^{-2}$ behavior (*Goldreich and Sridhar*, 1995; *Horbury et al.*, 2008), based on their assumption that the measured frequencies map to the parallel wavenumber $k_\parallel$. However, instead of an interpretation of a $k_\parallel$ spectrum, we will show in Section 5.4 that the observed spectrum is consistent with a Doppler-shifted $k_\perp$ turbulence spectrum. As we will see in Section 5.3, this means that Juno observed a nearly static wave field with no temporal changes.

5.2.2. Turbulence generator regions

As indicated in the beginning of Section 5.1, waves reflect at strong gradients in Alfvén velocity, i.e., at the ionosphere and at the torus boundary. Counter-propagating waves can establish a turbulent cascade via non-linear wave-wave interactions and cause a filamentation process. In the case of strong turbulence, a single 'collision' is sufficient for a significant deformation of the involved wave packets. For a weak turbulent process, several wave-wave interactions are required for the same effect. The corresponding magnetic fluctuation amplitudes are small compared to the background field in this case.

In the following, we take two distinct regions for the development of turbulence into account, inside and the outside the Io torus (see Figure 5.1). We do so because these regions are characterized by different turbulence natures as we will see in the next subsection. Outside the torus, the turbulence properties also depend on the waves interference region along the field line. Thus, we choose two turbulence generator locations as representatives for both turbulence cases, although turbulence generally is allowed to develop everywhere outside the torus. The first location is placed in between the torus boundary and the ionosphere at 4.3 R_J from the equator, in Figure 5.1 indicated as "mid". The second is located directly at the location of measurement in the high latitudes. At small sub-ion scales, turbulence is generally characterized as strong and thus, kinetic turbulence is possible at both regions as a result of shrinking non-linear time scales.

5.2.3. Characterization of the turbulence nature

The turbulent nature in the Io flux tube can be assessed by comparing involved interaction time scales. The dimensionless parameter $\epsilon = \tau_A/\tau_{nl}$ characterizes whether turbulence is strong or weak, with $\epsilon > 1$ for strong turbulence and $\epsilon < 1$ for weak turbulence (see e.g. *Saur et al.* (2002)). The characteristic interaction time of Alfvén waves in the torus region is $\tau_A = \int_{-2R_J}^{2R_J} v_A^{-1}(s)ds = 573\,\mathrm{s}$. The eddy turnover time as a measure for the deformation of a Alfvén wave package is characterized by a spatial change on order of the perpendicular wavelength $\lambda_\perp^{max}$ of the Alfvén wave package at a rate of the velocity fluctuation $\delta v_A = \frac{\delta B}{B_0} v_A$. Thus, this time scale is $\tau_{nl} = \frac{\lambda_\perp^{max}}{\delta v_A} = \frac{\lambda_\perp^{max}}{v_A}\frac{B_0}{\delta B}$, where $\lambda_\perp^{max} = 3.6 R_{Io}$ describes the largest perpendicular scale in the Io torus. Using an Alfvén velocity of $200\,\mathrm{km/s}$ (*Kivelson et al.*, 2004) and a ratio of $\frac{B_0}{\delta B} \approx 5$ for the largest wave amplitude (*Kivelson et al.*, 1996), we can estimate the non-linear time scale to $\tau_{nl} = 164\,\mathrm{s}$ close to Io. In conclusion, the ratio $\epsilon = \frac{\tau_A}{\tau_{nl}} = 3.49$ is slightly larger than one and indicates a strong turbulent interaction in the torus region. However, we like to note that the plasma parameters close to Io can temporally vary as a result of Io's position inside the torus or variable atmospheric conditions and thus might influence the time scales and the character of occurring turbulence. A decreased particle density leads to an enhanced Alfvén velocity and consequently to a reduced Alfvén time. Meanwhile, the non-linear time increases and finally might push ϵ below one and temporarily allow for weak turbulence in the torus region. Also, considering a reduced magnetic field perturbation according to *Chust et al.* (2005) of $\delta B^{rms} = 100\, nT$ would even lead to $\epsilon = 0.87$.

Now, we turn our attention to turbulence generator regions outside the torus. Estimation of the time scales similar to the torus region gives $\tau_A = \int_{2R_J}^{7R_J} v_A^{-1}(s)ds \approx 15\,\mathrm{s}$, and $\tau_{nl} = \frac{\lambda_\perp}{v_A}\frac{B_0}{\delta B} = 6.5\,\mathrm{s}$ for a location in the middle between the torus boundary and the ionosphere. We used a perpendicular scale of $\lambda_\perp = 2430\,\mathrm{km}$ according to the scale mapping within the flux tube as used in Section 5.1. The Alfvén speed and dipole magnetic field strength are $v_A = 0.37c$ and $B_0 = 1.5 \cdot 10^{-5}\,\mathrm{T}$ according to the field line models from *Su et al.* (2006). The fluctuation amplitude is estimated to $\delta B = 50\,\mathrm{nT}$ exploiting conservation of energy flux. The resulting time scale ratio is $\epsilon = 2.3$ and thus favors a strong turbulent process. However, if we place the turbulence generator towards the location of the Juno measurements in the high latitudes, we obtain a non-linear time scale of $\tau_{nl} = 18\,\mathrm{s}$ and consequently, $\epsilon = 0.83$. The quantities used for this estimate are $\frac{B_0}{\delta B} \approx \frac{3\cdot 10^5 nT}{30 nT}$, $v_A = 0.96c$ and $\lambda_\perp = 513\,\mathrm{km}$. The Alfvén speed is taken from *Sulaiman et al.* (2020). The fluctuation amplitude associated with turbulence is estimated by integration of the observed power spectrum from $f = 0.05\,\mathrm{Hz}$ to $800\,\mathrm{Hz}$. We observe that the location of the turbulence generator outside the torus influences the timescale ratio and also allows for weak turbulence conditions.

We like to note, even though the measurements indicate that the electric fluctuations have a primarily transverse nature, it is still reasonable to take kinetic Alfvén wave turbulence into consideration. The KAW's parallel electric field $\delta E_\parallel$, which is absent in the MHD regime, develops a field strength at least two orders of magnitude lower than the perpendicular field component $\delta E_\perp$ at smallest perpendicular scales in the high latitudes for the strong interaction strength $\bar{\alpha} = 0.9$. Even for a weak interaction with a limit of $\bar{\alpha} = 0$, $\delta E_\parallel$ is still an order of magnitude smaller than $\delta E_\perp$ as $\delta E_\parallel$ scales with $k_\parallel$ with respect to $\delta E_\perp$ (*Borovsky*, 1993). Hence, Juno still observes nearly transverse electric field signatures in case of kinetic Alfvén waves.

Table 5.1.: *Considered turbulence models in the Io flux tube. The perpendicular power spectral index is denoted by α (not to confuse with the interaction strength $\bar{\alpha}$). L describes the largest scale at which the energy is injected into the system and is chosen here to be equivalent to the effective diameter of Io, i.e., $3.6R_{Io}$, for equatorial turbulence. Anisotropy factors a_1 and a_2 account for the anisotropic nature of the wave fields close to Io.*

Description	$P(k_\perp) \propto k_\perp^\alpha$	**Wavenumber relation**	**Authors**
Strong (anisotropic) MHD turbulence	$\alpha = -5/3$	$k_\parallel = a_1^{strong} k_\perp^{2/3} L^{-1/3}$	*Goldreich and Sridhar* (1995)
Weak MHD turbulence	$\alpha = -2$	$k_\parallel = a_1^{Weak} \frac{\delta B}{B_0} k_\perp^{1/2} k_0^{1/2}$	*Galtier et al.* (2000) *Ng and Bhattacharjee* (1997) *Saur et al.* (2002, 2018b)
(Sub-ion scale) KAW turbulence	$\alpha = -7/3$	$k_\parallel = a_2^{KAW} k_\perp^{1/3} \rho_i^{-1/3} L^{-1/3}$ (MHD-breakdown at ρ_i) $k_\parallel = a_2^{KAW} k_\perp^{1/3} \lambda_i^{-1/3} L^{-1/3}$ (MHD-breakdown at λ_i)	*Howes et al.* (2008) *von Papen and Saur* (2015)

In Section 5.4 we analyze the temporal variability of the observed wave field from Juno's IFPT crossing, now explicitly considering the higher wave frequencies due to Alfvénic turbulence. The large-scale temporal and spatial estimates of the wave field from Section 5.1 help to constrain the parameter ranges for the parallel and perpendicular wavenumbers, which are needed for modeling. Based on the respective turbulence nature at the various generator regions, we apply three different turbulence models to define such wavenumber relationships: two MHD models and a sub-ion scale KAW turbulence approach. Depending on the importance of non-linear terms in the MHD equations, Alfvénic turbulence is categorized as weak or strong (*Saur et al.*, 2002). In the case of small fluctuations, $\delta B \ll B_0$, it requires several wave-wave interactions until wave-packages deform significantly. Thus, this kind of MHD turbulence is considered as weak and can be dealt using a perturbation approach for the MHD equations. For strong turbulence, non-linear effects leads to a significant deformation during a short interaction time. On scales smaller than the ion gyroradius, kinetic effects come into play, which modify the turbulent energy cascade. Consequently, these models differ in their spectral indices α, describing the amount of energy carried by the respective wave numbers (see appendix B). In the models it is assumed that energy is injected isotropically on largest scales. However, the cascading process itself is anisotropic due to the presence of the ambient magnetic field. For Alfvénic turbulence, models applied in this thesis consider the so-called critical balance assumption. It basically assumes a balance between the interaction time and the non-linear time required for the deformation of the involved wave packages (*Goldreich and Sridhar*, 1995; *Howes et al.*, 2008; *Saur et al.*, 2018b). From this assumption, a relationship between parallel and perpendicular wavenumbers can be derived defining the wave field. As a result, wave packages primarily cascade perpendicular to the background magnetic field. Thus, the wave packages successively get a more elongated shape along the ambient magnetic field. This is consistent with kinetic Alfvén waves, which assume $k_\perp \gg k_\parallel$. The relevant information regarding the investigated turbulence models are summarized in Table 5.1.

5.3. Wavenumber spectra based on turbulence theories

In the following we further investigate the spatio-temporal structures of the fluctuations. As discussed in Section 5.2, the interpretation of the observed power law in the magnetic power spectrum regarding its implied turbulence physics depends on the spatial and temporal structure of the observed frequencies.

5.3.1. Doppler shifting

For the interpretation of the IFPT Juno measurements we consider three different frames of reference. In the Io rest frame, the Alfvén waves are stationary on large scales. Thus, the large scale wave fluctuation quantities such as current density $\delta\vec{j}$, electric field $\delta\vec{E}$ and magnetic field $\delta\vec{B}$ do not change with time along the Alfvén characteristics. In the literature, the terminology "standing Alfvén wing" is commonly used (e.g., *Neubauer* (1980)) and thus is characterized with a frequency of $\omega^{Io}= 0$ in the Io rest frame. The superscript indicates the frame of reference to which the considered quantity is related to. In the frame rotating with Jupiter's magnetospheric plasma, i.e., the plasma rest frame, the Alfvén waves fluctuate at their intrinsic frequency ω^{B}. This frequency is described by dispersion relationships such as introduced in Chapter 3.5.2. The third frame of reference is the Juno spacecraft frame, in which the Juno measurements were obtained in the high latitudes. This frame moves relative to the other frames and observes the wave field at frequencies ω^{sc}.

To relate the frequencies in the relatively moving frames of reference, we start with the general Doppler expression given by numerous authors (e.g., *Howes et al.* (2014)) as

$$\omega^{sc} = \omega + \vec{k} \cdot \vec{v}_{rel}. \tag{5.3}$$

Here, ω^{sc} is the frequency observed in a frame (e.g., a spacecraft frame of reference) moving at velocity -$\vec{v}_{rel}$ relative to an other frame. The latter frame is the plasma rest frame where the wave fluctuates at its intrinsic frequency ω and is associated with a wavevector $\vec{k}$. We apply this expression to the introduced frames of reference and illustrate the effect on the observed frequency. At first, we consider only large scale Alfvén waves, i.e., in the limit of the standing Alfvén wing and thus $\omega^{Io} = 0$. The Io and plasma rest frame move relative to each other at a speed of $v_B^{Io} = -v_{Io}^{B} = 57\,\mathrm{km/s}$ at Io's orbital position. An observer moving with the plasma frame would observe the standing Alfvén wing as spatially convected (Doppler shifted) wave field with a "convection" frequency $\omega^{B} = \omega^{Io} + \vec{k} \cdot \vec{v}_{Io}^{B} = \vec{k} \cdot \vec{v}_{Io}^{B}$ (*Neubauer*, 1998). The high-latitude Juno spacecraft would sense the standing Alfvén wing at frequencies $\omega^{sc} = \vec{k} \cdot \vec{v}_{Io}^{sc}$. This is a convection of the Alfvénic wave field past the spacecraft in Juno's frame of reference similar to the equatorial example. Observing the same wave field with respect to the plasma rest frame results in $\omega^{sc} = \vec{k} \cdot (\vec{v}_{Io}^{sc} - \vec{v}_{Io}^{B}) = \vec{k} \cdot \vec{v}_{B}^{sc}$. Thus, the wave fluctuations can be considered as frozen-in when they are convected over the Juno spacecraft.

Now we ask the question whether the Taylor hypothesis still holds if ω^{Io} deviates from zero as a result of turbulence or related to plasma conditions in the torus. Explicit time variation due to torus variability are on the convection time scales past Io or even longer, i.e., the rotation period of Jupiter, which are significantly longer compared the Juno cross timing of 17 seconds. Hence, the latter variations are negligible in the interpretation of the Juno measurements. Therefore, we investigate role of temporal variations due to the evolution of turbulence in the Io flux tube tail. In this case we obtain a temporal contribution of the Alfvénic wave field in the form $\omega^B = \omega^{Io} + \vec{k} \cdot \vec{v}^{B}_{Io}$ in the plasma frame, which results in

$$\omega^{sc} = \omega^B(\vec{k}) + \vec{k} \cdot \vec{v}^{sc}_B \tag{5.4}$$

for an observer moving with the spacecraft relative to the plasma frame at a speed of $v^B_{sc} = -v^{sc}_B$.

Putting equation (5.4) in the context of the measurements reported during the PJ12 flyby by *Sulaiman et al.* (2020), the Juno instruments MAG and Waves measured fluctuating electromagnetic quantities of the spatio-temporal wave field as $\omega^{sc}(k_\perp, k_\parallel, \omega^B(\vec{k}))$ is a function of wavenumber vector $\vec{k}$ and wave frequency ω^B. We can further simplify expression (5.4) towards

$$\omega^{sc} \approx \omega^B(\vec{k}) + k_\perp v^{sc}_B \tag{5.5}$$

by considering Juno's highly inclined trajectory with respect to the local magnetic field, i.e., $\vec{v}^{B}_{sc} \perp \vec{B}_0$. However, this approximation also holds for smaller angles because we assume the existence of (anisotropic turbulently cascaded) inertial Alfvén waves in the high-latitudes with $k_\parallel \ll k_\perp$ (see Section 5.2).

The idea of the following subsections is to investigate if ω^B is still negligibly small compared to $k_\perp v^{sc}_B$ in equation (5.5) when a turbulent cascade evolves, i.e., if the Taylor hypothesis still holds in the spacecraft frame for $k_\perp > k^{min}_\perp$. In Section 5.1, we already demonstrated that the Taylor hypothesis holds for $k^{min}_\perp$, which corresponds to the width of the Io flux tube at location of the Juno crossing.

In the next step we assume the dispersion relationship for inertial Alfvén waves from equation (3.43) to represent ω^B in equation (5.5), which leads to

$$\omega^{sc} = \frac{k_\parallel v_{A,rel}}{\sqrt{1 + (k_\perp \lambda_e)^2}} + k_\perp v^{sc}_B. \tag{5.6}$$

We point out that the dispersion relation in equation (5.5) holds exactly in infinite and homogeneous plasmas. It is a good assumption if the wavelengths are significantly smaller than the size of the system. Regarding the infinity assumption, we point out that in case of the Io flux tube assuming $\omega^{Io} = 0$, equation (3.43) implies that the parallel wavelength in the Io rest frame is infinite. This is formally possible if we include the reflection of the waves at Jupiter's ionosphere, leading to a formally infinite downstream pattern of reflected waves (see wave reflection in e.g. *Neubauer* (1980) and *Kivelson et al.* (2004)). Returning to equation (5.6), the negligibility of ω^B compared to $k_\perp v^{sc}_B$ at the largest scales implies that associated $k^{min}_\parallel$ in equation (5.6) needs to be formally so small that $k^{min}_\parallel v^{rel}_A \approx k^{min}_\parallel c \ll k^{min}_\perp v^{sc}_B$.

The turbulent cascade evolves in the $k_\perp$ direction (*Goldreich and Sridhar* (1995), *Schekochihin et al.* (2009)), i.e., $k_\perp$ of the fluctuations grows larger. The parallel turbulent scales follow the perpendicular cascade according to the critical balance assumption, but the parallel scales do not drive it. Subsequently $k_\parallel$ grows as well, but generally slower than $k_\perp$ according to the critical balance assumption which is of the form $k_\parallel \sim k^{\beta}_\perp$ with $\beta < 1$. Therefore, the Taylor hypothesis is also expected to hold for $k_\perp$ larger than $k^{min}_\perp$. In Sections 5.3.2 and 5.4, we will study these evolutions in detail, which additionally depend on the nature of turbulent cascade and the non-linearities of the various dispersion relationships in the various plasma regimes.

Gershman et al. (2019) and *Sulaiman et al.* (2020) interpret the Juno measurements as true frequencies in the rest frame of the plasma based on the large wave velocity compared to the spacecraft speed. They conclude that Doppler shifting corrections are negligible (last term in equation (5.6)) and thus only interpret the observed frequency as temporal variations (wave frequency) according to the MHD dispersion relation for Alfvén waves, $\omega = k_\parallel v_{A,rel} \approx k_\parallel c$. This has a large impact on the interpretation of the magnetic power spectra regarding their nature of turbulence as discussed in Section 5.2. In the following, we will show that the Doppler shifted contribution in equation (5.6) instead plays a dominant role for the interpretation of the measured frequencies.

5.3.2. Wavenumber spectral ranges

Having derived an expression for the observable frequencies in the spacecraft frame in the high latitudes, we now introduce wavenumber spectral ranges for explicit modeling of generated fluctuation frequencies due to turbulence. Then, we relate these wavenumbers at their respective turbulence source locations to the high latitudes as the generated Alfvén waves propagate in a converging magnetic field geometry.

We consider a spectral range for the equatorial (eq) perpendicular wavenumbers in the torus region as $k_\perp^{eq} = [\frac{2\pi}{3.6R_{Io}} \text{ - } \frac{2\pi}{\rho_i^{eq}}]$, where the largest scale is related to Io's extended interaction region (see Section 5.1) and the smallest MHD scale is the equatorial ion gyroradius ρ_i^{eq}. At spatial scales comparable to the ion scales, a spectral break occurs, where the MHD turbulence turns into kinetic turbulence. However, there is an ongoing discussion in the literature about whether MHD turbulence turns into kinetic scale turbulence at the ion gyroradius or the ion inertial length scale λ_i (e.g. *Chen et al.* (2014), *Franci et al.* (2016)). For the Io flux tube, the decoupling of ions from the fluid motion as described by the ion inertial length might be especially interesting for turbulence in the high latitudes due to increased importance of ion inertia as a result from very low ion plasma beta. The consequences of the breakdown at both scales on the resulting wave characteristics are investigated in the following sections. For the sub-ion scales, we consider a spectral range of $k_\perp^{eq} = [\frac{2\pi}{\rho_i^{eq}} \text{ - } 10\frac{2\pi}{\rho_i^{eq}}]$ or λ_i^{eq} as smallest MHD scale, respectively. The largest wavenumber is chosen arbitrarily to cover sufficient parts of the considered frequency regime. We refer to the "ρ_i-case" and "ρ_i-MHD model" to indicate the spectral break to occur at the ion gyroradius scale for the turbulence model under concern. Analogously, we use the term "λ_i-case" and "λ_i-MHD model" for the spectral ranges and associated turbulence models considering a spectral break at the ion inertial length λ_i. A given superscript (eq, mid, hl) refers to the turbulence source location inside (eq) or outside the torus (mid,hl).

Applying the wavenumber relations from the different turbulence models given in Table 5.1, we calculate the associated parallel wavenumbers needed to characterize the waves. We introduce anisotropy factors in the wavenumber relationships (see Table 5.1) to account for the anisotropic nature of the wavefield at largest scales, i.e., at energy input scales. In this context, anisotropy refers to the elongated structure of the wave packages with $\lambda_\parallel > \lambda_\perp$ as a consequence of long plasma convection time. In particular, the MHD anisotropy factors a_1 are defined such that the largest perpendicular wavelength $\lambda_\perp^{max}$ matches the largest parallel scale $\lambda_\parallel^{max}$ as introduced in Section 5.1. Exemplary for the equatorial strong MHD turbulence model in Table 5.1, the anisotropy factor a_1^{strong} can be obtained from the minimum perpendicular and parallel wave numbers (see Section 5.1) of the form

$$k_{\parallel,eq}^{min} = \frac{2\pi}{T_{conv}(\bar{\alpha}) \cdot v_A^{Io}} = k_\parallel^{strong}(k_{\perp,eq}^{min}) = a_1^{strong} \cdot (k_{\perp,eq}^{min})^{2/3} L^{-1/3}, \tag{5.7}$$

where $k_{\perp,eq}^{min} = \frac{2\pi}{3.6 R_{Io}}$ is the largest perpendicular scale. The kinetic anisotropy factors a_2 are defined equivalently, now over the parallel wavenumber of the respective MHD turbulence model at its breakdown scale to smoothly connect the MHD and the kinetic regime.

The resulting set of wavenumbers $(k_\perp^{eq}, k_\parallel^{eq})$ are mapped along the flux tube towards the location of measurement in the high latitudes (superscript hl). The perpendicular scale maps according to

$$k_\perp^{hl} = k_\perp^{eq}\sqrt{\frac{B^{hl}}{B^{eq}}}, \tag{5.8}$$

based on conserved magnetic flux within the flux tube and assuming that the waves stay inside this flux tube. For the sake of simplicity, we assume a circular cross section for $k_\perp$, since the wavenumbers vary over several orders of magnitude. Therefore, small differences in the perpendicular directions have no significant influence on the spectral ranges. Considering that the wave frequency ω does not change along the field line, i.e., $\omega_{eq} = \omega_{hl}$ using equations (3.41) and (3.43) from Chapter 3.5.2, the parallel scale transforms according to

$$k_\parallel^{hl} = \frac{\omega_{eq}}{v_{A,rel}^{hl}}\sqrt{1 + (k_\perp^{hl}\lambda_e^{hl})^2} \tag{5.9}$$

$$= k_\parallel^{eq}\frac{v_{A,rel}^{eq}}{v_{A,rel}^{hl}}\sqrt{1 + (k_\perp^{eq})^2 \cdot \left((\rho_s^{eq})^2 + \frac{3}{4}(\rho_i^{eq})^2\right)}\sqrt{1 + (k_\perp^{hl}\lambda_e^{hl})^2}. \tag{5.10}$$

Again, the dipolar magnetic field strength and semi-relativistic Alfvén speed are denoted by B and $v_{A,rel} = \frac{v_A}{\sqrt{1 + (\frac{v_A}{c})^2}}$, respectively. The corresponding plasma length scales, i.e., ion gyroradius, ion-acoustic gyroradius and electron inertial length, are indicated by ρ_i, ρ_s and λ_e.

For large perpendicular scales, i.e., dispersionless MHD scales, the parallel mapping simplifies to

$$k_\parallel^{hl} = k_\parallel^{eq}\frac{v_{A,rel}^{eq}}{v_{A,rel}^{hl}}. \tag{5.11}$$

In Figure 5.2 we display how perpendicular scale and parallel scales of the turbulent fluctuations in the wing are related for the different turbulence models under consideration (Weak, strong and kinetic) and the different source location where turbulence can be driven (in torus or outside the torus). In the left panel, we show the related scales at the respective turbulence generator regions. In the right panel, scales are shown mapped to the location of Juno's measurements in the high latitudes. For the equatorial models, the largest parallel wavelength is $3.3\,R_J$ in the strong interaction strength of $\bar{\alpha} = 0.9$. As mentioned in Section 5.1, a weaker interaction strength results in a reduced convection time and hence in a smaller $\lambda_\parallel^{max} = T_{conv} v_A^{eq}$. For a weak interaction strength in the limit of $\bar{\alpha} = 0$, the parallel wavelengths are a factor of 10 smaller for all models. We show only the scales for the ρ_i-MHD breakdown scale as the λ_i-case are qualitatively similar (and identical up to the λ_i-MHD breakdown scale). The transition from MHD turbulence to ion-kinetic turbulence is visible as a change in the slope towards larger perpendicular wavenumbers.

The large-scale parallel wavelengths at their respective source locations (Figure 5.2 left) mapped to the high latitudes (Figure 5.2 right) will result in even larger parallel wavelength as a result of increasing Alfvén speed (see equation (5.11)). In contrast, for the small scales,

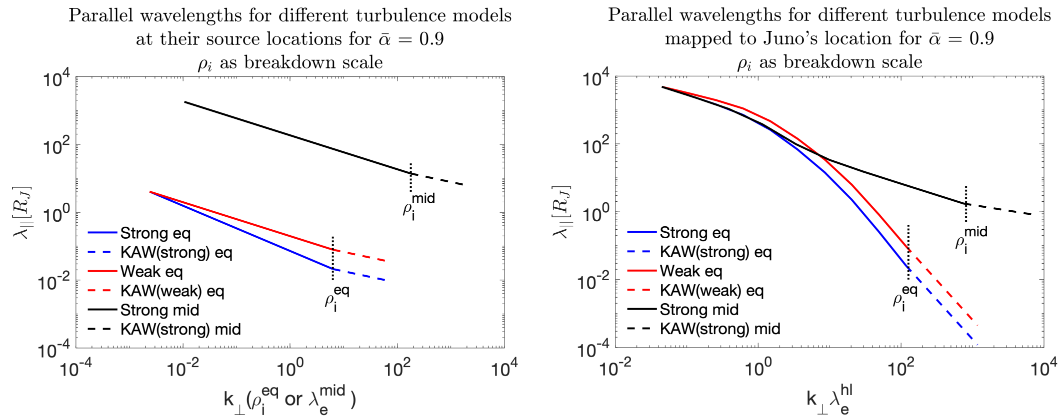

Figure 5.2.: *Parallel wavelengths (for $\bar{\alpha} = 0.9$) plotted against perpendicular scale based on turbulence originating at different locations with ion gyroradius ρ_i as MHD-breakdown scale. The horizontal axis considers the perpendicular wavenumber normalized to the local ion gyroradius for the equatorial models (eq) and the electron inertial length for the models with a source location outside the torus (mid). Left: Spectra at the respective source locations. Right: Mapped spectra to the location of the Juno measurements in the high latitudes.*

inertial effects counteract this increase based on decreasing perpendicular scale and lead to smaller parallel scales in the high latitudes than at the respective source locations. This effect is strongest for the equatorial case and thus parallel wavelength based on equatorial turbulence can cover various orders of magnitude in the high latitudes. However, it is very likely that large-scale waves will be partly reflected at the torus boundary due to a significant change in the Alfvén velocity (*Hess et al.*, 2010). This will affect waves associated with a strong interaction strength $\bar{\alpha}$ more than for a lower one. The small-scale waves can leave the torus undamped (with respect to reflection) and propagate to the high latitudes. These small-scale waves might undergo efficient wave-particle interaction and heat the observed ion and electron species towards high energies (*Clark et al.*, 2020; *Szalay et al.*, 2020a). The turbulence models with a source location outside the torus (see Figure 5.1) do not cover these small parallel scales, but instead account for even smaller perpendicular scales (because the local ρ_i-scale is smaller than at the equator), which is interesting for intense wave-particle interaction. Furthermore, waves with large parallel wavelength are generated by high latitude turbulence, which were not present for the torus based models as a consequence of discussed reflection, and might explain the lowest observed frequencies of the power spectrum from *Sulaiman et al.* (2020).

We are now picking up on the idea from Section 5.1 and investigate the increased width of the IFPT achieved by Alfvén waves entering neighboring field lines during their propagation. In the dispersive regime, the group velocity of Alfvén waves develops a perpendicular component. For example in the warm approximation for the Alfvén wave inside the torus (see equation (3.41)), the perpendicular group velocity is given by

$$v_{gr}^{\perp} = \frac{\partial \omega}{\partial k_\perp} = \frac{k_\parallel}{k_\perp} \frac{k_\perp^2(\rho_s^2 + \frac{3}{4}\rho_i^2)}{1 + k_\perp^2(\rho_s^2 + \frac{3}{4}\rho_i^2)} v_{gr}^{\parallel}. \tag{5.12}$$

Again, $k_\parallel$ and $k_\perp$ describe the parallel and perpendicular wavenumber with respect to the local background magnetic field. As visible, the perpendicular component $v_{gr}^{\perp}$ is much smaller than the parallel one ($v_{gr}^{\parallel}$) as a result of the anisotropic nature of small-scale Alfvén waves. Equivalent conclusions also hold for kinetic Alfvén waves in the cold limit. Building on the idea of *Borovsky* (1993), we integrate $v_{gr}^{\perp}$ with respect to the travel time along the flux tube. We carry out our calculations for the equatorial ion gyroradius as smallest MHD perpendicular scale and the corresponding parallel scale is retrieved from the turbulence models introduced in Table 5.1. The models used for the mapping of $k_\perp$ and $k_\|$ along the field line to the high latitudes are given by equations (5.8) and (5.9). For a strong interaction strength of $\bar{\alpha} = 0.9$, we find swept perpendicular distances of 19 km and 71 km for the weak and the strong MHD-turbulence model. For a weaker interaction strength $\bar{\alpha}$ this distance increases linearly with factor $(1-\bar{\alpha})$. In the limit of $\bar{\alpha} = 0$, we obtain a factor 10 larger values, i.e., 191 km and 708 km for both turbulence models. To conclude, the IFPT or generally the MAW can be significantly extended in the high latitudes by kinetic effects based on an equatorially located turbulence generator. The numbers suggest a larger interaction strength $\bar{\alpha}$ to be adequate for modeling.

5.4. Comparison of Doppler shifted frequency contributions for different turbulence models and turbulence generator locations

In this section, we compare the frequency contributions of the derived Doppler shifted frequency expression from equation (5.6) in the Juno spacecraft frame at the high latitudes for turbulence generator regions inside and outside the torus. We consider the introduced Alfvénic turbulence models from Section 5.2. Here we explicitly demonstrate that high frequency time-variability due to turbulent Alfvén waves in the IFPT are not detectable within Juno measurements, but Doppler-shifted spatial structures still dominate the time-series observed by the Juno spacecraft. In the following, we present the results for the strong interaction strength of $\bar{\alpha} = 0.9$. The conclusions are fully equivalent for weak interaction strengths.

5.4.1. Turbulence produced in torus and propagated into high latitudes

Beginning with the introduced perpendicular wavenumber spectral ranges in Section 5.3.2, we obtain the corresponding parallel wavenumbers from the turbulence relationships in Table 5.1 in the equatorial region. Proceeding from these sets of wavenumbers, we map them to the high latitudes according to the mapping relations introduced in Section 5.3.2. We finally deduce the frequency contributions to the observable frequency in the spacecraft frame. These are the wave frequency in the plasma frame and the Doppler shifted contribution as shown in equation (5.5). The wave frequencies are calculated by solving the dispersion relationship for the kinetic Alfvén wave from *Lysak* (2008). We use a routine from *Schreiner and Saur* (2017), which computes the wave frequency of the implicit dispersion relation via a Newton algorithm. The required plasma parameters used for its evaluation are based on the field line models from *Su et al.* (2006).

The resulting frequency contributions at the location of the Juno measurements are shown in Figure 5.3 for both MHD-breakdown scales $(\lambda_i^{eq}, \rho_i^{eq})$, which are highlighted by the vertical black line in the plots. The solutions consider an interaction strength of $\bar{\alpha} = 0.9$. As visible from the wave frequency contributions, the Alfvén wave goes into resonance reaching the equatorial cyclotron frequency $f_{ion}^{eq} = \frac{\Omega_i^{eq}}{2\pi}$ as expected in the warm regime from theory. This sets the upper frequency limit for temporal variations to be observable in the context of Alfvén waves. Thus, the investigation of Alfvénic turbulence located in the equatorial

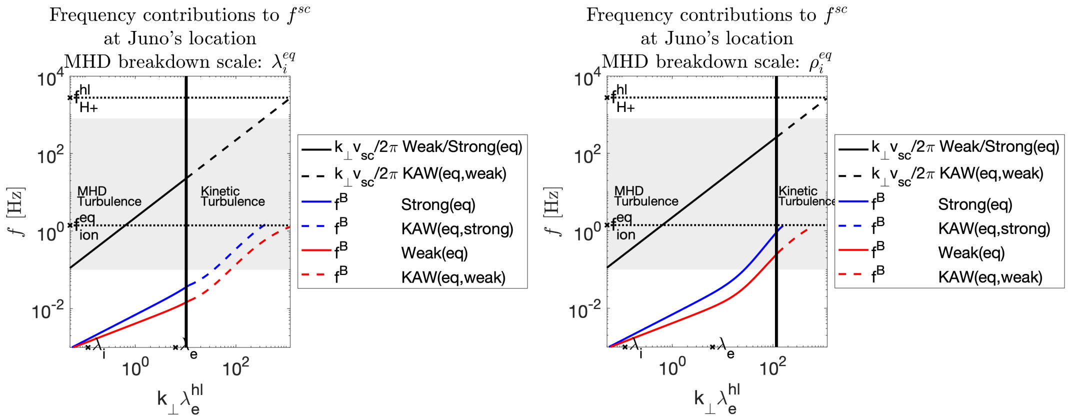

Figure 5.3.: *Doppler shifted frequencies (solid and dashed black lines) dominate over wave frequencies (blue and red lines) at the location of measurement calculated for a turbulence source location in the torus and various turbulence models. Left: Contributions for λ_i^{eq} as MHD-breakdown scale, indicated by the vertical black line. Right: Same for ρ_i^{eq}. The grey shaded region indicates the Juno-observed frequency range in the IFPT structure, f = [0.1 - 800] Hz. The horizontal dotted lines indicate the ion cyclotron frequencies in the torus region (eq) and the location of measurement in the high latitudes (hl). We consider a spacecraft speed of v_{sc} = 51 km/s according to Sulaiman et al. (2020).*

region (with $\omega^B < \Omega_i^{eq}$) automatically introduces an upper limit to temporal variations at high latitudes via ω-conservation when applying the mapping relations from equation (5.11) or (5.9), respectively. Hence, although the cyclotron frequency of the protons at high latitude Ω_i^{hl} is much larger than in the equatorial region due to the increase in magnetic field strength, the wave frequencies are still controlled by the equatorially generated frequencies.

The convective frequencies, i.e., the Doppler-shifted perpendicular wavelength scales, are represented by the solid and dashed black lines in both plots of Figure 5.3. These dominate over the wave frequencies from the respective turbulence models assuming a strong interaction strength of $\bar{\alpha} = 0.9$. Even in the limit of zero interaction strength, i.e., $\bar{\alpha} = 0$, the convective contributions still dominate the observable signal at the observed of the IFPT event regardless of the perpendicular spatial scale. These results are in accordance with the time scale comparisons from Section 5.1. This indicates that the magnetic fluctuation power spectrum from *Sulaiman et al.* (2020) needs to be interpreted with respect to the perpendicular wavenumber as $\omega^{sc} \simeq k_\perp v_B^{sc}$.

Now we turn to the question which frequency range can be covered by Alfvén waves for the given setup. The MHD turbulence models (weak, strong) cover an observable frequency range of f=[0.1 - 262] Hz in the ρ_i^{eq}-MHD breakdown case (Figure 5.3 right). Above, the KAW turbulence convective frequency contributions cover the remaining part towards the 800 Hz from the observations which corresponds to a scale of $k_\perp \lambda_e^{hl} = 360$, i.e., $\lambda_\perp = \frac{2\pi}{k_\perp} = 6 \cdot 10^{-2}$ km. In the λ_i^{eq}-case, the KAW convective contributions cover a broader frequency range, i.e., f = [23 - 800] Hz, as the ρ_i^{eq}-scale is much smaller than the λ_i^{eq}-scale. Both cases are associated with frequencies connected to the Waves instrument (above 50 Hz). However, it is unphysical that (kinetic) Alfvénic turbulence based on a ρ_i^{eq}-MHD breakdown scale originating in the torus can cover the whole frequency range in the high latitudes. For small perpendicular scales, i.e., the KAW range in Figure 5.3 (right), the Alfvén wave amplitude suffer from significant damping as its frequency reaches the cyclotron frequency. As a consequence, the propagating small-scale waves cannot reach the high-latitudes. By comparison, KAW turbulence as continuation of weak MHD turbulence is more plausible to cover a larger range of the observed frequencies than the strong MHD turbulence based KAW model, because the latter wave frequencies go into resonance at a larger perpendicular scale.

5.4.2. Turbulence generated outside the torus region

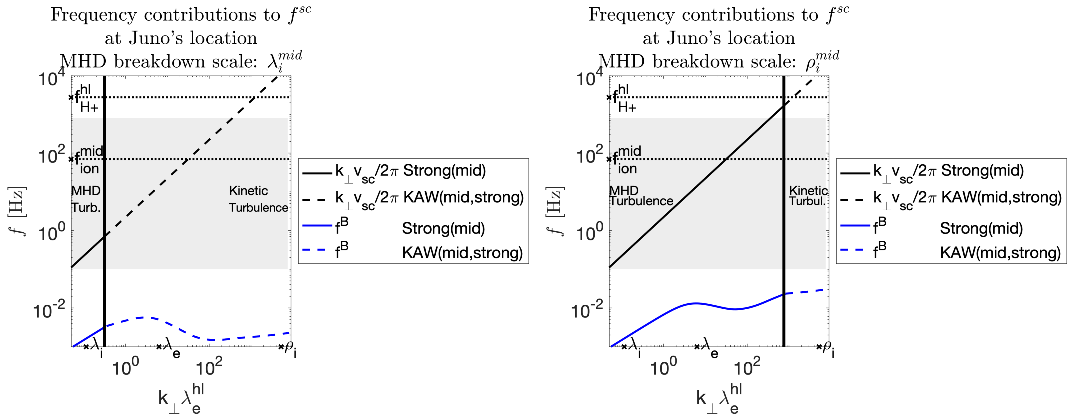

Figure 5.4.: *Doppler shifted frequencies (solid and dashed black lines) dominate over wave frequencies (blue lines) at the location of measurement calculated for a turbulence source location outside the torus at position mid (see Figure 5.1). Left: Frequency contributions for a* λ_i^{mid}*-MHD breakdown; Right: Same for* ρ_i^{mid} *as MHD-breakdown scale. Labels are the same as for Figure 5.3.*

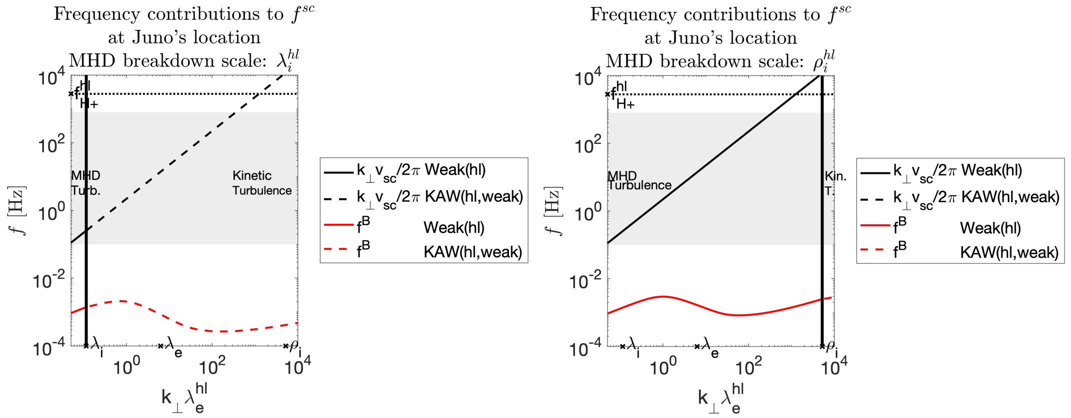

Figure 5.5.: *Wave (red lines) and Doppler (solid and dashed black lines) frequency contributions at the location of measurement based on turbulence source at the same location. Left: Frequency contributions for* λ_i^{hl}*-MHD breakdown; Right: Same for* ρ_i^{hl} *as MHD-breakdown scale. Labels are the same as for Figure 5.3.*

In the last section, we concluded that propagating small-scale equatorial Alfvén waves (KAWs) get damped on their way towards the high latitudes and cannot account for larger frequencies of the observations (at least for a ρ_i^{eq}-MHD breakdown). However, filamented KAWs originating outside the torus can reach the location of measurement within a wave period. They survive the significant amplitude damping setting in at small spatial scales, i.e., at the electron inertial length scale in the high latitudes. Hence, we investigate KAW turbulence originating outside the torus as a promising candidate to explain the spectral slope of the observed magnetic power spectrum (see Section 5.5).

The frequency contributions based on turbulence originating from the mid-latitude position mapped to the location of measurement are shown in Figure 5.4. Similar to the equatorial based turbulence, Juno observes only convection frequencies, and thus, the wave field would quasi-stationary convect past Juno. As a consequence, the observed power spectrum also needs to be interpreted with respect to the perpendicular wavenumber $k_\perp$. Equivalent conclusions can be drawn for high latitude turbulence location, shown in Figure 5.5. The major difference to the equatorial discussed case is the significantly changed MHD-breakdown scale for ρ_i and λ_i as $\beta_i \ll 1$ due the stronger background magnetic field and the decreased plasma density towards higher latitudes. Analyzing the convective frequencies of both figures, we identify a frequency of $f_{sc} = 0.7\,\mathrm{Hz}$ at the λ_i^{mid}-MHD breakdown scale (Figure 5.4) and $f_{sc} = 0.3\,\mathrm{Hz}$ for the λ_i^{hl}-MHD breakdown scale (Figure 5.5). For the corresponding ρ_i-cases, these frequencies lie significantly above 800 Hz. In the $\lambda_i^{mid,hl}$-MHD breakdown cases, KAW turbulence would take up large parts of the observed power spectrum. Based on the lack of reliable density data along the Io flux tube, parameters used in this study allow for some variability. Reduction of the number density by a factor of 7 is sufficient so that the ion inertial length scale corresponds to the largest perpendicular scale of the system in the high-latitude case. The mid-latitude case requires a density reduction by a factor of 60 for the same effect. Consequently, KAW-turbulence would cover the frequency range by its own and no MHD turbulence would set up. In the $\rho_i^{mid,hl}$-cases, KAW turbulence would not play any role for the desired frequency range. As discussed in Section 5.3.2, a MHD-breakdown at the λ_i-scale seems to be reasonable in the high latitudes. For the ρ_i-scale based MHD-breakdown, strong-MHD and weak-MHD turbulence cover the whole frequency range at the location of measurement for their respective generator locations. However, it is to be expected that Alfvén waves get significantly damped for observed frequencies above $\sim 50\,\mathrm{Hz}$ as they reach electron inertial length scales (*Saur et al.*, 2018b).

From the presented studies, we conclude that temporal variations of turbulent Alfvén waves, originating either in the equatorial region or outside the torus, are not expected to be observable by Juno in the high latitudes. Therefore, convective frequencies can be considered as the observed frequencies. The consequences for the turbulence models will be discussed in the next section.

5.5. Comparison of theoretical and observed turbulent magnetic power spectra in the high-latitudes

Based on our modeling studies from Section 5.4, we propose that the observed frequencies in the spacecraft frame are due to Doppler shifted perpendicular wavenumbers. This is contrary to the assumption of *Gershman et al.* (2019) and *Sulaiman et al.* (2020), who considered a relationship of the form $\omega^{sc} = k_\parallel v_A^{rel}$. Due to the anisotropic nature of filamentation of the considered magnetic turbulence models, energy cascades in perpendicular and parallel direction with different spectral indices. Consequently, the interpretation of the observed power spectral index changes with respect to the potential turbulence mechanism at work. In the following, we fit selected turbulence models to the observed power spectral density in the form of

$$P(f) = P_0 \left(\frac{f}{f_0} \right)^{\alpha} \tag{5.13}$$

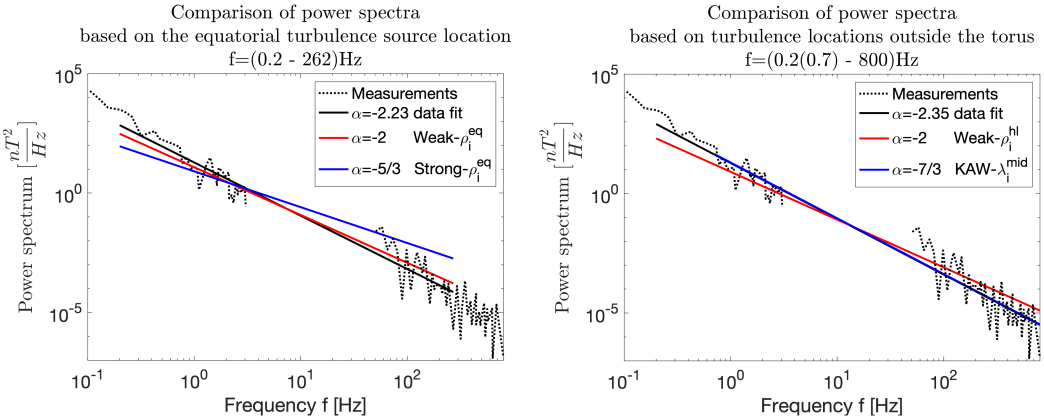

Figure 5.6.: *Power spectral density of the magnetic fluctuations from MAG and Waves data (black dotted lines) displayed together with fits to the data and the indicated turbulence models. Left: Fit with equatorial MHD turbulence models (ρ_i^{eq}-breakdown) in a frequency-range of f = [0.2 - 262] Hz. Right: Fit with high latitude turbulence models weak-ρ_i^{hl} and KAW-λ_i^{mid} in the frequency range f = [0.2(0.7) - 800] Hz according to the analysis of the turbulence frequencies. The minimal frequencies f = 0.2 Hz and f = 0.7 Hz refer to the weak-ρ_i^{hl} and KAW-λ_i^{mid} cases, respectively. The least-squares fitted lines (black solid lines) consider only the frequency ranges where the turbulent models apply.*

where f is the frequency in the spacecraft frame, $P_0 = P(f_0)$ describes the power spectral density at the minimal frequency f_0 and α denotes the spectral index. We choose $f_0 = 0.2\,\mathrm{Hz}$ for the analysis to avoid effects from leakage and aliasing in accordance with the choice of *Sulaiman et al.* (2020).

Assuming that the non overlapping MAG and Waves spectra are the result of a single cascading process in the inertial turbulence regime ($f = [0.2 - 800]\,\mathrm{Hz}$), *Sulaiman et al.* (2020) fits a spectral slope of $\alpha = -2.35 \pm 0.07$. However, the data fit allows for variability in the spectral slope, when considering only restricted frequency ranges and thus assuming a spectral break in the observed spectrum. Fitting only the MAG data ($f = [0.2 - 3]\,\mathrm{Hz}$) results in $\alpha = -2.96 \pm 0.22$ and for the Waves data ($f = [50 - 800]\,\mathrm{Hz}$) even in $\alpha = -3.51 \pm 0.36$. Both values for α are not considered here. Instead, we choose selected turbulence models from our analysis in Section 5.4 for comparison with the data involving both instruments frequency ranges.

The model turbulence power spectra in Figure 5.6 display a least-squares fits with their fixed spectral index (but variable P_0) to the respective data fit in logarithmic space. From the equatorial models (Figure 5.6 left), we show the strong MHD turbulence ($\alpha = -5/3$) and weak ($\alpha = -2$) MHD-ρ_i^{eq} turbulence models (see definition for MHD-ρ_i^{eq} in Section 5.3.2), which cover a frequency range of $f = [0.2 - 262]\,\mathrm{Hz}$. The corresponding data fit (green line) has a spectral index of $\alpha = -2.23 \pm 0.08$. From visual comparison, it is obvious that equatorial Weak turbulence suits the data fit better than the strong GS model, because a -2 slope fits better to a -2.23 slope than $-5/3$.

For the turbulence source locations outside the Io torus, fitted power spectra are shown for the weak MHD-ρ_i^{hl} and the KAW-λ_i^{mid} models in Figure 5.6 (right). As presented for the equatorial source location, strong turbulence in the mid latitudes also does not fit the data well and will be not considered here. While the weak turbulence model covers the whole frequency range, the KAW-range is restricted to $f = [0.7 - 800]\,\mathrm{Hz}$. The corresponding data fits exhibit an $\alpha = -2.35 \pm 0.07$ slope and an $\alpha = -2.31 \pm 0.08$ slope, respectively. The high-latitude Weak and the mid-latitude based KAW spectra fit the data fairly well.

Especially, the KAW spectral index is fully consistent within the errorbars of the fitted spectrum with values of $-7/3$ and -2.31 ± 0.08, respectively. A comparable conclusion can be also drawn the KAW-λ_i^{hl} model, which is not shown here.

Comparing theoretical and observed averaged wave amplitudes gives further insight into the physics. Here, we only discuss the data fit of the whole frequency range, i.e. $f = [0.2 - 800]$ Hz. From integration of the associated power spectrum over this frequency range, we come up with an average fluctuation amplitude of $\delta B = 12\,\mathrm{nT}$. Considering even smaller frequencies down to 0.1 Hz, we obtain $\delta B = 21\,\mathrm{nT}$. We can derive a theoretical model for the fluctuation amplitude, accounting only for geometric changes based on the converging magnetic field topology and conserved total wave power within a flux tube. We can express the resulting fluctuation amplitude in the high latitudes as

$$\delta B^{hl} = \delta B^{Io} \sqrt{\frac{B^{hl}}{B^{eq}} \frac{v_{A,rel}^{eq}}{v_{A,rel}^{hl}}}, \tag{5.14}$$

where $v_{A,rel}$ and B denotes the semi-relativistic Alfvén speed and the magnetic field strength at the equator and in the high-latitudes. Using an Io-related maximal fluctuation amplitude of $\delta B^{Io} = 400\,nT$, we can calculate the resulting fluctuation in the high-latitudes to $\delta B^{hl} = 148\,\mathrm{nT}$. This amplitude is significantly larger than the observed one. This is a hint that further physical processes occur in the system such as wave reflection and dissipation due to wave-particle interaction. Consequently, the Alfvén wave amplitude decreases during propagation. We forgo an exact calculation of the involved integrated power fluxes for the different turbulence models as these sensitively depend on the smallest frequency of concern because the energy input scales contain most power. This complicates a fair comparison for different frequency ranges. Furthermore, we restricted our analysis to frequencies larger than $f = 0.2\,\mathrm{Hz}$ to avoid effects from numerical issues.

We like to end our discussion with an evaluation of the energy cascade flux and thus of the heating efficiency for the weak and the KAW turbulence. The weak turbulent heating rate (*Ng and Bhattacharjee*, 1997; *Galtier et al.*, 2000; *Saur*, 2004) is given by

$$q_{turb}^{weak} = \frac{1}{\sqrt{\mu_0^3 \rho}} \frac{\delta B^4}{B_0} \frac{l_\parallel}{l_\perp^2} \tag{5.15}$$

in units of $\mathrm{W/m^3}$. Using $l_\parallel = \lambda_\parallel^{max} = 3.3\,R_J$ in case of $\bar{\alpha} = 0.9$, $l_\perp = \lambda_\perp^{max} = 3.6 R_{Io}$, $\rho = 4.3 \cdot 10^{-17}\,\mathrm{kg/m^3}$, $B_0 = 2000\,\mathrm{nT}$ and $\delta B = 400\,\mathrm{nT}$ as estimates for an equatorial turbulence source location, we find $q_{turb}^{weak} = 7.4 \cdot 10^{-9}\,\mathrm{W/m^3}$. From integration of this energy flux density over the flux tube volume up to the torus boundary, we can estimate the turbulence heating power to $4.2 \cdot 10^{13}$ W. Note, this is the cascade rate of the turbulence to smaller scales. It does not necessarily mean the energy is dissipated within the torus, but when in particular the small-scale fluctuations of this cascade are transmitted through the torus boundaries, the dissipation can occur at high latitudes. This value proves the efficiency of weak turbulence to transfer sufficient energy towards the particles and finally account for the observed emissions in infrared and UV. Their corresponding electron input energies are on the order of 10^9 - 10^{11} W (*Saur et al.*, 2013). A similar estimate can be provided for KAW turbulence using

$$q_{turb}^{KAW} = \frac{\delta B^3}{\sqrt{\mu_0^3 \rho}} \frac{\lambda_i}{l_\perp^2}, \tag{5.16}$$

which is an adapted version from *von Papen et al.* (2014) for the ion inertial length λ_i. Applying this formula to a turbulence source location at mid latitudes using $l_\perp = \lambda_i^{mid} = 332\,\text{km}$, $\rho = 10^{-20}\,\text{kg/m}^3$ and $\delta B^{mid} = 50\,\text{nT}$, we find $q_{turb}^{KAW} = 2.7 \cdot 10^{-9}\,\text{W/m}^3$. Integrating q_{turb}^{KAW} over the flux tube volume outside the torus boundary results in a dissipation rate of $7.2 \cdot 10^{12}\,\text{W}$. To conclude, weak MHD as well as sub-ion KAW turbulence are associated with significant energy cascades and thus dissipation rates, which is an indication that turbulence is indeed a realistic mechanism to transfer energy from large-scale magnetic field perturbations into the charged particles and finally account for the observation of the Io footprint and IFPT phenomena. In particular, estimation of instantaneous Poynting fluxes for the discussed weak MHD and kinetic turbulence cases gives values of $1.9\,\text{W/m}^2$ and $1.0\,\text{W/m}^2$, respectively. These underpin the heating potential compared to the observed JADE electron energy flux density of $580\,\text{mW/m}^2$ (*Szalay et al.*, 2020b).

We show that weak-MHD turbulence in the torus or KAW turbulence developed outside the Io torus are reasonable mechanisms for the observed spectrum. Strong-MHD turbulence is not a likely candidate to explain the power spectrum. We cannot clearly exclude models based on their associated power or MHD-breakdown scale. This is also caused by the MAG and Waves data gap between $f = [5\text{ - }50]\,\text{Hz}$. Hence, predictions regarding spectral breaks are difficult to assess. For example the Weak-λ_i^{eq} model with a frequency range of $f = [0.2\text{ - }28]\,\text{Hz}$ from Section 5.4.1 cannot be satisfyingly constrained by the data and introduces a uncertainty in the interpretation. Model fittings considering only the MAG data in the low-frequency range will give non-satisfying results regarding the investigated turbulence models with the steep slope of $\alpha = -2.96 \pm 0.22$ as mentioned in the beginning of this section. However, observations in Jupiter's and Saturn's equatorial region show that low-frequency turbulence is not fully stationary and might not be fully developed all the time, which results in a time-variable spectral slope at low frequencies (*von Papen et al.*, 2014; *Tao et al.*, 2015; *Saur*, 2021). Therefore the low frequency part of the spectrum of the Io flux tube at high latitudes might be variable as well. This needs to be investigated by analysis of further Io flux tube and tail crossings.

5.6. Concluding remarks

Our analysis is sensitive to assumed model parameters used in this study. Especially the density and the magnetic field strength have significant influence on the plasma length scales and hence on the mapping relations and involved frequencies for the turbulence models. However, even with the assumption of a dipolar magnetic field, higher-order moments from the dynamo field are found to significantly contribute only closer to Jupiter than the IFPT crossing (*Connerney et al.*, 2018).

Additionally, temporal variability of the parameters owing to Io's position within the torus and unknown dynamic processes introduces a further complexity to the system. For instance, temporal and spatial variability of the spectral index is observed in the equatorial region (*Chust et al.*, 2005) and complicates strong conclusions on the acting turbulence mechanism in the IFPT. The wave field at Io is anisotropic at largest scales as a consequence of different time scales of wave propagation and plasma convection. We account for this anisotropy behavior with the usage of anisotropy factors in the turbulence models. Physical interpretation of the high-latitude data as result of mixed states of turbulence (influencing the spectral index) or a non-fully developed state of the cascade (which restricts the frequency range of the turbulent waves) is not fully accessible with the given Juno data basis. We interpret at least the lower regime of the observed frequencies in the IFPT to originate from Alfvénic turbulence. We point out that further studies are needed to investigate the evolution of turbulent fluctuations in bound systems, such as the Jupiter system or the Io flux tube which is limited within the boundaries of Jupiter's magnetosphere and its ionospheres (see also discussion in *Saur* (2021)).

CHAPTER 6

Alfvénic turbulence in flux tubes connected to the main emissions

In this chapter, we will compactly investigate Alfvénic turbulence in the middle magnetosphere similar to Chapter 5. We discuss our expectations on the observable dynamics of the turbulent Alfvén wave field. We consider an equatorial turbulence region between $L = 20$ and $L = 30$ as representatives for the middle equatorial magnetosphere as likely to map to the main emissions (*Allegrini et al.*, 2020).

6.1. Characterization of the wave field

In the first step, we introduce the largest scales associated with the initial Alfvénic wave field in the middle magnetospheric plasma sheet region. As reference perpendicular wavelength we use $\lambda_{\perp,eq}^{max} = 1\,R_J$ according to *Saur et al.* (2018b). Mapped to the Jovian ionosphere using dipolar mapping, we obtain a width of 290 km at high latitudes for the L-shell of 25. We note that the simple dipolar mapping results in larger widths than true M-shell mapping. This is reasoned by the distended magnetic field lines in radial direction due to currents flowing in the plasma sheet modifying the dipole magnetic field. For increasing distances beyond L-shells of 20, this effect gradually sets in. This requires a more realistic magnetic field description towards larger distances (*Khurana et al.*, 2004). The width of the main auroral emissions extends up to 1000 km as mentioned in Section 2.2. This is an indication that a larger radial region than the $1\,R_J$ perpendicular wave scale in the equator is involved in the dynamics related to the main emissions. From *Saur* (2004) we know that significant turbulence activity spans a region of up to $10\,R_J$ in the middle magnetosphere, i.e., L-shells between 20 - 30. Hence, from a physical perspective, the main emissions have to be connected to this extended region of wave populated field lines. We will compare the dissipation for different L-shells in Chapter 8.3. For regions outside this range, a significant drop in turbulent activity has been observed. This drop is in conformity with the observation of a latitudinally confined band for the main emissions.

In lack of a simple characteristic time scale in the middle magnetosphere, we cannot clearly constrain the initial parallel extent of the large-scale Alfvénic wave field using the MHD dispersion relation as in the case of Io. A suitable candidate to be evoked in this context might be diffusion times associated with the interchange motions of flux tubes. For

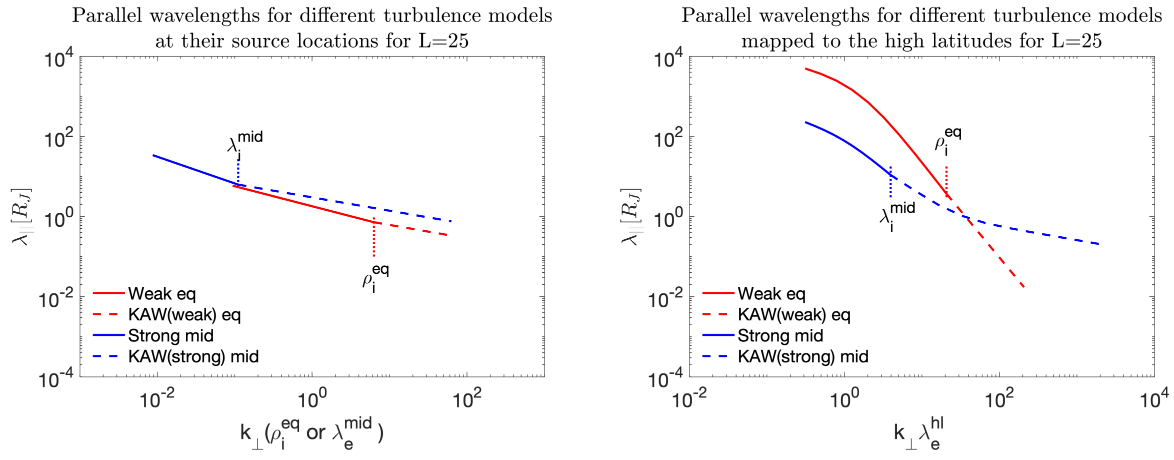

Figure 6.1.: *Parallel wavelengths plotted against perpendicular wave scale based on equatorial and mid-latitudinal turbulence for L=25. Left: Spectra are displayed at their source region with indicated MHD breakdown scales. The horizontal axis considers the perpendicular wavenumber normalized to the local ion gyroradius ρ_i^{eq} for the equatorial models (eq) and the electron inertial length λ_e^{mid} for the source location outside the torus (mid). Right: Mapped spectra to the location of the Juno measurements in the high latitudes.*

simplicity, as a guess for equatorial turbulence based on flux tube interchange motion, we consider the extent of the mass-loaded plasma sheet to be a potential parallel scale $\lambda_{\parallel,eq}^{max}$. Observations indicate a thickness of the plasma sheet of $\approx 4\,R_J$ in the middle magnetosphere. However, due to dawn-dusk asymmetries, its extent is larger in the dusk sector (*Khurana*, 1992; *Khurana et al.*, 2004). Considering weak Alfvénic turbulence in the equatorial region as proposed by *Saur et al.* (2002), the largest parallel scale can be calculated to $\lambda_{\parallel,eq}^{max} = [19.2, 5.9, 5.7]\,R_J$ for $L = 20$, 25 and 30, respectively. These values, using an anisotropy factors of $a_1 = 1$ (see Table 5.1), express a slightly weaker anisotropic large-scale behavior regarding the perpendicular scale than estimated in the Io flux tube. The value for L=20 is largest compared to the further out located positions due to the parameter combination of a weak magnetic fluctuation amplitude of $\delta B = 3\,\mathrm{nT}$ (*Saur et al.*, 2003) and factor of 2 - 3 stronger background field of $B_0 = 57\,\mathrm{nT}$. The given value also reduces, when considering $\delta B = 5\,\mathrm{nT}$ as *Saur et al.* (2018b) takes into account. The scale height of the *Bagenal and Delamere* (2011) density model from Chapter 4 has a value of $\sim 3.5\,R_J$ above the center of the plasmasheet in this region. Hence, the extent of the plasmasheet is consistent with the $L = 25$ and $L = 30$ parallel scales and we only constrain the maximal wavelength for $L = 20$ wave field towards $6\,R_J$ to be consistent with the other locations.

As a second potential generator region for the evolution of turbulence, we consider the mid-latitudes. Similar to the Io-case, we locate our reference position 'mid' in the middle between the plasma sheet and Jupiter's ionosphere. We adapt the flux tube extent outside the plasma sheet as largest parallel scale of the wave field such as employed in the calculations by *Saur et al.* (2003) and *Saur* (2004). The corresponding perpendicular scale, $\lambda_{\perp,mid}^{max} = 0.4\,R_J$, is mapped from the equator. In Figure 6.1, we display the spectral relation between perpendicular and parallel scales for the turbulent fluctuations. We take Weak-ρ_i^{eq} and Strong-λ_i^{mid} turbulence and their kinetic extensions into account. In the upcoming Section 6.2, we motivate our choice for these models by calculating time scales involved in the turbulent interactions. In the left panel, the scales are shown at their respective source regions. Whereas MHD turbulence makes up a major part of the investigated equatorial wave scales, kinetic turbulence covers larger part of the mid-latitude wavenumber spectrum. The implications for the observability of spectral indices in high latitude power spectra will be investigated in Chapter 8. In the right panel of Figure 6.1, scales are shown mapped to the high latitudes. Similar to the Io flux tube, large parallel wave scales are elongated during propagation in a rising Alfvén speed plasma environment towards the high latitudes. Dispersive effects on smaller scales counter this increase as the corresponding propagation speed is reduced. Thus, smaller parallel wave scales are not stretched similarly to large ones. For smallest parallel scales, we can even observe a compression, as inertial effects in the strong inertial Alfvén regime lead to reduced phase speeds compared to the source regions.

6.2. Turbulence in the middle magnetosphere

Weak MHD turbulence in the middle equatorial magnetosphere was proposed by *Saur et al.* (2002). Calculating the time scales relevant to turbulence, we come up with Alfvén travel timescales of $\tau_A = [650, 871, 1094]\,\mathrm{s}$ in the plasma sheet of thickness $4\,R_J$ at the three representative locations $L = [20, 25, 30]$. Details for the meaning of the variables in this section are provided in Chapter 5.2.3. For the non-linear time scales $\tau_{nl} = \frac{\lambda_\perp^{max}}{v_A^{eq}\frac{\delta B^{eq}}{B^{eq}}}$, we obtain $\tau_{nl} = [3177, 1251, 1567]\,\mathrm{s}$. The resulting timescale ratios are unexceptionally smaller than one with values of $\epsilon = \frac{\tau_A}{\tau_{nl}} = [0.2, 0.7, 0.7]$. For our estimates, we use $\lambda_\perp^{max} = 1\,R_J$ as reference scale and $\delta B = [3, 5, 3]\,\mathrm{nT}$ for the fluctuation amplitudes. Using the approximately factor two larger wave scale as *Saur et al.* (2002), the ratios even half and promote even more clearly weak turbulence. As concluded by *Saur et al.* (2002), weak turbulence conditions are best fulfilled in the inner equatorial region.

Analyzing the energy cascade flux similar to the Io flux tube in the previous chapter using equation (5.15), we come up with $q_{eq}^{weak} = [0.9, 15.9, 4.6] \cdot 10^{-15}\,\mathrm{W/m^3}$. We use the following parameters for the $L = 25$ estimate: $\lambda_\perp = 1\,R_J$ and $\lambda_\parallel = 5.9\,R_J$ from the previous section, $B_0^{eq} = 29\,nT$, $\delta B^{eq} = 5\,\mathrm{nT}$ (*Saur et al.*, 2002), and $\rho^{eq} = 6.1 \cdot 10^{-23}\,\mathrm{kg/m^3}$. As can be seen, weak turbulence is strongest at an L-shell of 25. Integrating a log-averaged flux of $4.0 \cdot 10^{-15}\,\mathrm{W/m^3}$ over an equatorial plasma sheet volume from L=20 - 30 with a height of $2\,R_J$ above the center, we obtain an estimate of the overall power of $4.6 \cdot 10^{12}\,\mathrm{W}$ available for auroral heating. If we define the edge of the plasma sheet to be located, where the density profile from *Bagenal and Delamere* (2011) has dropped to its $1/e$-value, i.e., at a height of $4\,R_J$, the volume and correspondingly the power estimate gets a factor of two larger. We can also increase the energy flux by considering a larger equatorial fluctuation amplitude of $\delta B^{eq} = 5\,\mathrm{nT}$ for L=20 as *Saur et al.* (2018b), which also doubles the log-average power estimate. To conclude, weak equatorial turbulence can provide sufficient power for the main emissions in accordance with the estimates from *Saur et al.* (2003) and *Saur* (2004), who used a larger parallel scale on the order of the field line length.

Now we turn to turbulence at mid-latitudes. In contrast to the Io flux tube, the Alfvén waves spend a significant amount of time outside the plasma sheet due to the longer field lines and relative weak background magnetic field. Travel times outside a $2\,R_J$ half-thick extended plasmasheet can be calculated to $\tau_A = [394, 584, 1023]\,\mathrm{s}$ using the *Bagenal and Delamere* (2011) density model for the Alfvén speed profile. Major reason for the increase in travel time towards larger L-shells lies in the reduced magnetic field strength and consequently in smaller Alfvén speeds v_A compared to inner-located regions. The eddy turnover times can be estimated to $\tau_{nl} = [242{,}115{,}168]\,\mathrm{s}$ using following numbers for the $L = 25$ estimate: $\lambda_{\perp,max}^{mid} = 0.4\,R_J$ mapped from equator, $\lambda_{\parallel,max}^{mid} = 31\,R_J$, $B_0^{mid} = 180\,\mathrm{nT}$

and $\delta B^{mid} = 1.2\,\mathrm{nT}$ from the geometric model in Chapter 4 due to a lack of observational constraints in this region. The resulting ratios of the time scales can be estimated to $\epsilon = \tau_A/\tau_{nl} = [1.63, 5.1, 6.1]$ for the three field lines. Especially the magnetic fluctuation amplitude δB and the extent of the plasma sheet have a sensitive influence on these values. Using an extended plasma sheet with half-thickness of $4\,R_J$ for L=25 leads to a nearly factor two reduced travel time of $\tau_A = 327\,\mathrm{s}$. In combination with a factor two larger magnetic field fluctuation weak turbulence conditions are enabled. So the nature of MHD turbulence might depend on local time, i.e., the longitudinal dependence of the plasma sheet thickness. Additionally, it might also undergo changes during stronger flux tube interchange activity, potentially triggered by the compression of the dayside magnetosphere during its rotation. From the given ratios, strong MHD-turbulence is favored for larger L-shells, similar to the trend of plasma sheet turbulence.

Assuming the ion inertial length λ_i^{mid} to be related to the MHD-breakdown of turbulence, we find that sub-ion kinetic Alfvén wave turbulence also provides a significant source of power with densities of $q_{mid}^{KAW} = [1.4, 11.6, 3.8] \cdot 10^{-14}\,\mathrm{W/m^3}$. Again, we used the same parameter set given in the previous paragraph for $\mathrm{L} = 25$ estimate and additionally $\lambda_i^{mid} = 2.27 \cdot 10^3\,\mathrm{km}$. Integrating the lowest power density value over the flux tube volume from above the $4\,R_J$ plasma sheet edge to the ionosphere between $\mathrm{L} = 20$ - 30 (which is twice the equatorial volume due to its parallel extent), we obtain an energy flow of $6 \cdot 10^{13}\,\mathrm{W}$ associated with KAW-turbulence. Thus, KAW-λ_i^{mid} turbulence is also interesting to investigate in more detail as it can provide a factor of 10 larger power than weak equatorial turbulence. For a MHD breakdown at ion gyroradius scales ρ_i^{mid}, the corresponding KAW power densities are two orders of magnitude smaller and will be not dealt in the following considerations.

6.3. Doppler shifting analysis

Now we apply the Doppler shift analysis from Chapter 5 to the parameter space in the middle magnetosphere associated with the main auroral emissions. The reference for the analysis are the corresponding Juno observations during the Perijove 1 (PJ1) main auroral region crossing at a height of $0.8\,R_J$ presented by *Gershman et al.* (2019). They investigated MAG data in a slightly narrower low-frequency range of [0.1 - 3] Hz compared to the study of *Sulaiman et al.* (2020). Similarly, *Gershman et al.* (2019) identified a power-law shaped magnetic power spectrum with a slightly steeper spectral index of $\alpha = -2.29 \pm 0.09$ than observed in the Io flux tube.

Using the constraints for the large-scale wave field introduced in the previous section 6.1, we model the convected and temporal contributions to the observable spacecraft frequency. For the perpendicular wavenumbers, the corresponding spectral range of $k_\perp^{eq} = [\frac{2\pi}{R_J} \text{ - } 10\frac{2\pi}{\rho_i^{eq}}]$ is taken into account. This range includes the MHD breakdown scales ρ_i and λ_i at both source regions. Together with the introduced parallel scales, these spectra are mapped towards Juno's location at high latitudes, which crossed the region with a speed of $v_B^{sc} = 50\,\mathrm{km/s}$. Wave frequencies are evaluated using the *Lysak* (2008) solution from equation (3.48).

The comparisons of the resulting frequency contributions in case of weak equatorial turbulence are shown in Figure 6.2 for both breakdown scales, i.e., ρ_i^{eq} and λ_i^{eq}. The interpretation is similar to weak turbulence in the Io flux tube. Juno observed the constructed turbulent wave field as being quasi-stationary convected. Although *Gershman et al.* (2019) use $f = 0.1\,\mathrm{Hz}$ as lower limit for their analysis of parallel wavelengths, the data power spectrum in their Figure 2 seems to give consistent signals for even lower frequencies. Thus,

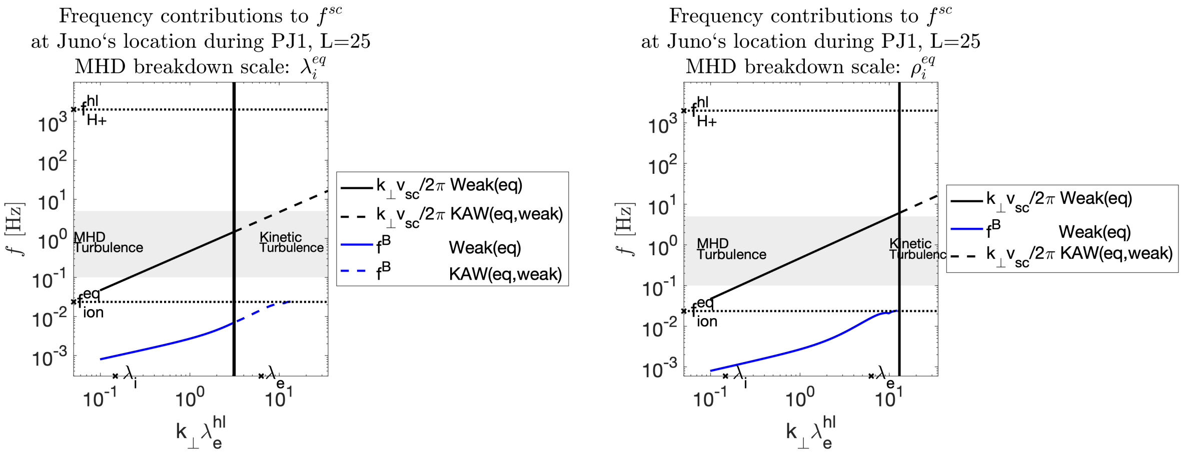

Figure 6.2.: *Comparison of convected(solid and black dashed lines) and wave frequency (blue lines) at Juno's location due to equatorial weak-MHD and KAW turbulence. Results are shown for the λ_i^{eq} (left) and ρ_i^{eq} (right) MHD breakdown scale at L=25, respectively.*

we conclude our mapped largest perpendicular scale to be reasonably consistent with the measurements. An increase of our $f^{min} = 0.05\,$Hz can be be generated using a smaller perpendicular scale. The generation of large wave scales is determined by the concrete interaction of flux tubes during the interchange motion process and potentially underlies temporal evolution. In this contest, larger scales are possible as well, e.g., $\lambda_\perp = 1.7\,R_J$ from *Saur et al.* (2002). However, given the data basis from *Gershman et al.* (2019), we cannot access this aspect further. The situation is similar for field lines $L = 20$ and $L = 30$, which together span a smallest detectable frequency range of f^{min}= [0.03 - 0.08] Hz due to a convected wave structure past Juno. The corresponding plots are shown in Appendix C. The convective frequency increases for further away located L-shells as a consequence of the weakened magnetic field strength in the plasma sheet, which affects the mapping of perpendicular scales. Besides, we can identify that the wave frequency goes into equatorial cyclotron resonance at scales corresponding to electron inertial length in the given high latitude representation. Thus, we do not expect KAW-ρ_i^{eq} turbulence to be present at high latitudes. Moreover, gyroradius breakdown scales are associated with observable frequencies between 5 - 9 Hz for the L=20 - 30 and hence will be not observable in the frequency range investigated by *Gershman et al.* (2019) anyway. For the λ_i^{eq}-MHD breakdown, the transition towards KAW-turbulence occurs at frequencies around 1.5 Hz for all equatorial locations. This limits shifts towards lower frequencies of $f = [0.4, 0.6, 0.9]$ Hz considering turbulence generated outside the torus for $L = [20, 25, 30]$.

The results for $L = 20$ and $L = 25$ based on strong-λ_i^{mid} and KAW turbulence are presented in Figure 6.3. The figure for $L = 30$ is provided in Appendix C and shows qualitatively the same situation as for $L = 25$. Whereas for these both locations the Doppler-shifted frequency contributions dominate the observable spacecraft frequencies, the situation is more unclear for L=20. Here, as can be seen in the left panel of Figure 6.3, temporal wave dynamics is on the order of the convective contribution for MHD scales. Consequently, Juno would not observe a pure $k_\perp$ power spectrum as in the other investigated cases, which corresponds to a spectral index of $\alpha = -5/3$ for strong MHD turbulence. For the temporally related $k_\parallel$ spectrum in case of strong MHD turbulence, the spectral index of the power spectral density exhibits a $\alpha = -2$ dependency (*Goldreich and Sridhar*, 1995; *Horbury et al.*, 2008). Thus, we expect a mixing of both dynamics and an intermediate spectral index to be observed by Juno in this situation. For perpendicular wave scales

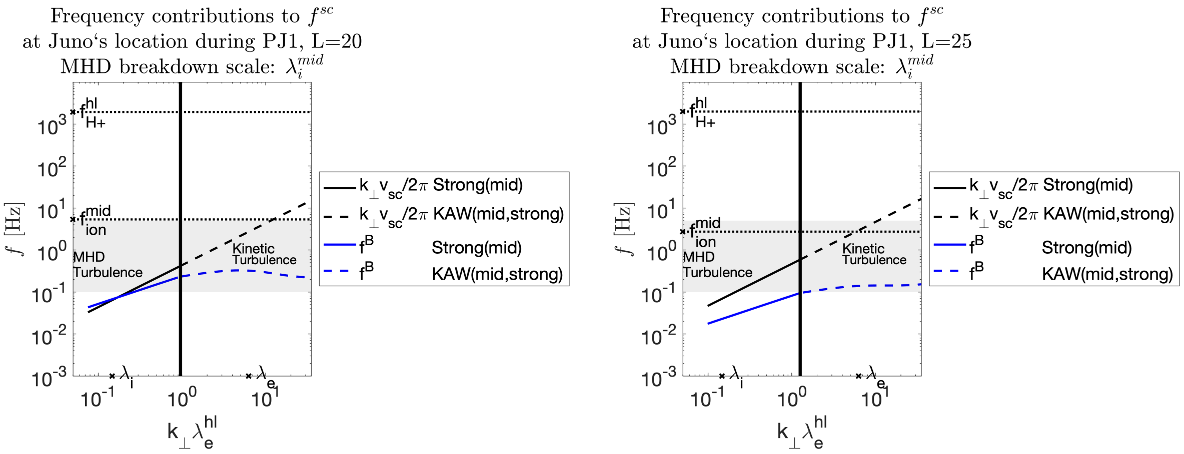
Frequency contributions to f^{sc} at Juno's location during PJ1, L=20 MHD breakdown scale: λ_i^{mid}

Frequency contributions to f^{sc} at Juno's location during PJ1, L=25 MHD breakdown scale: λ_i^{mid}

__Figure 6.3.:__ Comparison of convected and wave frequency at Juno's location due to strong-MHD and KAW turbulence at mid latitudes with λ_i^{mid} as MHD breakdown scale for L=20 (left) and L=25 (right).

smaller than λ_i^{mid}, the spectral index again develops a pure $k_\perp$ nature with a spectral index of $\alpha^{KAW} = -7/3$ as the wave frequency decreases due to inertial dispersive effects. The root cause for the change in temporal dominance of the signal with L-shell lies in the different Alfvén speeds. The considered turbulence generator locations for $L = 25$ and $L = 30$ are located in the Alfvénic transition region. For $L = 20$, the generator location already lies in the cold regime where the interplay of magnetic field strength and density leads to a factor of 2 - 3 larger Alfvén speed, which affects the estimate of the wave frequency. Thus, $L \sim 20$ delineates the transition for which the perpendicular spatial structure of the turbulent wave field will be visible for low frequencies for locations further away.

Our analysis suggests that weak equatorial turbulence and mid-latitude KAW turbulence are potential candidates to account for the power spectral observations of *Gershman et al.* (2019). Whereas weak turbulence has a slightly less steep spectral index, KAW turbulence fits well in the observed range of $\alpha = -2.29 \pm 0.09$. However, in contrast to the Io flux tube analysis, KAW turbulence covers a less extended frequency range. Thus, strong-MHD turbulence should be observable at large scales which is associated with a reduced perpendicular spectral index of $-5/3$. In the case that the temporal dynamics of the wave field is observed, such as partly indicated from modelings for $L = 20$, the spectral index would evolve from -2 to $-7/3$ at the breakdown scale, which we cannot resolve with the given observations. In the following sections, we quantify the dissipative properties of kinetic Alfvén waves along field lines based on turbulence at both generator locations.

CHAPTER 7

Alfvénic spectral character along auroral field lines

In this chapter, we give an overview of the local spectral behavior of Alfvénic turbulence along auroral field lines. We concentrate on the L-shell of 25 as representative for the field lines. Based on the findings from the previous chapter, we investigate equatorial weak MHD turbulence and mid-latitudinal strong MHD turbulence generator locations. On sub-ion kinetic scales, we extend these models by KAW turbulence, which affects the wave field in terms of wavelength and magnetic field fluctuation amplitude. We illustrate the wave's local dispersive and dissipative properties and related electric fields along the field lines to show consistency with the theoretical expectations on wave dynamics for the parameter space encountered in the magnetosphere. For the analysis, we concentrate on two kind of species. One with thermal electron and ion temperatures according to the plasma sheet observations in the middle magnetosphere (see Chapter 4). For the other case, we consider hotter temperatures of T_e=T_i= 2.5 keV along auroral field lines to illustrate the effect of temperature on the wave characteristics. Such temperatures are used in modelings for example by *Cowley and Bunce* (2001) and *Saur et al.* (2018b) at the high latitudes.

7.1. Equatorial turbulence

To study the required turbulent spectral regime, we choose a perpendicular spectral wavenumber range of $k_\perp^{eq} = [\frac{2\pi}{R_J}\,\text{-}\,10\frac{2\pi}{\rho_i^{eq}}]$ in the plasma sheet similar to the previous chapter. This range is mapped together with the parallel wavenumbers along the field line. With the help of the hot plasma dispersion relation (equation (3.19)) and the one from *Lysak* (2008) (equation (3.48)), we can locally evaluate the spectral properties of the kinetic Alfvén wave at various locations along the field line. To visualize the wave's spectral behavior, we plot the dispersion, dissipation and electric field at these locations. These already give first indications what to expect for particle acceleration. For the plasma parameters, we use the field line models presented and developed in Chapter 4.

In Figure 7.1, we show the color coded spectral dispersion of the Alfvén wave, which corresponds to the parallel phase velocity normalized to its MHD value, i.e., $\frac{\omega_r}{k_\parallel v_{A,rel}}$. Grey colors indicate no dispersion, whereas blue and red values show an increase or decrease of the phase speed with respect to the MHD Alfvén speed. The vertical axis, i.e., $k_\perp \lambda_e$, is a measure for the perpendicular wave scale, where small values resemble the conventional

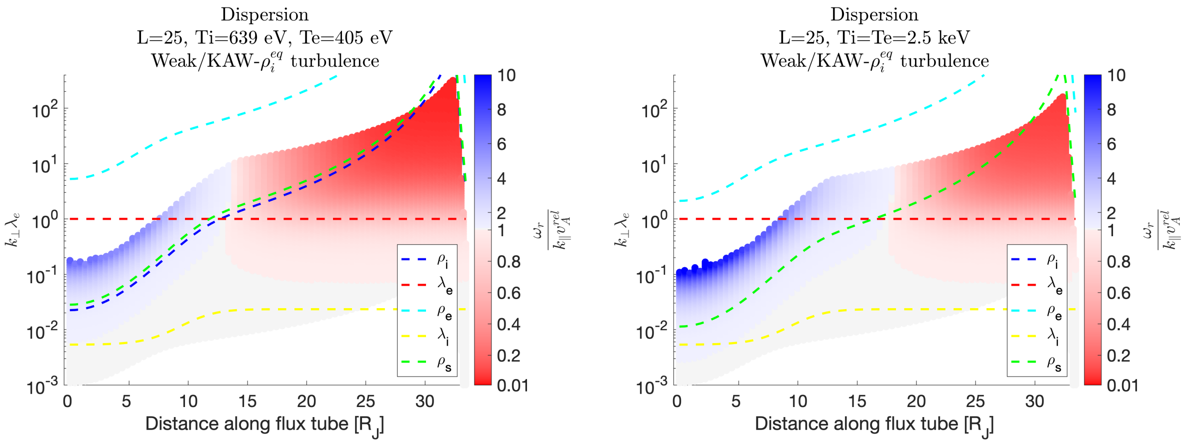

Figure 7.1.: *Weak and kinetic equatorial turbulence spectral plot of dispersion for a thermal species (left) and a hot species (right) along the L=25 field line in the middle magnetosphere. Small distances along the field line corresponds to the equatorial plasma sheet region, whereas large distances correspond to the high latitude region of Jupiter. The dashed lines represent the local plasma scales at their $1/(2\pi)$-value to illustrate the connection between the onset of dispersion and plasma scales. We consider the ion gyro- and acoustic radii (ρ_i, ρ_s), the ion and electron inertial length (λ_i,λ_e) and the electron gyroradius ρ_e.*

MHD behavior and larger values account for the kinetic regime. The corresponding scales are shown as dashed lines along the field line and represent their $(2\pi)^{-1}$ value, i.e., where the product of the plasma length scale and $k_\perp$ scales to one. The plotted plasma scales along the field line refer to the local ion gyro- and acoustic radius ρ_i and ρ_s (blue and green lines), the electron gyroradius ρ_e (cyan) and the ion and electron inertial lengths λ_i(yellow) and λ_e (red). We can clearly distinguish three regions. On large perpendicular scales, the wave shows no dispersion as expected from theory (see Chapter 3). However, close to the equatorial region (for small distances along the field line), the phase velocity grows for smaller scales beginning at ion gyro- and acoustic radius for both, the hot and the reduced *Lysak* (2008) solution consistently. Thus, this behavior is qualitatively in agreement with the solutions from equations (3.41) and (3.42) in the warm Alfvén regime, i.e., $\beta\frac{m_i}{m_e} > 1$. Dispersion is strongest when the Alfvén wave goes in resonance at the ion cyclotron frequency in the plasma sheet, which happens for scales slightly smaller than $k_\perp\rho_i \simeq 2\pi$. Consequently, we do not expect KAW-ρ_i^{eq} turbulence to play a major role in auroral acceleration as these waves will be damped significantly early on during propagation in the plasma sheet. We explicitly investigate this in Chapter 8. In the high-latitude regime close to Jupiter (large distance along field line), dispersion leads to a reduction in propagation speed for perpendicular wave scales smaller than the electron inertial length. Thus, this region corresponds to the cold electron Alfvén regime in accordance with the expectation from Section 4.2. These both regimes are separated by a narrow transition region, where $\rho^2 = \rho_i^2 + \rho_s^2 \simeq \lambda_e^2$. There, kinetic and inertial dispersive effects balance each other at large and small scales. It is important to note that the ion plasma-β needs to be included in expression (3.40) for a correct determination of the transition region in case of the middle magnetosphere, especially for unequal ion and electron temperatures. For the thermal populations, using the plasma parameter models from Chapter 4, the crossing distance lies at $\sim 13R_J$ along the L=25 field line with a total extent of 33 R_J. Hence, the cold region is more extended than the warm regime. For a hot ion and electron species with temperatures of T_i=T_e= 2.5 keV, the transition region moves towards 18 R_J along the

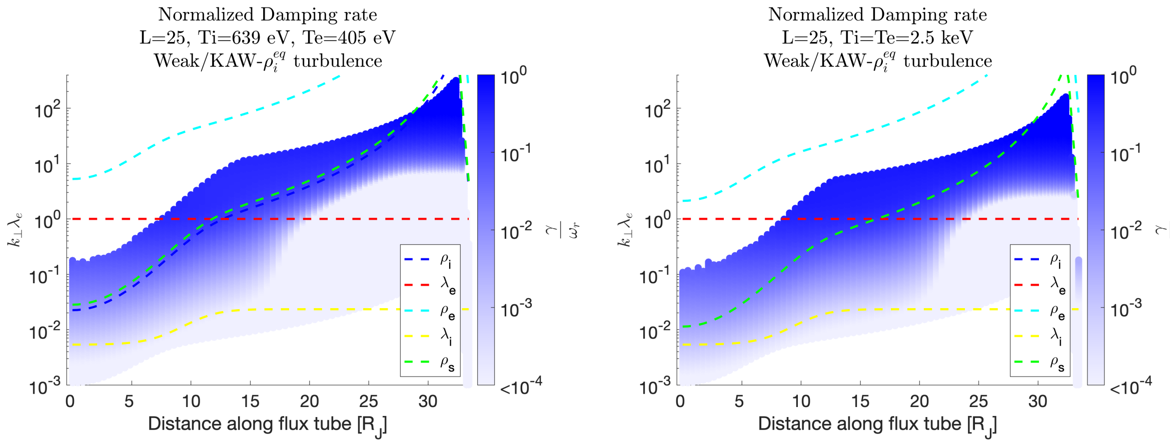

Figure 7.2.: *Weak and kinetic equatorial turbulence spectral plot of dissipation for a thermal species (left) and a hot species (right) along the L=25 field line in the middle magnetosphere.*

field line as ρ^2 gets larger. The corresponding modeling result is shown in Figure 7.1(right). From these studies, we can conclude that the relative size of the different plasma scales control the dispersion of the kinetic Alfvén waves as expected from theory and has been already investigated by *Saur et al.* (2018b) for chosen locations in the equator and in the high latitudes. As visible for the investigated parameter regime, the electron gyroradius and the ion inertial length do not play a role for the dispersive properties of the Alfvén wave.

The normalized damping rate of the kinetic Alfvén wave as a measure of particle energization is presented in Figure 7.2 for both species. In the warm regime, we can identify that the set-in of significant damping is controlled by the ion acoustic radius and/or ion gyroradius, consistent with the derived expression (3.52) from Chapter 3. As we will show in Section 7.3, the electron temperature, and thus, the electron thermal speed take a major role in the dissipation characteristics along auroral field lines for the investigated parameter set. As a result, the reduced *Lysak* (2008) damping rate is a good approximation to the hot one and can be used to assess electron Landau damping. At the smallest perpendicular scales in the plasma sheet (the warm electron regime), the damping rate is strongest and can be attributed to ion cyclotron resonance as the wave frequency approaches ion cyclotron frequency. For our research interest of waves propagating towards Jupiter, this regime is not in our particular interest and will be not further considered as these waves get fully dissipated within very short times. But still, this effect is interesting for perpendicular heating in the plasma sheet as proposed by *Saur et al.* (2018b). We are interested in waves, which undergo intense wave-particle interaction in regions closer to Jupiter so that sufficient amounts of wave energy can be transferred to auroral particles.

In the cold region, damping is controlled by the electron inertial length scale. For the hot species (T_i=T_e=2.5 keV), the set-in of damping is shifted towards larger perpendicular scales. This effect is also clearly observable considering only hot electrons (see Figure D.2 in Appendix D). Such an electron temperature dependency, which is not covered by the derived cold analytic expression (3.54), was also observed by *Saur et al.* (2018b) and will be also investigated at chosen locations in the next section.

A further interesting peculiarity of the damping rate is the existence of damping in the transition regime even in the proposed "absence" of a parallel electric field as stated by *Su* (2009). However, only the real part of the wave electric field vanishes in accordance

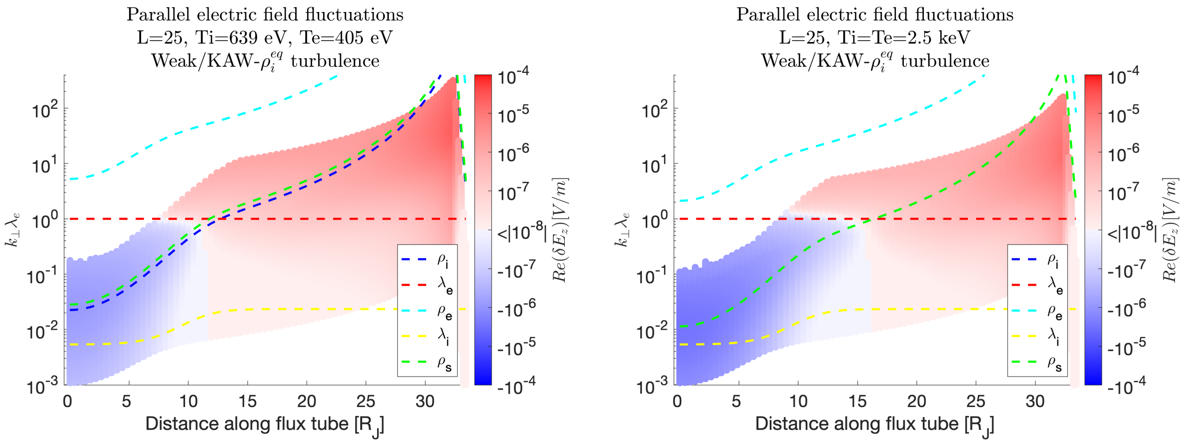

Figure 7.3.: *Weak and kinetic equatorial turbulence spectral plot of the parallel electric field (real part) for a thermal species (left) and a hot species (right) along the L=25 field line in the middle magnetosphere.*

with expression (3.64) at least for scales larger than the electron inertial length (see discussion in next passage). Corresponding contour plots of the imaginary part of the parallel electric are provided in Figure D.3 of Appendix D. To conclude, wave dispersion is not a necessary condition for the occurrence of Landau damping. Balancing of electron pressure and electron inertial effects seems to support parallel electric fields and can still enable wave damping in the transition region. From the comparison of the damping rates from both species in Figure 7.2, we can also see that increasing electron temperatures lead to an extension of the region at which damping sets in at large scales. Its effect on the resulting heating potential of particles in the high latitudes will be discussed in Chapter 8.

For the calculation of the implemented electric field expressions from Chapter 3.5.5, we considered the turbulent spectral wave magnetic amplitudes

$$\delta\hat{B}(s,k_\perp) = \delta B(s,k_\perp^{min}) \left(\frac{k_\perp}{k_\perp^{min}}\right)^{\alpha/2}, \tag{7.1}$$

from Appendix B. The spectral index is denoted by $\alpha < 0$ and $k_\perp^{min}$ is smallest perpendicular wavenumber at the respective field line position s. For the large scale fluctuations $\delta B(s,k_\perp^{min})$, we used our developed field line model from Chapter 4. We justify our approach in Appendix B. We like to note that our representation of the fluctuation amplitudes allows us to interpret the Fourier components as observable quantities in units of nT. Coming back to the electric field, for small perpendicular scales the reduced magnetic fluctuation amplitude also reduces the related electric field amplitude. The remaining part of the parallel electric field component, i.e., the parallel polarization relation $\delta E_z/\delta B_y$, can compensate this decrease for weak turbulence (due to the linear δB-dependence) as the corresponding polarization relation has a $k_\perp$-dependence at larger scales (see equations (3.60) and (3.64)). However, the perpendicular polarization relation $\delta E_x/\delta B_y$ has a weaker $k_\perp$-dependency on large scales. As a result, δE_x gradually decreases with smaller wave scale as shown in Figure 7.4 for both species. In these plots, we explicitly did not take damping of the wave amplitude along the field line into account. Damping will be considered in the upcoming Chapter 8, where we explicitly quantify heating along auroral field lines. The conclusions, we draw in this chapter, are independent of the consideration of fluctuation amplitude besides of quantification of electric field along the field line.

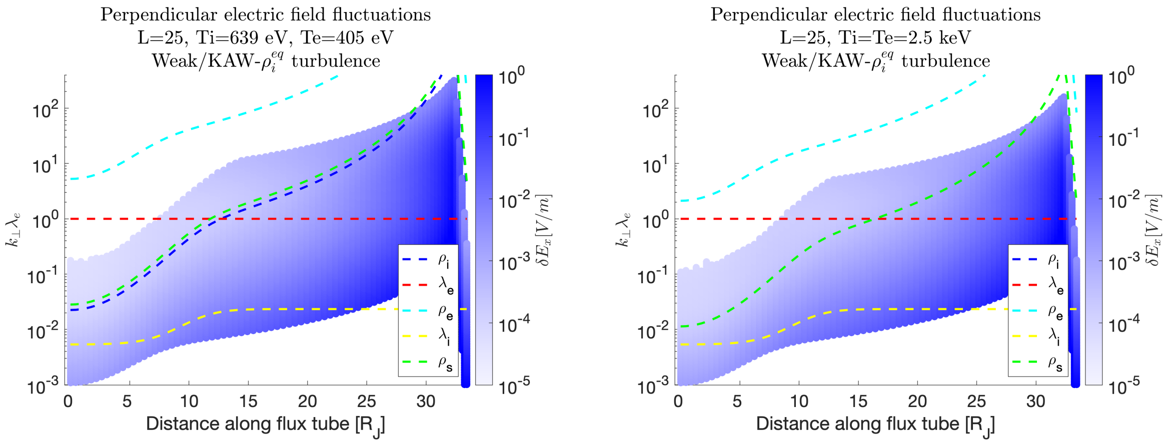

Figure 7.4.: *Weak and kinetic equatorial turbulence spectral plot of the perpendicular electric field (real part) for a thermal species (left) and a hot species (right) along the L=25 field line in the middle magnetosphere.*

The real part of the parallel wave electric field in Figure 7.3 illustrates the analytic expectations for the various Alfvén regimes. Namely, the warm and the cold regime show reversed polarities as discussed in Section 3.5.5. For the investigated populations with $T_e \sim T_i$, the sign reversal occurs at similar locations as for wave dispersion discussed above. Interestingly, the location of sign reversal shifts in the respective transition region for stronger imbalance of temperatures. Instead, it seems to be defined by the balance of ion acoustic radius ρ_s and electron inertial length λ_e. Thus, low electron temperatures shift the transition towards the plasma sheet and large temperatures in the other direction. The transition regions for electric field and wave dispersion fully coincide only for an electron species with a temperature significantly larger than for the ions. For our species under consideration with $T_e \sim T_i$, this effect of minor importance and does not require further inspection. It might be interesting for the potential generator location outside the plasma sheet, as in the cold regime damping already occurs at smaller perpendicular scales. Supplementary modelings with separately large ion and electron temperatures are exemplary shown in Figure D.4 of Appendix D in order to support our statements.

A peculiarity in the real part of the parallel electric field (hot and Lysak based solution), which is not present in the analytic solution, is a further sign reversal at perpendicular scales around $k_\perp \lambda_e \approx 1$ in the warm Alfvén regime for the species shown in Figure 7.3. Together with the same modeling studies from the above mentioned Appendix D, we propose its occurrence to have an explicit temperature ratio dependency according to $k_\perp \lambda_e \sim \sqrt{\frac{T_e}{T_i}}$. Only for significantly larger ion temperatures $T_i > 10^2 T_e$, the real part of the parallel electric field in the warm regime would have the same polarity as in the inertial Alfvén regime in a spectral range potentially interesting for our case. Thus, in the context of auroral heating this effect is of minor importance as it occurs on too small scales given the parameter space. The imaginary part of the parallel electric field does not exhibit any sign reversals and its amplitude plays a minor role compared to the real part. The only exceptions of a major role are given in the transition regime (where the real component has a sign reversal) and in the inertial regime close to Jupiter.

From the inspection of amplitudes, we can spot that the real part of the parallel electric field is largest in the highest latitudes with maximal values around 10^{-4} V/m. A similar conclusion holds for the imaginary part. Hence, we can expect strongest damping in this

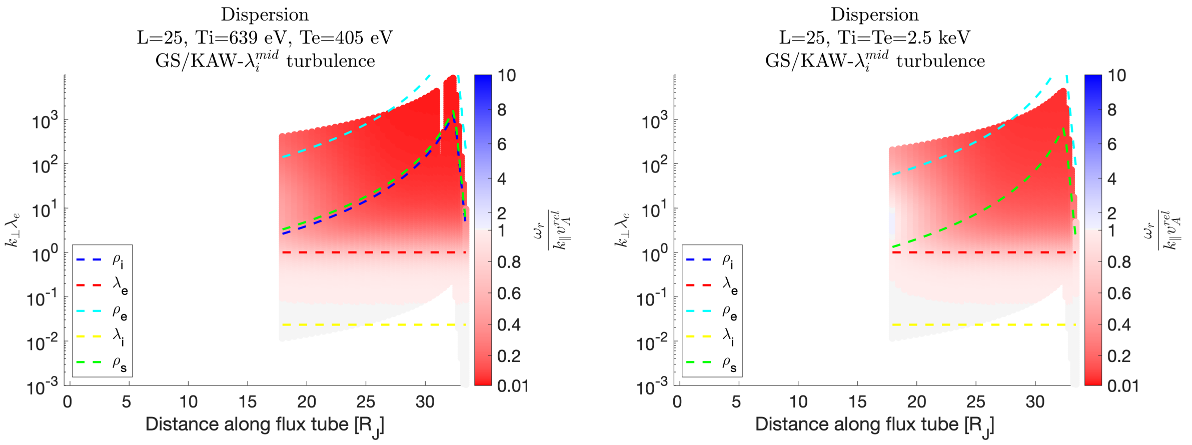

Figure 7.5.: *Spectral dispersion along the L=25 field line for a thermal (left) and hot (right) species based strong MHD and kinetic turbulence. The generator location is in the middle between the plasma sheet and Jupiter's ionosphere.*

region, which coincides with the observations from the damping rate analysis from above. This increase in the electric field is also a consequence of the dependency of the parallel electric field on Alfvén speed, which increases towards Jupiter (see analytic expressions (3.60) and (3.64)). As already said, this amplitude does consider the residual magnetic fluctuation amplitude considering damping.

7.2. Turbulence generator outside the plasma sheet

For the mid-latitudinal generator region for turbulence in between the plasma sheet and the Jovian ionosphere, we only show the evolution of upward propagating waves towards Jupiter. Of course, reflecting and non-linearly interacting waves are allowed to propagate in both directions along the magnetic field. These will propagate forth and back and establish an equilibrium state, which we represent by this generator location. In Figures 7.5 and 7.6, we display local spectral dispersion and damping characteristics for both temperature sets. We can identify that the general Alfvén characteristics are similar to the equatorial turbulence case. Here, the generator location is at the edge of the transition region towards the inertial Alfvén regime depending on temperature. For the hot species, we can see that damping sets in at a larger wave scale due to the shifted transition regime compared to the thermal one. Thus, we expect slightly stronger damping on Alfvén waves for the hot species. In contrast to equatorial turbulence, waves do not need to cross the warm regime during propagation to the high latitudes. As a result, waves are not significantly damped away until they reach the ionosphere and can account for auroral particle acceleration even on the smallest scales. This makes this generator location particularly interesting to investigate in the context of wave-particle interaction. We like to note that strong MHD turbulence is associated with a smaller spectral index, which results in more energy on smaller waves scales compared to weak MHD turbulence. On large scales, weak turbulence is associated with larger fluctuation amplitudes. We will show in Chapter 8.2 that the difference between both is of minor significance for the investigated spectral range. Instead, we expect the difference in parallel scales for equatorial and mid-latitude turbulence to play a role in auroral heating (see Figure 6.1). We quantitatively discuss the implications from both turbulence locations in Chapter 8.2.

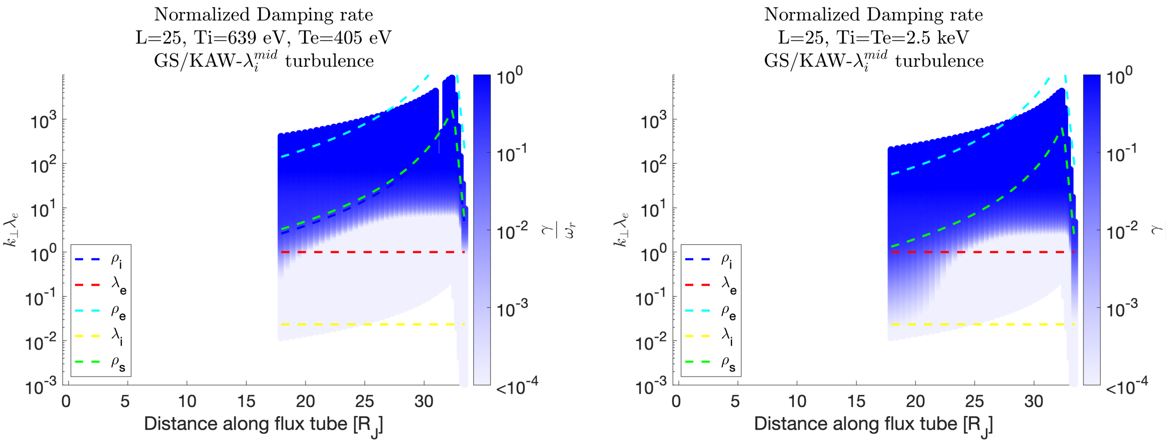

__Figure 7.6.:__ Normalized spectral damping rate along the L=25 field line for a thermal (left) and hot (right) species based Strong MHD and kinetic turbulence. The generator location is in the middle between the plasma sheet and Jupiter's ionosphere.

7.3. Damping at specific positions

In this section, we discuss the spectral dissipation properties of kinetic Alfvén waves presented in the preceding section. We focus on three representative locations along the field line: in the plasma sheet, in the transition region and in the high latitudes. Furthermore, we investigate the contributions to the hot damping rate from Landau and cyclotron damping for chosen cases. For the latter task, we apply formula (3.78) from Chapter 3.5.7. This expression allows us to extract the dissipative contributions to the hot damping rate due to resonant wave-particle interaction. Thanks to the dielectric tensor's additive nature, we are in particular able to separate contributions from ions and electrons. So powerful in theoretical consideration, in practical use, this approach sensitively depends on stable solutions for wave frequency and hot damping rate as these determine the real and imaginary parts of the parallel and perpendicular electric field components. These in turn additionally depend on the real and imaginary parts of the tensor elements like the expression (3.78) itself depends on the anti-hermetian contributions of the tensor. As a consequence, we only present chosen cases, where the evaluation gives meaningful and stable results.

In Figure 7.7, we display the normalized damping rates in the plasma sheet for various electron temperatures with fixed ion temperatures of 639 eV (left plot) and 2.5 keV (right plot) from the previous section. The solutions due to the hot plasma dispersion relation are shown as solid lines. The ones from the reduced *Lysak* (2008) dispersion relation for the kinetic Alfvén wave are denoted by dashed lines using the same colors as for the hot solutions. We can validate that both solutions coincide for most cases, which strongly indicates that electron Landau damping is a major contributor to the total hot damping rate in this parameter regime. From the observable strong electron temperature but weak ion temperature dependency, we can conclude that the ion acoustic radius ρ_s is the most important scale for the strength of electron Landau damping. This is supported by the derived analytic approximation from equation (3.52), which illustrates this $k_\perp^2 \rho_s^2$ dependency in the limit of hot electrons. A comparison of the derived analytic approximation with the numerical hot and *Lysak* (2008) solutions is shown in the appended Figure D.8. This also validates the consistency of the analytic expression.

A closer analysis of the hot $T_i = 2.5\,keV$ case reveals that the hot damping rate is larger than the Lysak electron Landau damping rate in the equator. This can be easily explained

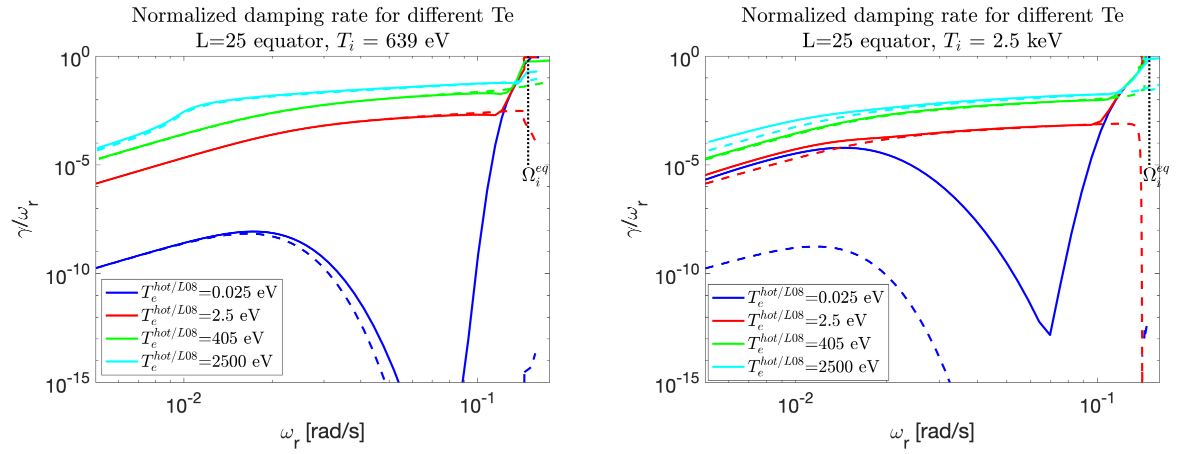

Figure 7.7.: *Parameter study for the normalized damping rate in the plasma sheet for ion temperatures of T_i= 639 eV(left) and T_i= 2.5 keV(right). Damping rate is plotted against wave frequency to illustrate the effect of cyclotron damping.*

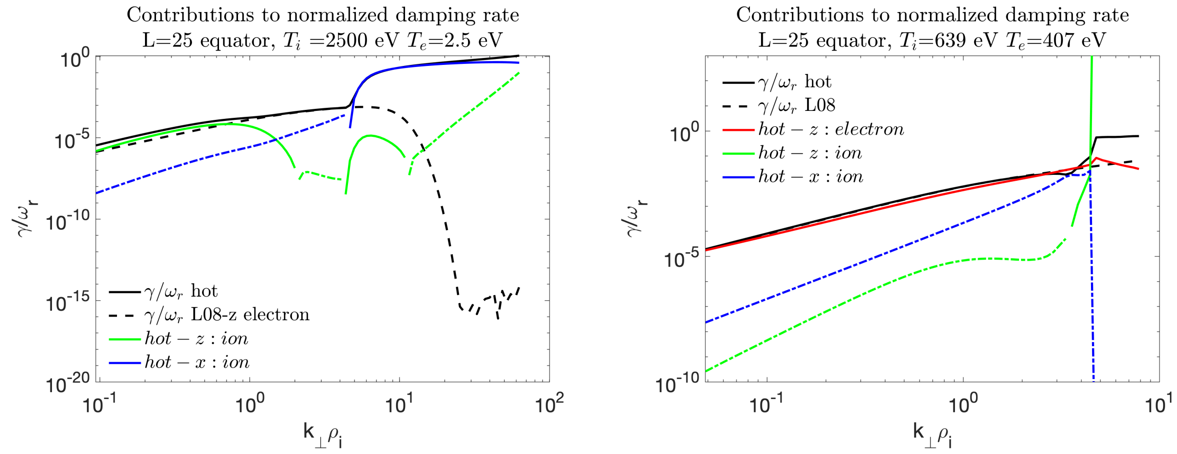

Figure 7.8.: *Decomposition of the hot normalized damping rate into its contributions from different wave-particle interaction mechanisms for two chosen temperature sets.*

by considering that the ion plasma beta reaches $\beta_i \simeq 1$ in the plasma sheet for this temperature. The effect is evident comparing the damping rates for T_e= 0.025 eV for both ion temperatures in Figure 7.7. Here, electron Landau damping is negligibly small, whereas the ion Landau damping rate significantly rises for the increased ion temperature. For L-shells larger than 30 in the equator, we expect ion Landau damping to gain importance as the ion plasma beta increases successively (*Khurana et al.*, 2004). Thus, the reduced Lysak model gets increasingly inaccurate for modeling of the total damping rate for this region.

Reaching ion cyclotron frequency, the hot damping rate undergoes a significant increase for all temperatures in Figure 7.7 consistently. We attribute this effect to ion cyclotron damping, which we address in the next paragraph. If we plot the damping rates against a spatial scale instead, the sudden increases seem not to be physically driven but a numerical issue. Hence, we decided to plot the damping rates against wave frequency in Figure 7.7 to illustrate that the apparent immediate increase in the hot damping rate towards cyclotron frequency is indeed a consistent physical feature related to wave frequency. For the cases considered, we can conclude that ion cyclotron damping is a highly efficient wave-particle interaction mechanism, which results in strong perpendicular ion heating within a single wave period.

We can validate the hypothesis of significant ion Landau damping acting at large ion temperatures by investigating the species contributions to the hot damping rate using the expression (3.78). In Figure 7.8, we show the damping contributions from ions and electrons in parallel and perpendicular direction. For the low electron temperature case (left panel), we can identify that the damping due to ions in parallel direction, i.e., ion Landau damping, gives significant contributions exceeding the electron Landau damping contribution. The latter one is represented by the black-dashed lined Lysak solution because the separation approach from the hot contribution failed for the parallel component. For perpendicular wave scales smaller than the ion gyroradius, the ion Landau damping rate is not a major contributor to the total damping rate anymore. From then on, we cannot trust the ion damping rate due to the several sign reversals undergone (indicated by the same colored but dashed-dotted lines). Contributions with inverted sign would counteract the damping rate and would represent a wave instability and hence growing wave amplitudes. From a physical perspective, we do not expect such a behavior for a Maxwellian distributed species in parallel direction. Instead, we propose a spectral evolution of ion Landau damping equivalent to electron Landau damping because both wave-particle interaction mechanisms are based on the same resonant principle. The electron Landau damping rate consistently continues the hot damping rate for these scales and dominates the overall damping rate at smaller scales. Thus, ion Landau damping is not expected to contribute to damping any further. As mentioned in the last paragraph, ion cyclotron damping is expected to act on the wave reaching ion cyclotron frequency. This is consistent with the significant onset of perpendicular ion heating (blue solid line) dominating the hot damping rate at the largest wavenumbers. Considering the thermal species in the right plot of Figure 7.8, electron Landau damping dominates the spectral behavior of the damping rate. Unfortunately, the ion contributions cannot be well retrieved. In particular for the largest wavenumbers in the equator, the perpendicular electric field gets unstable reaching ion cyclotron frequency and hence, obtaining a reliable perpendicular ion cyclotron damping rate fails.

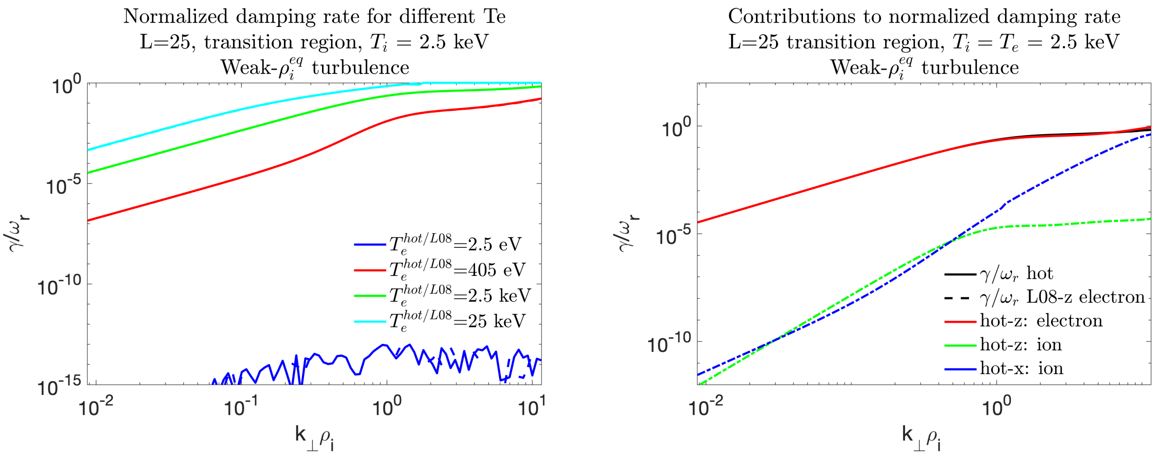
Normalized damping rate for different Te
L=25, transition region, T_i = 2.5 keV
Weak-ρ_i^{eq} turbulence

Contributions to normalized damping rate
L=25 transition region, $T_i = T_e$ = 2.5 keV
Weak-ρ_i^{eq} turbulence

Figure 7.9.: *Left: Study of the dependence of the normalized damping on electron temperature in the Alfvénic transition region. Right: Decomposition of the hot normalized damping rate into its contributions from different wave-particle interaction mechanisms for* $T_e = T_i$*=2.5 keV.*

In the transition region, where dispersive effects on wave frequency are only weakly pronounced, we also investigate the damping properties based on equatorial turbulence. From

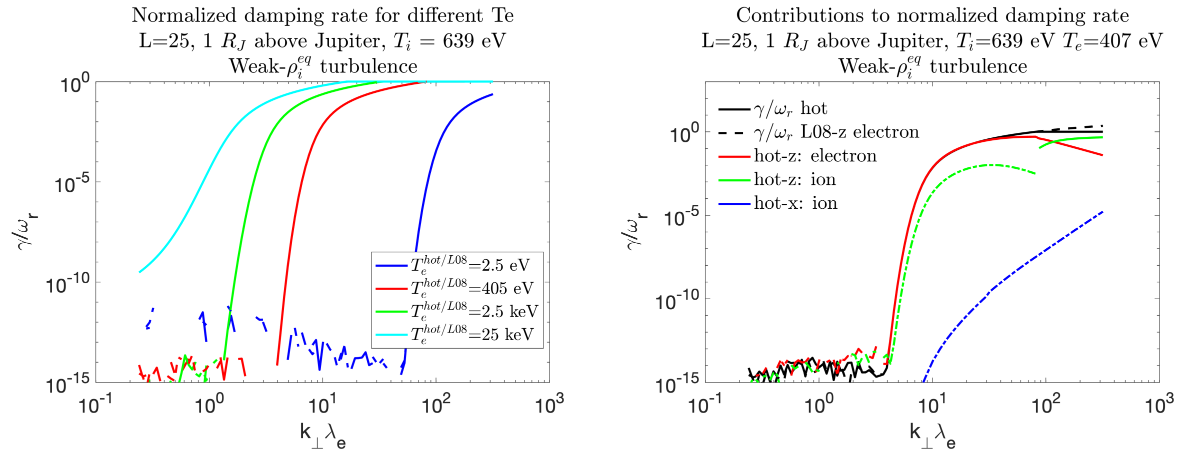

Figure 7.10.: *Left: Study of the dependence of the normalized damping on electron temperature in the high latitudes. Right: Decomposition of the hot normalized damping rate into its contributions from different wave-particle interaction mechanisms for the thermal species.*

the left plot of Figure 7.9, it is evident that rising electron temperatures also lead to an increase in the damping strength similar to the plasma sheet. The hot and Lysak damping rate coincide, meaning that electron Landau damping is the mechanism at work. This is also supported by single contributions in the right plot. Even though, the ion Landau contribution is not trustworthy due to its reversed sign, we do not expect significant contributions as the ion plasma beta is significantly smaller than in the equatorial region. The efficiency of electron Landau damping is even increased by an order of magnitude compared to the equatorial region at small scales due to the increased Alfvén speed.

In the high latitudes, damping is controlled by the electron inertial length scale, known from the analytic expression in equation (3.54). Additionally, we can observe a strong electron temperature dependency in the left plot of Figure 7.10. For significant damping at a scale of $k_\perp \lambda_e \sim 1$, large electron temperatures of $T_e = 2.5\,\text{keV}$ are required at least. Thus, Landau damping favors hot electrons in the high latitudes for efficient acceleration at larger scales. From the corresponding right plot, using a relatively low electron temperature of T_e=407 eV, it seems that ion Landau damping sets in at smaller scales around $k_\perp \lambda_e = 10$. This might be explained by considering that inertial effects lead to a decrease of parallel phase speed, shifting the resonance speed increasingly away from the tail of the ion velocity distribution. As a consequence of their smaller mass and related thermal speed, more electrons are able to interact with the wave on larger scales.

To sum up, as long as the ion temperature is not too large so that $\beta_i \sim 1$, electron Landau damping is a major driver for the damping strength in the plasma sheet for larger perpendicular scales. Consequently, the reduced *Lysak* (2008) solution is an appropriate model for the hot plasma damping rate. These solutions show consistent results for our investigated parameter regime along the field line. For small wave scales in the high latitudes, ion Landau damping can additionally play a role in auroral heating of protons. This aspect is investigated in the next chapter. The method of hot damping rate decomposition is highly sensitive to the correct determination of the tensor elements, the wave frequency, total damping rate and the electric field components, their real and imaginary parts respectively. If any of these components diverge, this approach is not useful anymore. However, for some cases we were able to retrieve physically meaningful results.

CHAPTER 8

Resonant wave-particle interaction along auroral field lines

In this chapter, we focus on the quantification of particle acceleration due to wave-particle interactions based on the results from Chapters 6 and 7. Therefore, we analyze the properties of the monochromatic kinetic Alfvén waves propagating along main auroral field lines due to turbulence generators inside and outside the plasma sheet. Investigated properties comprise electric field components, damping rate, dissipated power density, particle responses and and the particle heating rate. In particular, we include resonant wave damping into the description of the magnetic fluctuation amplitude, which has been neglected in the preceding chapter. We compare the results with the theoretical expectations and modeling results from the previous chapter. The modeling results are presented based on the hot plasma dispersion relationship, but also for the simplified *Lysak* (2008) solution to show consistency of both models for the investigated parameter regime. In the presented plots, we use the acronyms 'hot' and 'L08' to refer to both cases. Moreover, we specify the region along the field lines where significant particle acceleration occurs and discuss the associated acceleration mechanisms. Based on this analysis, we finally address the question of the relevance of Alvénic turbulence for Jupiter's auroral emissions.

In the following, we do not model the full global evolution of the propagating turbulent wave field in the inhomogeneous plasma medium. Our local modeling approach with uncorrelated turbulent monochromatic waves based on the mentioned dispersion relations allows us to investigate the details of the acceleration mechanisms of particles in the context of aurora. We gain information on those properties of kinetic Alfvén waves that are necessary for intense wave-particle interaction. These details give us insight into the requirements and efficiency of auroral heating by Alfvénic turbulence. We also do not consider reflection of wave energy. Thus, we cannot appropriately model the large-scale behavior of the Alfvén wave field with our model. On smaller wave scales, where the relevant wave-particle interaction processes takes place, our approach is better justified. We discuss the requirements of validity in more detail in Chapter 9.1.

8.1. Weak turbulence in the plasma sheet

In this section, we analyze the evolution of monochromatic kinetic Alfvén waves along auroral field lines based on weak-MHD turbulence in the plasma sheet. We concentrate on the reference models for the plasma populations along the L-shell of 25 (see Chapter 4) with the temperatures investigated in Chapter 7. For a more detailed and quantitative analysis, we track the evolution of monochromatic waves along the field line that originate in the plasma sheet at the largest scale $k_{\perp,1}^{eq} = \frac{2\pi}{R_J}$, at the onset of wave dispersion $k_{\perp,2}^{eq} = \frac{1}{2\pi}\frac{2\pi}{\rho_i^{eq}}$ and at a smaller scale of $k_{\perp,3}^{eq} = \frac{6}{10}\frac{2\pi}{\rho_i^{eq}}$. The latter wave scale is associated with the strongest dissipation at high latitudes. The corresponding wave quantities were taken from the locally calculated spectral solutions along the whole field lines by mapping the perpendicular scales along the field line according to $k_\perp(s) = k_\perp^{eq}\sqrt{\frac{B(s)}{B^{eq}}}$. Here, s denotes the field line position similar to the other chapters. In the presented plots, we use the convention that small distances along the field line represent the equatorial plasma sheet region and large distances represent the high latitude region up Jupiter's ionosphere.

8.1.1. Residual magnetic fluctuation amplitude

For physical quantities involving the magnetic fluctuation amplitude $\delta B(s)$, such as the electric field components, current densities and dissipated power densities, we now consider resonant damping as energy loss process for the monochromatic fluctuation amplitudes. The damping factor on the scaled fluctuation amplitude $\delta\hat{B}(s, k_\perp)$ from equation (7.1) is included as

$$\delta\hat{B}(s, k_\perp) = \delta B(s, k_\perp^{min}) \left(\frac{k_\perp}{k_\perp^{min}}\right)^{\alpha/2} exp\left(\frac{1}{2}\int_{s=eq}^{s} \frac{\gamma(k_\perp, \tilde{s})}{v_{gr,\parallel}(k_\perp, \tilde{s})} d\tilde{s}\right). \tag{8.1}$$

based on derived wave energy expression (4.13). Physically, the latter term represents the exponential decay of the wave amplitude due to resonant wave-particle interaction with local damping properties $\gamma(k_\perp, s)$, weighted by its travel time through the respective regions. We explicitly take dispersive effects on the propagation speed $v_{gr,\parallel} = \frac{\partial\omega_r}{\partial k_\parallel}$ into account, which determine how long the wave is damped in a certain region. Slower propagation speeds lead to an intensification of wave-particle interaction with the respective damping characteristics of the wave, whereas faster speeds lead to a reduced interaction time. In the plasma sheet, thermal effects on dispersion lead to an increase of propagation speed. Hence, dispersive waves might escape strongly damped regions even in the case of a significant damping rate. In the inertial Alfvén regime, dispersion acts to reduce the propagation speed on smaller wave scales. To keep the evaluation of expression (8.1) simple, we consider the parallel phase velocity $v_{ph,\parallel} = \frac{\omega_r}{k_\parallel}$ for determining the propagation speed. From the analytic dispersion relation for the wave frequency in the warm regime (see equation (3.42)), we know that non-linearity in terms of the parallel wavenumber only enters close to the cyclotron frequency. Consequently, $v_{gr,\parallel}$ is well approximated by the parallel phase velocity for our spectral range of interest.

The effect of damping on the magnetic fluctuation amplitude of the kinetic Alfvén wave is visible in Figure 8.1. Solid lines show the undamped fluctuation amplitude for the three wavenumbers mentioned before. Outside the plasma sheet, the amplitude generally decreases. This decrease is a consequence of the successive reduction in number density n and fewer heavy ions m_i, which carry the Alfvén wave. Towards Jupiter, the mass density $\rho = m_i \cdot n$ is so low and the background magnetic field so strong, that displacement current corrections lead to a significant increase in the fluctuation amplitude in order to maintain power conservation in the converging magnetic field line geometry.

Due to the power law-like behavior of the Alfvénic fluctuations with respect to $k_\perp$ as a fundamental property of turbulence, less energy is available on small wave scales. The

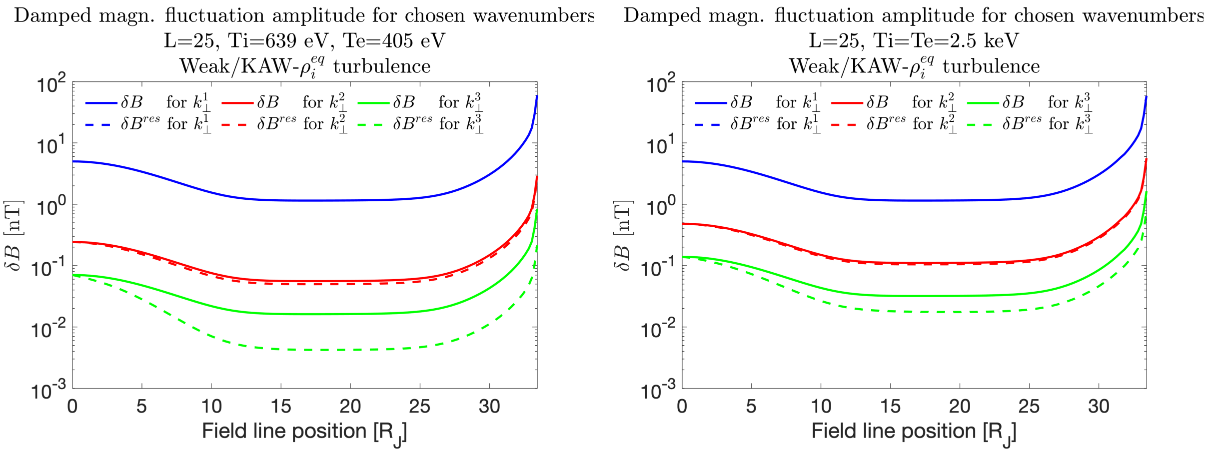

Figure 8.1.: *Scaled magnetic field fluctuation along the field line based on thermal (left) and hot (right) species for three chosen equatorial wavenumbers:* $k^{eq}_{\perp,1} = \frac{2\pi}{R_J}$, $k^{eq}_{\perp,2} = \frac{1}{\rho_i^{eq}}$ *and* $k^{eq}_{\perp,3} = \frac{6}{10}\frac{2\pi}{\rho_i^{eq}}$. *Solid lines represent undamped amplitudes, dashed lines display the residual damped amplitudes.*

---

dashed lines represent the residual wave amplitudes with resonant damping along the field lines. We see that the wave amplitudes at small scales, i.e., large wavenumbers, are mostly affected by inclusion of damping. The described behavior agrees with our finding that damping is generally stronger on smaller scales than on large ones. When we choose a much smaller wave scale than shown in the plot, damping along the field line gets sufficiently strong so that these small-scale Alfvén waves can not reach Jupiter anymore. Consequently, there is a smallest scale for which waves can propagate to the auroral acceleration region and control the power input for auroral emissions.

8.1.2. Electric field components

Now we discuss the electric fields of monochromatic kinetic Alfvén waves, which consider the damped magnetic fluctuation amplitudes. We do not separately deal with real and imaginary parts of the Fourier electric field components. Instead, we calculate effective fields in time domain with which the particles interact according to

$$\delta E^{eff} = \sqrt{\left\langle \left(\mathrm{Re}\left(\delta E_0(\omega) e^{i(\vec{k}\cdot\vec{r}-\omega t)} \right) \right)^2 \right\rangle} \tag{8.2}$$

$$= \frac{1}{\sqrt{2}} |\delta E_0(\omega)|. \tag{8.3}$$

Here, the temporal average over a wave period is denoted by $\langle \quad \rangle$. We like to note that the calculated values consider the scaled magnetic fluctuations in units of nT. Figure 8.2 shows the parallel and perpendicular electric field components for the same wave scales and species discussed in the previous section. The perpendicular electric field component increases towards Jupiter by three orders of magnitude as a consequence of increasing Alfvén speed. Comparing the results for the chosen wavenumbers, we can see that dispersive effects do not significantly modify the amplitude. A major driver that controls the spectral results is the modified magnetic fluctuation amplitude, which shrinks towards smaller scales. From the analytic results, we expect an increase in δE_x for scales smaller than the ion gyroradius ρ_i^{eq} which can partially counteract the shrinking magnetic fluctuation. However, our choice of wavenumbers is restricted to larger scales as the kinetic Alfvén wave goes into cyclotron

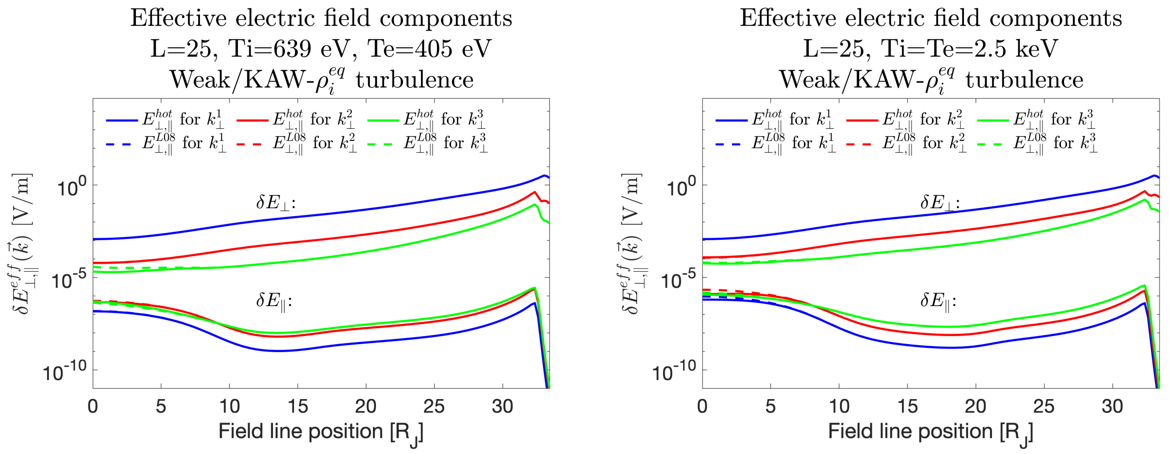

Figure 8.2.: *Parallel and perpendicular effective electric field components along the L=25 field line based on thermal (left) and hot (right) species for three chosen equatorial wavenumbers:* $k^{eq}_{\perp,1} = \frac{2\pi}{R_J}$, $k^{eq}_{\perp,2} = \frac{1}{\rho_i^{eq}}$ *and* $k^{eq}_{\perp,3} = \frac{6}{10}\frac{2\pi}{\rho_i^{eq}}$. *The electric field components consider the residual damped fluctuation amplitudes. In each plot, the upper three lines refer to* $\delta E_\perp$, *whereas the lower three lines refer to* $\delta E_\parallel$. *Solid lines represent the hot solution, dashed ones are based on the Lysak solution.*

resonance at such scales. In the high latitude region, these waves would also result in an increase in electric field strength as scales much smaller than the electron inertial length λ_e would be involved. The effective parallel electric field component instead increases for smaller scales. For the smallest scales, it peaks to $3 \cdot 10^{-6}\,\mathrm{V/m}$ at high latitudes for the thermal species. Considering the species with temperatures of $T_e = T_i = 2.5\,\mathrm{keV}$ in the right panel, the maximum value is slightly increased to $\delta E_\parallel^{max} = 6 \cdot 10^{-6}\,\mathrm{V/m}$. The peak in the inertial Alfvén regime coincides with the location along the field line where $k_\perp^2 \lambda_e^2$ from the analytic cold electric field expression (3.64) maximizes. In terms of plasma properties, this is where the ratio B/n maximizes, and correspondingly, where the Alfvén speed v_A is largest. Therefore, the plasma density has a large impact on the strength of the parallel electric field and on the acceleration of electrons at high latitudes. In Sections 8.1.6 and 8.1.7, we present modeling studies investigating the implications of a reduced density and reduced ionospheric scale height for the acceleration of particles. These parameters also affect the strength of the electric fields. This is important, because from the found peak parallel electric fields in this section we only generate electrons with characteristic energies up to 430 eV assuming an acceleration region of $1\,R_J$. Such energies are too small to account for the observations of keV - MeV JEDI electrons in the auroral region by *Mauk et al.* (2017c).

8.1.3. Normalized damping rate

Now we turn to the discussion of the normalized damping rate γ/ω_r for the three wave scales. These are presented in Figure 8.3 for both species. We notice that wave damping strongly depends on the chosen wave scale tracked along the field line. Regarding the largest wave scale, $k_{\perp,1}(s) = \frac{2\pi}{R_J}\sqrt{\frac{B(s)}{B^{eq}}}$, the damping rate is strongest in the warm Alfvén regime but too weak to account for significant damping in this region. Towards Jupiter, it even vanishes in the inertial Alfvén regime. Consequently, these large-scale waves can propagate nearly undamped to the high latitudes as long as reflection processes are ignored. This drop in the damping rate can be easily explained if we realize that

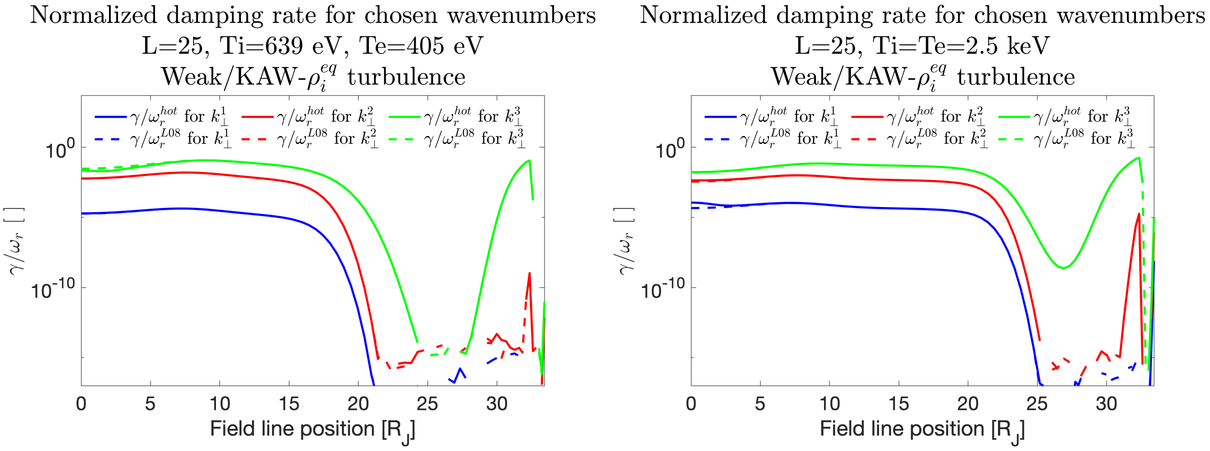

Figure 8.3.: Normalized damping rate along the field line based on thermal (left) and hot (right) species for three chosen equatorial wavenumbers: $k^{eq}_{\perp,1} = \frac{2\pi}{R_J}$, $k^{eq}_{\perp,2} = \frac{1}{\rho^{eq}_i}$ *and* $k^{eq}_{\perp,3} = \frac{6}{10}\frac{2\pi}{\rho^{eq}_i}$. *Solid lines represent the hot solutions, dashed ones are based on the Lysak solutions.*

$k_{\perp,1}\lambda_e < 1$ in this region. From the analysis in Chapter 7.3 we know that the damping rate is effectively absent at comparable waves scales considering the thermal species with an electron temperature of $T_e = 407\,\mathrm{eV}$. Only for the largest chosen wavenumber (green lines), wave-particle interaction allows for stronger damping rates at low altitudes above Jupiter coinciding with the maximum parallel electric field. In this region, electron Landau damping is the dominant acceleration mechanism. However, the onset of strong Landau damping in the acceleration region is related to equatorial wave scales with non-negligible damping in an extended region in the warm electron regime. Small-scale Alfvén waves in the equatorial region with significant damping rates of $\gamma/\omega_r \sim 1$ are able to heat the plasma sheet ions over cyclotron damping as investigated by *Saur* (2004). This damping is associated with significant energy losses for the waves. Thus, we cannot chose arbitrarily small wave scales in the equatorially located turbulence generator region. Such small-scale waves, even though theoretically connected to significant damping rates close to Jupiter, have already decayed in the the plasma sheet. We conclude that there is a wave scale-related trade-off between the damping rate and the residual magnetic field fluctuation that controls the efficiency of wave-particle interaction in the acceleration region. We will validate this expectation in Section 8.1.7. From comparison of both species, we can clearly see that damping in the inertial regime is increased for hot electrons. This result makes hotter species in the inertial regime more interesting to investigate than the cold one.

8.1.4. Dissipated power density

To examine the dependency of residual magnetic fluctuation amplitude and required damping strength in greater detail, the dissipated power density p_{abs} is taken into account as it combines both quantities. The associated expressions have been introduced in Chapter 3.5.7 by equations (3.76) and (3.79), respectively. The residual magnetic fluctuation amplitude δB enters p_{abs} over the electric field in a quadratic way. Thus, the power density absorbed by the particles sensitively depends on δB. Moreover, the absorbed power density is essential to determine the power which can be placed into the atmosphere via accelerated particles. These numbers can be compared to observations. Consequently, the resulting absorbed power is an important quantity to evaluate whether Alfvénic turbulence is relevant for driving Jupiter's auroral emissions. In Figure 8.3, we present the absorbed

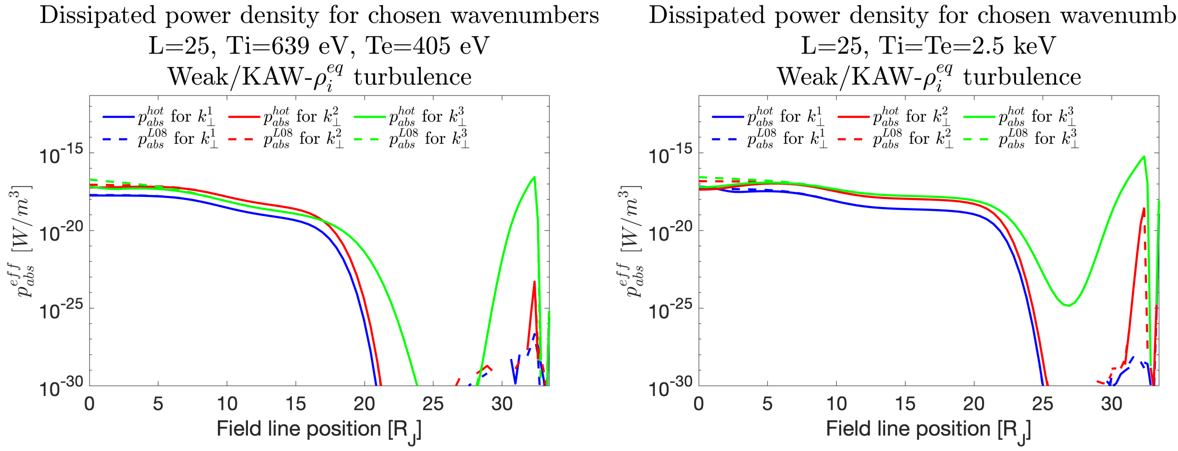

Figure 8.4.: *Effectively absorbed power density along the field line based on thermal (left) and hot (right) species for three chosen equatorial wavenumbers:* $k_{\perp,1}^{eq} = \frac{2\pi}{R_J}$, $k_{\perp,2}^{eq} = \frac{1}{\rho_i^{eq}}$ *and* $k_{\perp,3}^{eq} = \frac{6}{10}\frac{2\pi}{\rho_i^{eq}}$. *Solid lines represent the hot solutions, dashed ones are based on the Lysak solutions.*

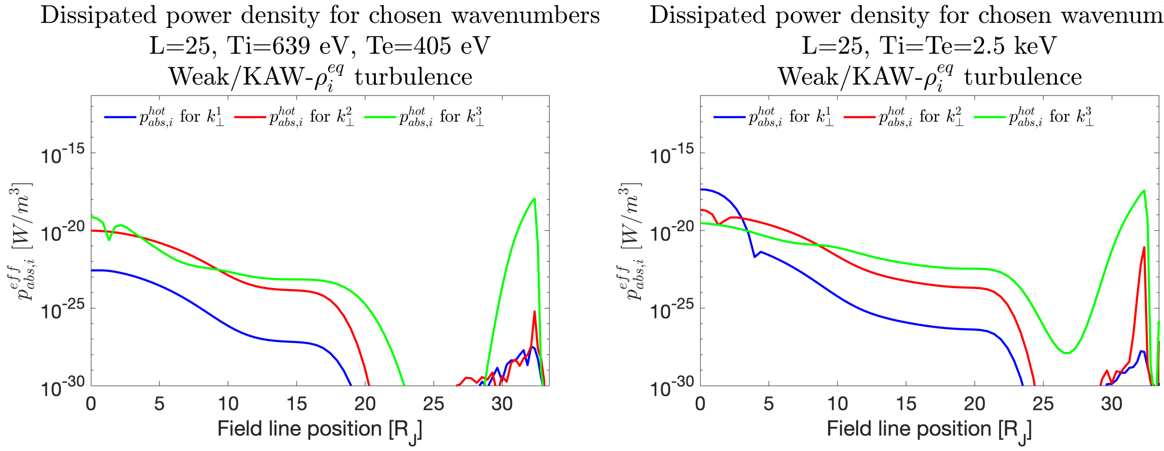

Figure 8.5.: *Effectively absorbed power density by ions in parallel direction along the field line based on thermal (left) and hot (right) species for three chosen equatorial wavenumbers:* $k_{\perp,1}^{eq} = \frac{2\pi}{R_J}$, $k_{\perp,2}^{eq} = \frac{1}{\rho_i^{eq}}$ *and* $k_{\perp,3}^{eq} = \frac{6}{10}\frac{2\pi}{\rho_i^{eq}}$.

spectral power densities for both species along the field line. The qualitative behavior is similar to the normalized damping rate. The described effect of damping on the residual magnetic fluctuation amplitude becomes visible for the smallest scale in case of the thermal species (left panel, green line). Here successive damping is strong enough so that the efficiency of energy transfer is reduced compared to $k_{\perp,2}$ (red lines). Thus, the choice of an even smaller wave scale will eventually lead to a fully diminished wave amplitude at high latitudes. We choose $k_{\perp,3}$ such that the power transfer maximizes at high latitudes. For the thermal species, we obtain a peak absorbed power density of $p_{abs} = 3 \cdot 10^{-17}\,\mathrm{W/m^3}$. Considering the hotter species with $T_e = T_i$ =2.5 keV, we obtain $p_{abs} = 6 \cdot 10^{-16}\,\mathrm{W/m^3}$. As discussed in Chapter 7, the electron temperature is a relevant driver for the increase in damping and related energy transfer towards particles as a consequence of electron Landau damping. Related total energy fluxes and comparison to observed values will be discussed in Section 8.5.

For completeness of the discussion, we also plot the contribution to the power density absorbed by ions in parallel direction in Figure 8.5. This is associated with ion Landau

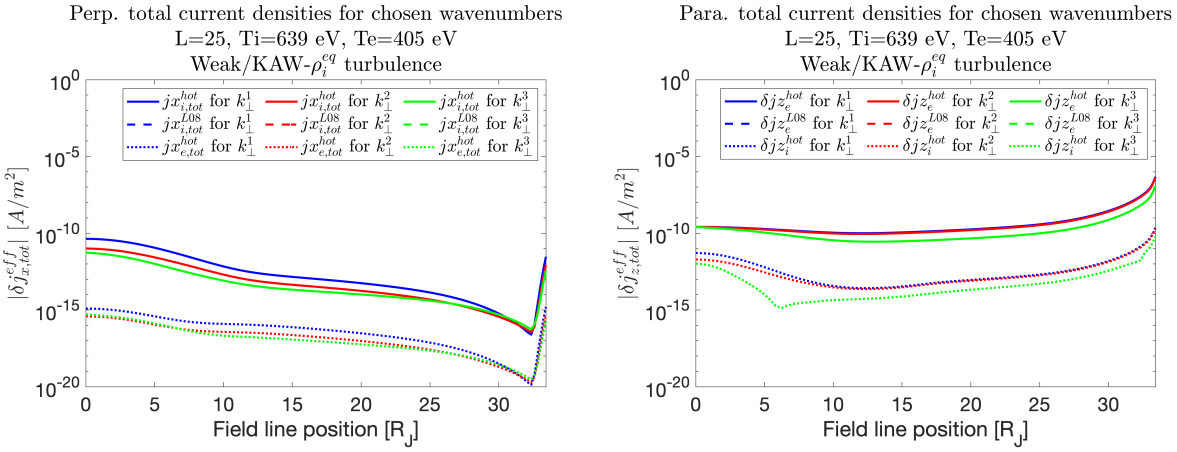

Figure 8.6.: *Total perpendicular (left) and parallel (right) ion and electron responses in terms of current densities along the field line for three chosen equatorial wavenumbers:* $k_{\perp,1}^{eq} = \frac{2\pi}{R_J}$, $k_{\perp,2}^{eq} = \frac{1}{\rho_i^{eq}}$ *and* $k_{\perp,3}^{eq} = \frac{6}{10}\frac{2\pi}{\rho_i^{eq}}$. *The label 'L08' refers to currents calculated using tensor elements and wave frequency from the Lysak (2008) solution.*

damping. As expected, larger ion temperatures increase the number of ions, which can participate in resonant wave-particle interaction. Consequently, more power is dissipated by the wave. We can identify that, similar to electron Landau damping, the high latitude region gives the strongest contributions. But still, we note that ion Landau damping is a factor of 100 weaker than electron Landau damping in the hot electron case. Thus, we do not expect protons to have relevant effect on the auroral energy budget.

8.1.5. Particle responses

Now, we discuss the ion and electron responses due to the presence of the KAW along the L=25 field line based on the current density expressions introduced in Chapter 3.5.6. We qualitatively evaluate if these responses gives physical reasonable results we expect from theory (Chapter 3.5) and investigate, to what extent wave-particle interactions between KAWs and ions/electrons affect the responses.

In Figure 8.6(left), we present the total perpendicular ion and electron responses according to expression (3.68). We can identify that the perpendicular KAW current density is carried by the ions. This observation matches our expectation that the ion polarization drift is majorly contributing to the perpendicular response for these wave scales. For larger ion temperatures, the response is slightly increased as dispersive effects modify the perpendicular electric field. The electron polarization drift responses (dotted line) are by the factor of $\frac{m_e}{m_i}$ smaller than the ion one. Thus, they do not play an important role for perpendicular wave dynamics. Along the field line, we can observe that the ion response continuously decreases. At high latitudes, the perpendicular ion response reduces by five orders of magnitude compared to its equatorial value. The drop in the ion response results from the stronger magnetic field in the inertial regime and the corresponding smaller gyroradius of the ions. Thus, the parallel electron response due to the KAW is mainly responsible to carry the current (see Figure 8.6(right)). We can identify an increase of the parallel electron response closer to Jupiter with a peak value of $8 \cdot 10^{-7}$ A/m^2. This value is of the same order as currents that are mapped to the ionosphere from observed equatorial currents using $\delta j^{hl} = \frac{B^{hl}}{B^{eq}} \delta j^{eq}$ (e.g. *Saur et al.* (2002, 2018b); *Mauk and Saur* (2007)). Also *Kotsiaros et al.* (2020) estimated field-aligned currents to be $1.3 \cdot 10^{-6}$ A/m^2

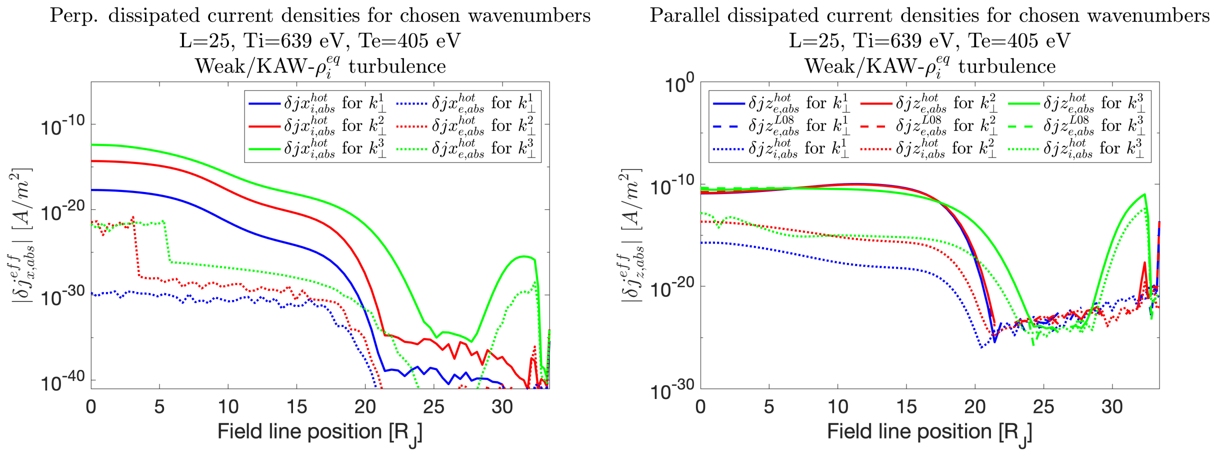

Figure 8.7.: *Perpendicular (left) and parallel (right) ion and electron responses related to dissipation processes along the field line for three chosen equatorial wavenumbers:* $k^{eq}_{\perp,1} = \frac{2\pi}{R_J}$, $k^{eq}_{\perp,2} = \frac{1}{\rho_i^{eq}}$ *and* $k^{eq}_{\perp,3} = \frac{6}{10}\frac{2\pi}{\rho_i^{eq}}$. *The label 'L08' refers to currents calculated using tensor elements and wave frequency from the Lysak (2008) solution. Note that there is no perpendicular dissipation contribution in the Lysak theory, neither for electrons nor for ions.*

---

in the ionosphere based on Juno measurements. From expression (3.72), we can deduce that the parallel electron response is the strongest particle response from interactions with KAW as $\delta j^e_z \sim \mu_0 \nabla \times \delta \vec{B}_\perp$ for $k_\perp \gg k_\parallel$. Thus, the magnetic fluctuation amplitude and the perpendicular wave scale dictate the maximum parallel Alfvénic current. To conclude on the current responses, these behave as expected from theory. Moreover, Alfvénic turbulent fluctuations in the plasma sheet support a connection to the high latitudes based on the observations.

In the next step we analyze responses that are connected to dissipation processes. These responses are in phase with the respective electric field component and thus allow for intense-wave particle interaction. We calculate the responses with expression (3.77) and show the results in Figure 8.7. We see that increasing wavenumbers lead to increased responses. Consistent with electron Landau damping, the parallel electron responses are strongest along the field line. The parallel ion responses are weaker as expected for the less significant influence of ion Landau damping compared to electron Landau damping. For increasing ion temperatures we can observe an increase in the ion response. However, these responses have some numerical issues (cf. appended Figure E.2). The parallel ion response also gains importance at high latitudes, although it is one order of magnitude weaker than the electron responses. We consider the electron response as trustworthy because it coincides with the calculated response from the Lysak model. Thus, the ion response seems to be a consistent feature in this region because it has a similar shape as the electron response. Nonetheless, we generally need to be careful about the interpretation of ion responses as modeling studies for the damping rate in Chapter 7.3 already showed numerically unstable results for ions. For the larger temperature set (cf. appended Figure E.2), the electron response increases stronger than the ion response in this region.

At high latitudes, we can also observe a perpendicular response of the ions. The perpendicular ion response only sets in at small wave scales. Its amplitude is more than 10 orders of magnitude smaller than in the equator and it is negligible compared to the parallel electron response. Hence, we do not consider the associated perpendicular ion cyclotron damping to have an important role in the inertial regime. Perpendicular ion responses become important in the plasma sheet for $\omega \sim \Omega_i$ as a consequence of the cyclotron heating process.

In conclusion, the concept of 'dissipative currents' can be used similarly to expression (3.78) in order to physically assess whether a damping mechanism is active. As expected, the parallel dissipative electron response is strongest along the field line. However, dissipative currents suffer from similar numerical problems as the dissipated power density (equation (3.78)) as both expressions have the same dependency on the tensor elements. For electrons, the tensor elements are stable. For ions, dissipative currents need to be interpreted with caution.

8.1.6. Influence from a low-density species

We want to address the question, whether a dilute superthermal species can undergo efficient wave-particle interaction in the presence of the kinetic Alfvén wave. Observations in the plasma sheet and the high latitudes (e.g. *Kivelson et al.* (2004), *Dougherty et al.* (2017),*Mauk et al.* (2018)) confirm that also dilute superthermal species are present in the magnetosphere. From our previous modeling studies on the damping rate and the cold analytic damping expression, we know that the electron inertial length is a sensitive parameter for the efficiency of electron Landau damping at high latitudes. Up to now, we considered a bulk species with the density model developed in Chapter 4. Thus, we expect that a dilute hot electron species has a strong influence on damping characteristics since its inertial length becomes larger.

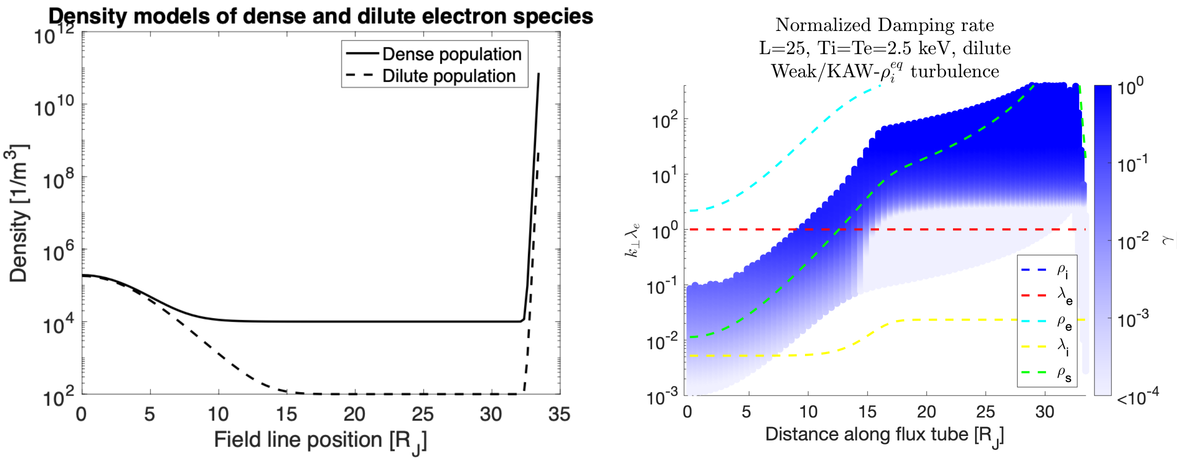

Figure 8.8.: *Left: Number density field line model considering a dilute species (1%) outside the plasma sheet in comparison to the bulk species model used in previous sections. Right: Spectral representation of normalized damping rate for the dilute species along the L=25 field line in the middle magnetosphere.*

The available code for solving the dispersion relation for the KAW is not suited to consider several ion and electron species simultaneously. Thus, we need to discuss the implications for modeling with a reduced density for a dilute electron and proton species in the absence of a bulk species. In the analysis of the contributions to the total hot damping rate in Section 7.3, we saw that Landau damping is a species related phenomenon whose significance is controlled by the ion and electron species separately. For wave-particle interaction, we expect that the respective local resonance condition for the single Maxwellian distributed species determines the strength of Landau damping. This notion is easy to understand,

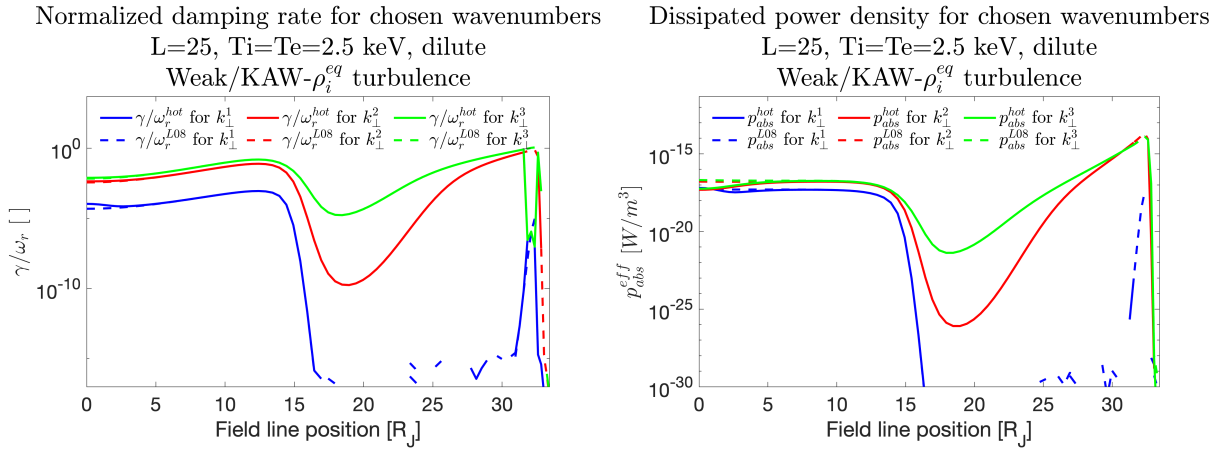

Figure 8.9.: *Normalized damping rate (left) and effective absorbed power density (right) for the dilute (1%) species along the field line for three chosen equatorial wavenumbers:* $k_{\perp,1}^{eq} = \frac{2\pi}{R_J}$, $k_{\perp,2}^{eq} = \frac{1}{\rho_i^{eq}}$ *and* $k_{\perp,3}^{eq} = \frac{1}{4}\frac{2\pi}{\rho_i^{eq}}$. *Solid lines represent the hot solutions, dashed ones are based on the Lysak solutions.*

---

considering that each particle moving at phase velocity can efficiently interact with the wave. The idea also applies to the mathematical structure of the general dielectric tensor and equation (3.78), where the anti-hermetian contributions from several species simply add up. In contrast to damping, wave dispersion and thus propagation speed is controlled by total population. We can demonstrate this as follows:

On MHD scales and neglecting displacement currents, the dispersion relation for the Alfvén wave in a plasma with several ion species behaves as $\frac{k_\parallel^2 c^2}{\omega^2} = \sum_s \varepsilon_{xx}^s = \sum_s \frac{c^2}{v_{A,s}^2}$. Here, $v_{A,s} = \frac{B}{\sqrt{\mu_0 m_s n_s}}$ describes the Alfvén speed for the separate species with masses m_s and densities n_s. This dispersion relation results in a reduced phase speed of

$$v_{ph} = \frac{\omega}{k_\parallel} = \frac{B}{\sqrt{\mu_0 \sum_s m_s n_s}} \tag{8.4}$$

compared to a single ion species as the plasma becomes 'denser'. Likewise, when we include a second electron species into the dispersion relation from *Lysak and Lotko* (1996), we can derive the following dispersion relation in the inertial electron limit

$$\frac{\omega_r^2}{k_\parallel^2 v_{A,rel}^2} = \frac{1}{1 + k_\perp^2 \left(\sum_s \frac{1}{\lambda_{e,s}^2}\right)^{-1}}. \tag{8.5}$$

Here, the inertial lengths for the single electron species are denoted by $\lambda_{e,s} = c\sqrt{\frac{\varepsilon_0 m_e}{n_s e^2}}$. Comparing this dispersion relation to the one from equation (3.43), we can see that this description is consistent with the single electron species case. In our case of interest, the bulk electron species will control the 'effective' electron inertial length $\lambda_{e,eff} = \left(\sum_s \frac{1}{\lambda_{e,s}^2}\right)^{-1/2}$ and the set-on of dispersive effects. Thus, we conclude that the dispersive characteristics of the kinetic Alfvén wave sensitively depend on bulk plasma properties, which carry the Alfvén wave.

Reducing the proton number density in the inertial Alfvén regime, to maintain quasi-neutrality with electrons, will lead to a larger MHD Alfvén speed. At high latitudes, where we expect the strongest damping, $v_{A,rel}$ already approaches the speed of light. Therefore, a reduced proton density does not significantly change the wave propagation velocity on MHD scales. On electron inertial length scales, dispersive effects successively reduce the phase velocity. Consequently, damping rates calculated solely for the dilute species outside the plasma sheet, do not fully reflect the true damping rate of the kinetic Alfvén wave for this species because we ignore the effect of the bulk species on dispersion.

To initially investigate if significant wave-particle interaction can happen at the separate λ_e scale for the dilute species, we take the parallel electric field as a proxy for wave damping. We consider the dielectric tensor element $\varepsilon_{zz} \sim -\sum_s \frac{\omega_{ps}^2}{\omega^2}$ in the cold electron limit similar to the expression used for a single electron species in Chapter 3.5.5. The electron plasma frequency of the single species is denoted by ω_{ps}. Under the use of the derived dispersion relation (equation (8.5)), we can express the real part of the inertial electric field (expression (3.57)) as

$$\delta E_z = -\frac{c^2 k_x}{\omega \varepsilon_{zz}} \delta B_y = \frac{k_z}{k_x} v_{A,rel} \frac{k_x^2 \lambda_{e,eff}^2}{\sqrt{1 + k_x^2 \lambda_{e,eff}^2}} \delta B_y \,. \tag{8.6}$$

This expression already gives a strong indication that damping is still controlled by the effective bulk electron inertial length and not by the separate species scales. A verification of this hypothesis still requires numerical modeling as the imaginary part of the electric field can also develop significant amplitudes in this regime. This topic is left for future research. Nonetheless, the following study is valuable to assess if larger wave scales at the generator location can lead to significant damping at high latitudes and generally investigate the effect of a reduced plasma density on dissipation.

For our study, we reduce the background floor number density of $10^4\,\mathrm{m}^{-3}$ by a factor of 100 (1% of bulk species). This number density corresponds to an increase of the electron inertial length by a factor of 10 outside the plasma sheet. The resulting density model is presented in Figure 8.8(left). The Alfvénic properties in the plasma sheet are still identical to the previous sections. The density transition towards the dilute region is based on the same scale height law from Chapter 4. Comparing the spectral damping rate properties from Figure 8.8(right) to the one from the dense bulk species (cf. Figure 7.2), we see that damping in the inertial regime is significant with $\gamma/\omega_r \sim 1$ over a broader spectral regime. Moreover, we can also see an extension of the inertial Alfvén regime as a result of increased inertial lengths. In Figure 8.9(left), we track the damping rate for the three wavenumbers similar to the previous sections. The drop towards the inertial regime occurs $7\,R_J$ further away from Jupiter along the field line (s=$15\,R_J$) compared to the bulk case (cf. Figure 8.4). Thus, a slightly larger equatorial wave scale $k_{\perp,3} = \frac{1}{4}\frac{2\pi}{\rho_i^{eq}}$ could be chosen at which the absorbed power density maximizes in the high latitude region. The related spectral power density in the right panel of Figure 8.9 shows a peak value of $2 \cdot 10^{-14}\,\mathrm{W/m^3}$. This value is a factor of 36 larger than this for bulk species, which we attribute to the increase in parallel electric field at high latitudes. In the likely case that the effective electron inertial length controls the onset of wave damping in the inertial Alfvén regime for the additional dilute species, we will not see the intense increase in electric field and consequently, also not in absorbed power. Even though, from the modelings in Section 7.3 we still expect a dilute energetic population with a large electron temperature to be energized more efficiently than a colder one by the kinetic Alfvén wave at high latitudes. Support is theoretically given by the resonance condition, which needs to be fulfilled for each species separately. Here, the electron temperature enters over the thermal speed and thus explicitly control the efficiency of damping. Density and and related distribution function of the superthermal species will additionally control the number of particles to efficiently interact with the wave.

8.1.7. Influence from ionospheric scale height on power spectral density

A further effect, we identified to have crucial influence on the calculated power transfer rates due to KAWs is the ionospheric scale height. In the models discussed in the previous sections, we used a scale height of H= 4200 km similar to *Lysak and Song* (2020). *Su et al.* (2006) additionally considered in their study scale heights down to 800 km. *Kotsiaros et al.* (2020) used a scale height of H= 200 km based on H_3^+ observations with an ionospheric temperature of 0.1 eV to estimate Birkeland currents in the auroral region. Thus, we think that a drastically reduced ionospheric scale height is more realistic than used by *Lysak and Song* (2020). Additional support for using a reduced scale height comes from magnetic field fluctuations in the auroral region by *Gershman et al.* (2019). They observed root-mean-square fluctuations of 20 nT, which agree well with our undamped fluctuation amplitude of 26.1 nT based on our model from Chapter 4.3 but with a reduced scale height. They also observed peak values of 100 nT. For H=4200 km, we gain a lower undamped fluctuation amplitude of 9.3 nT at the location of maximum heating. In the following, we will show that this has far-reaching consequences regarding the calculation of dissipated powers in the high latitude region.

By choosing a reduced scale height, the strong increase in density occurs at a location closer to Jupiter along the field line. In this region, the background magnetic field undergoes a strong increase as well. Consequently, the location of the maximum B/n-ratio and likewise of the largest Alfvén speed also shifts closer to Jupiter, and thus, allows for stronger Alfvénic parallel electric fields. This new location is also associated with an increased magnetic field fluctuation, which further increases the electric field.

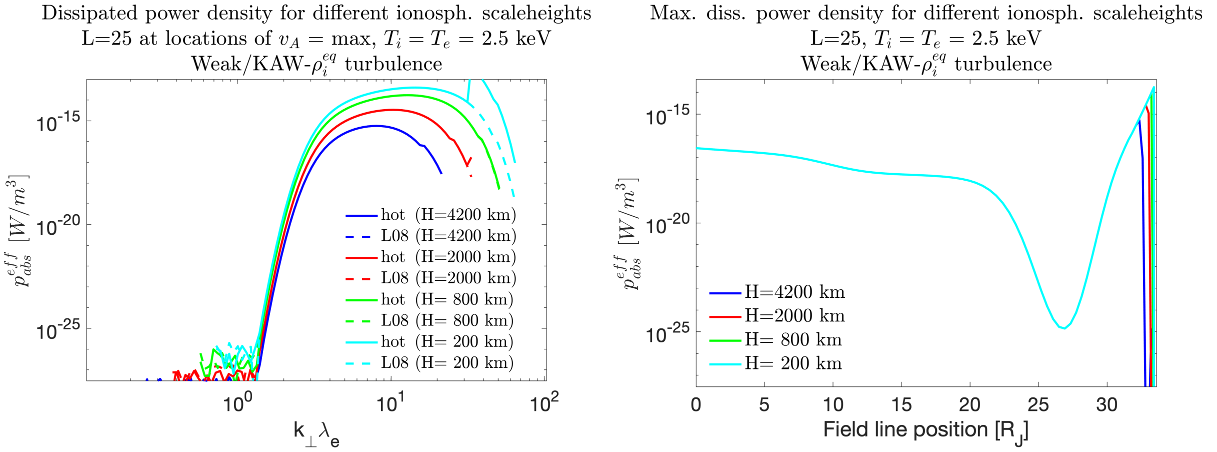

Figure 8.10.: *Left: Spectral power dissipation at locations of largest Alfvén speed for the respective ionospheric scale heights based on equatorial turbulence. Right: Evolution of maximum power dissipation along the L=25 field line for the same scale heights.*

In Figure 8.10(left), we display the spectral behavior of the dissipated wave power for three different scale heights at the respective locations of maximum B/n in the high latitude region. The calculations are carried out for the hot species, i.e. $T_e = T_i$= 2.5 keV. To obtain the spectral dissipated power density, we integrated all the damping contributions along the field lines tracked for each wavenumber separately as done for presented cases in the previous sections. The result demonstrates that there is a smallest perpendicular wave scale for which the dissipated power maximizes as discussed in previous sections. For smaller scales, the magnetic fluctuation amplitude is naturally smaller due to the turbulent cascade and additionally experiences stronger damping during propagation. Consequently, the resulting electric field amplitude is smaller and wave-particle interaction will be less efficient. In the other extreme case, i.e., for large scales, damping is effectively not present at high latitudes and eventually leads to insignificant energy transfer to particles.

Now, we turn to the discussion of dissipation due to different scale heights. The H= 4200 km case represents the reference case used for the previous modeling studies. From Figure 8.10, we can identify three effects related to a reduced scale height. First, the spectral width of intense dissipation in the left panel becomes wider. This widening is a result of the increased background magnetic field closer to Jupiter, which simultaneously enhances the perpendicular wavenumber and magnetic fluctuation amplitude. However, due to our rescaled fluctuation amplitudes (see equation B.4), we need to be careful when comparing spectral widths from different field line positions. The consequences of the spectral width on the calculation of overall power are discussed in Section 8.5. Second, the strongest dissipation for the H=200 km case, i.e., $p_{abs}^{max} = 3.9 \cdot 10^{-14}\, W/m^3$, is about two orders of magnitude stronger than for the reference case with $p_{abs}^{max} = 5.7 \cdot 10^{-16}\, W/m^3$. The third effect is visible in Figure 8.10(right). Here, we compare the maximum power dissipation along the field line for a monochromatic wave with an equatorial scale of $k_{\perp,3} = 0.6 \frac{2\pi}{\rho_i^{eq}}$ for the different ionospheric scale heights. The location of strongest acceleration moves from an altitude of $1.1\, R_J$ above the ionosphere for the reference scale height towards an altitude of $0.06\, R_J$ for H=200 km. Thus, a reduced scale height results in an extended acceleration region and increases the dissipation volume.

The scale height effect on the calculation of maximized power density can be estimated from MHD quantities at the locations of maximized electric field. We use the power density expression (3.76) and the analytic cold parallel electric field expression (3.64) (neglecting thermal effects) to approximate

$$p_{abs,2}^{max} \approx \left(\frac{\delta E_{\|,2}}{\delta E_{\|,1}}\right)^2 \cdot p_{abs,1}^{max} \approx \left(\frac{k_{\perp,2}\lambda_{e,2}^2}{k_{\perp,1}\lambda_{e,1}^2}\frac{\delta B_2}{\delta B_1}\right)^2 \cdot p_{abs,1}^{max} \simeq \frac{B_2}{B_1}\left(\frac{\delta B_2}{\delta B_1}\right)^2 \cdot p_{abs,1}^{max} \,. \qquad (8.7)$$

This expression relates the maximum power densities at locations of strongest parallel electric field for the different scale heights. These locations are indicated by the indices 1 and 2. We also used $\frac{k_{\perp,2}}{k_{\perp,1}} = \sqrt{\frac{B_2}{B_1}}$, $\lambda_{e,1} = \lambda_{e,2}$, and assumed the contributions from the anti-hermetian tensor elements to be similar at both locations for this simple estimate. Evaluating the power density ratio for the case of H_1=4200 km and H_2=200 km, we come up with a value of 62. That is already very close to the exact calculation for the power densities given in the previous paragraph, which results in a ratio of 68. This result highlights the importance of the location for maximum heating. Consequently, a variable start of the ionosphere (taken to be $0.02\, R_J$ above the 1bar-level) or potential day- and night side asymmetries of the ionosphere, have a dramatic consequence for the maximum power to be transferred to the auroral particles. Equation (8.7) shows a strong magnetic field dependence, considering that $\left(\frac{\delta B_2}{\delta B_1}\right)^2 \sim \frac{B_2}{B_1}$ holds in the low-density region based on our wave energy model (4.13). Thus, we expect that longitudinal changes in the high-latitudinal background magnetic field (see *Connerney et al.* (2018)) affect the efficiency of the strongly localized Alfvénic particle heating and finally, the morphology of the auroral

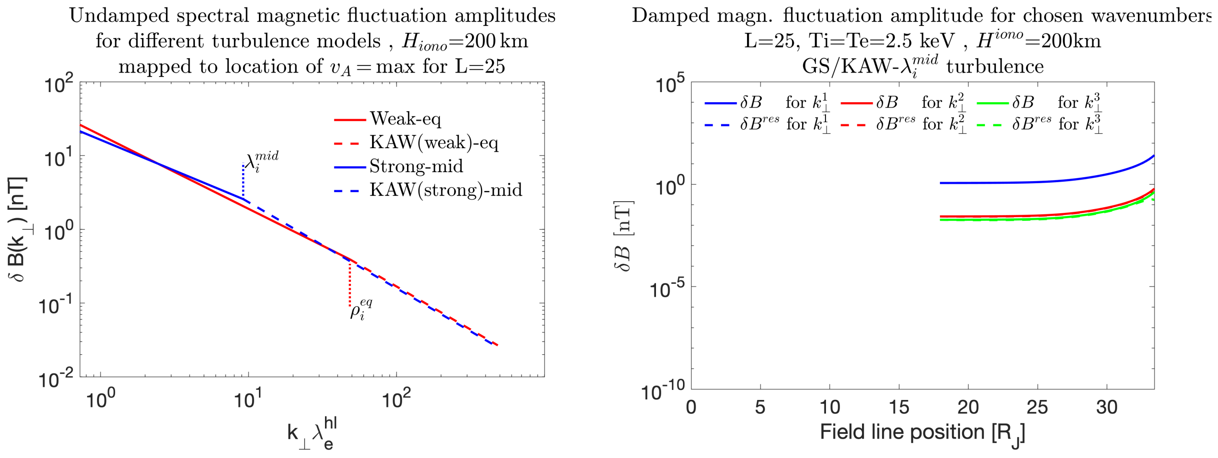

Figure 8.11.: *Left: Undamped spectral magnetic field fluctuations at location of strongest dissipation (H^{iono}=200 km) for Weak-ρ_i^{eq} and Strong-λ_i^{mid} turbulence with KAW-turbulence extension. Indicated scales delineates the spectral MHD turbulence breakdowns. Right: Undamped and residual magnetic fluctuations along L=25 field line for mid-latitudinal turbulence generator for three chosen equatorial wavenumbers:* $k^{mid}_{\perp,1} = \frac{2\pi}{R_J}\sqrt{\frac{B_{mid}}{B_{eq}}}$, $k^{mid}_{\perp,2} = 2 \cdot \frac{2\pi}{\lambda_i^{mid}}$ *and* $k^{mid}_{\perp,3} = 0.4\frac{1}{\lambda_e^{mid}}$. *Solid lines represent undamped amplitudes, dashed lines display the residual damped amplitudes.*

emissions. These considerations also underline that the increase in power density can be simultaneously applied to our investigated thermal species and to other field lines as well.

8.2. Turbulence generator outside the plasma sheet

For the turbulence generator outside the plasma sheet, we performed a similar analysis as for equatorial turbulence in preceding Section 8.1. In this section, we only present the study for the hot species with $T_e = T_i = 2.5\,\mathrm{keV}$. To estimate the maximum potential for auroral heating, we additionally concentrate on model results with an ionospheric scale height of H=200 km. Although waves are generally allowed to propagate in both directions along the field line, we only present the waves that propagate towards Jupiter.

From the modeling studies shown in this section, we found that the maximum dissipated power at high latitudes is associated with perpendicular wavelengths smaller than the ion inertial length λ_i^{mid} at the generator location outside the plasma sheet. Consequently, KAW-turbulence is the relevant driver of particle acceleration for the generator location outside the plasma sheet. The corresponding relevant perpendicular wavenumbers mapped to the high latitudes are similar to these from equatorial turbulence, where we identified weak-MHD turbulence as the relevant wave generator for damping above Jupiter. The overlapping wavenumber ranges can be attributed to the equally strong undamped spectral magnetic field fluctuations for both turbulence models (cf. Figure 8.11(left)). However, equatorially launched small-scale wave packages, which get damped in the warm region already, result in weaker residual magnetic fluctuations and electric fields above Jupiter. This statement is expressed by Figure 8.12(left), where we plot the normalized damping starting from the generator location. Mid-latitudinal originating turbulent waves do not experience the damping in the warm Alfvén region while traveling to Jupiter in contrast to waves originating in the plasma sheet. Eventually, auroral heating due to weak equatorial turbulence will be weaker compared to KAW turbulence outside the plasma sheet. Interestingly, even though waves with much smaller perpendicular scales can propagate to Jupiter based on mid-latitudinal turbulence, the corresponding magnetic fluctuations are

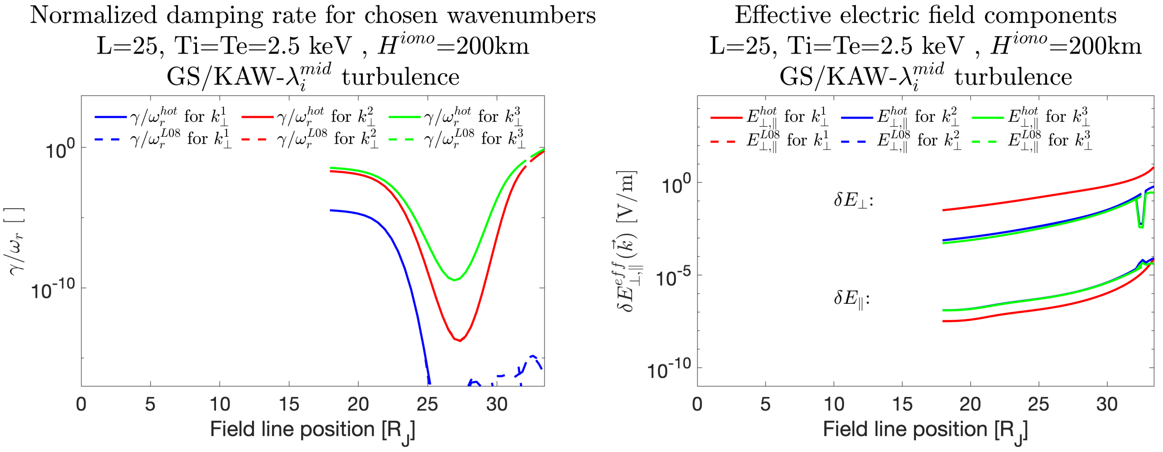

Figure 8.12.: *Normalized damping rate and effective electric field components (right) along L=25 field line for mid-latitudinal turbulence generator for three chosen equatorial wavenumbers given in the caption of Figure 8.11. Solid and dashed lines represent the coinciding calculations based the hot and the Lysak solution (L08), respectively. The peaks in the dotted lines in the left panel are numerically caused.*

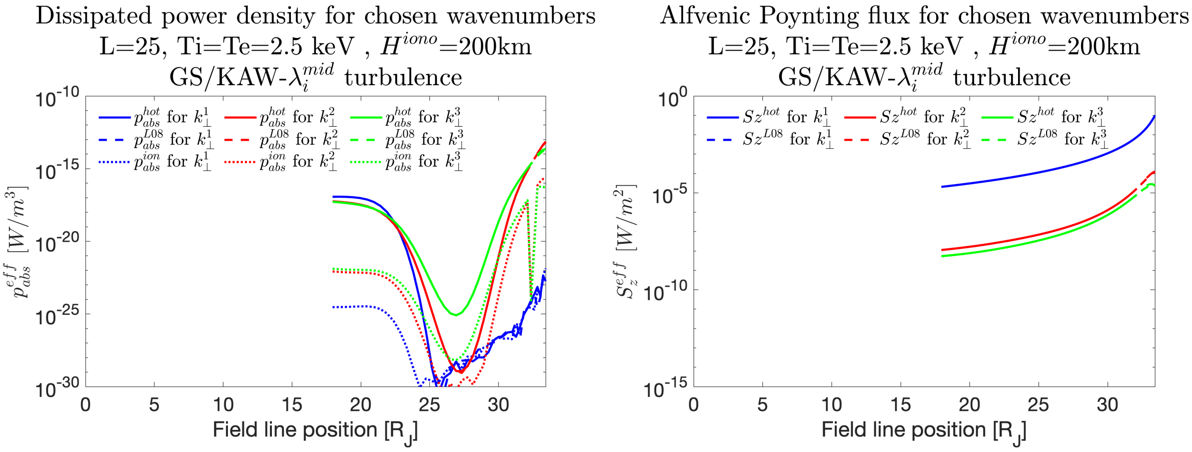

Figure 8.13.: *Dissipated power density along L=25 field line for mid-latitudinal turbulence generator for three chosen equatorial wavenumbers given in the caption of Figure 8.11. Solid and dashed lines represent the coinciding calculations based the hot and the Lysak solution (L08), respectively.*

too small to account for much stronger damping compared to equatorially launched waves. The undamped magnetic fluctuation amplitude controls the amount of dissipated power and does not require highly efficient damping with $\gamma/\omega_r \sim 1$. Thus, residual and undamped magnetic fluctuations, provided in Figure 8.11(right), are nearly coincident. Based on our analysis, we merely increase the wave dissipation at high latitudes by shifting the generator location deeper into the inertial Alfvén regime. Consequently, the dissipated power in the auroral region is insensitive towards changes of the turbulence generator in this regime and we do not need to further investigate this aspect.

Additionally, the parallel wave scales from the mid-latitudinal generator location reveal shorter parallel scales at high latitudes in the spectral range of maximum power dissipation than the corresponding weak turbulent waves (cf. Figure 6.1(right) from Chapter 6.1). This effect strengthens the parallel KAW electric fields as well. From Figure 8.12(right) we can extract a peak effective parallel electric field of $9 \cdot 10^{-5}$ V/m, which corresponds to characteristic heated electrons on the order of 6.5 keV. Thus, this electric field is a factor of 15 stronger than discussed for the weak equatorial turbulence case in Section 8.1.2. The difference comes mainly due to the increased ionospheric scale height of $H = 4200\,\mathrm{km}$ discussed previously. The corresponding maximum dissipated power density from Figure 8.13(left) is also increased to $7 \cdot 10^{14}\,\mathrm{W/m^3}$ at high latitudes and coincides with the Lysak based solution. Consequently, electron Landau damping is the major dissipation process.

Contributions to dissipation due to ion Landau damping are shown as dotted lines in Figure 8.13(left). Similarly to the investigated equatorial case, the contributions to ion Landau damping show a similar reduction by two orders of magnitude with respect to the electron contribution at high latitudes. The corresponding power density transfer to the ions peaks at $2 \cdot 10^{-16}\,\mathrm{W/m^3}$. Thus, ion Landau damping only plays a minor role for the auroral power input.

Now, we shortly discuss the Poynting flux carried by the Alfvén waves. In the right panel of Figure 8.13, the effective parallel Alfvénic Poynting flux (cf. *Lysak and Song* (2003))

$$S_z^{eff} = \frac{1}{2\mu_0} Re(\delta E_x^* \delta B_y) \tag{8.8}$$

is presented for three wave scales. Towards smaller waves scales, the contributions shrink as expected from the quadratic magnetic fluctuation dependency. Thus, the largest wave scale effectively determines how much energy flux is transported through a cross section. Towards higher latitudes, the transported energy flux rises as a result of power conservation in the converging magnetic field geometry. The Poynting flux peaks at $0.1\,\mathrm{W/m^2}$ above the ionosphere for the largest scale. This value corresponds to the estimate from *Saur et al.* (2018b) and is on the same order as the observations from *Gershman et al.* (2019) and *Mauk et al.* (2017c). The authors reported characteristic fluxes of 0.08 - $0.1\,\mathrm{W/m^2}$. Our estimate for the mid-latitudinal magnetic fluctuation amplitude is based on the developed power conserving expression from equation (4.13). Thus, the *Saur et al.* (2018b) estimate gives a similar result as we also considered $\delta B^{eq} = 5\,\mathrm{nT}$ in the equatorial region for the mapping.

8.3. Comparison to L-shells of 20 and 30

Up to now, we considered an L-shell of 25 for the Alfvénic dynamics. In this section, we are interested to examine the efficiency of wave-particle interaction at high latitudes for the bounding L-shells of 20 and 30 which map to the main auroral region as well. We compare their strengths and take conclusion for the calculation of total dissipated power in the whole acceleration region.

The overall dispersive and dissipative properties of the Alfvén wave remain the same for other L-shells. Major changes concern the length of the respective field lines and changed plasma parameters in the plasma sheet region like increased temperatures towards larger equatorial distances and decreased background magnetic field strength and density. For the middle magnetosphere, the parameter combination causes a decrease of the Alfvén velocity towards larger radial distances. A more significant difference is the magnetic field fluctuation amplitude which maximizes at L=25 and is reduced at both other locations in our model. These changes affect the resulting wave scales and amplitudes at high latitudes as ratios of equatorial to high-latitudes values for density and magnetic field dictates the potential energization.

In Figure 8.14, we compare the parallel electric fields of small-scale monochromatic KAW due to weak equatorial turbulence along the different L-shells for both temperature cases.

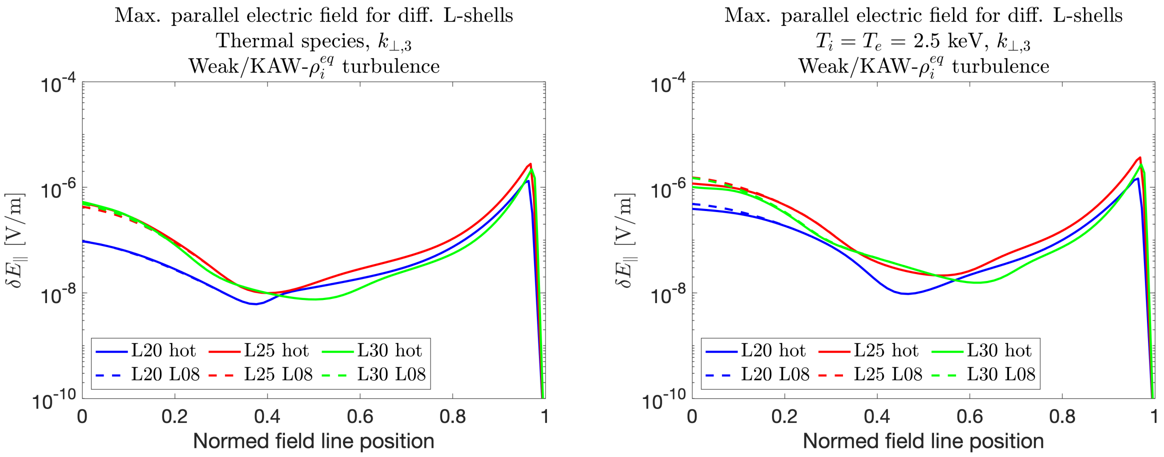

Figure 8.14.: *Maximum effective parallel electric field along the different L-shells (lengths normed to one) based on thermal species (left) and hot species(right). The respective wave scales are* $k^{eq}_{\perp,L=20} = [0.35, 0.4]\frac{2\pi}{\rho_i^{eq}}$, $k^{eq}_{\perp,L=25} = [0.55, 0.55]\frac{2\pi}{\rho_i^{eq}}$ *and* $k^{eq}_{\perp,L=30} = [0.6, 0.63]\frac{2\pi}{\rho_i^{eq}}$. *The first number denotes the wave scale for the thermal species, the second for the hot one.*

We choose the perpendicular wave scales such that their respective dissipation approximately maximizes close to Jupiter. The weaker field in the equatorially warm Alfvén regime for L=20 (blue line) is caused by the corresponding choice of the equatorial wavenumber as it allows for some variability in the high latitude region to maximize the power density (see flat spectra in Figure 8.10). We see that the peak electric field for all field lines are on a similar level within a factor of 2. For L=30, its peak value is closer to the maximum from L=25 than for L=20.

The reason is that the density contrast and background magnetic field contrast between the equator and the high latitudes is slightly larger for L=30 due the equatorial variability of the plasma parameters. Thus, positions further out can balance the effect from the difference in equatorial magnetic fluctuation amplitude of $\delta B = 3\,\mathrm{nT}$ for L=30 to $\delta B = 5\,\mathrm{nT}$ for L=25 as used in our model (see Chapter 4.3). For L=20, we used a value of $3\,\mathrm{nT}$. Nonetheless, the fluctuation amplitude underlies some variability so that increases in δB are plausible. *Saur et al.* (2018b) consider a fluctuation amplitude of $\delta B = 5\,\mathrm{nT}$ for L=20, which would increase our electric field value towards the values of the other L-shells. We obtain same effect for the dissipated power in Figure 8.15, where δB enters quadratically. Also the extent of the acceleration region shows a similar behavior for the three field lines. The extent of the acceleration region is important to determine the total dissipated power of the KAWs, which is transferred towards auroral particles. The root cause that the acceleration region seems shorter for L=30 lies in the normalized field line presentation. Here, the acceleration region takes a smaller portion with respect to its total field line extent than for the other field lines. The situation is equivalent for turbulence outside the plasma sheet (not presented).

In summary, we conclude that considering the L-shell of 25 as representative for the middle magnetosphere is justified. This result allows us to approximate the total amount of power transferred to the auroral particles (see Chapter 8.5) by neglecting the latitudinal variation due to different field lines.

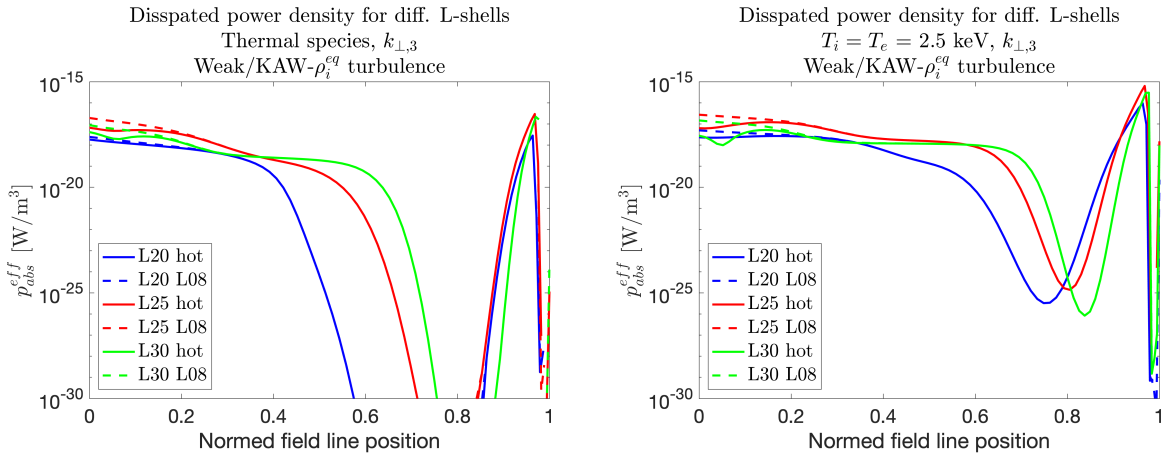

Figure 8.15.: *Maximum power dissipation along the different L-shells (lengths normed to one) based on thermal species (left) and hot species(right). The respective wave scales are* $k^{eq}_{\perp,L=20} = [0.35, 0.4]\frac{2\pi}{\rho_i^{eq}}$, $k^{eq}_{\perp,L=25} = [0.55, 0.55]\frac{2\pi}{\rho_i^{eq}}$ *and* $k^{eq}_{\perp,L=30} = [0.6, 0.63]\frac{2\pi}{\rho_i^{eq}}$. *The first number denotes the wave scale for the thermal species, the second for the hot one.*

8.4. Particle heating rates due to kinetic Alfvén waves

We are interested in evaluating the efficiency of particle acceleration by estimating the energy per unit time particles obtain through effective heating by monochromatic kinetic Alfvén waves in a unit volume. Similar to *Saur* (2004), we can estimate the heating rate from the dissipated power density $p^e_{abs} = ne\Delta T^e_\parallel/\tau$ using the ideal gas law as

$$\frac{\Delta T^e_\parallel}{\tau} = \frac{p^e_{abs}}{e\,n}. \tag{8.9}$$

Here, $\Delta T^e_\parallel$ describes the increase in electron energy in units of eV during the interaction time τ in the volume element of concern. The elementary charge is denoted by e and n is the electron density. In Figure 8.16, we show the parallel heating rates of electrons (equation 8.9) and equivalently ions for different wave scales along the L=25 field line.

From comparison of parallel and perpendicular heating rates, we can see that the ions are only heated on the order of the electrons in the plasma sheet. At high latitudes, perpendicular ion heating is negligibly small and parallel ion heating is at least two orders of magnitude weaker than for electrons. Parallel electron heating in the high latitude region gives the most significant amount with a heating rate of 11 eV/s. This value is too small to heat electrons in the acceleration region towards energies of 10 - 50 keV, such as estimated in literature to account for auroral emissions (*Bhardwaj and Gladstone*, 2000; *Clarke et al.*, 2004). The reason lies in the density considered in equation 8.9. Resonant Landau damping is a wave-particle interaction mechanism which acts only locally in velocity space around the phase velocity. Consequently, the energy provided by the wave is transferred only to a small subset of electrons with number density δn_e. Similar to the derivation of the hot dielectric tensor from Chapter 3.4, this perturbed density can be expressed by the zero-order velocity moment of the perturbed electron distribution function δf_e as

$$\delta n_e = \int d\vec{v}\delta f_e\,. \tag{8.10}$$

As this approach comprises a lengthy derivation and also requires a numerical treatment, we are interested in a simpler way to address this issue. Our approach to estimate the perturbed electron number density δn_e is to calculate a differential electron number density around the phase velocity. We piecewise integrate the Maxwellian distribution of the electrons in a segment with velocities smaller and larger than the phase speed of the wave at the wave scale $k_\perp$ of strongest heating efficiency. We then consider the differential number density to be effectively heated by Landau damping. The related expression reads

$$\delta n_e \approx \int_{v_{ph}-\Delta v}^{v_{ph}} f_0^e dv_\parallel - \int_{v_{ph}}^{v_{ph}+\Delta v} f_0^e dv_\parallel \tag{8.11}$$

$$= \frac{n_0}{2}\left[2 \cdot \mathrm{erf}\left(\frac{v_{ph}}{v_{th,e}}\right) - \mathrm{erf}\left(\frac{v_{ph}-\Delta v}{v_{th,e}}\right) - \mathrm{erf}\left(\frac{v_{ph}+\Delta v}{v_{th,e}}\right)\right]. \tag{8.12}$$

Here, $\mathrm{erf}(x) = \frac{2}{\sqrt{\pi}}\int_0^x e^{-t^2}dt$ denotes the error function and f_0^e is the Maxwellian distribution for electrons with thermal speed $v_{th,e}$. Integrating over the whole Maxwellian distribution gives the total number density n_0. For simplicity, we consider our derived result of maximum damping in Chapter 3.5.4 for a phase velocity of $v_{ph} = \sqrt{\frac{3}{2}}v_{th,e}$ in the inertial Alfvén regime. Furthermore, we assume a resonance width of $\pm\Delta v = 0.05v_{ph}$ for particles to be involved in the damping process. We receive a subset electron number density of $\delta n_e = 1.2 \cdot 10^{-3} n_0$. For $\Delta v = 0.01v_{ph}$ and $\Delta v = 0.1v_{ph}$, we obtain $\delta n_e = 4.6 \cdot 10^{-5} n_0$ and $\delta n_e = 4.6 \cdot 10^{-3} n_0$, respectively. Thus, for $\Delta v = 0.05v_{ph}$, around 0.1% of the available particles are effectively heated. From the inverse density dependency in equation 8.9, we see that the heating rate for the related electrons increases by a factor of 1000 towards 11 keV/s, which is on the order of the expectation. But still, this estimate is sensitive to a change in resonance width Δv. We suppose that the duration of the interaction will determine the portion of the affected electrons.

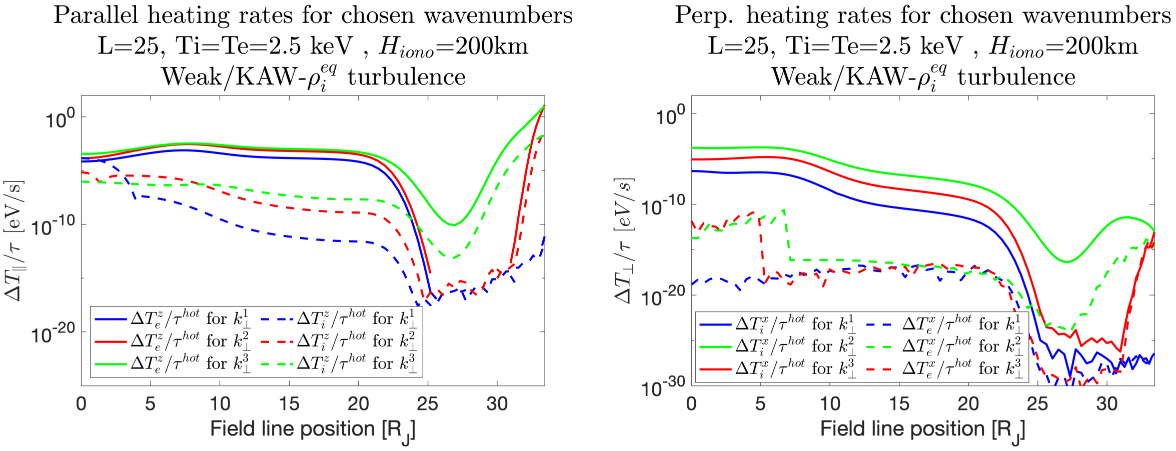

Figure 8.16.: *Local parallel (left) and perpendicular (right) heating rates for ions and electrons along the L=25 field line based on the field line density model from Chapter 4.1 with an ionospheric scale height of 200 km.*

In the high latitude region, the interaction time is very short due to the large wave speed, whereas in the plasma sheet, waves propagate at a slower speed. Thus, energy can be distributed towards a larger portion of particles in the plasma sheet, which significantly reduces the heating there towards values presented in Figure 8.16. *Saur* (2004) comes up with a heating rate of $2 \cdot 10^{-2}$ eV/s for L=21 in the plasma sheet considering the whole ion population. The plasma sheet heating rates in Figure 8.16 do not reflect the maximum potential in this region as we concentrate on waves that are able to propagate towards the high latitudes. Consequently, our heating rates are smaller than the estimate from *Saur* (2004) in the equatorial region.

Focusing again on the high latitudes, if we consider an electron travel time of $\tau_e = \frac{1R_J}{v_{th,e}} = 2.4\,\mathrm{s}$ for $T_e = 2.5\,\mathrm{keV}$ in this region, we obtain a heating temperature of $\Delta T_e = 26\,\mathrm{keV}$ as a rough estimate. From the estimate based on the effective electric field in Section 8.2, we obtained a smaller value of $\Delta T_e = 6.5\,\mathrm{keV}$. These energies are on the order of the expectation for electrons needed to account for the main auroral emissions, i.e., 10 - 50 keV. We like to mention that this estimate requires that the single electrons have to leave the wave and precipitate onto the atmosphere before the wave phase reverses. Due to the wave's oscillatory nature, the electric field decelerates electrons again during the other wave phase and lose their increase in momentum (*Hess et al.*, 2010). For the ions we are not able to estimate an improved heating rate with the approach developed above. The ion thermal velocity is much smaller than for the electrons due to the difference in mass, so that the resonance is located on the tail of the ion distribution function. This range is associated with a very weak gradient. Hence, we expect that only a very small portion of the high-latitude protons will be involved in ion Landau damping.

8.5. Estimation of total auroral input power

In this section we are finally interested in estimating the overall power that is available for auroral heating based on Alfvénic turbulence. From the analyses in the previous sections, we found that the ionospheric scale height and the electron temperature have strong influence on the calculation of the dissipated power density in the acceleration region above Jupiter. Thus, we take care for the different cases and compare their results. We also discuss these estimates regarding their relevance to account for the observed powers.

Table 8.1.: *Compilation of maximum dissipated powers* p_{abs}^{max} *above Jupiter for thermal and hot plasma species based on the investigated turbulence generators for an L-shell of 25. We considered different ionospheric scale heights H.*

$\mathbf{p_{abs}^{max}}$ [W/m^3]	thermal		hot	
L=25	H=4200 km	H=200 km	H=4200 km	H=200 km
Weak/KAW-ρ_i^{eq}	$2.7{\cdot}10^{-17}$	$2.6{\cdot}10^{-15}$	$5.7{\cdot}10^{-16}$	$3.9{\cdot}10^{-14}$
Strong/KAW-λ_i^{mid}	$2.4{\cdot}10^{-16}$	$2.1{\cdot}10^{-14}$	$1.7{\cdot}10^{-15}$	$6.7{\cdot}10^{-14}$

To keep our estimate of the total dissipated power simple, we assume that KAWs from the neighboring field lines transfer equivalent amounts of wave energy to the electrons. This assumption is supported by the analysis carried out in Section 8.3. In Table 8.1, we summarize the peak power densities dissipated by monochromatic KAWs from our analysis in the previous sections. The values consider the power dissipated at the respective locations of strongest wave dissipation for both scale heights and both, the hot and thermal particle species. Motivated by our modeling studies, we suggest the acceleration region to have a short extension of $1\,R_J$. *Cowley and Bunce* (2001) considered an extended region of 3 - 4 R_J in their modelings based on a quasi-static nature of main emissions. This length characterizes the dissipation volume required for the power calculation according to $P_{abs} = \int p_{abs} dV_{diss}$ in units of Watt [W]. For simplicity, we approximate p_{abs} to be constant to get an impression of the maximum expectable input power, i.e., $P_{abs} \approx p_{abs} V_{diss}$.

In the case of equatorial turbulence with the thermal species and large scale height, we estimate the auroral input power to be $3 \cdot 10^9$ W. This power is too small to account for the observed UV auroral emissions on the order of $[3 - 10] \cdot 10^{12}$ W (*Saur et al.*, 2003). Additionally, we need to be aware that only some fraction of the total input power is converted into light emissions. *Cowley and Bunce* (2001) assume a conversion efficiency of 20 % to drive UV aurora, which results in a necessary power input of $[1.5-5] \cdot 10^{13}$ W. Even in the shortest scale height case, monochromatic kinetic Alfvén waves only provide a power of $2.9 \cdot 10^{11}$ W for the electrons. Likewise, KAWs due to turbulence outside the plasma sheet does not transfer enough power either. For the hot electron species in the beneficial case of the small scale height, this turbulence' generated KAW dissipate $7.8 \cdot 10^{12}$ W. This value is at least on the order of the required power. An equatorially launched wave again provides a factor of 1.8 weaker power. These numbers highlight the fact that monochromatic waves alone are not sufficient to power the auroral emissions with our idealized calculations.

So far, we did not consider yet that turbulence generates a spectrum of waves. These waves are not hindered to propagate towards the auroral region and similarly can contribute to heating. In Figure 8.10(left) of Section 8.1.7, we have already investigated the spectral behavior of the dissipated power density in the acceleration region. If we now include a wave spectrum in the discussion of the auroral heating process, we need to spectrally integrate over a range of wavenumbers to estimate the total dissipated energy flux. We consider a wavenumber range of $\frac{k_{\perp,2}\lambda_e - k_{\perp,1}\lambda_e}{k_{\perp,0}\lambda_e} = \frac{10-6}{0.24} = 16.6$ for the H=4200 km case, and $\frac{k_{\perp,2}\lambda_e - k_{\perp,1}\lambda_e}{k_{\perp,0}\lambda_e} = \frac{22-8}{0.72} = 19.4$ for H=200 km. For these ranges, we assume the spectra to be nearly constant, which simplifies the integration procedure to a simple multiplication. In the given interval ranges we also account for the rescaling of the magnetic fluctuation amplitudes introduced in Appendix B, which enters the integration of the power spectrum with the $\frac{1}{k_{\perp,0}}$ factor. $k_{\perp,0}$ represents the smallest wavenumber considered. The λ_e factors in the above ranges are included for convenience to directly read off the intervals from the spectra.

For weak equatorial turbulence we obtain a power input of $[0.6 - 8.4] \cdot 10^{13}$ W for the thermal and hot electrons in case of H=200 km, for turbulence outside the plasma sheet even $[4.5 - 14] \cdot 10^{13}$ W. For the large scale height case of H=4200 km, the largest input energy of is found to be $3 \cdot 10^{12}$ W for the hot electron species in case of turbulence outside the plasma sheet. From these estimates, we consider both turbulence generators as potential drivers for auroral heating. Our calculations also show, besides the importance to consider wave spectra, the sensitivity of the estimates on the density profile above the ionosphere. It affects the extent of the acceleration region and the maximum dissipated power density. We consider an ionospheric scale height of 800 km, as also plotted in Figure 8.10, to still result in significant contributions for hot electrons. Consequently, temporally variable magnetospheric conditions and also asymmetries with effects on 1) the ionospheric extent and generally the density in the acceleration region, 2) the generated wave scales during the turbulence cascade process, and 3) the local magnetic field strength, can sensitively control the heating conditions above Jupiter. Addititionally, we see that a heated hot electron species results in larger input powers than for thermal electrons by an order of magnitude. Thus, it will be also interesting to study the wave dissipation due to a dilute keV-MeV interacting electron species as routinely observed in auroral region (cf. Chapter 2). Our previous analysis on ion Landau damping instead does not suggest protons to control the energetics of the main emissions. We like to note, that still some ions might be heated and account for rare events of bi-directional flows observed by Juno.

In Chapter 10, we provide an extended summary of the results obtained in the course of the various modeling studies in this chapter. Based on these findings and the assumptions made in this thesis, we highlight aspects relevant for future studies.

CHAPTER 9

Wave-particle interactions in the Io flux tube

In this chapter, we analyze the energetics and acceleration processes in the Io flux tube based on turbulent Alfvén waves. We adapt the knowledge we gained in the analysis of the middle magnetosphere (Chapter 8) and compactly discuss relevant aspects for the Io flux tube. Moreover, we explicitly investigate heating of protons perpendicular to the local magnetic field as recently observed in the Io flux tube.

9.1. Energetics in the Io flux tube

Juno observations at high latitudes in the Io flux tube propose a turbulent nature of the Alfvénic fluctuations. In Chapter 5 we concluded that Alfvénic turbulence is a reasonable cause to control the energetics in the Io flux tube. Based on our findings, we now investigate the acceleration processes and related power transfer within the Io flux tube. Our procedure is similar to the analysis of resonant-wave particle interactions in the middle magnetosphere from Chapter 8.

In our previous analysis of the power dissipation due to kinetic Alfvén waves along main auroral field lines, we highlighted its sensitivity to the density and electron temperature in the acceleration region. Thus, we like to start with some comments on the density model used for the Io flux tube. In Figure 9.1(left), we show the density model from *Su et al.* (2006) together with the model applied by *Lysak and Song* (2020). The latter is similar to the one constructed for the middle magnetosphere in our analysis (see Chapter 4.1). The major differences concern the ionospheric scale height and the floor density value outside the Io torus region. The model from *Su et al.* (2006) has a floor density of $1.6 \cdot 10^6\, m^{-3}$, which is a factor of 160 larger than our density value. Due to the lack of data in the dilute region of the Io flux tube, it is hard to elaborate on realistic densities. With Io as a massive source of plasma, it is reasonable that plenty of electrons and ions can populate along the flux tube, which makes larger densities more likely outside the torus region than in the middle magnetosphere. However, also the temperatures of the single species and related pressures will play a role in the distribution of particles along the field line. The thermal temperatures of the bulk species are considered to be significantly lower than in the middle magnetosphere.

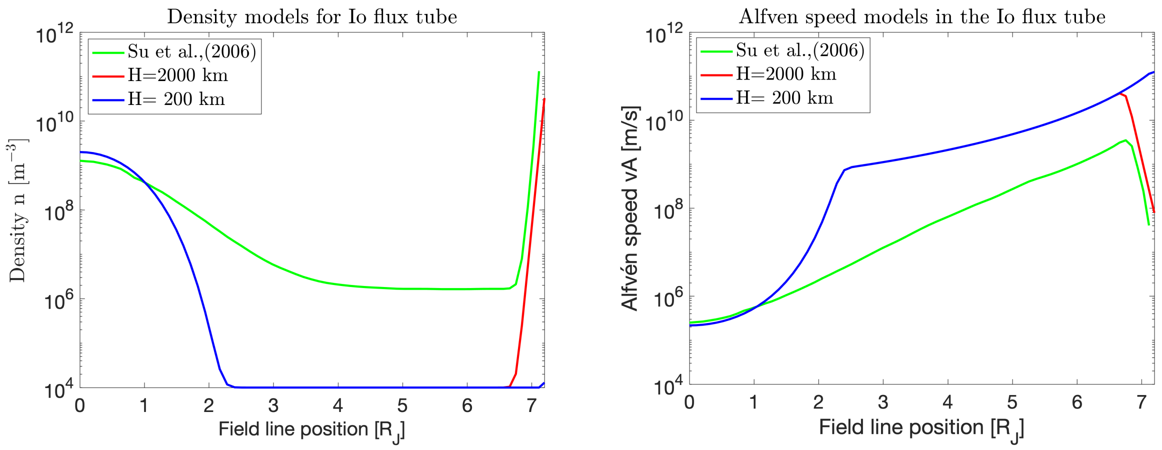

Figure 9.1.: *Density (left) and Alfvén speed (right) model along the Io flux tube. The Su et al. (2006) model has a density floor value of* $1.6 \cdot 10^{6}\ m^{-3}$ *and an ionospheric scale height of 2000 km. Our model has a density floor value of* $10^{4}\ m^{-3}$*, plotted for scale heights of 200 km and 2000 km.*

Su et al. (2003) also studied the effect of secondary electrons from Jupiter's auroral atmosphere (*McNutt et al.* (1990); *Ajello et al.* (2001)) on the resulting density profile along the field lines based on their static Vlasov description. For a sufficient strong secondary electron density, an auroral density cavity is formed above the ionosphere, where only a dilute hot electron species is present. In this region, with an extent of $R_J/2$ in their model, the density drops by more than one order of magnitude compared to the ambient region. *Ray et al.* (2009) produced a similar modeling result and a cavity density as low as our $10^{4}\,\mathrm{m}^{-3}$. Such a localized depletion of particles above the ionosphere strongly supports significant wave dissipation and ultimately strong electron fluxes. This region is still not well investigated enough owing to the survey designs of past spacecraft missions. With the ongoing Juno mission, such models will successively be built in the future at least for regions close for Jupiter. Thus, density profiles still rely on model assumptions so far. The ionospheric scale height for the *Su et al.* (2006) model is 2000 km, which is larger than used by *Hess et al.* (2010)(H=1142 km) or proposed by *Kotsiaros et al.* (2020)(H=200 km).

The final aspect in which the density models from Figure 9.1 deviate from each other concerns the transition from the torus boundary to the high latitudes. For the *Su et al.* (2006) model, the transition is much smoother and hence the torus region is more extended compared to the other model. It is clear that a strong density contrast, and consequently a short gradient length scale, strongly influences the validity of the so-called WKB assumption. The WKB assumption allows us to track the evolution of the wave properties in terms of local dispersion relations as long as the phase velocity changes slowly over scales of a wavelength. In the opposite case, when the parallel wavelength is much larger than the variation in Alfvén speed, the wave will undergo reflection processes, by which only a portion of wave energy is transmitted (*Deift and Goertz*, 1973). As a result, large portions of large-scale wave energy gets trapped within the torus region (*Hess et al.*, 2010). In the framework of equatorial Alfvénic turbulence, such counter propagating wave packages can non-linearly interact with each other and establish a wave energy cascade process towards smaller scales. These small-scale waves are able to escape the torus boundary and reach the high latitudes. For auroral particle heating processes, we consider the different transitions of the torus boundary density profile not to be directly relevant for the investigation of Landau damping as intense wave-particle interactions occur on local scales. As we do

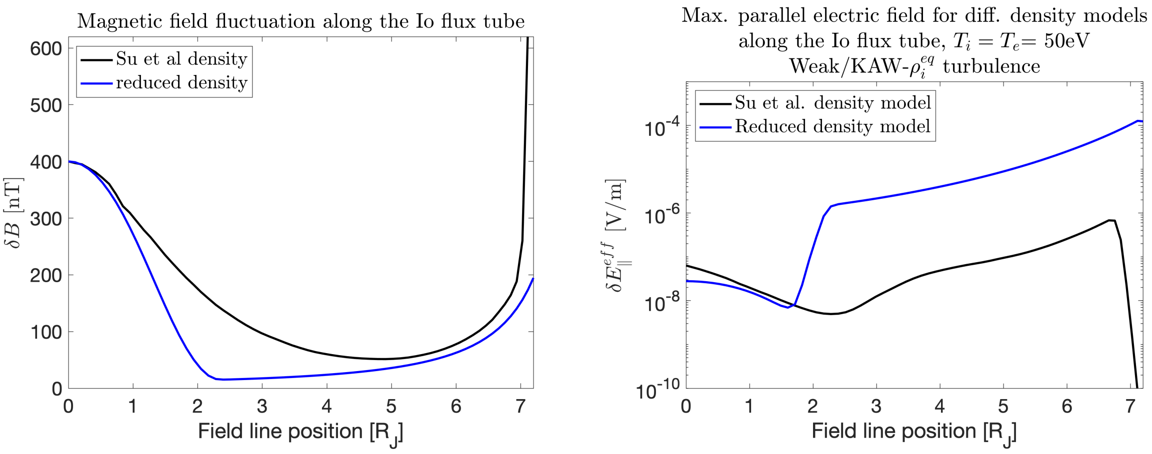

Figure 9.2.: *Large-scale Magnetic fluctuation (left) and maximal parallel electric field (right) along the Io flux tube based on the Su et al. (2006) density model and our reduced density model. The electric fields considers fluctuation ampltiudes of $\delta B^{hl}(k_{\perp,3}) = (0.2\,,\,2.1)\,nT$ for the Su et al. (2006) and the other model (using $H = 200\,km$), respectively.*

not quantitatively consider wave reflection within this thesis, the steepness of the torus boundary transition is not our prime interest.

The Alfvén speed profile and the magnetic fluctuation amplitude are directly affected by a change in density. Whereas the torus profiles for the Alfvén speed $v_A = B/\sqrt{\mu_0 m_i n}$ are similar in Figure 9.1(right), the reduced density in the inertial regime leads to an order of magnitude larger Alfvén speeds. As outlined in Chapter 8.1.2, based on this quantity we can infer the location of strongest dissipation. This location is also controlled by the ionospheric scale height, which shifts the maximum Alfvén speed position closer to Jupiter. Thereby dissipation increases due to the increase in magnetic field strength.

In Figure 9.2(left), we display the large-scale magnetic field fluctuation amplitude model developed in Chapter 4.3 for both density models with $\delta B^{eq} = 400\,\mathrm{nT}$. The slight deviations in the fluctuation amplitude between both density models in the region s=5 - 6.7 R_J arise from a small increase in background dipole magnetic field used by *Su et al.* (2006) compared to ours. The moderate increase in both fluctuation amplitudes in this region originates from the increase in background magnetic field towards Jupiter. The followed strong increase in amplitude towards the ionosphere comes from the significant drop in Alfvén speed as a consequence of strongly increasing density. For our model, we did not fully resolve this region as it requires a fine sampling of local solutions. We modeled solutions towards the location of maximal Alfvén speed in case of the minimal ionospheric scale height of H= 200 km. As we can see from the parallel electric field based on the *Su et al.* (2006) density model in Figure 9.2(right), the strong increase in magnetic fluctuation after the point of v_A =max. (left panel) is not sufficient to maintain a significant electric field amplitude. From the comparison, we conclude that a reduced density supports strong electric fields up to $10^{-4}\,V/m$. It also increases the electron inertial length λ_e by a factor of 12 and facilitates intense wave-particle interaction at larger wave scales.

In Figures 9.3 and 9.4, we compare the spectral dispersion and dissipation properties of kinetic Alfvén waves based on weak MHD-ρ_i^{eq} turbulence for both density models. From the strong increase in the electron inertial length around s= 2 R_J, we can see that the transition towards the inertial regime is shifted by one Jupiter radius towards the plasma sheet. This highlights the importance of electron interaction with the kinetic Alfvén wave along major

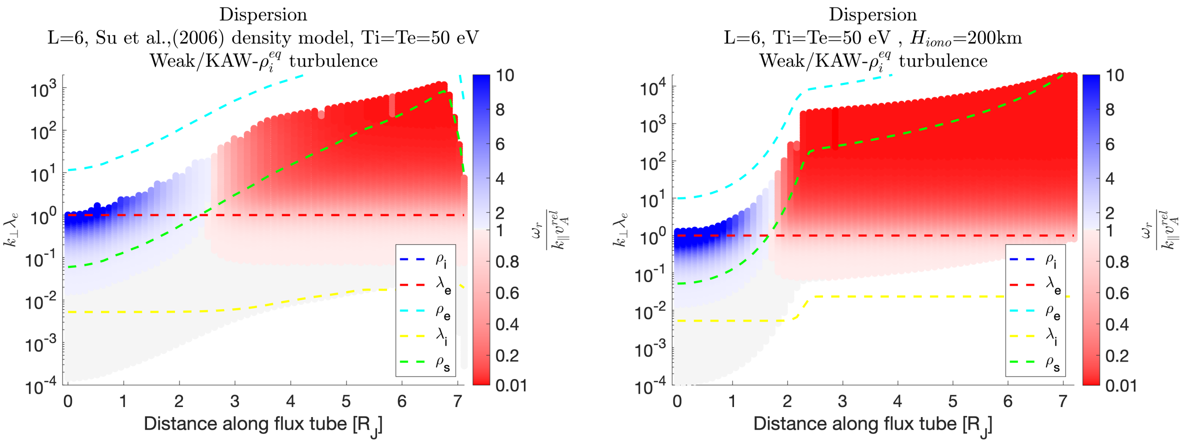
Dispersion
L=6, Su et al.,(2006) density model, Ti=Te=50 eV
Weak/KAW-ρ_i^{eq} turbulence

Dispersion
L=6, Ti=Te=50 eV , H_{iono}=200km
Weak/KAW-ρ_i^{eq} turbulence

Figure 9.3.: *Weak-MHD and kinetic equatorial turbulence spectral plot of dispersion along the Io flux tube (L=6) based the density model from Su et al. (2006) (left) and a density model with the reduced floor density a smaller ionospheric scale height (right). Small distances along the flux tube indicates the Io torus region, whereas large distances correspond to the high latitude region of Jupiter. The dashed lines represent the local plasma scales at its* $1/(2\pi)$*-value to illustrate the connection between the onset of dispersion and plasma scales. We consider the ion gyro- and acoustic radii (*ρ_i*,* ρ_s*), the ion and electron inertial length (*λ_i*,*λ_e*) and the electron gyroradius* ρ_e*. The non-coinciding representation is a result of the deviating local electron inertial length scales used as reference scale.*

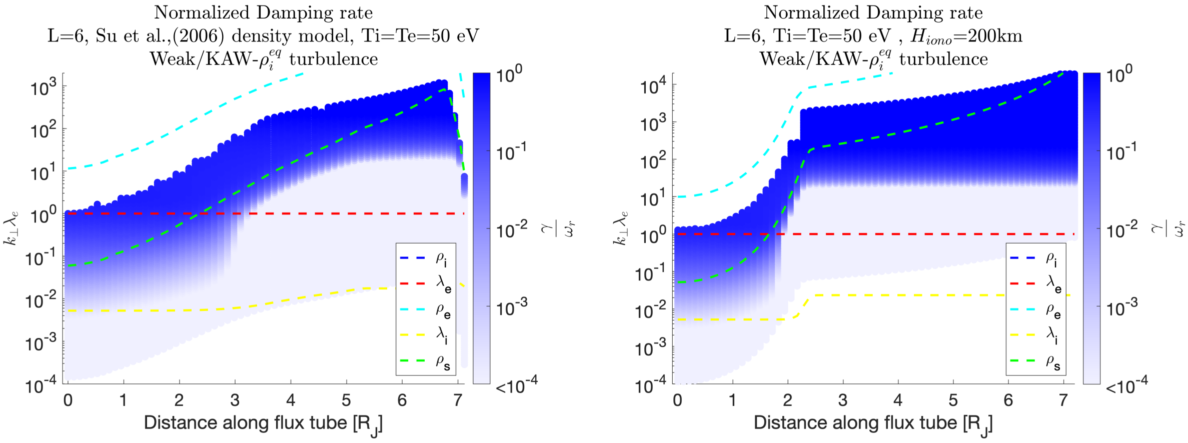
Normalized Damping rate
L=6, Su et al.,(2006) density model, Ti=Te=50 eV
Weak/KAW-ρ_i^{eq} turbulence

Normalized Damping rate
L=6, Ti=Te=50 eV , H_{iono}=200km
Weak/KAW-ρ_i^{eq} turbulence

Figure 9.4.: *Weak and kinetic equatorial turbulence spectral plots of dissipation along the Io flux tube for the same density models as in the dispersion plots from Figure 9.3.*

parts of the Io flux tube and reduces damping in the torus region. Consequently, more wave energy can be transported to the high latitudes. Even in the high density case, the inertial regime is still more extended than the warm Alfvén regime. A further consequence of a reduced density is that a larger fraction of the considered wave scales, i.e., $k_\perp^{eq} = [\frac{2\pi}{3.6R_{Io}} - \frac{2\pi}{\rho_i^{eq}}]$ for weak equatorial turbulence, lies in the regime in which damping is significant in the high latitudes. This aspect is shown further below.

The damping rates reveal that inertial damping generally becomes important only for perpendicular wavenumbers larger than $k_\perp \lambda_e > 20$ for the presented case of $T_e = 50\,eV$. We would like to point out that similar to the middle magnetospheric analysis, the electron temperature significantly controls the wave-particle interaction. This statistically allows more particles to be accelerated by Landau damping. In the literature, also hotter electron

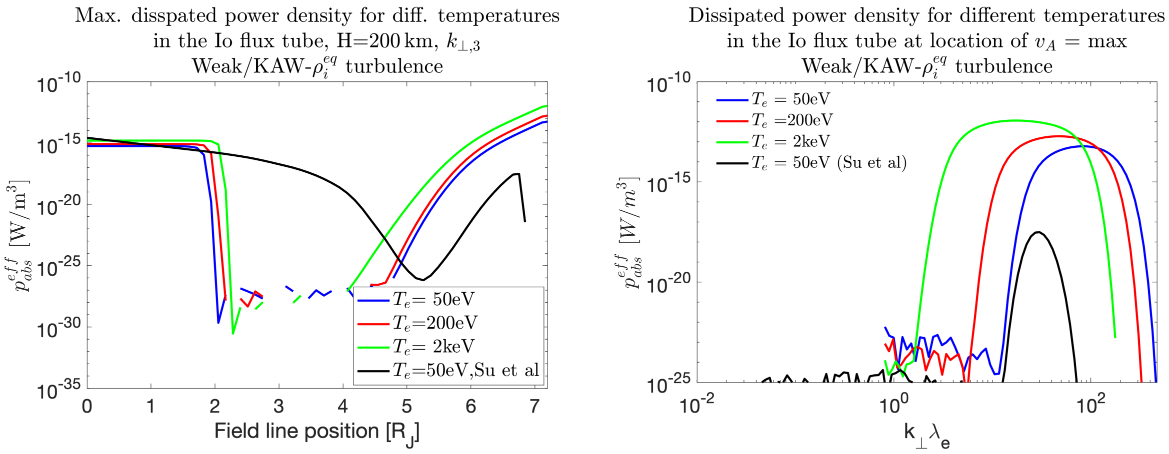

Figure 9.5.: *Left: Maximal dissipated power density along the Io flux tube for different temperatures based on the hot solutions. The corresponding equatorial perpendicular wave scales are* $k_{\perp,3} = 0.26\frac{2\pi}{\rho_i^{eq}}$ *for the Su et al. (2006) density model and* $k_{\perp,3} = 0.18\frac{1}{\rho_i^{eq}}$ *for the remaining models. The black line indicates the the dissipated power density for Su et al. (2006) model. Right: Resulting spectral distribution of dissipated power density at the respective locations of maximal dissipation.*

populations were observed during the Voyager epoch. For example *Dougherty et al.* (2017), *Scudder et al.* (1981) and *Sittler and Strobel* (1987) reported on hot electron populations in the torus region with $T_e = 200\,\text{eV}$. The temperature of $T_e = 50\,\text{eV}$ as considered by *Su et al.* (2006) is more representative of a thermal bulk electron species. Hence, we investigate the dissipated wave power dependence on temperature.

In Figure 9.5, we present the maximum dissipated power density p_{abs} for three different temperatures. From the left panel, the maximal dissipated power density in the acceleration region ranges between $[0.8 - 10] \cdot 10^{-13}\,\text{W/m}^3$. As expected, larger temperatures are associated with increased damping. Interestingly, even for the low electron temperature case of 50 eV, we generate power densities larger than calculated for the main auroral acceleration region. The main driver for this difference is the strongly increased magnetic fluctuation amplitude in the Io flux tube compared to the middle magnetosphere. Even if we consider an Io-related fluctuation amplitude of $\delta B^{eq} = 100\,\text{nT}$, the generated power densities (a factor of 16 smaller) still compensate the reduced heating efficiency in the Io flux tube as a consequence of a low electron temperature compared to the main auroral field lines.

Weak equatorial Alfvénic turbulence lead to heating in the Io torus region with dissipated power densities around $10^{-15}\,\text{W/m}^3$. From comparison with the result based on the *Su et al.* (2006) density model (black line), we can see that the region of damping gets extended and a more gradual transition towards the dilute region occurs. At high latitudes, the corresponding peak dissipated power density of $5 \cdot 10^{-18}\,\text{W/m}^3$ is negligible compared to the other models. This underpins the importance of the existence of an auroral density cavity above the ionosphere as discussed earlier. The wave dissipation is also sensitive to the location of the acceleration region to benefit from Jupiter's strong magnetic field similar to the main emission region.

In the right panel of Figure 9.5, we plot the spectral distribution of the dissipated power density at the location of strongest damping in the high latitude region based on the hot dispersion relation. The dissipation is effectively driven by electron Landau damping coin-

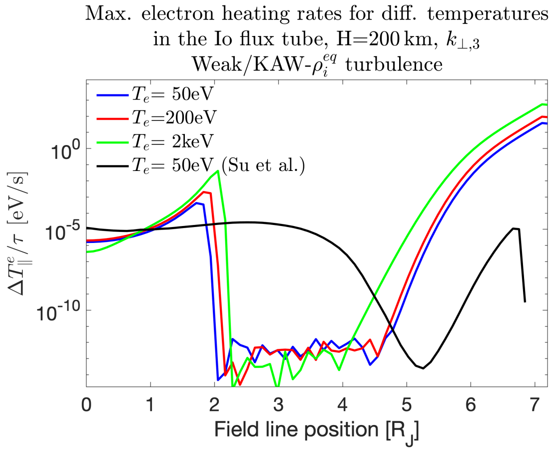

Figure 9.6.: *Parallel electron heating rates along the Io flux tube for different temperatures. The corresponding equatorial perpendicular wave scales are* $k_{\perp,3} = 0.26\frac{2\pi}{\rho_i^{eq}}$ *for the Su et al. (2006) density model and* $k_{\perp,3} = 0.18\frac{1}{\rho_i^{eq}}$ *for the remaining models. The black line indicates the damping rate based on the Su et al. (2006) density model.*

---

ciding with the *Lysak* (2008) based solution, which is not presented here for convenience. As anticipated, larger electron temperatures lead to an onset of strong power transfer at larger waves scales and also increase the maximum damping. However, the spectral width of strongest damping increases for smaller temperatures. For the hot electron species, the width (values above $10^{-14}\,\mathrm{W/m^3}$) ranges between $k_\perp\lambda_e = [3 - 100]$, for T_e=200 eV it is $k_\perp\lambda_e = [12 - 150]$, and for T_e=50 eV the corresponding width is $k_\perp\lambda_e = [30 - 200]$. The total power transferred towards the particles is discussed below.

Comparing the electron heating rates $\Delta T_{\|}^{e}/\tau$ in Figure 9.6 based on equation 8.9, we obtain an equivalent situation as expected for the dissipated powers. In the plasma sheet, the heating rates for the constructed density model increase towards rates of $3\cdot10^{-4} - 3\cdot10^{-2}\,\mathrm{eV/s}$ as a consequence of the successively reducing density towards the torus boundary at $2\,R_J$. The result based on the smooth density model from *Su et al.* (2006) does not exhibit this peak. However, due to the damping in the transition region, the region of heating is more extended than for the other density profile. The role of a lower density for the heating rate becomes clear at high latitudes, where $\Delta T_{\|}^{e}$ peaks at [40 - 500] eV/s for the different temperatures. These values are five to six orders of magnitude larger than for the *Su et al.* (2006) based heating rate. Nonetheless, as explained in Chapter 8.4, Landau damping acts locally in velocity space. Consequently, the heating rates underestimate the true ones as the released power gets distributed among fewer particles than considered. With an effective density of $\delta n_e = 0.002n$ similar to Chapter 8.4, we obtain maximum electron heating rates on the order of [20 - 250] keV/s. These values are larger than for the main emissions because of the increased magnetic fluctuation amplitude (see Chapter 8.4).

Now, we like to discuss the role of ion Landau damping in the acceleration region. In Figure 9.7, we show the spectral contributions to dissipation from ion and electron Landau damping above Jupiter based on equation (3.76). We consider a large temperature of $T_i = T_e = 2\,\mathrm{keV}$. As can be seen, the field-aligned ion contribution exhibits a sign reversal similar to the discussion in Chapter 7.3. The dashed-lined contribution counteracts damping at larger scales, even though much weaker than the dissipation contribution due to electron Landau damping. We only consider the solid-lined ion contribution to be physically

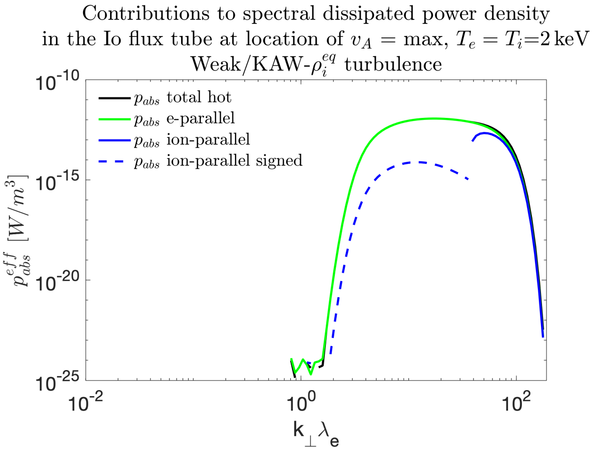

Figure 9.7.: *Contributions from ion and electron Landau damping to spectral dissipated power density at the location of maximal dissipation in the high latitudes.*

reasonable. Ions are much heavier than electrons and, consequently, the wave resonance speed lies on the tail of the ion Maxwellian distribution function. Only on the smallest wave scales, i.e., $k_\perp \lambda_e^{hl} > 40$, the resonant wave phase speed moves towards the ion thermal speed as a result of wave dispersion and allows for ion Landau damping. Unfortunately, we cannot display ion contributions along the field line for such scales, as the ion contribution is numerically unstable along the field line. Nonetheless, we expect ion Landau to play a minor role in auroral heating. From the given plot, we can extract a peak dissipation value of $p_{abs} = 2 \cdot 10^{-13}\,\mathrm{W/m^3}$, which is already an order of magnitude smaller than for the electrons. Furthermore, the corresponding spectral width is much smaller compared to the electrons. For ion temperatures smaller than 2 keV, the contribution is shifted to even smaller wave scales. At these scales, total powers will be negligible to effectively contribute to the auroral energy budget. This finding is in accordance with Juno observations, which only show rare events of bi-directional pitch-angle distributions of energetic protons (*Mauk et al.*, 2018).

Now, we shortly discuss the turbulence generator outside the Io torus. Based on our analysis in Chapter 5, we consider strong-MHD and KAW turbulence for modeling. In Figure 9.8, the dissipated power density for a plasma temperature of 200 eV is displayed for three wavenumbers similar to the presentation in Chapter 8. As a consequence of the turbulence generator location outside the Io torus, kinetic Alfvén waves can dissipate more energy than for equatorial turbulence. Furthermore, the largest parallel scales are initially constrained towards the length of field line extent outside the torus. Thus, the turbulent waves develop shorter scales at high latitudes than for equatorial turbulence, which is advantageous for the strength of the parallel electric field. With the choice of the dilute density model, the ion inertial length λ_i^{mid} is so large, that the majority of the wave spectrum is driven by KAW-turbulence, in contrast to equatorial turbulence. But even in the analysis with the *Su et al.* (2006) density model in Chapter 5, we have already concluded that sub-ion kinetic turbulence accounts for major parts of the spectrum. Although associated magnetic fluctuations are smaller on small wave scales than for equatorial turbulence due to the increased spectral index of $\alpha^{KAW} = -7/3$, a generator outside the torus can locally dissipate up to $p_{abs} = 10^{-12}\,\mathrm{W/m^3}$ in the high latitude region.

Now we turn to the quantification of total electron input energy flux available for the Io footprint emissions. Similar to the main auroral region, we spectrally integrate the absorbed power densities over a wavenumber band associated with the strongest energy

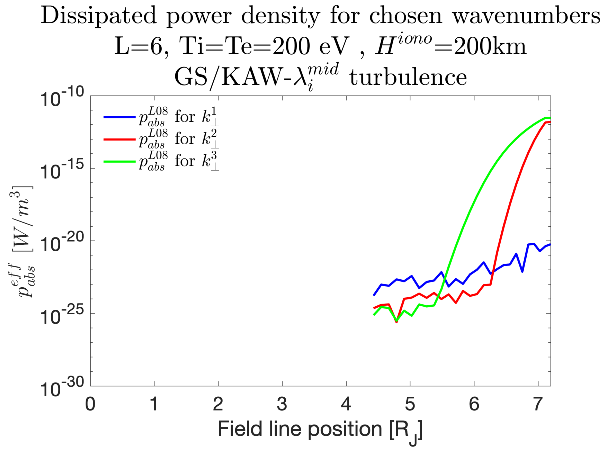

Figure 9.8.: *Dissipated power density along the Io flux tube for mid-latitudinal turbulence generator for three chosen wavenumbers:* $k_{\perp,1}^{mid} = \frac{2\pi}{\lambda_i^{mid}}$, $k_{\perp,2}^{mid} = 0.4\frac{2\pi}{\lambda_e^{mid}}$ *and* $k_{\perp,3}^{mid} = 0.7\frac{2\pi}{\lambda_e^{mid}}$.

transfer to get a rough estimate for the total power. For the power densities, we consider $p_{abs} = [7{\cdot}10^{-14}, 2{\cdot}10^{-13}, 10^{-12}]\,\mathrm{W/m^3}$ for $T_e = [50, 200, 2000]\,eV$, respectively. To spectrally integrate, we consider the rescaled narrow widths of $\frac{k_{\perp,2}\lambda_e - k_{\perp,1}\lambda_e}{k_{\perp,0}\lambda_e}|_{T_e=50\,eV} = \frac{200-50}{0.81} = 185.2$, $\frac{k_{\perp,2}\lambda_e - k_{\perp,1}\lambda_e}{k_{\perp,0}\lambda_e}|_{T_e=200\,eV} = \frac{90-25}{0.81} = 80.2$ and $\frac{k_{\perp,2}\lambda_e - k_{\perp,1}\lambda_e}{k_{\perp,0}\lambda_e}|_{T_e=2\,keV} = \frac{32-25}{0.81} = 8.6$. These have been extracted from Figure 9.5(right). Integration over a dissipation volume of $1.3 \cdot 10^{21}\,\mathrm{m}^3$ with a parallel extent of the acceleration region of $0.5\,R_J$, we obtain total input powers of P $= [1.7, 2.1, 5.1] \cdot 10^{10}$ W for increasing electron temperature. In the case of KAW turbulence outside the torus for the $T_e = 200\,\mathrm{eV}$ species, we obtain a factor of 3.2 larger estimate of $6.7 \cdot 10^{10}$ W. These results are on order of values established in the literature. *Hess et al.* (2010) reported on required input energies of P $\approx 10^{10}$ W and also *Saur et al.* (2013) gave a range of $[4 - 300] \cdot 10^9$ W derived from observations in FUV range. Variations in intensity are associated with Io's position within the periodical plasma sheet motion in the tilted ambient magnetic field.

Conditions for the effectiveness of damping are relaxed if shorter parallel wave scales are involved in the wave-particle interaction process. For a reduced interaction strength of $\bar{\alpha} = 0.5$ in the case of weak turbulence at Io, the smallest parallel wavenumber $k_\parallel$ increases by a factor of 5. This shorter constraining scale imprints on the whole turbulence spectrum and maps to the wave field at high latitudes and modifies the efficiency of power transfer with a quadratic dependency over $\delta E_\parallel$. The available wave energy also depends on reflection properties, which can be as high as 50 % at maximum for large scales according to *Hess et al.* (2010). However, small-scale waves are less affected by this effect.

For the *Su et al.* (2006) density model, the scaling factor for the spectral power integration is significantly smaller with $k_{\perp,0}\lambda_e = 0.04$ at high latitudes due to the weaker magnetic field at the further out located maximum Alfvén speed (larger ionospheric scale height). However, we only obtain a total power dissipation of $7 \cdot 10^5$ W in the acceleration region. Consequently, available turbulent energy goes into heating of the plasma sheet for this density model. This aspect is visible in Figure 9.9, which shows the KAW damping rates for both density models and different temperatures. When the damping rate maximizes at high latitudes for the *Su et al.* (2006) model, the corresponding damping rate in the Io torus region is already two orders of magnitude stronger compared to the other damping rates. Thus, dissipation in the acceleration region for the previous model can only occur at the smallest scales for which energy is already used to heat the equatorial region.

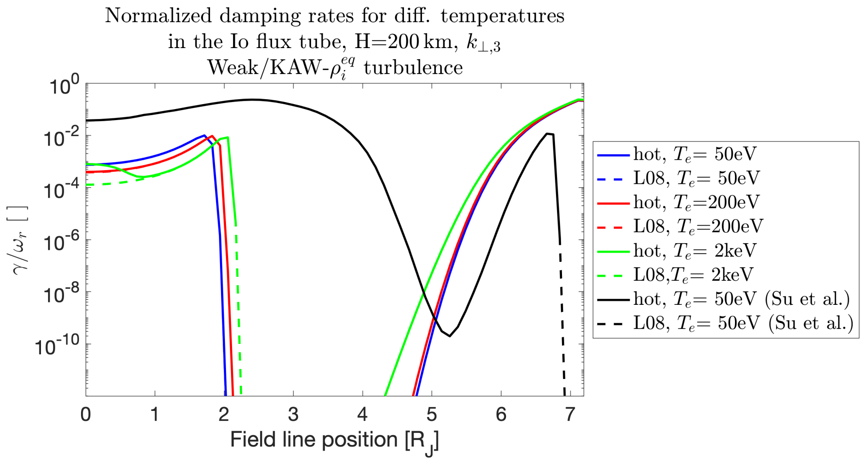

Figure 9.9.: *Normalized damping rates along the Io flux tube for different temperatures. Solid lines show the damping rate due to the hot plasma dispersion relation, dashed lines for the reduced Lysak (2008) model (L08). The corresponding equatorial perpendicular wave scales are* $k_{\perp,3} = 0.26\frac{2\pi}{\rho_i^{eq}}$ *for the Su et al. (2006) density model and* $k_{\perp,3} = 0.18\frac{1}{\rho_i^{eq}}$ *for the remaining models. The black lines indicates the damping rates based on the Su et al. (2006) density model.*

This result highlights the necessity of an ionospheric scale height smaller than H = 4200 km in combination with the presence of a density cavity. Also hot electron wave-particle interaction is most likely responsible for the observed emissions. From our calculations, we furthermore expect proton Landau damping to play a minor role as the corresponding spectral range most likely is much narrower than this for the corresponding electrons.

9.2. Non-resonant perpendicular ion heating

In this section, we finally like to investigate perpendicular ion heating in the Io flux tube. During several Juno crossings, heated proton populations were observed by the JADE and JEDI instrument on-board of Juno. *Szalay et al.* (2020a) reported on an upward proton population in JADE data with energies of 0.3 - 0.6 keV and associated energy flux of 0.5 - 2 mW/m^2. They concluded that its acceleration region is located about 0.9 - 2.5 R_J above Jupiter. After the heating phase, these particles moved towards Juno conserving the first adiabatic moment. Consequently, field-aligned acceleration would generate populations restrained to small pitch angles. Thus, it is thought that a perpendicular heating mechanism is responsible for these proton populations. Additional high-energetic Juno/JEDI observations in this region from *Clark et al.* (2020) reveal an upward proton population with energies around 50 keV - 1 MeV concentrated along the loss cone. These particles carry an energy flux of 10 - 100 mW/m^2.

From our analysis in the previous chapters, we did not find strong evidence for the significance of perpendicular ion heating due to resonant cyclotron damping with Alfvén waves at high latitudes. Similar to the main auroral acceleration region (see Figure 8.16(right) in Chapter 8.4), we obtain proton heating rates of $\Delta T_\perp/\tau \sim 10^{-11}$ eV/s. Of course, we expect the heating rate to be stronger as only a low amount of protons is able to go into cyclotron resonance. As explained, we are not able to adequately quantify the involved density. Moreover, this process happens only on the smallest wave scales. These waves are most likely already damped due to efficient electron Landau damping during propagation in the Io flux tube. Furthermore, these waves are associated with small amplitudes so

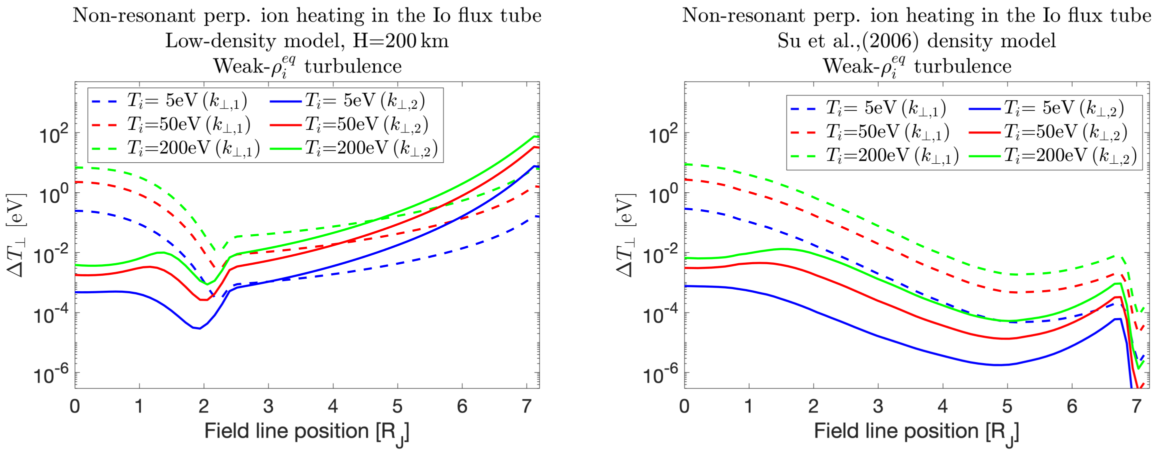

Figure 9.10.: *Non-resonant perpendicular ion heating according to Lu and Li (2007) in the Io flux tube based on equatorial weak-MHD turbulence with* $\delta B^{eq} = 100\,nT$*. We consider two chosen non-dispersive equatorial wavenumbers for modeling:* $k_{\perp,1}^{eq} = \frac{2\pi}{3.6R_{Io}}$ *and* $k_{\perp,2}^{eq} = \frac{1}{4}\frac{1}{\rho_i^{eq}}$*.*

that efficient damping does not lead to strong energy transfer anymore. Besides resonant wave-particle interaction with Alfvén waves and ion cyclotron waves, *Clark et al.* (2020) suggested a non-resonant Alfvén wave heating mechanism from *Lu and Li* (2007). This mechanism has been introduced in Chapter 3.6 and we apply it in the following.

In contrast to the resonant interaction, this perpendicular heating process is based on MHD Alfvén waves. Thus, we will quantify the heating for non-dispersive wave scales. We consider equatorially launched monochromatic Alfvén waves, which are damped on their way to Jupiter. The large-scale magnetic fluctuation amplitude is chosen to be $\delta B^{eq} = 100\,\text{nT}$. Similar to the resonant damping case from equation (8.1), we take non-resonant damping of the magnetic fluctuation amplitude into account according to the expression

$$\delta\hat{B}(s,k_\perp) = \delta B(s,k_\perp^{min}) \left(\frac{k_\perp}{k_\perp^{min}}\right)^{\alpha/2} exp\left(-\int_{s=eq}^{s} \frac{d\tilde{s}}{2\tau(\tilde{s})v_{A,rel}(\tilde{s})}\right). \tag{9.1}$$

Here, $\tau = \frac{\pi}{k_\parallel v_{th,i}}$ characterizes the time on which the heating process saturates and $v_{A,rel}(s)$ is the local Alfvén speed. In Figure 9.10, we present the heating $\Delta T_\perp$ from equation (3.84) along the Io flux tube for two wavelengths and different temperatures. Calculations were carried out for both density profiles investigated in the previous section. Generally, large wavelengths (small $k_\perp$ and $k_\parallel$) are associated with increased turbulent magnetic fluctuation amplitudes, but the corresponding saturation time is larger. On the contrary, increased temperatures decrease the saturation time and make the heating more efficient as can be clearly seen from the modeling results. Whereas large wave scales are still favored for heating in the Io torus, at high latitudes smaller wavelengths are associated with heating. We can also identify that the lower density outside the torus significantly controls the heating in this regime as it inversely enters the heating expression. The decreased density is only slightly balanced by the associated reduced magnetic fluctuation amplitude (see Section 9.2), which also enters the heating expression quadratically.

The different populations are only heated to approximately their initial temperature at maximum in the low-dense case. Thus, we infer that only hot proton populations in a density cavity discussed in the previous section might be able to be locally heated sufficiently strong in order to account for the observed JADE observations from *Szalay et al.*

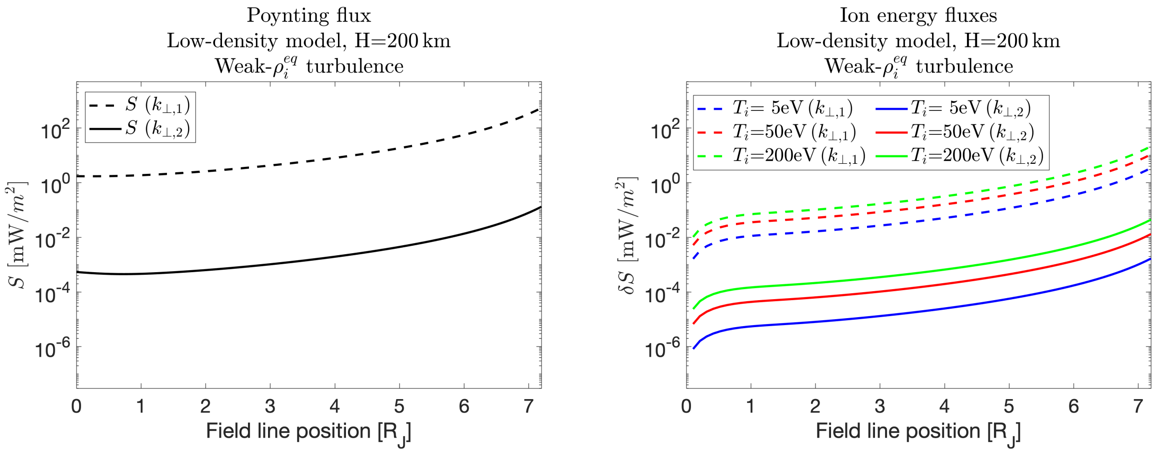

Figure 9.11.: *Poynting (left) and ion energy fluxes (right) for the same wave scales as used in Figure 9.10.*

(2020a). The particle energy fluxes for this species are on the order of $4 \cdot 10^{-2}$ mW/m^2, which can be seen in Figure 9.11(right). These are lower than those from the *Szalay et al.* (2020a) observations with the numbers given at the beginning of this section. Even though heating is weaker for large scales ($k_{\perp,1}$) in case of the low-density model at high latitudes, corresponding particle fluxes are still larger compared to the $k_{\perp,2}$-wave. This is explained by considering that at smaller wave scales less energy is available which can be converted into heating. Corresponding Alfvénic Poynting fluxes are shown in the left panel. Thus, only during burst events with $\delta B_{eq} = 400\,\mathrm{nT}$, related energy fluxes would be sufficient and also related would be increased. However, the heating mechanism from *Lu and Li* (2007) is not able to energize protons up the MeV energy range, which is associated with the populations from *Clark et al.* (2020). The presented study solely focused on monochromatic MHD Alfvén waves. As an outlook, it might be interesting to quantify non-resonant proton heating mechanism due to a spectrum of Alfvén waves such as proposed by *Wang et al.* (2006).

CHAPTER 10

Summary and future aspects

In this thesis, we investigated the relevance of Alfvénic turbulence and related wave-particle interaction processes for Jupiter's auroral emissions. Juno spacecraft observations at low-altitude regions above Jupiter connected to the Io flux tube and the main emissions provided strong hints on a dominating role of Alfvén waves in related particle energization processes. Besides bi-directional electron pitch-angle distributions, data prominently reveal broadband energy distributions for auroral electrons. Furthermore, low-frequency magnetic power spectra exhibit a power law-like behavior, which is indicative for wave turbulence. Using these and further system-related information, we characterized turbulence in these regions and examined the spectral dispersion and dissipation properties of associated kinetic Alfvén waves. Although the idea of Alfvénic turbulence in these regions is already discussed in literature, no concrete modeling studies on wave-particle interactions with propagating turbulent Alfvén waves in an inhomogeneous medium have been carried out so far.

Turbulence in the Io flux tube is established by the complex interaction of Io and the streaming torus plasma. Alfvénic perturbations are generated, which propagate along the magnetic field lines. Based on wave reflections at the Jovian ionosphere and at the Io torus boundary, an energy cascade process is established. By the related non-linear wave-wave interactions, wave energy is transported towards smaller spatial and temporal scales. The generated waves turn into kinetic Alfvén waves during their propagation in the inhomogeneous plasma environment. On kinetic scales of the plasma, the waves develop dispersive and dissipative properties and generate parallel electric fields, which allow for intense Landau damping. In the high-latitude region of Jupiter, we assume the kinetic Alfvén waves to significantly heat particles responsible for the Io footprint emissions. For the middle magnetosphere, i.e., radial distances of 20 - 30 Jupiter radii, non-continuous flux tube interchange motions are thought to be the generator of the observed Alfvénic turbulence in the plasma sheet. By similar reflection processes, we hypothesize kinetic Alfvén waves to efficiently generate auroral particle precipitation. Based on this notion, we investigated Alfvénic turbulence in both regions in greater detail.

In order to assess the nature of turbulence in both regions, we started with a basic characterization of the large-scale wave field. For the Io flux tube, we considered an equatorially extended region of $3.6\,R_{Io}$ to be representative for the largest perpendicular wave scale. This scale has shown to map well to the high latitude region crossed by Juno and connected to the Io footprint emissions considering dispersive effects on Alfvén waves. We took the plasma convection time past Io as reference for the estimate of the longest parallel wave scale generated by Io's local plasma interaction. These scales constrained the turbulence models, we applied in our further analyses. We investigated different generator locations regarding the nature of turbulence. We found that weak-MHD turbulence inside the Io torus and strong-MHD together with sub-ion kinetic Alfvén wave turbulence outside the Io torus are valiable candidates for a detailed examination. Based on a simple comparison of plasma convection time and crossing time of Juno through the Io flux tube tail, we inferred that the observed power spectral density is associated with the spatial Alfvénic wave field. This is in contrast to the basic assumption of a temporal variable wave field to be observed by Juno as assumed by *Gershman et al.* (2019) and *Sulaiman et al.* (2020). A detailed inspection of spatial and temporal scales associated with kinetic Alfvén waves supports our re-interpretation of the observed power spectral index to map towards perpendicular wavenumber. From the comparison of the observed and theoretical power spectral indices, and additional estimation of energy cascade fluxes, we showed that weak turbulence in the torus and KAW turbulence outside the torus further support the idea of Alfvénic turbulence in the Io flux tube. An analogous analysis carried out for middle magnetospheric field lines, connected to the main auroral emissions, revealed a similar situation. Here, estimates for the large scales defining the wave field were taken as 1 R_J for the perpendicular scale and the extent of the plasma sheet as characteristic for plasma sheet turbulence. Outside the torus, the field line extent between plasma sheet and the Jupiter ionosphere was taken as characteristic for the KAW turbulent wave field.

Based on this characterization of the wave fields, we investigated the spectral properties of kinetic Alfvén waves along field lines due to weak-MHD and KAW turbulence in both auroral systems. To do so, we constructed profiles for the relevant plasma parameters based on prior models from literature and associated observations. In this context, we developed a model for residual wave energy density along the magnetic field lines based on the electromagnetic Poynting theorem. We included dissipation processes from resonant and non-resonant wave-particle interaction in the model description. With this model, we implemented expressions for the perpendicular and parallel wave electric field components and corresponding particle responses, which depend on the magnetic fluctuation amplitude. Both quantities sensitively depend on the dispersive and dissipative properties of the wave. Modeling results confirmed that along auroral field lines both dispersive limits of the kinetic Alfvén wave are captured, known from theoretical considerations. Thus, a full description of the KAW properties, especially in the transition region, requires to solve a generalized dispersion relation such as the model from *Lysak* (2008) or the hot plasma dispersion relation. We applied both dispersion relations for plasma parameters found in the regions of concern. For a major range of these parameters, the solutions give coinciding results. Thus, we confirmed that electron Landau damping is the dominating dissipation mechanism in the Io flux tube and along main auroral field lines as well. We analytically showed that its onset is related to the acoustic length scale ρ_s and the electron inertial length scale λ_e, in the warm and cold Alfvén regime, respectively. On the basis of numerical modelings, we also found that the KAW exhibits strong electron Landau damping in the transition region as $v_{th,e} \simeq v_A^{rel}$. Even in the limiting case of balancing dispersive effects from electron pressure and inertia, the KAW seems to develop a parallel electric field.

Nonetheless, we found that other damping contributions are present as well. For perpendicular scales slightly smaller than the equatorial ion gyroradius, the KAW develops frequencies close to ion cyclotron frequency, which allows for cyclotron damping of heavy ions in the Io torus and plasma sheet. Towards larger radial distances, the cyclotron frequency decreases due to the weakening ambient magnetic field, and thus, might explain increasing ion temperatures in the plasma sheet as suggested by *Saur* (2004).

Ion Landau damping due to KAWs, which is only included in the description based on the hot plasma dispersion relation, is active on the smallest wave scales investigated in the context of this thesis. It only develops a major role in wave dissipation at larger wave scales for cases where the electron thermal velocity would be equal or smaller than the ion thermal velocity. For our investigated regions this means, that the ion temperature needs to be at least on the order of keV to play a role in wave-particle interaction. Thus, only at high latitudes, we expect ion Landau damping to be active, however on wave scales smaller than λ_e. In the equatorial region, we expect it to contribute for radial distances beyond an L-shell of 30 so far turbulence is present in this large-β_i region.

Based on this global characterization of the KAW properties, we quantified dissipation of monochromatic turbulent kinetic Alfvén waves propagating along the field lines. From our previous analysis, we considered the plasma sheet and the mid-latitudes as source regions of turbulence. To track the evolution of the wave magnetic and electric field fluctuations along the field lines, we considered the local dispersion solutions to be representative for the wave properties. This local approach requires the validity of the WKB approximation, which demands weak variations in the wave speed over a wavelength. Whereby this assumption is violated on large wave scales, on small more local scales, it is better justified. As we are interested in the dissipation characteristics of the KAW, we consider this local approach to result in reasonable estimates because wave damping was found to act on small wave scales.

We found that the strength of particle heating due to kinetic Alfvén waves at high latitudes depends on several aspects. From our prior analysis, we know that the smallest wave scales with $k_\perp \lambda_e > 1$ locally support strong damping on the order of $\gamma/\omega_r \simeq 1$ in this region. However, there are two effects which limits the amount of energy transferred to the particles. In the case of equatorial turbulence, small high latitude wave scales are associated with small wave scales in the plasma sheet. Consequently, for such scales, electron Landau damping and ion cyclotron damping in the plasma sheet have been proven to fully damp the propagating wave before reaching the high latitude region. Thus, no wave energy is left, which could be converted into particle energy. The second effect which limits the energy transfer concerns the magnetic fluctuation amplitude. Due to the power law-like distribution of the turbulent wave energy, small wave scales are related to smaller magnetic fluctuation amplitudes compared to larger scales. These amplitudes directly enter the electric field expressions and counteract the favored dispersive effects on their strengths. As a result, even though the damping rate predicts high efficiency of wave-particle interactions at smallest scales, less energy is transferred towards the particles. We figured out, that KAW turbulence with a source region outside the Io torus and the plasma sheet primarily suffer from this effect. In contrast to an equatorial source location, mid-latitude generated waves are not damped an smallest scales before reaching the acceleration region. However, their energy input on particles is not significantly larger than for the equatorial turbulence generator. We considered this trade-off between the damping rate and the fluctuation amplitude in our calculations by taking the absorbed power density into account.

We carried out parameter studies for a thermal ion and electron species with temperatures extracted from observations in the plasma sheet and a hot ion and electron species as commonly used at high latitudes, for both using the same density profile. As expected, larger temperatures lead to stronger energy transfer due to electron Landau damping. Additionally, we investigated whether a dilute but hot electron species is preferentially heated by

KAWs in the presence of a thermal bulk species. From derived analytic considerations for a multi-species plasma, we do not expect that the KAW damping rate will have a set on at a separate electron inertial length scale, which is much larger than for the bulk species. However, we could not validate this expectation based on the available single species dispersion relation solver code. Nonetheless, we validated that a reduced bulk density in the inertial Alfvén regime lead to stronger dissipation of wave energy. Furthermore, we identified a strong dependency of the dissipated power density on the density profile above the Jovian ionosphere. A short ionospheric scale height of 200 km shifts the location of maximal heating $\sim 1\,R_J$ closer towards Jupiter compared to a scale height of 4200 km, as taken from the study of *Su et al.* (2006). At this new location the background magnetic field is stronger. The related magnetic fluctuation amplitudes simultaneously increase, and thus, support stronger electric fields. We calculated a peak effective electric field strength of 10^{-4} V/m, which corresponds to a characteristic electron energy on the order of 6.5 keV. Based on a different approach over heating rates, we estimated a heating of 26 keV. These values are in a range required to drive UV auroral emissions. From comparison of weak equatorial turbulence and KAW turbulence outside the plasma sheet, we concluded that kinetic Alfvén waves, generated at the latter location, can drive more intense particle acceleration at high latitudes. Related maximum dissipated power densities at high latitudes from both turbulence generators are $[3.9\,,\,6.7]\cdot 10^{-14}$ Wm^{-3} for a 2.5 keV electron species.

Based on this prior analysis, we estimated total powers dissipated in the acceleration region. For a rough estimate, we considered the region for L=20 - 30 R_J to equally dissipate wave energy. By integrating over the dissipation volume and the spectral range of maximized dissipation, we calculated maximum auroral input powers of $8.4\cdot 10^{13}$ W and $13\cdot 10^{13}$ W for weak and KAW turbulence with their respective source regions, respectively. These estimates considered a hot electron species of T_e =2.5 keV and a ionospheric scale height of H=200 km. For thermal species, we got a factor of 3-14 reduced estimates. Also for an increased ionospheric scale height, input power is reduced. The derived estimates are sufficient to account for the main auroral emissions. The results also highlighted the strong impact of the electron temperature and the ionospheric scale height on the resulting auroral input power.

We also performed a similar analysis for Alfvénic turbulence in the Io flux tube. The wave properties along the flux tube revealed equivalent dispersion properties for KAWs as for the middle magnetosphere. In contrast to the main auroral field lines, temperatures of bulk species are considerably lower than for field lines in the middle magnetosphere, but the fluctuation amplitude is much stronger. These counteracting effects compensates each other so that the dissipated power density of monochromatic KAWs is not reduced, but even increased with values of $[0.7\,,\,2]\cdot 10^{-13}$ Wm^{-3}. We compared the power dissipation for the density model provided by *Su et al.* (2006) and a constructed model with a reduced density. The related powers clearly demand for a close-in located density cavity above the Io footprint to generate sufficient strong wave-particle interactions required for particle acceleration. In the low density case, we received a power of $7\cdot 10^{10}$ W, for the density model based on *Su et al.* (2006) only $7\cdot 10^{5}$ W.

Finally, we investigated perpendicular ion heating in the Io flux tube motivated by Juno/JADE and JEDI observations of heated proton populations from *Szalay et al.* (2020a) and *Clark et al.* (2020), respectively. We considered a non-resonant heating mechanism according to *Lu and Li* (2007). Our study revealed that only initially hot protons at high latitudes can be sufficiently heated in the presence of the density cavity. Even then, our modeling results can only explain the JADE observations. The much hotter JEDI observed proton species needs to be heated by a different mechanism.

Coming back to the objectives of this thesis from Chapter 2.6, we took first systematic steps to investigate Alfvénic turbulence in regions connected to the main auroral and the Io footprint emissions in more detail. Nonetheless, our analysis revealed aspects which needs to be addressed in the future studies.

10.1. Future developments

Theoretical studies are needed which focus on the development and evolution of turbulent wave fields in constrained inhomogeneous systems such as in the Jupiter magnetic field. In inhomogeneous media, we do not know how the energy is injected on large scales. The turbulence theories assume the energy supply on isotropic scales, which is not given for example in the case of the Io flux tube. Thus, we constrained the wavenumber relationships to physically reasonable scales by the introduction of anisotropy factors. It will be also of particular interest to investigate the effect of curved magnetic field lines on the evolution of the $k_{\|}/k_{\perp}$-ratio based on the deformation turbulent eddies experience. This ratio will have consequences for the strength of the parallel electric fields, and consequently, for the effectiveness of Landau damping. To stay in the context of turbulence, further observations in the investigated systems are needed to further constrain the turbulent properties. Such studies will help to discriminate and rule out turbulence theories with respect to their source location, involved wave frequencies, spectral breaks and spectral indices. Especially the investigation of the temporal dependency of the power spectral index in the dynamic Jupiter system will be beneficial. Also the influence of dissipation on the spectral index might be interesting to investigate for smaller wave scales.

Our analysis of the dissipation properties of KAWs and resulting power estimates stressed the necessity to consider a multi-component plasma. For its constituents, namely, thermal bulk and hot dilute ion and electron species, sophisticated density profiles are required with special attention to the ionospheric scale height and the potential presence of auroral cavities. With these profiles, the derived dispersion relation from equation (3.49) or the general hot plasma dispersion can be solved to model the wave properties. In this context, incorporation of the *Connerney et al.* (2018) higher order magnetic field description will be worth investigating. Deviations from the dipole field will locally influence the strength of wave dissipation. Consequently, we expect that asymmetry in the morphology of the main auroral emissions might be directly related to the longitudinal dependence of the Jovian magnetic field. Additionally, the influence of a current sheet magnetic field model on the dissipated power in the acceleration region is worth investigating regarding weak equatorial turbulence. A reduced equatorial magnetic field strength leads to shorter parallel and perpendicular wavelengths on dispersive scales at high latitudes. Thus, stronger parallel electric fields can be driven driven and account for stronger wave damping.

From our analysis, main auroral electrons are accelerated towards 6 - 26 keV at the high latitudes by KAWs. However, these energies are too low to explain the existence of highly energetic particles up MeV energies, as observed by the Juno/JEDI instrument (*Mauk et al.*, 2017b). Thus, wave-particle interaction with relativistic electrons will be valuable to investigate in more detail. We expect that Landau damping will set in at larger wave scales as more resonant particles are present compared to thermal species. In the relativistic framework, two effects modify the wave-particle interactions. On the one hand, the resonance condition is altered by the introduction of the Lorentz factor, by which the perpendicular particle velocity comes into play for cyclotron damping. On the other hand, a full relativistic framework needs to consider a modified distribution function. In the case of the Maxwellian distribution, the generalization is known as the Maxwell-Jüttner distribution (*Livadiotis*, 2016). The resulting distribution function exhibits a different shape than the corresponding classic Maxwellian, which affects the efficiency of Landau damping. Such considerations are relevant for electron energies larger than 200 keV as routinely observed by Juno/JEDI. The relativistic dielectric tensor is discussed for example in the books of *Brambilla* (1998) and *Swanson* (2008). The related dispersion relation is only numerically solvable such as done by *Verscharen et al.* (2018). Further considerations in this field of study are presented for example in *Lazar and Schlickeiser* (2006) and *Pétri and Kirk* (2007).

Generally, dispersion relations based on other distribution functions, such as the κ- distribution, will be interesting for hot species as well. *Gaelzer and Ziebell* (2014) and also *Khan et al.* (2019) derived dispersion relations for the kinetic Alfvén wave similar to *Lysak and Lotko* (1996) but based on κ-distributions. Further attention might be laid onto the evolution of the distribution function. Our calculations assumed that the background distribution function thermalizes sufficient fast after the wave-particle interaction process so that the next incoming wave can undergo the process with the same efficiency. Thus, there is no flattening of the distribution function around resonance. Such non-linear effects might alter the efficiency of the Landau interaction. These consideration, however, require a non-linear theory.

Finally, it will be important to consider reflection for the residual wave energy carried by propagating large-scale Alfvén wave. This will be of particular interest for the Io flux tube due to the significant gradient in Alfvén speed at the torus boundary (*Hess et al.*, 2010).

Appendix

A. Electromagnetic quantities, their units and constants

Table A.1.: *Used electromagnetic quantities and their units*

Symbol	Physical quantity	Unit
$\vec{E}$	Electric field	V/m
$\vec{D}$	Electric displacement field	As/m^2
$\vec{B}$	Magnetic induction	Vs/m^2
$\vec{H}$	Magnetic field	A/m
$\vec{j}$	electric current density	A/m^2
I	Electric current	A
ϱ	Electric charge density	As/m^3
c	$= 299792458\,\frac{\mathrm{m}}{\mathrm{s}}$: Speed of light	
k_B	$= 1.38 \cdot 10^{-23}\,\frac{\mathrm{J}}{\mathrm{K}}$: Boltzmann constant	
q_s	Electric charge for species s	As
e	$= 1.602 \cdot 10^{-19}\,\mathrm{C}$: elementary charge	
$\underline{\underline{\sigma}}$	Electric conductivity tensor	S/m
$\underline{\underline{\varepsilon}}$	(Relative) dielectric tensor	[ ]
ε_0	$= 8.854 \cdot 10^{-11}\,\frac{\mathrm{As}}{\mathrm{Vm}}$: free-space dielectric permittivity	
$\mu = \mu_0 \mu_r$	Magnetic permeability	Vs/Am
μ_0	$= 4\pi \cdot 10^{-7}\frac{\mathrm{Vs}}{\mathrm{Am}}$: free-space magnetic permeability	
μ_r	Relative magnetic permeability	[ ]
t	Time	s
f	Frequency	1/s
$\omega = 2\pi f$	Angular frequency	1/s

B. Representation of power spectra in the context of turbulence

We assume that the energy of the turbulent wave field is contained in the perpendicular wavenumbers $k_\perp$. The corresponding power spectral density P is given by

$$P(k_\perp) = P_0 \left(\frac{k_\perp}{k_{\perp,0}} \right)^\alpha , \tag{B.1}$$

where P and $P_0 = P(k_{\perp,0})$ are in units of $(nT)^2/k_\perp$ and $\alpha < -1$ denotes the spectral index of the turbulence model under consideration. The corresponding spectral magnetic field fluctuations can be expressed as

$$\delta B(k_\perp) = \delta B_0 \left(\frac{k_\perp}{k_{\perp,0}} \right)^{\alpha/2} , \tag{B.2}$$

where $\delta B_0 = \delta B(k_{\perp,0}) = \sqrt{P_0}$ is in units of $(nT)/\sqrt{k_\perp}$. Now we apply the Parseval theorem to relate the energy contained in the spectra to the physical space via

$$< \delta B(t)^2 >= \int_{k_{\perp,0}}^{k_{\perp,max}} P_0 \left(\frac{k_\perp}{k_{\perp,0}} \right)^\alpha dk_\perp = \frac{P_0 k_{\perp,0}}{|\alpha| - 1} k_{\perp,0}^{-(1+\alpha)} \left[\frac{1}{k_{\perp,0}^{-(\alpha+1)}} - \frac{1}{k_{\perp,max}^{-(\alpha+1)}} \right] \approx \frac{P_0 k_{\perp,0}}{|\alpha| - 1} \tag{B.3}$$

In the last step, we assumed that $k_{\perp,max} \gg k_{\perp,0}$. This has the consequence that the turbulent energy is concentrated in the largest scale. From this, we are motivated to reformulate the spectral fluctuation amplitude as

$$\delta \hat{B}(k_\perp) := \sqrt{P_0 k_{\perp,0}} \left(\frac{k_\perp}{k_{\perp,0}} \right)^{\alpha/2} , \tag{B.4}$$

where we use $P_0 k_{\perp,0} = (|\alpha| - 1) < \delta B(t)^2 >= k_{\perp,0} \delta B_0^2$ in units of $(nT)^2$ from the integral above. The inclusion of the spectral index α in the definition of our new amplitude is important to enable an energetically fair comparison of different turbulence models. Reason is that a weaker spectral decay such as for strong MHD turbulence ($\alpha = -5/3$) compared to weak turbulence ($\alpha = -2$) would lead to more spectral energy if the correction is neglected. With our definition, we also redefine the unit of our spectral fluctuation amplitude from $(nT)/\sqrt{k_\perp}$ towards nT. This is no problem as we only introduced a constant shift on the spectral amplitude with the inclusion of $k_{\perp,0}$. The advantage is that the spectral monochromatic amplitudes can be now interpreted as observable amplitudes. However, we need to care for this amplitude shift when we consider spectrally integrated quantities in order to conserve energy.

C. Further comparisons of frequency contributions for equatorial turbulence at L=20 and L=30

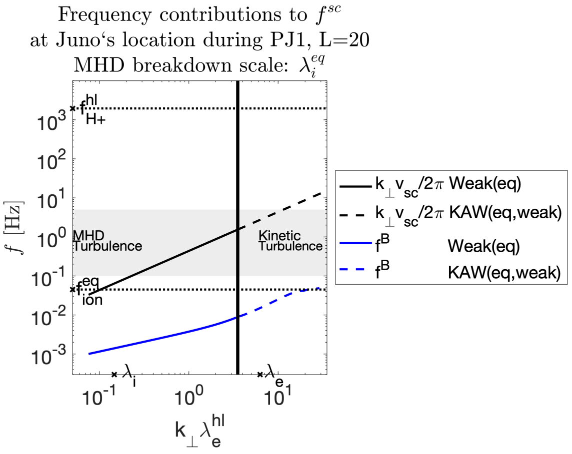
Frequency contributions to f^{sc} at Juno's location during PJ1, L=20 MHD breakdown scale: λ_i^{eq}

Frequency contributions to f^{sc} at Juno's location during PJ1, L=20 MHD breakdown scale: ρ_i^{eq}

Figure C.1.: *Doppler shifted frequencies (solid and black dashed lines) dominate over wave frequencies (blue lines) in the high latitudes for a L-shell of 20. Weak and KAW turbulence model results are shown for a MHD-breakdown scale model at* λ_i^{eq} *(left) and* ρ_i^{eq} *(right).*

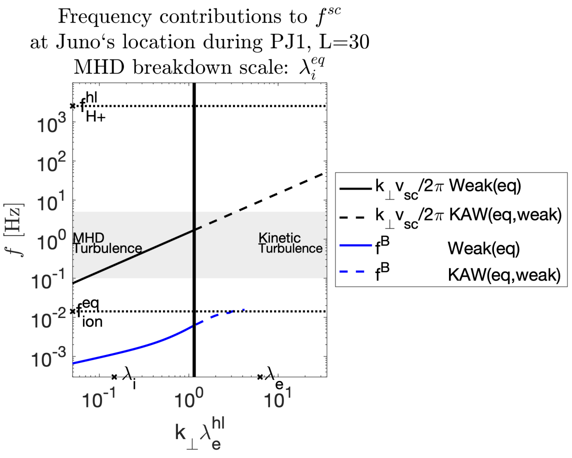
Frequency contributions to f^{sc} at Juno's location during PJ1, L=30 MHD breakdown scale: λ_i^{eq}

Frequency contributions to f^{sc} at Juno's location during PJ1, L=30 MHD breakdown scale: ρ_i^{eq}

Figure C.2.: *Doppler shifted frequencies (solid and black dashed lines) dominate over wave frequencies (blue lines) in the high latitudes for a L-shell of 30. Weak and KAW turbulence model results are shown for a MHD-breakdown scale model at* λ_i^{eq} *(left) and* ρ_i^{eq} *(right).*

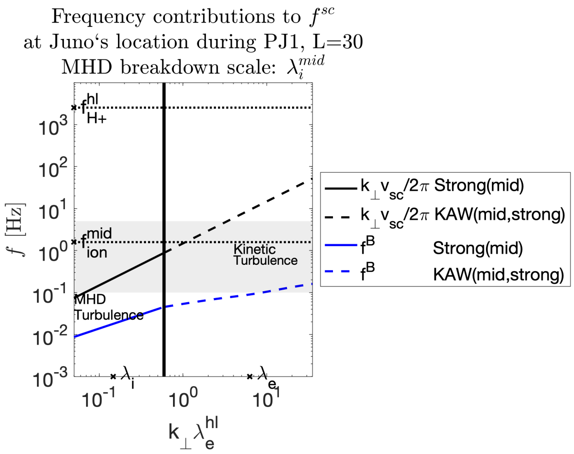

Figure C.3.: *Doppler shifted frequencies (solid and black dashed lines) dominate over wave frequencies (red lines) in the high latitudes due to for a L-shell of 30. Considered MHD-breakdown scale for the strong turbulence model is* λ_i^{mid}.

D. Further modelings for Chapter 7

In the following, we present modeling studies, which support our statements from Chapter 7 and serve as additional information for the analysis.

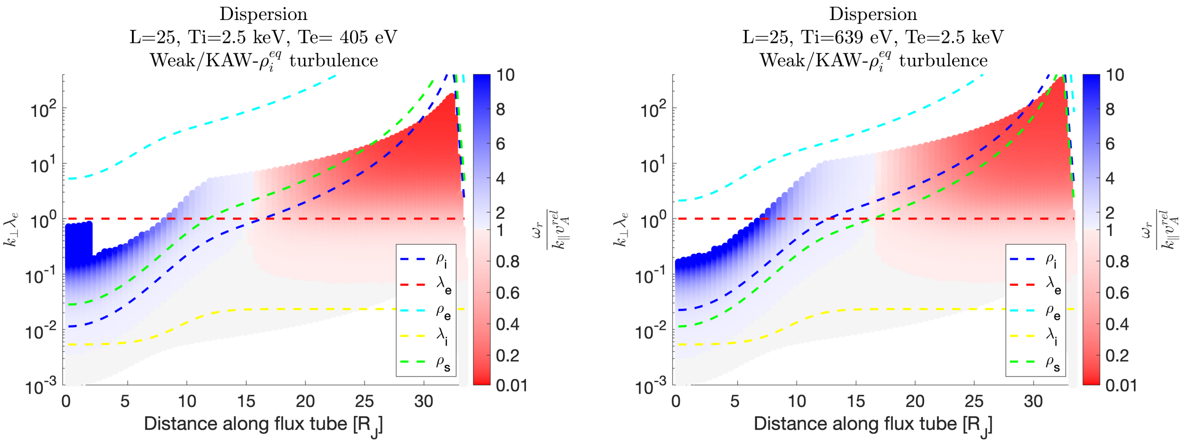

Figure D.1.: *Weak and kinetic equatorial turbulent spectral plots of dispersion for a thermal electron but hot ion species (left) and a hot electron but thermal ion species (right) along the L=25 field line in the middle magnetosphere. Local plasma scales are indicated by dashed lines.*

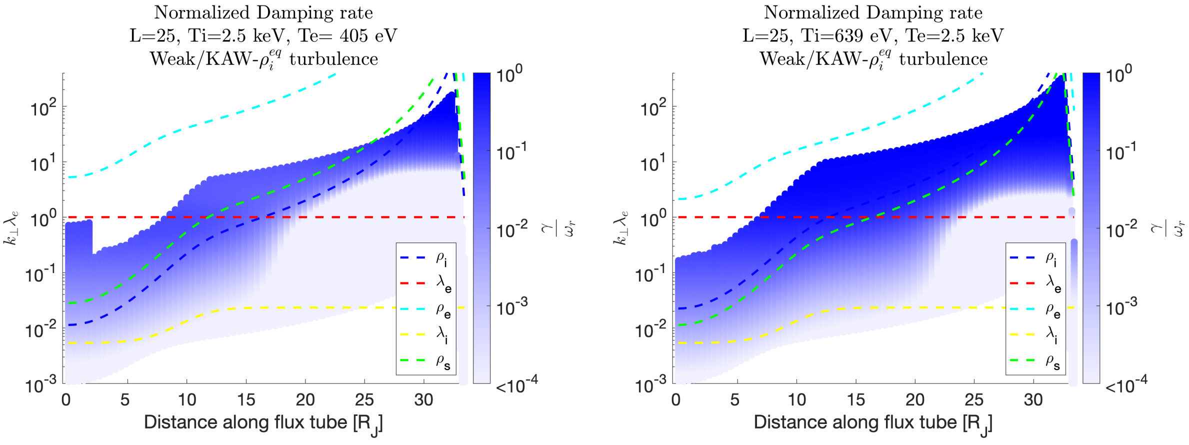

Figure D.2.: *Weak and kinetic equatorial turbulent spectral plots of the normalized damping strength for a thermal electron but hot ion species (left) and a hot electron but thermal ion species (right) along the L=25 field line in the middle magnetosphere. Local plasma scales are indicated by dashed lines.*

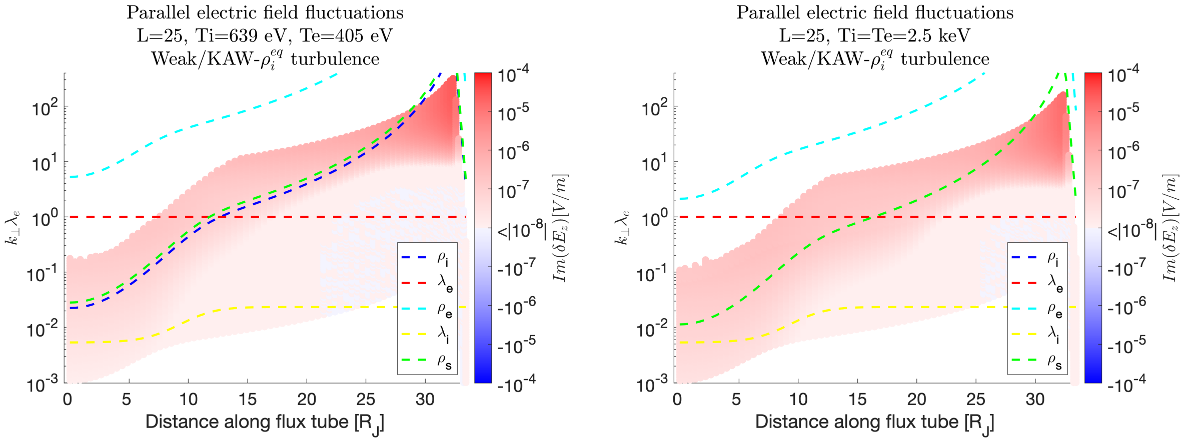
Parallel electric field fluctuations
L=25, Ti=639 eV, Te=405 eV
Weak/KAW-ρ_i^{eq} turbulence

Parallel electric field fluctuations
L=25, Ti=Te=2.5 keV
Weak/KAW-ρ_i^{eq} turbulence

Figure D.3.: *Weak and kinetic equatorial turbulent spectral plots for the imaginary part of the parallel electric field for a thermal (left) and a hot (right) species along the L=25 field line in the middle magnetosphere. Local plasma scales are indicated by dashed lines.*

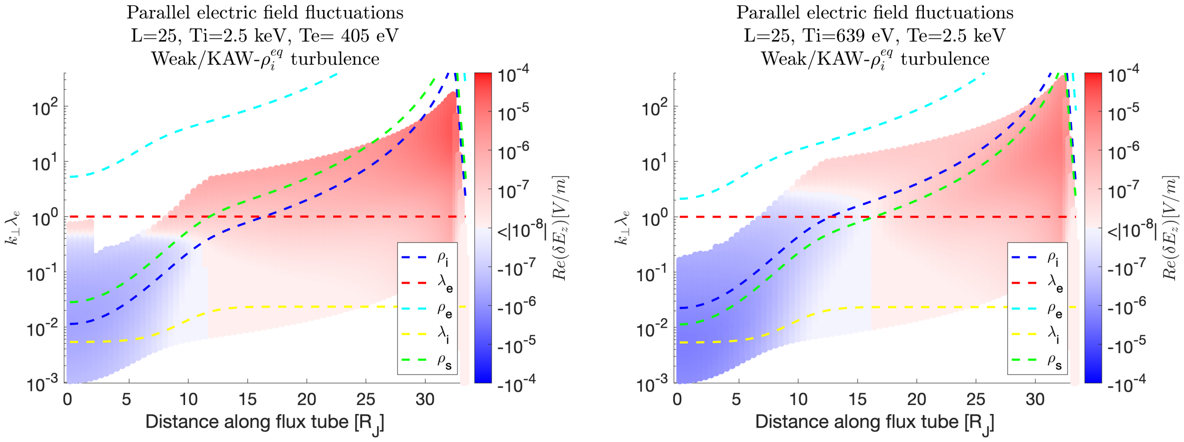
Parallel electric field fluctuations
L=25, Ti=2.5 keV, Te= 405 eV
Weak/KAW-ρ_i^{eq} turbulence

Parallel electric field fluctuations
L=25, Ti=639 eV, Te=2.5 keV
Weak/KAW-ρ_i^{eq} turbulence

Figure D.4.: *Weak and kinetic equatorial turbulent spectral plots for the real part of the parallel electric field strength for a thermal electron but hot ion species (left) and a hot electron but thermal ion species (right) along the L=25 field line in the middle magnetosphere. Local plasma scales are indicated by dashed lines.*

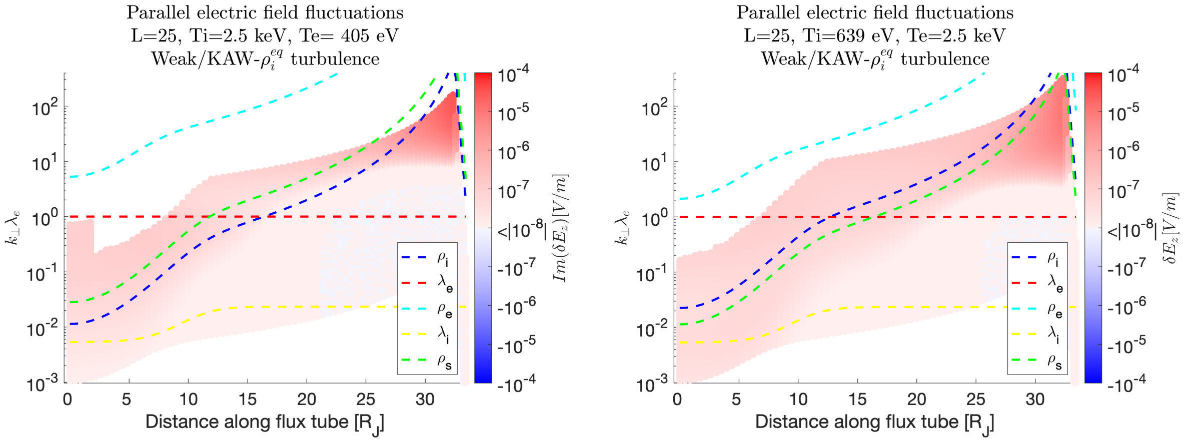
Parallel electric field fluctuations
L=25, Ti=2.5 keV, Te= 405 eV
Weak/KAW-ρ_i^{eq} turbulence

Parallel electric field fluctuations
L=25, Ti=639 eV, Te=2.5 keV
Weak/KAW-ρ_i^{eq} turbulence

Figure D.5.: *Weak and kinetic equatorial turbulent spectral plots for the imaginary part of the parallel electric field for a thermal (left) and a hot (right) species along the L=25 field line in the middle magnetosphere. Local plasma scales are indicated by dashed lines.*

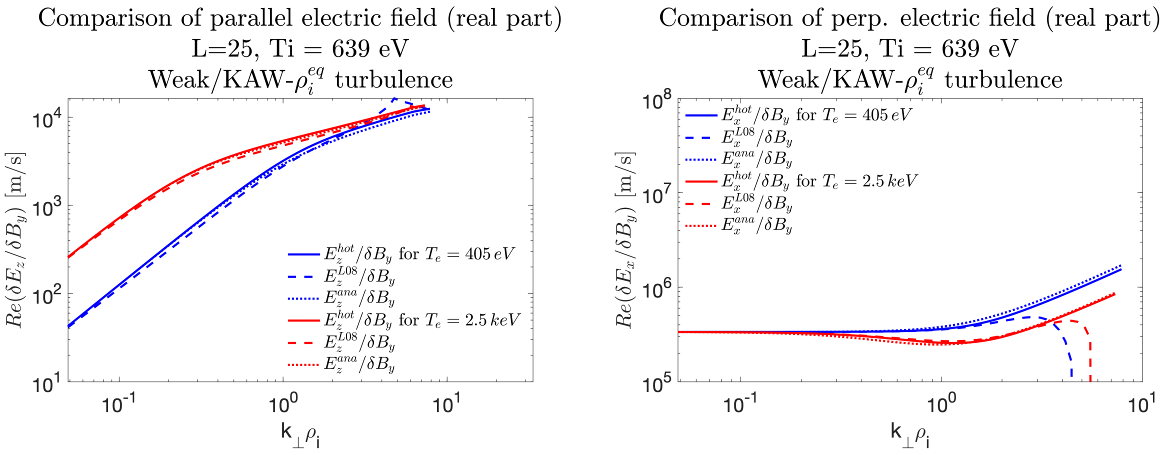

Figure D.6.: *Analytic comparison of the real parts of the parallel (left) and perpendicular (right) electric field with the Lysak (2008) and hot solution in the warm electron regime.*

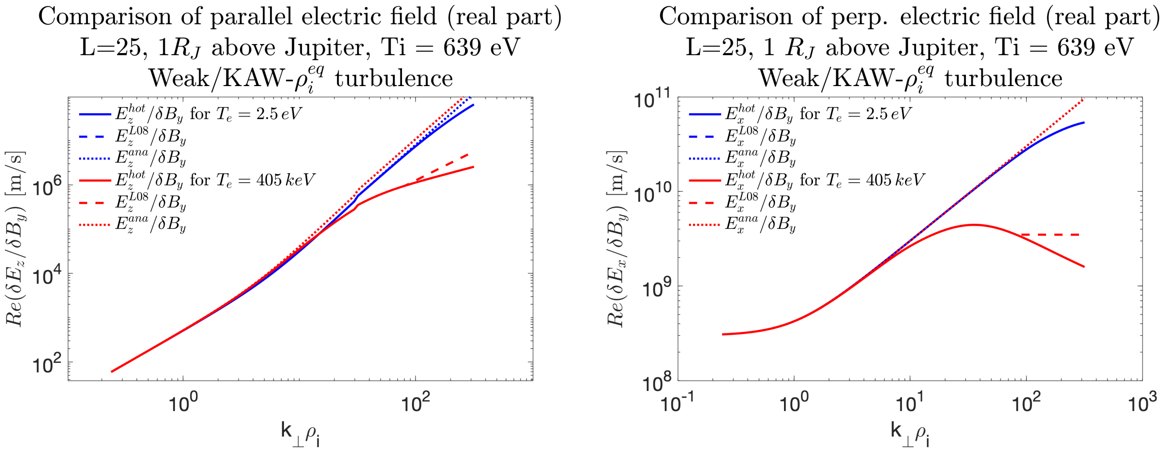

Figure D.7.: *Analytic comparison of the real parts of the parallel (left) and perpendicular (right) electric field with the Lysak (2008) and hot solution in cold electron regime.*

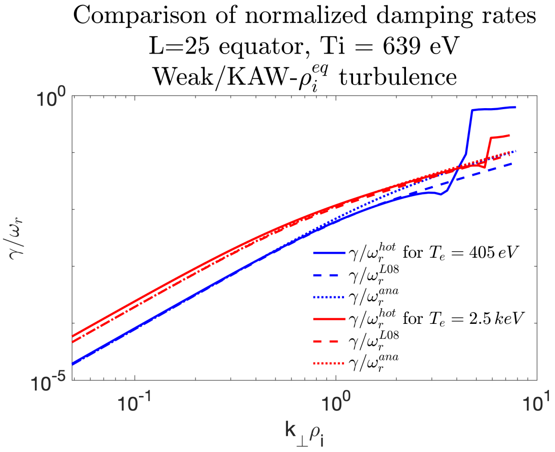

Figure D.8.: *Comparison of the analytic normalized damping rate with the Lysak (2008) and hot solution in the warm electron regime.*

E. Further modelings for Chapter 8

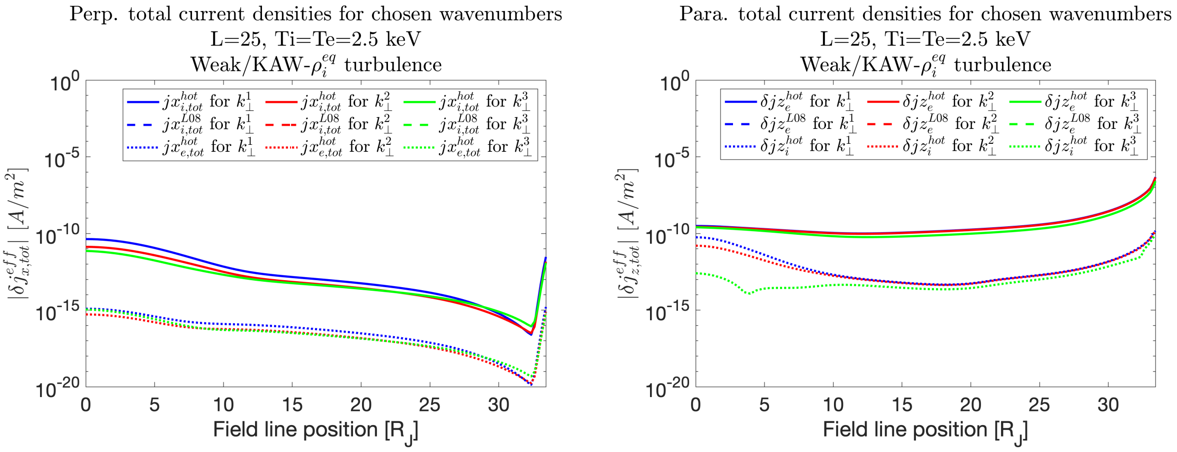

Figure E.1.: *Total perpendicular (left) and parallel (right) ion and electron responses in terms of current densities along the field line for three chosen equatorial wavenumbers:* $k^{eq}_{\perp,1} = \frac{2\pi}{R_J}$, $k^{eq}_{\perp,2} = \frac{1}{\rho_i^{eq}}$ *and* $k^{eq}_{\perp,3} = \frac{2}{3}\frac{2\pi}{\rho_i^{eq}}$. *The label 'L08' refers to currents calculated using tensor elements and wave frequency from the Lysak (2008) solution.*

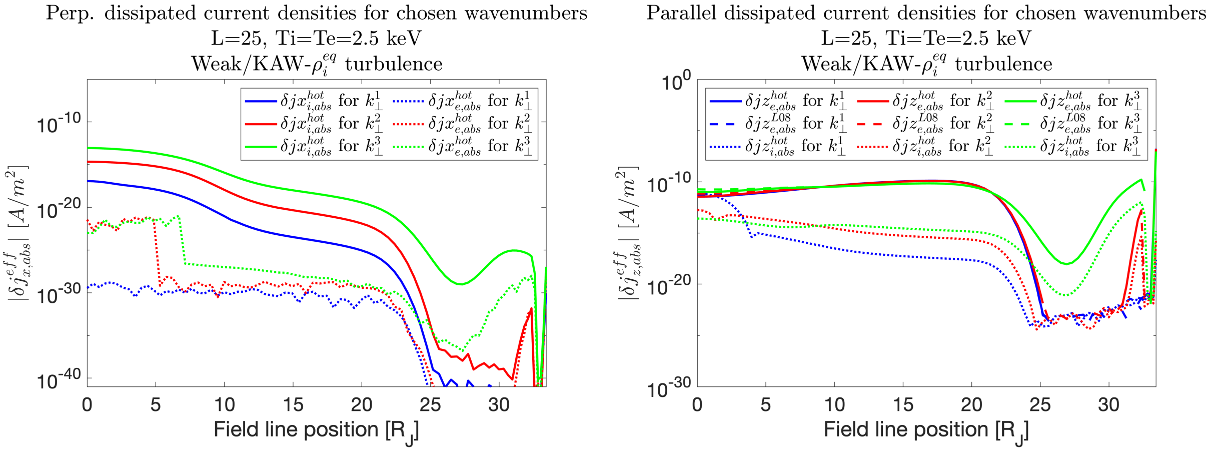

Figure E.2.: *Perpendicular (left) and parallel (right) ion and electron responses related to dissipation processes along the field line for three chosen equatorial wavenumbers:* $k^{eq}_{\perp,1} = \frac{2\pi}{R_J}$, $k^{eq}_{\perp,2} = \frac{1}{\rho_i^{eq}}$ *and* $k^{eq}_{\perp,3} = \frac{2}{3}\frac{2\pi}{\rho_i^{eq}}$. *The label 'L08' refers to currents calculated using tensor elements and wave frequency from the Lysak (2008) solution. Consider that there is no perpendicular dissipation contribution in the Lysak theory.*

Bibliography

Acuna, M. H., F. M. Neubauer, and N. F. Ness (1981), Standing Alfvén Wave Current System at Io: Voyager 1 Observations, *Journal of Geoophyical Research*, *86*(A10), 8513–8521, doi:10.1029/JA086iA10p08513.

Ajello, J. M., D. E. Shemansky, W. R. Pryor, A. I. Stewart, K. E. Simmons, T. Majeed, J. H. Waite, G. R. Gladstone, and D. Grodent (2001), Spectroscopic Evidence for High-Altitude Aurora at Jupiter from Galileo Extreme Ultraviolet Spectrometer and Hopkins Ultraviolet Telescope Observations, *Icarus*, *152*(1), 151–171, doi:10.1006/icar.2001.6619.

Allegrini, F., et al. (2020), Energy Flux and Characteristic Energy of Electrons Over Jupiter's Main Auroral Emission, *Journal of Geophysical Research (Space Physics)*, *125*(4), e27693, doi:10.1029/2019JA027693.

Bagenal, F., and P. A. Delamere (2011), Flow of mass and energy in the magnetospheres of Jupiter and Saturn, *Journal of Geophysical Research (Space Physics)*, *116*(A5), A05209, doi:10.1029/2010JA016294.

Bagenal, F., et al. (2017), Magnetospheric Science Objectives of the Juno Mission, *Space Science Reviews*, *213*(1-4), 219–287, doi:10.1007/s11214-014-0036-8.

Barbosa, D. D. (1981), Dissipation and turbulent heating of plasma in Jupiter's magnetosphere, *Geophysical Research Letters*, *8*(10), 1111–1114, doi:10.1029/GL008i010p01111.

Barbosa, D. D., A. Eviatar, and G. L. Siscoe (1984), On the acceleration of energetic ions in Jupiter's magnetosphere, *Journal of Geophysical Research*, *89*(A6), 3789–3800, doi:10.1029/JA089iA06p03789.

Barnes, A. (1966), Collisionless Damping of Hydromagnetic Waves, *Physics of Fluids*, *9*(8), 1483–1495, doi:10.1063/1.1761882.

Baumjohann, W., and R. Treumann (2012), *Basic Space Plasma Physics (Revised Edition)*, World Scientific Publishing Company, doi:10.1142/9781848168961.

Belcher, J. W., C. K. Goertz, J. D. Sullivan, and M. H. Acuna (1981), Plasma observations of the Alvén wave generated by Io, *Journal of Geophysical Research*, *86*(A10), 8508–8512, doi:10.1029/JA086iA10p08508.

Bhardwaj, A., and G. R. Gladstone (2000), Auroral emissions of the giant planets, *Reviews of Geophysics*, *38*(3), 295–354, doi:10.1029/1998RG000046.

Bigg, E. K. (1964), Influence of the Satellite Io on Jupiter's Decametric Emission, *Nature*, *203*(4949), 1008–1010, doi:10.1038/2031008a0.

Blöcker, A., J. Saur, L. Roth, and D. F. Strobel (2018), MHD Modeling of the Plasma Interaction With Io's Asymmetric Atmosphere, *Journal of Geophysical Research (Space Physics)*, *123*(11), 9286–9311, doi:10.1029/2018JA025747.

Bonfond, B., D. Grodent, J. C. Gérard, A. Radioti, J. Saur, and S. Jacobsen (2008), UV Io footprint leading spot: A key feature for understanding the UV Io footprint multiplicity?, *Geophysical Research Letters*, *35*(5), L05107, doi:10.1029/2007GL032418.

Bonfond, B., J. Saur, D. Grodent, S. V. Badman, D. Bisikalo, V. Shematovich, J. C. Gérard, and A. Radioti (2017), The tails of the satellite auroral footprints at Jupiter, *Journal of Geophysical Research (Space Physics)*, *122*(8), 7985–7996, doi:10.1002/2017JA024370.

Borovsky, J. E. (1993), Auroral arc thicknesses as predicted by various theories, *Journal of Geophysical Research*, *98*(A4), 6101–6138, doi:10.1029/92JA02242.

Brambilla, M. (1998), *Kinetic Theory of Plasma Waves: Homogeneous plasmas*, Oxford University Press, New York.

Brice, N., and T. R. Mcdonough (1973), Jupiter's radiation belts, *Icarus*, *18*(2), 206–219, doi:10.1016/0019-1035(73)90204-2.

Broadfoot, A. L., et al. (1979), Extreme Ultraviolet Observations from Voyager 1 Encounter with Jupiter, *Science*, *204*(4396), 979–982, doi:10.1126/science.204.4396.979.

Brown, R. A. (1976), A model of Jupiter's sulfur nebula., *The Astrophysical Journal*, *206*, L179–L183, doi:10.1086/182162.

Burke, B. F., and K. L. Franklin (1955), Observations of a Variable Radio Source Associated with the Planet Jupiter, *Journal of Geophysical Research*, *60*(2), 213–217, doi:10.1029/JZ060i002p00213.

Chakrabarti, S., and M. Galand (2010), Aurora on Jupiter: A Magnetic Connection with the Sun and the Medicean Moons, in *Galileo's Medicean Moons: Their Impact on 400 Years of Discovery*, vol. 269, edited by C. Barbieri, S. Chakrabarti, M. Coradini, and M. Lazzarin, pp. 71–79, doi:10.1017/S1743921310007283.

Chané, E., J. Saur, and S. Poedts (2013), Modeling Jupiter's magnetosphere: Influence of the internal sources, *Journal of Geophysical Research (Space Physics)*, *118*(5), 2157–2172, doi:10.1002/jgra.50258.

Chen, C. H. K., L. Leung, S. Boldyrev, B. A. Maruca, and S. D. Bale (2014), Ion-scale spectral break of solar wind turbulence at high and low beta, *Geophysical Research Letters*, *41*(22), 8081–8088, doi:10.1002/2014GL062009.

Chust, T., A. Roux, W. S. Kurth, D. A. Gurnett, M. G. Kivelson, and K. K. Khurana (2005), Are Io's Alfvén wings filamented? Galileo observations, *Planetary and Space Science*, *53*(4), 395–412, doi:10.1016/j.pss.2004.09.021.

Clark, G., et al. (2018), Precipitating Electron Energy Flux and Characteristic Energies in Jupiter's Main Auroral Region as Measured by Juno/JEDI, *Journal of Geophysical Research (Space Physics)*, *123*(9), 7554–7567, doi:10.1029/2018JA025639.

Clark, G., et al. (2020), Energetic Proton Acceleration Associated With Io's Footprint Tail, *Geophysical Research Letters*, *47*(24), e90839, doi:10.1029/2020GL090839.

Clarke, J. T. (2012), Auroral Processes on Jupiter and Saturn, in *Auroral Phenomenology and Magnetospheric Processes: Earth and Other Planets*, vol. 197, pp. 113–121, Washington DC American Geophysical Union Geophysical Monograph Series, doi: 10.1029/2011GM001199.

Clarke, J. T., H. W. Moos, S. K. Atreya, and A. L. Lane (1980), Observations from earth orbit and variability of the polar aurora on Jupiter, *The Astrophysical Journal*, *241*, L179–L182, doi:10.1086/183386.

Clarke, J. T., et al. (1996), Far-Ultraviolet Imaging of Jupiter's Aurora and the lo "Footprint", *Science*, *274*(5286), 404–409, doi:10.1126/science.274.5286.404.

Clarke, J. T., et al. (1998), Hubble Space Telescope imaging of Jupiter's UV aurora during the Galileo orbiter mission, *Journal of Geophysical Research*, *103*(E9), 217, doi:10.1029/98JE01130.

Clarke, J. T., D. Grodent, S. W. H. Cowley, E. J. Bunce, P. Zarka, J. E. P. Connerney, and T. Satoh (2004), Jupiter's aurora, in *Jupiter. The Planet, Satellites and Magnetosphere*, vol. 1, pp. 639–670, Cambridge University Press.

Connerney, J. E. P., and T. Satoh (2000), The H_3^+ ion: a remote diagnostic of the jovian magneto sphere, in *Astronomy, physics and chemistry of* H_3^+, vol. 358, pp. 2359–2559, doi:10.1098/rsta.2000.0661.

Connerney, J. E. P., R. Baron, T. Satoh, and T. Owen (1993), Images of Excited H_3^+ at the Foot of the Io Flux Tube in Jupiter's Atmosphere, *Science*, *262*(5136), 1035–1038, doi:10.1126/science.262.5136.1035.

Connerney, J. E. P., et al. (2017), The Juno Magnetic Field Investigation, *Space Science Reviews*, *213*(1-4), 39–138, doi:10.1007/s11214-017-0334-z.

Connerney, J. E. P., et al. (2018), A New Model of Jupiter's Magnetic Field From Juno's First Nine Orbits, *Geophysical Research Letters*, *45*(6), 2590–2596, doi:10.1002/2018GL077312.

Cowley, S., and E. Bunce (2001), Origin of the main auroral oval in Jupiter's coupled magnetosphere–ionosphere system, *Planetary and Space Science*, *49*(10), 1067 – 1088, doi:https://doi.org/10.1016/S0032-0633(00)00167-7, magnetosphere of the Outer Planets Part II.

Cowley, S. W. H., and E. J. Bunce (2003), Corotation-driven magnetosphere-ionosphere coupling currents in SaturnÂ's magnetosphere and their relation to the auroras, *Annales Geophysicae*, *21*(8), 1691–1707, doi:10.5194/angeo-21-1691-2003.

Cowley, S. W. H., E. J. Bunce, and J. D. Nichols (2003), Origins of Jupiter's main oval auroral emissions, *Journal of Geophysical Research (Space Physics)*, *108*(A4), 8002, doi: 10.1029/2002JA009329.

Cramer, N. (2001), *The Physics of Alfvén waves*, Wiley-VCH, Berlin.

Crary, F. J. (1997), On the generation of an electron beam by Io, *Journal of Geophysical Research*, *102*(A1), 37–50, doi:10.1029/96JA02409.

Crary, F. J., and F. Bagenal (1997), Coupling the plasma interaction at Io to Jupiter, *Geophysical Research Letters*, *24*(17), 2135–2138, doi:10.1029/97GL02248.

Damiano, P. A., P. A. Delamere, B. Stauffer, C. S. Ng, and J. R. Johnson (2019), Kinetic Simulations of Electron Acceleration by Dispersive Scale Alfvén Waves in Jupiter's Magnetosphere, *Geophysical Research Letters*, *46*(6), 3043–3051, doi:10.1029/2018GL081219.

Das, A. C., and W. H. Ip (1992), Particle acceleration by kinetic Alfvén waves in the Io plasma torus, *Planetary and Space Science*, *40*(11), 1499–1502, doi:10.1016/0032-0633(92)90046-Q.

Das, A. C., and W. H. Ip (2000), Field aligned current and particle acceleration in the near-Io plasma torus, *Planetary and Space Science*, *48*(2-3), 127–131, doi:10.1016/S0032-0633(99)00086-0.

Deift, P. A., and C. K. Goertz (1973), The propagation of Alfven waves along Io's flux tube, *Planetary and Space Science*, *21*(8), 1417–1429, doi:10.1016/0032-0633(73)90233-X.

Delamere, P. A., and F. Bagenal (2010), Solar wind interaction with Jupiter's magnetosphere, *Journal of Geophysical Research (Space Physics)*, *115*(A10), A10201, doi:10.1029/2010JA015347.

Delamere, P. A., F. Bagenal, R. Ergun, and Y. J. Su (2003), Momentum transfer between the Io plasma wake and Jupiter's ionosphere, *Journal of Geophysical Research (Space Physics)*, *108*(A6), 1241, doi:10.1029/2002JA009530.

Dougherty, L. P., K. M. Bodisch, and F. Bagenal (2017), Survey of Voyager plasma science ions at Jupiter: 2. Heavy ions, *Journal of Geophysical Research (Space Physics)*, *122*(8), 8257–8276, doi:10.1002/2017JA024053.

Dougherty, M. K., D. J. Southwood, A. Balogh, and E. J. Smith (1993), Field-aligned currents in the Jovian magnetosphere during the Ulysses flyby, *Planetary and Space Science*, *41*(4), 291–300, doi:10.1016/0032-0633(93)90024-V.

Elliott, S. S., D. A. Gurnett, W. S. Kurth, G. Clark, B. H. Mauk, S. J. Bolton, J. E. P. Connerney, and S. M. Levin (2018a), Pitch Angle Scattering of Upgoing Electron Beams in Jupiter's Polar Regions by Whistler Mode Waves, *Geophysical Research Letters*, *45*(3), 1246–1252, doi:10.1002/2017GL076878.

Elliott, S. S., D. A. Gurnett, W. S. Kurth, B. H. Mauk, R. W. Ebert, G. Clark, P. Valek, F. Allegrini, and S. J. Bolton (2018b), The Acceleration of Electrons to High Energies Over the Jovian Polar Cap via Whistler Mode Wave-Particle Interactions, *Journal of Geophysical Research (Space Physics)*, *123*(9), 7523–7533, doi:10.1029/2018JA025797.

Elliott, S. S., et al. (2020), The Generation of Upward-Propagating Whistler Mode Waves by Electron Beams in the Jovian Polar Regions, *Journal of Geophysical Research (Space Physics)*, *125*(6), e27868, doi:10.1029/2020JA027868.

Ergun, R. E., C. W. Carlson, J. P. McFadden, F. S. Mozer, and R. J. Strangeway (2000), Parallel electric fields in discrete arcs, *Geophysical Research Letters*, *27*(24), 4053–4056, doi:10.1029/2000GL003819.

Erkaev, N. V., V. S. Semenov, V. A. Shaidurov, D. Langmayr, H. K. Biernat, and H. O. Rucker (2001), Propagation of nonlinear slow waves produced by pressure pulses along the Io flux tube, *Advances in Space Research*, *28*(10), 1481–1488, doi:10.1016/S0273-1177(01)00550-6.

Erkaev, N. V., V. S. Semenov, V. A. Shaidurov, D. Langmayr, H. K. Biernat, and H. O. Rucker (2002), Investigation of MHD slow shocks propagating along the Io flux tube, *International Journal of Geomagnetism and Aeronomy*, *3*(1), 67–76.

Franci, L., S. Landi, L. Matteini, A. Verdini, and P. Hellinger (2016), Plasma Beta Dependence of the Ion-scale Spectral Break of Solar Wind Turbulence: High-resolution 2D Hybrid Simulations, *The Astrophysical Journal*, *833*(1), 91, doi:10.3847/1538-4357/833/1/91.

Frank, L. A., and W. R. Paterson (1999), Intense electron beams observed at Io with the Galileo spacecraft, *Journal of Geophysical Research*, *104*(A12), 28,657–28,670, doi:10.1029/1999JA900402.

Fried, B. D., and S. D. Conte (1961), *The Plasma Dispersion Function*, Academic press, New York.

Frisch, U. (1995), *Turbulence: The Legacy of AN Kolmogorov*, Cambridge University Press.

Gaelzer, R., and L. F. Ziebell (2014), The dispersion relations of dispersive Alfvén waves in superthermal plasmas, *Journal of Geophysical Research (Space Physics)*, *119*(12), 9334–9356, doi:10.1002/2014JA020667.

Galtier, S., S. V. Nazarenko, A. C. Newell, and A. Pouquet (2000), A weak turbulence theory for incompressible magnetohydrodynamics, *Journal of Plasma Physics*, *63*(5), 447–488, doi:10.1017/S0022377899008284.

Gary, S. P., and J. E. Borovsky (2004), Alfvén-cyclotron fluctuations: Linear Vlasov theory, *Journal of Geophysical Research (Space Physics)*, *109*(A6), A06105, doi:10.1029/2004JA010399.

Gekelman, W., S. Vincena, D. Leneman, and J. Maggs (1997), Laboratory experiments on shear Alfvén waves and their relationship to space plasmas, *Journal of Geophysical Research*, *102*(A4), 7225–7236, doi:10.1029/96JA03683.

Gérard, J.-C., V. Dols, R. Prangé, and F. Paresce (1994), The morphology of the north Jovian ultraviolet aurora observed with the Hubble Space Telescope, *Planetary and Space Science*, *42*(11), 905–917, doi:10.1016/0032-0633(94)90051-5.

Gérard, J. C., et al. (2019), Contemporaneous Observations of Jovian Energetic Auroral Electrons and Ultraviolet Emissions by the Juno Spacecraft, *Journal of Geophysical Research (Space Physics)*, *124*(11), 8298–8317, doi:10.1029/2019JA026862.

Gershman, D. J., et al. (2019), Alfvénic Fluctuations Associated With Jupiter's Auroral Emissions, *Geophysical Research Letters*, *46*(13), 7157–7165, doi:10.1029/2019GL082951.

Glassmeier, K. H. (1995), Ultralow-frequency pulsations: Earth and Jupiter compared, *Advances in Space Research*, *16*(4), 209–218, doi:10.1016/0273-1177(95)00232-4.

Glassmeier, K. H., and M. Scholer (1991), *Plasmaphysik im Sonnensystem.*, BI Wissenschaftsverlag Mannheim.

Goertz, C. K., and R. W. Boswell (1979), Magnetosphere-ionosphere coupling, *Journal of Geophysical Research: Space Physics*, *84*(A12), 7239–7246, doi:10.1029/JA084iA12p07239.

Goertz, C. K., and W. H. Ip (1982), On the structure of the Io torus, *Planetary and Space Science*, *30*(9), 855–864, doi:10.1016/0032-0633(82)90128-3.

Goldreich, P., and D. Lynden-Bell (1969), Io, a jovian unipolar inductor, *Astrophysical Journal*, *156*, 59–78, doi:10.1086/149947.

Goldreich, P., and S. Sridhar (1995), Toward a Theory of Interstellar Turbulence. II. Strong Alfvénic Turbulence, *The Astrophysical Journal*, *438*, 763, doi:10.1086/175121.

Hallinan, G., et al. (2015), Magnetospherically driven optical and radio aurorae at the end of the stellar main sequence, *Nature*, *523*(7562), 568–571, doi:10.1038/nature14619.

Hasegawa, A. (1976), Particle acceleration by MHD surface wave and formation of aurora, *Journal of Geophysical Research*, *81*(A28), 5083–5090, doi:10.1029/JA081i028p05083.

Hasegawa, A., and L. Chen (1974), Plasma Heating by Alfvén-Wave Phase Mixing, *Physical Review Letters*, *32*(9), 454–456, doi:10.1103/PhysRevLett.32.454.

Hasegawa, A., and L. Chen (1976), Kinetic processes in plasma heating by resonant mode conversion of Alfvén wave, *Physics of Fluids*, *19*(12), 1924–1934, doi:10.1063/1.861427.

Hasegawa, A., and C. Uberoi (1982), *The Alfvén wave.*, Technical Information Center, U.S. Department of Energy.

Hess, S. L. G., P. Delamere, V. Dols, B. Bonfond, and D. Swift (2010), Power transmission and particle acceleration along the Io flux tube, *Journal of Geophysical Research (Space Physics)*, *115*(A6), A06205, doi:10.1029/2009JA014928.

Hill, T. W. (1979), Inertial limit on corotation, *Journal of Geophysical Research*, *84*(A11), 6554–6558, doi:10.1029/JA084iA11p06554.

Hill, T. W. (2001), The Jovian auroral oval, *Journal of Geophysical Research*, *106*(A5), 8101–8108, doi:10.1029/2000JA000302.

Hill, T. W., and F. C. Michel (1976), Heavy ions from the Galilean satellites and the centrifugal distortion of the Jovian magnetosphere, *Journal of Geophysical Research*, *81*(25), 4561, doi:10.1029/JA081i025p04561.

Hill, T. W., and V. M. Vasyliūnas (2002), Jovian auroral signature of Io's corotational wake, *Journal of Geophysical Research (Space Physics)*, *107*(A12), 1464, doi:10.1029/2002JA009514.

Hollweg, J. V. (1999), Kinetic Alfvén wave revisited, *Journal of Geophysical Research*, *104*(A7), 14,811–14,820, doi:10.1029/1998JA900132.

Horbury, T. S., M. Forman, and S. Oughton (2008), Anisotropic Scaling of Magnetohydrodynamic Turbulence, *Physical Review Letters*, *101*(17), 175005, doi:10.1103/PhysRevLett.101.175005.

Howes, G. G., S. C. Cowley, W. Dorland, G. W. Hammett, E. Quataert, and A. A. Schekochihin (2006), Astrophysical Gyrokinetics: Basic Equations and Linear Theory, *The Astrophysical Journal*, *651*(1), 590–614, doi:10.1086/506172.

Howes, G. G., S. C. Cowley, W. Dorland, G. W. Hammett, E. Quataert, and A. A. Schekochihin (2008), A model of turbulence in magnetized plasmas: Implications for the dissipation range in the solar wind, *Journal of Geophysical Research (Space Physics)*, *113*(A5), A05103, doi:10.1029/2007JA012665.

Howes, G. G., K. G. Klein, and J. M. TenBarge (2014), Validity of the Taylor Hypothesis for Linear Kinetic Waves in the Weakly Collisional Solar Wind, *The Astrophysical Journal*, *789*(2), 106, doi:10.1088/0004-637X/789/2/106.

Isbell, J., A. J. Dessler, and J. Waite, J. H. (1984), Magnetospheric energization by interaction between planetary spin and the solar wind, *Journal of Geophysical Research*, *89*(A12), 10,716–10,722, doi:10.1029/JA089iA12p10716.

Jacobsen, S., F. M. Neubauer, J. Saur, and N. Schilling (2007), Io's nonlinear MHD-wave field in the heterogeneous Jovian magnetosphere, *Geophysical Research Letters*, *34*(10), L10202, doi:10.1029/2006GL029187.

Janser, S., J. Saur, G. Clark, A. H. Sulaiman, and J. R. Szalay (2022, submitted), Properties of turbulent Alfvénic fluctuations and wave-particle interaction associated with Io's footprint tail, doi:xxx.

Jones, S. T., and Y. J. Su (2008), Role of dispersive Alfvén waves in generating parallel electric fields along the Io-Jupiter fluxtube, *Journal of Geophysical Research (Space Physics)*, *113*(A12), A12205, doi:10.1029/2008JA013512.

Kane, M., B. H. Mauk, E. P. Keath, and S. M. Krimigis (1995), Hot ions in Jupiter's magnetodisc: A model for Voyager 2 low-energy charged particle measurements, *Journal of Geophysical Research*, *100*(A10), 19,473–19,486, doi:10.1029/95JA00793.

Kao, M. M., G. Hallinan, J. S. Pineda, I. Escala, A. Burgasser, S. Bourke, and D. Stevenson (2016), Auroral Radio Emission from Late L and T Dwarfs: A New Constraint on Dynamo Theory in the Substellar Regime, *The Astrophysical Journal*, *818*(1), 24, doi:10.3847/0004-637X/818/1/24.

Kennel, C. F., and F. Engelmann (1966), Velocity Space Diffusion from Weak Plasma Turbulence in a Magnetic Field, *Physics of Fluids*, *9*(12), 2377–2388, doi:10.1063/1.1761629.

Khan, I. A., Z. Iqbal, and G. Murtaza (2019), Perturbed electromagnetic field and Poynting flux of kinetic Alfvén waves in kappa distributed space plasmas, *European Physical Journal Plus*, *134*(2), 80, doi:10.1140/epjp/i2019-12487-3.

Khurana, K. K. (1992), A Generalized Hinged-Magnetodisc Model of Jupiter's Nightside Current Sheet, *Journal of Geophysical Research*, *97*(A5), 6269–6276, doi:10.1029/92JA00169.

Khurana, K. K., M. G. Kivelson, V. M. Vasyliunas, N. Krupp, J. Woch, A. Lagg, B. H. Mauk, and W. S. Kurth (2004), The configuration of Jupiter's magnetosphere, in *Jupiter. The Planet, Satellites and Magnetosphere*, vol. 1, pp. 593–616, Cambridge University Press.

Kivelson, M. G., K. K. Khurana, R. J. Walker, J. Warnecke, C. T. Russell, J. A. Linker, D. J. Southwood, and C. Polanskey (1996), Io's Interaction with the Plasma Torus: Galileo Magnetometer Report, *Science*, *274*(5286), 396–398, doi:10.1126/science.274.5286.396.

Kivelson, M. G., K. K. Khurana, C. T. Russell, and R. J. Walker (1997), Intermittent short-duration magnetic field anomalies in the Io torus: Evidence for plasma interchange?, *Geophysical Research Letters*, *24*(17), 2127–2130, doi:10.1029/97GL02202.

Kivelson, M. G., F. Bagenal, W. S. Kurth, F. M. Neubauer, C. Paranicas, and J. Saur (2004), Magnetospheric interactions with satellites, in *Jupiter. The Planet, Satellites and Magnetosphere*, vol. 1, pp. 513–536, Cambridge University Press.

Klein, K. G., G. G. Howes, J. M. TenBarge, and F. Valentini (2020), Diagnosing collisionless energy transfer using field-particle correlations: Alfvén-ion cyclotron turbulence, *Journal of Plasma Physics*, *86*(4), 905860402, doi:10.1017/S0022377820000689.

Knight, S. (1973), Parallel electric fields, *Planetary and Space Science*, *21*(5), 741 – 750, doi:https://doi.org/10.1016/0032-0633(73)90093-7.

Kollmann, P., E. Roussos, C. Paranicas, E. E. Woodfield, B. H. Mauk, G. Clark, D. C. Smith, and J. Vandegriff (2018), Electron Acceleration to MeV Energies at Jupiter and Saturn, *Journal of Geophysical Research (Space Physics)*, *123*(11), 9110–9129, doi:10.1029/2018JA025665.

Kotsiaros, S., J. E. P. Connerney, and Y. M. Martos (2020), Analysis of Eddy Current Generation on the Juno Spacecraft in Jupiter's Magnetosphere, *Earth and Space Science*, *7*(7), e01061, doi:10.1029/2019EA001061.

Krupp, N., A. Lagg, S. Livi, B. Wilken, J. Woch, E. C. Roelof, and D. J. Williams (2001), Global flows of energetic ions in Jupiter's equatorial plane: First-order approximation, *Journal of Geophysical Research*, *106*(A11), 26,017–26,032, doi:10.1029/2000JA900138.

Kurth, W. S., G. B. Hospodarsky, D. L. Kirchner, B. T. Mokrzycki, T. F. Averkamp, W. T. Robison, C. W. Piker, M. Sampl, and P. Zarka (2017), The Juno Waves Investigation, *Space Science Reviews*, *213*(1-4), 347–392, doi:10.1007/s11214-017-0396-y.

Landau, L. D. (1946), On the vibrations of the electronic plasma, *Journal of Physics (USSR)*.

Lazar, M., and R. Schlickeiser (2006), Relativistic kinetic dispersion theory of linear parallel waves in magnetized plasmas with isotropic thermal distributions, *New Journal of Physics*, *8*(5), 66, doi:10.1088/1367-2630/8/5/066.

Leamon, R. J., C. W. Smith, N. F. Ness, and H. K. Wong (1999), Dissipation range dynamics: Kinetic Alfvén waves and the importance of β_e, *Journal of Geophysical Research*, *104*(A10), 22,331–22,344, doi:10.1029/1999JA900158.

Li, W., et al. (2021), Quantification of Diffuse Auroral Electron Precipitation Driven by Whistler Mode Waves at Jupiter, *Geophysical Research Letters*, *48*(19), e95457, doi:10.1029/2021GL095457.

Livadiotis, G. (2016), Modeling anisotropic Maxwell-Jüttner distributions: derivation and properties, *Annales Geophysicae*, *34*(12), 1145–1158, doi:10.5194/angeo-34-1145-2016.

Lu, Q., and X. Li (2007), Heating of ions by low-frequency Alfvén waves, *Physics of Plasmas*, *14*(4), 042303, doi:10.1063/1.2715569.

Lysak, R. L. (2008), On the dispersion relation for the kinetic Alfvén wave in an inhomogeneous plasma, *Physics of Plasmas*, *15*(6), 062901, doi:10.1063/1.2918742.

Lysak, R. L., and W. Lotko (1996), On the kinetic dispersion relation for shear Alfvén waves, *Journal of Geophysical Research*, *101*(A3), 5085–5094, doi:10.1029/95JA03712.

Lysak, R. L., and Y. Song (2000), The Role of Alfvén Waves in the Formation of Auroral Parallel Electric Fields, *Washington DC American Geophysical Union Geophysical Monograph Series*, *118*, 147, doi:10.1029/GM118p0147.

Lysak, R. L., and Y. Song (2003), Kinetic theory of the Alfvén wave acceleration of auroral electrons, *Journal of Geophysical Research (Space Physics)*, *108*(A4), 8005, doi:10.1029/2002JA009406.

Lysak, R. L., and Y. Song (2008), Propagation of kinetic Alfvén waves in the ionospheric Alfvén resonator in the presence of density cavities, *Geophysical Research Letters*, *35*(20), L20101, doi:10.1029/2008GL035728.

Lysak, R. L., and Y. Song (2020), Field Line Resonances in Jupiter's Magnetosphere, *Geophysical Research Letters*, *47*(18), e89473, doi:10.1029/2020GL089473.

Mauk, B., and F. Bagenal (2012), Comparative Auroral Physics: Earth and Other Planets, *Washington DC American Geophysical Union Geophysical Monograph Series*, *197*, 3–26, doi:10.1029/2011GM001192.

Mauk, B. H., and J. Saur (2007), Equatorial electron beams and auroral structuring at Jupiter, *Journal of Geophysical Research (Space Physics)*, *112*(A10), A10221, doi:10.1029/2007JA012370.

Mauk, B. H., B. J. Anderson, and R. M. Thorne (2002), Magnetosphere-Ionosphere Coupling at Earth, Jupiter, and Beyond, *Washington DC American Geophysical Union Geophysical Monograph Series*, *130*, 97, doi:10.1029/130GM07.

Mauk, B. H., D. G. Mitchell, R. W. McEntire, C. P. Paranicas, E. C. Roelof, D. J. Williams, S. M. Krimigis, and A. Lagg (2004), Energetic ion characteristics and neutral gas interactions in Jupiter's magnetosphere, *Journal of Geophysical Research (Space Physics)*, *109*(A9), A09S12, doi:10.1029/2003JA010270.

Mauk, B. H., et al. (2017a), The Jupiter Energetic Particle Detector Instrument (JEDI) Investigation for the Juno Mission, *Space Science Reviews*, *213*(1-4), 289–346, doi:10.1007/s11214-013-0025-3.

Mauk, B. H., et al. (2017b), Juno observations of energetic charged particles over Jupiter's polar regions: Analysis of monodirectional and bidirectional electron beams, *Geophysical Research Letters*, *44*(10), 4410–4418, doi:10.1002/2016GL072286.

Mauk, B. H., et al. (2017c), Discrete and broadband electron acceleration in Jupiter's powerful aurora, *Nature*, *549*(7670), 66–69, doi:10.1038/nature23648.

Mauk, B. H., et al. (2018), Diverse Electron and Ion Acceleration Characteristics Observed Over Jupiter's Main Aurora, *Geophysical Research Letters*, *45*(3), 1277–1285, doi:10.1002/2017GL076901.

McComas, D. J., et al. (2017), The Jovian Auroral Distributions Experiment (JADE) on the Juno Mission to Jupiter, *Space Science Reviews*, *213*(1-4), 547–643, doi:10.1007/s11214-013-9990-9.

McNutt, R. L., J. W. Belcher, and H. S. Bridge (1981), Positive ion observations in the middle magnetosphere of Jupiter, *Journal of Geophysical Research*, *86*(A10), 8319–8342, doi:10.1029/JA086iA10p08319.

McNutt, R. L., F. Bagenal, and R. M. Thorne (1990), Observation of auroral secondary electrons in the Jovian magnetosphere, *Geophysical Research Letters*, *17*(3), 291–294, doi:10.1029/GL017i003p00291.

Mura, A., et al. (2018), Juno observations of spot structures and a split tail in Io-induced aurorae on Jupiter, *Science*, *361*(6404), 774–777, doi:10.1126/science.aat1450.

NASA (2021), Juno Science Objectives, `https://www.jpl.nasa.gov/news/press_kits/juno/science/`, Last access: 15th December 2021.

Neubauer, F. M. (1980), Nonlinear standing Alfvén wave current system at Io: Theory, *Journal of Geophysical Research*, *85*(A3), 1171–1178, doi:10.1029/JA085iA03p01171.

Neubauer, F. M. (1998), The sub-Alfvénic interaction of the Galilean satellites with the Jovian magnetosphere, *Journal of Geophysical Research*, *103*(E9), 19,843–19,866, doi:10.1029/97JE03370.

Ng, C. S., and A. Bhattacharjee (1997), Scaling of anisotropic spectra due to the weak interaction of shear-Alfvén wave packets, *Physics of Plasmas*, *4*(3), 605–610, doi:10.1063/1.872158.

Nichols, J., and S. Cowley (2004), Magnetosphere-ionosphere coupling currents in Jupiter's middle magnetosphere: effect of precipitation-induced enhancement of the ionospheric Pedersen conductivity, *Annales Geophysicae*, *22*(5), 1799–1827, doi:10.5194/angeo-22-1799-2004.

Nishida, A. (1976), Outward diffusion of energetic particles from the Jovian radiation belt, *Journal of Geophysical Research*, *81*(10), 1771, doi:10.1029/JA081i010p01771.

Paschmann, G., S. Haaland, and R. Treumann (2003), *Auroral Plasma Physics*, vol. 103, Kluwer Academic Publishers, doi:10.1007/978-94-007-1086-3.

Pétri, J., and J. G. Kirk (2007), Numerical solution of the linear dispersion relation in a relativistic pair plasma, *Plasma Physics and Controlled Fusion*, *49*(3), 297–308, doi:10.1088/0741-3335/49/3/008.

Piddington, J. H., and J. F. Drake (1968), Electrodynamic Effects of Jupiter's Satellite Io, *Nature*, *217*(5132), 935–937, doi:10.1038/217935a0.

Piel, A. (2010), *Plasma Physics: An Introduction to Laboratory, Space, and Fusion Plasmas*, Springer, New York, doi:10.1007/9783642104916.

Pontius, J., D. H., and T. W. Hill (1982), Departure from corotation of the Io plasma torus: Local plasma production, *Geophysical Research Letters*, *9*(12), 1321–1324, doi:10.1029/GL009i012p01321.

Prangé, R., D. Rego, D. Southwood, P. Zarka, S. Miller, and W. Ip (1996), Rapid energy dissipation and variability of the Io-Jupiter electrodynamic circuit, *Nature*, *380*(6573), 460, doi:10.1038/380460a0.

Prangé, R., D. Rego, L. Pallier, J. Connerney, P. Zarka, and J. Queinnec (1998), Detailed study of FUV Jovian auroral features with the post-COSTAR HST faint object camera, *Journal of Geophysical Research*, *103*(E9), 20,195–20,216, doi:10.1029/98JE01128.

Quataert, E. (1998), Particle Heating by Alfvénic Turbulence in Hot Accretion Flows, *The Astrophysical Journal*, *500*(2), 978–991, doi:10.1086/305770.

Ray, L. C., Y. J. Su, R. E. Ergun, P. A. Delamere, and F. Bagenal (2009), Current-voltage relation of a centrifugally confined plasma, *Journal of Geophysical Research (Space Physics)*, *114*(A4), A04214, doi:10.1029/2008JA013969.

Ray, L. C., R. E. Ergun, P. A. Delamere, and F. Bagenal (2010), Magnetosphere-ionosphere coupling at Jupiter: Effect of field-aligned potentials on angular momentum transport, *Journal of Geophysical Research (Space Physics)*, *115*(A9), A09211, doi:10.1029/2010JA015423.

Sahraoui, F., G. Belmont, and M. L. Goldstein (2012), New Insight into Short-wavelength Solar Wind Fluctuations from Vlasov Theory, *The Astrophysical Journal*, *748*(2), 100, doi:10.1088/0004-637X/748/2/100.

Sandel, B. R., et al. (1979), Extreme Ultraviolet Observations from Voyager 2 Encounter with Jupiter, *Science*, *206*(4421), 962–966, doi:10.1126/science.206.4421.962.

Satoh, T., J. E. P. Connerney, and R. L. Baron (1996), Emission Source Model of Jupiter's H_3^+ Aurorae: A Generalized Inverse Analysis of Images, *Icarus*, *122*(1), 1–23, doi:10.1006/icar.1996.0106.

Saur, J. (2004), Turbulent Heating of Jupiter's Middle Magnetosphere, *The Astrophysical Journal*, *602*(2), L137–L140, doi:10.1086/382588.

Saur, J. (2021), Turbulence in the Magnetospheres of the Outer Planets, *Frontiers in Astronomy and Space Sciences*, *8*, 56, doi:10.3389/fspas.2021.624602.

Saur, J., H. Politano, A. Pouquet, and W. H. Matthaeus (2002), Evidence for weak MHD turbulence in the middle magnetosphere of Jupiter, *Astronomy & Astrophysics*, *386*, 699–708, doi:10.1051/0004-6361:20020305.

Saur, J., A. Pouquet, and W. H. Matthaeus (2003), An acceleration mechanism for the generation of the main auroral oval on Jupiter, *Geophysical Research Letters*, *30*(5), 1260, doi:10.1029/2002GL015761.

Saur, J., F. M. Neubauer, J. E. P. Connerney, P. Zarka, and M. G. Kivelson (2004), Plasma interaction of Io with its plasma torus, in *Jupiter: The Planet, Satellites and Magnetosphere*, vol. 1, pp. 537–560, Cambridge University Press.

Saur, J., T. Grambusch, S. Duling, F. M. Neubauer, and S. Simon (2013), Magnetic energy fluxes in sub-Alfvénic planet star and moon planet interactions, *Astronomy & Astrophysics*, *552*, A119, doi:10.1051/0004-6361/201118179.

Saur, J., C. Fischer, A. Wennmacher, P. D. Feldman, L. Roth, D. F. Strobel, and A. Reiners (2018a), The UV Spectrum of the Ultracool Dwarf LSR J1835+3259 Observed with the Hubble Space Telescope, *The Astrophysical Journal*, *859*(1), 74, doi:10.3847/1538-4357/aabb55.

Saur, J., et al. (2018b), Wave-Particle Interaction of Alfvén Waves in Jupiter's Magnetosphere: Auroral and Magnetospheric Particle Acceleration, *Journal of Geophysical Research (Space Physics)*, *123*(11), 9560–9573, doi:10.1029/2018JA025948.

Saur, J., C. Willmes, C. Fischer, A. Wennmacher, L. Roth, A. Youngblood, D. F. Strobel, and A. Reiners (2021), Brown dwarfs as ideal candidates for detecting UV aurora outside the Solar System: Hubble Space Telescope observations of 2MASS J1237+6526, *Astronomy and Astrophysics*, *655*, A75, doi:10.1051/0004-6361/202040230.

Schekochihin, A. A., S. C. Cowley, W. Dorland, G. W. Hammett, G. G. Howes, E. Quataert, and T. Tatsuno (2009), Astrophysical Gyrokinetics: Kinetic and Fluid Turbulent Cascades in Magnetized Weakly Collisional Plasmas, *The Astrophysical Journal Supplement Series*, *182*(1), 310–377, doi:10.1088/0067-0049/182/1/310.

Schreiner, A., and J. Saur (2017), A Model for Dissipation of Solar Wind Magnetic Turbulence by Kinetic Alfvén Waves at Electron Scales: Comparison with Observations, *The Astrophysical Journal*, *835*(2), 133, doi:10.3847/1538-4357/835/2/133.

Scudder, J. D., E. C. Sittler, and H. S. Bridge (1981), A survey of the plasma electron environment of Jupiter: A view from Voyager, *Journal of Geophysical Research*, *86*(A10), 8157–8179, doi:10.1029/JA086iA10p08157.

Sittler, E. C., and D. F. Strobel (1987), Io plasma torus electrons: Voyager 1, *Journal of Geophysical Research*, *92*(A6), 5741–5762, doi:10.1029/JA092iA06p05741.

Stasiewicz, K., et al. (2000), Small Scale Alfvénic Structure in the Aurora, *Space Science Reviews*, *92*, 423–533.

Stéfant, R. J. (1970), Alfvén Wave Damping from Finite Gyroradius Coupling to the Ion Acoustic Mode, *Physics of Fluids*, *13*(2), 440–450, doi:10.1063/1.1692938.

Stix, T. H. (1992), *Waves in plasmas*, Springer-Verlag, New York.

Streltsov, A. V., W. Lotko, J. R. Johnson, and C. Z. Cheng (1998), Small-scale, dispersive field line resonances in the hot magnetospheric plasma, *Journal of Geophysical Research*, *103*(A11), 26,559–26,572, doi:10.1029/98JA02679.

Su, Y.-J. (2009), Electromagnetic interaction between Jupiter's ionosphere and the Io plasma torus, in *Cosmic Magnetic Fields: From Planets, to Stars and Galaxies*, vol. 259, edited by K. G. Strassmeier, A. G. Kosovichev, and J. E. Beckman, pp. 271–282, doi:10.1017/S1743921309030610.

Su, Y.-J., R. E. Ergun, F. Bagenal, and P. A. Delamere (2003), Io-related Jovian auroral arcs: Modeling parallel electric fields, *Journal of Geophysical Research (Space Physics)*, *108*(A2), 1094, doi:10.1029/2002JA009247.

Su, Y.-J., S. T. Jones, R. E. Ergun, F. Bagenal, S. E. Parker, P. A. Delamere, and R. L. Lysak (2006), Io-Jupiter interaction: Alfvén wave propagation and ionospheric Alfvén resonator, *Journal of Geophysical Research (Space Physics)*, *111*(A6), A06211, doi:10.1029/2005JA011252.

Sulaiman, A. H., et al. (2020), Wave-Particle Interactions Associated With Io's Auroral Footprint: Evidence of Alfvén, Ion Cyclotron, and Whistler Modes, *Geophysical Research Letters*, *47*(22), e88432, doi:10.1029/2020GL088432.

Swanson, D. (2008), *Plasma Kinetic Theory*, Chapman and Hall/CRC, doi:10.1201/b15901.

Szalay, J. R., et al. (2018), In Situ Observations Connected to the Io Footprint Tail Aurora, *Journal of Geophysical Research (Planets)*, *123*(11), 3061–3077, doi:10.1029/2018JE005752.

Szalay, J. R., et al. (2020a), Proton Acceleration by Io's Alfvénic Interaction, *Journal of Geophysical Research (Space Physics)*, *125*(1), e27314, doi:10.1029/2019JA027314.

Szalay, J. R., et al. (2020b), A New Framework to Explain Changes in Io's Footprint Tail Electron Fluxes, *Geophysical Research Letters*, *47*(18), e89267, doi:10.1029/2020GL089267.

Tao, C., F. Sahraoui, D. Fontaine, J. Patoul, T. Chust, S. Kasahara, and A. Retinò (2015), Properties of Jupiter's magnetospheric turbulence observed by the Galileo spacecraft, *Journal of Geophysical Research (Space Physics)*, *120*(4), 2477–2493, doi:10.1002/2014JA020749.

Thorne, R. M. (1983), *Physics of the Jovian magnetosphere. 12. Microscopic plasma processesin the Jovian magnetosphere.*, pp. 454–488, Cambridge University Press.

Treumann, R., and W. Baumjohann (1997), *Advanced Space Plasma Physics*, Imperial College Press, doi:10.1142/p020.

Tsurutani, B. T., et al. (1997), Plasma wave characteristics of the Jovian magnetopause boundary layer: Relationship to the Jovian aurora?, *Journal of Geophysical Research*, *102*(A3), 4751–4764, doi:10.1029/96JA02785.

Van Helden, A. (1989), *Galileo Galilei: Sidereus Nuncius, or, The Sidereal Messenger*, University of Chicago Press, Chicago.

Vasavada, A. R., A. H. Bouchez, A. P. Ingersoll, B. Little, C. D. Anger, and Galileo SSI Team (1999), Jupiter's visible aurora and Io footprint, *Journal of Geophysical Research*, *104*(E11), 27,133–27,142, doi:10.1029/1999JE001055.

Vasyliunas, V. M. (1983), *Physics of the Jovian magnetosphere. 11. Plasma distribution and flow.*, pp. 395–453, Cambridge University Press.

Verscharen, D., K. G. Klein, B. D. G. Chandran, M. L. Stevens, C. S. Salem, and S. D. Bale (2018), ALPS: the Arbitrary Linear Plasma Solver, *Journal of Plasma Physics*, *84*(4), 905840403, doi:10.1017/S0022377818000739.

Vogt, M. F., S. Gyalay, E. A. Kronberg, E. J. Bunce, W. S. Kurth, B. Zieger, and C. Tao (2019), Solar Wind Interaction With Jupiter's Magnetosphere: A Statistical Study of Galileo In Situ Data and Modeled Upstream Solar Wind Conditions, *Journal of Geophysical Research (Space Physics)*, *124*(12), 10,170–10,199, doi:10.1029/2019JA026950.

von Papen, M., and J. Saur (2015), Forward Modeling of Reduced Power Spectra from Three-dimensional k-space, *The Astrophysical Journal*, *806*(1), 116, doi:10.1088/0004-637X/806/1/116.

von Papen, M., J. Saur, and O. Alexandrova (2014), Turbulent magnetic field fluctuations in Saturn's magnetosphere, *Journal of Geophysical Research (Space Physics)*, *119*(4), 2797–2818, doi:10.1002/2013JA019542.

Wang, C. B., C. S. Wu, and P. H. Yoon (2006), Heating of Ions by Alfvén Waves via Nonresonant Interactions, *Physical Review Letters*, *96*(12), 125001, doi:10.1103/PhysRevLett.96.125001.

Weiss, J. W. (2004), Appendix 2: Planetary parameters, in *Jupiter. The Planet, Satellites and Magnetosphere*, vol. 1, pp. 699–706, Cambridge University Press.

Wu, D. J., and C. Fang (1999), Two-Fluid Motion of Plasma in Alfvén Waves and the Heating of Solar Coronal Loops, *The Astrophysical Journal*, *511*(2), 958–964, doi:10.1086/306712.

Research Data Management

The data, codes and scripts that were produced and written for this thesis are archived on the server
`neptun@geo.Uni-koeln.DE`
via the path
`/raid0/archivierung/absolventen_archivierung/2022_PhD_SJanser_Aurora_Jupiter`.
All data can be accessed via the Institute for Geophysics and Meteorology at the University of Cologne.
Necessary information about the structure of the archive are summarized in a *README*.
The overall structure consists of two folders. The folder `Codes_and_Scripts` archives the necessary codes and scripts that we used to simulate physical processes, analyze data and generate images. The folder `modeling_data` stores the results from the modeling runs used for analysis.

Acknowledgements

Last but not least, I would like to thank

- Prof. Dr. Joachim Saur for giving me the opportunity to work on this fascinating project and all the support and supervision over the last years. Furthermore, I would like to thank him for kicking off and establishing contacts and collaborations with other scientists in the field. I am also grateful to him for offering me the possibility to work in the office during the pandemic.
- Prof. Dr. Bülent Tezkan for being the second supervisor.
- Dr. Daniel Verscharen for his interest and collaboration in our project.
- Dr. Jamey Szalay, Dr. Ali Sulaiman and Dr. George Clark for collaboration on interesting projects regarding Juno data.
- Prof. Dr. Robert Lysak for an interesting discussion during the online MOP meeting.
- all members of the "Eties" and "Ageos" working groups for wonderful years. Special thanks go to Christian Fischer, Stephan Schlegel, Stefan Schöttle, Clarissa Willmes, Wiebke Mörbe, Janina Hansen, Kendra Gilmore and Sophia Schiebel for fun times and having sympathetic ears whenever needed.
- the GSGS, in particular Dr. Karin Boessenkool for organizing many interesting courses.
- Christian, Stephan, Kendra, Stefan, Annika, Sebastian and Gianna for proof-reading.
- the German Research Foundation (DFG) who has partly funded this project.
- and finally my family!

Eidesstattliche Erklärung

Hiermit versichere ich an Eides statt, dass ich die vorliegende Dissertation selbstständig und ohne die Benutzung anderer als der angegebenen Hilfsmittel und Literatur angefertigt habe. Alle Stellen, die wörtlich oder sinngemäß aus veröffentlichten und nicht veröffentlichten Werken dem Wortlaut oder dem Sinn nach entnommen wurden, sind als solche kenntlich gemacht. Ich versichere an Eides statt, dass diese Dissertation noch keiner anderen Fakultät oder Universität zur Prüfung vorgelegen hat; dass sie - abgesehen von unten angegebenen Teilpublikationen und eingebundenen Artikeln und Manuskripten - noch nicht veröffentlicht worden ist sowie, dass ich eine Veröffentlichung der Dissertation vor Abschluss der Promotion nicht ohne Genehmigung des Promotionsausschusses vornehmen werde. Die Bestimmungen dieser Ordnung sind mir bekannt. Darüber hinaus erkläre ich hiermit, dass ich die Ordnung zur Sicherung guter wissenschaftlicher Praxis und zum Umgang mit wissenschaftlichem Fehlverhalten der Universität zu Köln gelesen und sie bei der Durchführung der Dissertation zugrundeliegenden Arbeiten und der schriftlich verfassten Dissertation beachtet habe und verpflichte mich hiermit, die dort genannten Vorgaben bei allen wissenschaftlichen Tätigkeiten zu beachten und umzusetzen. Ich versichere, dass die eingereichte elektronische Fassung der eingereichten Druckfassung vollständig entspricht.

Teilpublikationen:
Janser, S., Saur, J., Clark, G., Sulaiman, A. H., & Szalay, J. R. (2022, submitted), Properties of turbulent Alfvénic fluctuations and wave-particle interaction associated with Io's footprint tail, Journal of Geophysical Research (Space Physics).

Köln, 3. Januar 2022